

MODEL PREDICTIVE CONTROL SCHEMES FOR THE MITIGATION OF NATURAL HAZARDS: THEORETICAL AND EXPERIMENTAL STUDIES

A Dissertation

Submitted to the Graduate School
of the University of Notre Dame
in Partial Fulfillment of the Requirements
for the Degree of

Doctor of Philosophy

by

Gang Mei, B.E., M.S.

Ahsan Kareem, Director

Department of Civil Engineering and Geological Sciences

July, 2001

© Copyright by

GANG MEI

2001

All Rights Reserved

MODEL PREDICTIVE CONTROL SCHEMES FOR THE MITIGATION OF NATURAL HAZARDS: 'THEORETICAL AND EXPERIMENTAL STUDIES

Abstract

by

Gang Mei

Active and semi-active control devices, e.g., active mass dampers and dampers with controllable damping, respectively, have been studied to enhance the performance of structures during earthquakes and strong winds. Efficient control schemes are needed to drive these control devices. The focus of this study is on the development of Model Predictive Control (MPC) based schemes for earthquake and wind excited structures. The MPC scheme is based on an explicit use of a prediction model of the system response to obtain control actions by minimizing an objective function. Optimization objectives include minimization of the difference between the predicted and reference responses and minimization of the control effort subjected to prescribed constraints.

A general form of the MPC scheme was first employed for controlling building response under earthquake excitation using active control devices. The constrained MPC scheme was then investigated. This scheme takes into account hard constraints to accommodate the physical limits on the control force and structural response. In addition to the active systems, semi-active control devices, e.g., semi-active mass dampers and semi-active tuned liquid column dampers were also studied using the constrained MPC scheme.

An autoregressive (AR) model that uses real-time ground motion measurements to model ground motions as a feedforward link in the MPC based feedforward-feedback scheme was employed for controlling earthquake induced response. This MPC based feedforward-feedback scheme offers an adaptive control action essential for effectively mitigating the load effects induced by evolutionary ground motions. For wind excited structures, an efficient wind loading model based on a combination of AR and Karhunen-Loeve expansion was developed. The MPC based feedforward-feedback control scheme, based on this wind loading model, effectively reduces the wind induced structural response.

A shaking table and a small-scale structural model with an active mass damper were utilized for experimentally validating these control schemes. Experimental validation of MPC based schemes provides proof-of-concept, and facilitates prototyping of this control strategy for full-scale implementation to reduce damage caused by natural hazards through response reduction. Finally, a full-scale building for wind-excited benchmark problem was investigated to implement MPC based schemes for a range of prescribed parameters.

The numerical and experimental studies conducted here suggest that MPC is a simple, effective, economical control scheme that can take into consideration practical design and implementation issues in structural control applications. This study has laid a foundation for the development of future applications of MPC based schemes on full-scale structures.

DEDICATION

To my dear wife, Aimei

and

my parents

TABLE OF CONTENTS

TABLE OF CONTENTS	iii
LISTS OF TABLES	v
LISTS OF FIGURES	vii
ACKNOWLEDGEMENTS	xiii
CHAPTER 1	1
1.1 Literature Review	3
1.2 Overview of the Dissertation	11
CHAPTER 2	14
2.1 Problem Formulation	16
2.2 Model Predictive Control (MPC) Scheme	17
2.3 Numerical Examples and Analysis	20
2.3.1 Analysis of a Single-Story Building Using the MPC Scheme	21
2.3.2 Analysis of A Three-Story Building Using the MPC Scheme	26
2.3 Summary	29
CHAPTER 3	31
3.1 Constrained Model Predictive Control (MPC) Scheme	33
3.2 Numerical Examples and Analysis	36
3.2.1 SDOF Building using Active Tendon	36
3.2.2 Three-story Building Using Active Tendon	43
3.2.3 Three-Story Building using AMD	49
3.3 Summary	54
CHAPTER 4	56
4.1 SATMD and SATLCD Models	58
4.1.1 SATMD	58
4.1.2 SATLCD	60
4.2 Examples	63
4.2.1 SDOF System	64
4.2.2 Multi-Story Building	73
4.3 Summary	77
CHAPTER 5	78
5.1 Problem Formulation	79
5.2 Acceleration Feedback and State Estimator	79
5.3 MPC Using Acceleration Feedback	80
5.4 Numerical Examples	83
5.4.1 Active Tendon System	83
5.4.1.1 SDOF Building	83
5.4.1.2 Three-Story Building	87
5.4.2 Active Mass Damper	90

5.4.2.1 SDOF System	91
5.4.2.2 Three-Story Building	93
5.5 Summary	95
CHAPTER 6	97
6.1 Feedforward Model	98
6.1.1 Pre-Established Earthquake Model: Kanai-Tajimi	98
6.1.2 Real-time Model of Earthquake	100
6.2 Structure-Excitation Model	101
6.3 Model Predictive Control Scheme with Feedforward-Feedback Link	101
6.4 Numerical Examples and Analysis	104
6.4.1 MPC/Kanai-Tajimi Control Scheme	104
6.4.2 MPC-AR Control Scheme	108
6.4.3 Analysis of A Three-Story Building Using the MPC-AR Model	114
6.5 Summary	118
CHAPTER 7	120
7.1 Proper Orthogonal Decomposition of Wind Loading	121
7.2 Autoregressive (AR) Model	124
7.3 State-Space Model of the Wind Field	125
7.4 Wind Field For a Four-Story Building	127
7.5 Wind Load Model For Nanjing Tower	131
7.5.1 State-Space Realization of Wind Velocity	133
7.5.2 Model Reduction of State-Space Representation	142
7.6 Feedforward-Feedback Based Controller Design for Nanjing Tower	144
7.7 Summary	150
CHAPTER 8	152
8.1 Experimental Setup	152
8.2 Design of Shaking Table Operations	154
8.3 System Identification	162
8.4 MPC Using Acceleration Feedback	170
8.5 Placement of Accelerometers	178
8.6 Feedforward-Feedback Control	179
8.7 Constrained MPC Scheme	185
8.8 Summary	190
CHAPTER 9	192
9.1 Problem Description	193
9.2 Results and Discussion	197
9.2.1 Nominal Building	197
9.2.2 Buildings with +15% of Original Stiffness	199
9.3 Summary	202
CHAPTER 10	206
REFERENCES	211

LISTS OF TABLES

Table 2.1	Comparison between the uncontrolled response and MPC	24
Table 2.2	Mass, Stiffness, and Damping Matrices of the Example Building	27
Table 2.3	Response of a Three-Story Building using MPC Scheme	27
Table 3.1	Comparison between the MPC without Constraints and MPC with Constraints	37
Table 3.2	Comparison between MPC with no or weak constraints and MPC with strict constraints for a 3-story building using active tendon	44
Table 3.3	Comparison between MPC with no/weak Constraints and MPC with Constraints for a Building using AMD	50
Table 4.1	Data for the SDOF, TMD and TLCD	64
Table 4.2	Summary of Main Results using SATMD	66
Table 4.3	Summary of Main Results using SATLCD	70
Table 4.4	Responses of the five-story building	75
Table 5.1	Comparison Between MPC with State FB and MPC with Acceleration FB	84
Table 5.2	Comparison of Results Obtained from Various Accelerometer Layouts	88
Table 5.3	Comparison between the MPC with state FB and acceleration FB (AMD)	92
Table 5.4	Comparison of Results Obtained Using Various Accelerometer Layouts	95
Table 6.1	Comparison between the MPC/Kanai-Tajimi model and MPC	107
Table 6.2	Comparison between the MPC-AR model and MPC	110
Table 6.3	Performance of MPC-AR scheme under Kobe and Hachinohe earthquakes	112
Table 6.4	Comparison of MPC-AR and MPC Schemes Using a Three-Story Building	115
Table 7.1	Comparison of σ values Using Different Estimation Methods	131
Table 7.2	σ Values of Wind Velocity Using Full State-Space Representation (32 States)	141
Table 7.3	σ Values of Wind Velocity Using Six-Eigenvalue State-Space	

	Representation (12 States)	143
Table 7.4	Geometric Properties of Nanjing Tower	145
Table 7.5	Tower Response Under Different Control Schemes	150
Table 8.1	Structure Acceleration Response	176
Table 8.2	Structural Acceleration Response with Different Accelerometer Locations	179
Table 8.3	Structure Acceleration Response under Scaled El Centro Earthquake (Pseudo Real-Time MPC-AR)	180
Table 8.4	Structure Acceleration Response under Scaled Kobe Earthquake (Pseudo Real-Time MPC-AR)	183
Table 8.5	Structure Acceleration Response using Constrained MPC	189
Table 9.1	Evaluation criteria for across-wind excitations	203
Table 9.2	Peak Response using Passive (TMD), LQG and MPC schemes	203
Table 9.3	RMS Response using Passive (TMD), LQG and MPC schemes	204
Table 9.4	Evaluation criteria for across-wind excitations	204
Table 9.5	Results of MPC for +15% building	205
Table 9.6	Results of MPC for -15% building	205

LISTS OF FIGURES

Figure 1.1	(a) Citicorp Center using TMD.....	6
Figure 1.1	(b) Shinjuku Tower using HMD.....	6
Figure 2.1	(a) Basic MPC scheme.....	18
Figure 2.1	(b) FF-FB control system.....	18
Figure 2.2	SDOF active tendon system.....	21
Figure 2.3	Comparison of uncontrolled building displacement with MPC scheme.	22
Figure 2.4	Comparison of uncontrolled building acceleration with MPC scheme.	23
Figure 2.5	Control force using MRC scheme.....	23
Figure 2.6	Comparison of RMS of displacement and control force between MPC and H2 control	25
Figure 2.7	Comparison between MPC and H2 control.	26
Figure 2.8	3-story building using active tendon control	26
Figure 2.9	Comparison of uncontrolled top floor displacement with MPC scheme.	28
Figure 2.10	Comparison of uncontrolled top floor acceleration with MPC scheme.	28
Figure 2.11	Control force using MPC scheme.....	29
Figure 3.1	Building displacement under no control and under MPC with no constraints and weak constraints.....	38
Figure 3.2	Building acceleration under no control and under MPC with no constraints and weak constraints.....	38
Figure 3.3	Control force under MPC (no constraints and weak constraints)	39
Figure 3.4	Increment of control force under MPC (no constraints and weak constraints).....	39
Figure 3.5	Building displacement under no control and under MPC with strict constraints.	40
Figure 3.6	Building acceleration under no control and under MPC with strict constraints.	41
Figure 3.7	Control force under MPC with strict constraints	41
Figure 3.8	Increment of control force under MPC with strict constraints.....	42
Figure 3.9	Building displacement under no control and under	

	MPC with no/weak constraints.....	45
Figure 3.10	Building acceleration under no control and under MPC with no/weak constraints.....	45
Figure 3.11	Control force under MPC with no/weak constraints.....	46
Figure 3.12	Increment of control force under MPC with no/weak constraints.....	46
Figure 3.13	Building displacement under no control and under MPC with strict constraints	47
Figure 3.14	Building acceleration under no control and under MPC with strict constraints	47
Figure 3.15	Control force under MPC with strict constraints	48
Figure 3.16	Increment of control force under MPC with strict constraints.....	48
Figure 3.17	3-story building using AMD.....	49
Figure 3.18	Building displacement under no control and under MPC with strict constraints	51
Figure 3.19	Building acceleration under no control and under MPC with strict constraints	51
Figure 3.20	Control force under MPC with strict constraints	52
Figure 3.21	Increment of control force under MPC with strict constraints.....	52
Figure 3.22	Displacement of AMD under MPC with no constraints.....	53
Figure 3.23	Displacement of AMD under MPC with strict constraints.....	53
Figure 4.1	SDOF system with SATMD	59
Figure 4.2	Semi-active actuator.....	59
Figure 4.3	SDOF system with SATLCD	60
Figure 4.4	Time-varying constraints using SATMD.....	65
Figure 4.5	Building displacement vs. time using active and SATMD control based on MPC constrained scheme.....	67
Figure 4.6	Control force vs. time: Active Control force based on MPC constrained scheme	67
Figure 4.7	SA Control force based on MPC constrained scheme.....	68
Figure 4.8	Time-varying constraint using SATLCD.....	69
Figure 4.9	Displacement of SATLCD using Clipped-LQR and MPC with constraints	71
Figure 4.10	Head loss verses time.....	71
Figure 4.11	Control force of SATLCD using Clipped-LQR and MPC scheme consider constraints.....	72
Figure 4.12	Performance index vs. using SATLCD based on MPC scheme.....	72
Figure 4.13	Comparison of the simulated and target PSD of wind velocity at 5-th level.	74
Figure 4.14	Time history of wind velocity at 5-th level.....	74
Figure 4.15	Comparison of displacement responses under no control, passive control, clipped LQR, and constrained MPC	76

Figure 4.16	Control forces under clipped LQR and constrained MPC scheme.....	76
Figure 5.1	Transfer function from ground acceleration to floor acceleration.....	85
Figure 5.2	Comparison of uncontrolled and controlled displacement with acceleration FB.....	85
Figure 5.3	Comparison of uncontrolled and controlled acceleration with acceleration FB.....	86
Figure 5.4	Control force for MPC acceleration FB.....	86
Figure 5.5	Bode plot of ground motion to the 1st floor acceleration (All floor feedback).....	89
Figure 5.6	Bode plot of ground motion to 3rd floor acceleration (All floor feedback).....	89
Figure 5.7	Uncontrolled and controlled third floor acceleration.....	90
Figure 5.8	Control force using active tendon.....	90
Figure 5.9	SDOF building using AMD.....	91
Figure 5.10	Bode plot of ground motion to floor acceleration using AMD.....	92
Figure 5.11	Uncontrolled and controlled floor acceleration using AMD.....	93
Figure 5.12	Bode plot of ground motion to the 1st floor acceleration (All floor feedback using AMD).....	94
Figure 5.13	Bode plot of ground motion to the 3rd floor acceleration (All floor feedback using AMD).....	94
Figure 6.1	FF-FB control system	102
Figure 6.2	Displacement response without control and with MPC/Kanai-Tajimi scheme.....	105
Figure 6.3	Displacement response using MPC/Kanai-Tajimi and MPC schemes.....	106
Figure 6.4	Acceleration using MPC/Kanai-Tajimi model and MPC schemes.....	106
Figure 6.5	Control forces using MPC/Kanai-Tajimi model and MPC schemes.....	107
Figure 6.6	1940 El Centro earthquake.....	108
Figure 6.7	Comparison of displacement response without control and with MPC-AR scheme.....	109
Figure 6.8	Comparison of acceleration response without control and with MPC-AR scheme.....	109
Figure 6.9	Comparison of displacement response between MPC-AR and MPC schemes.....	110
Figure 6.10	Comparison of acceleration response between MPC-AR and MPC schemes.....	111
Figure 6.11	Comparison of control forces between MPC-AR and MPC schemes.....	111
Figure 6.12	Control performance of LQG-AR and MPC-AR with different prediction and control horizons.....	113

Figure 6.13	Displacement under Kobe earthquake without control and with MPC-AR scheme.....	113
Figure 6.14	Displacement under Hachinohe earthquake without control and with MPC-AR scheme.	114
Figure 6.15	Comparison of first floor displacement between no control and MPC-AR scheme.....	115
Figure 6.16	Comparison of top floor displacement between no control and MPC-AR scheme.....	116
Figure 6.17	Comparison of first floor acceleration between no control and MPC-AR scheme.....	116
Figure 6.18	Comparison of top floor acceleration between no control and MPC-AR scheme.....	117
Figure 6.19	Control force using MRC-AR scheme.....	117
Figure 7.1	Elements of first eigenvector at different frequencies	123
Figure 7.2	Eigenvalues of XPSD at different frequencies	123
Figure 7.3	Time histories of the processes whose PSDs are the eigenvalues of the wind velocity XPSD, $S(f)$	129
Figure 7.4	Time histories of wind velocity at 1st, 2nd, 3rd and 4th floors generated by the state-space approach.	129
Figure 7.5	XPSDs of the target and the simulated velocities. (1) 1-1 floor XPSD. (2) 1-2 floor XPSD. (3) 1-3 floor XPSD. (4) 1-4 floor XPSD.....	130
Figure 7.6	Nanjing Tower --- lumped 16 degree of freedom representation.	132
Figure 7.7	First row of XPSD, $S(f)$	133
Figure 7.8	Comparison between the target XPSD $S_{3-3}(f)$ (dashed line) and the simulated XPSD $S_{ww3-3}(f)$ (solid line).....	134
Figure 7.9	Comparison between the target XPSD $S_{6-6}(f)$ (dashed line) and the simulated XPSD $S_{ww6-6}(f)$ (solid line).....	134
Figure 7.10	Comparison between the target XPSD $S_{14-14}(f)$ (dashed line) and the simulated XPSD $S_{ww14-14}(f)$ (solid line).	135
Figure 7.11	Comparison between the target XPSD $S_{16-16}(f)$ (dashed line) and the simulated XPSD $S_{ww16-16}(f)$ (solid line).	135
Figure 7.12	Comparison between the target XPSD $S_{1-2}(f)$ (dashed line) and simulated PSD $S_{ww1-2}(f)$ (solid line).....	137
Figure 7.13	Comparison between the target XPSD $S_{1-3}(f)$ (dashed line) and simulated PSD $S_{ww1-3}(f)$ (solid line).....	137
Figure 7.14	Comparison between the target XPSD $S_{2-3}(f)$ (dashed line) and simulated PSD $S_{ww2-3}(f)$ (solid line).....	138
Figure 7.15	Comparison between the target XPSD $S_{5-10}(f)$ (dashed line) and simulated PSD $S_{ww5-10}(f)$ (solid line).	138
Figure 7.16	Comparison between the target XPSD $S_{1-16}(f)$ (dashed line) and simulated XPSD $S_{ww1-16}(f)$ (solid line) in log-log coordinate.....	139
Figure 7.17	Comparison between the target XPSD $S_{1-16}(f)$ (dashed line) and simulated XPSD $S_{ww1-16}(f)$ (solid line)	

	in linear coordinate.....	139
Figure 7.18	Time histories of wind velocity at 1st, 5th, 10th and 16th levels of Nanjing Tower generated by state-space representation.	140
Figure 7.19	Acceleration PSD at the 10th level.....	148
Figure 7.20	Acceleration PSD at the 12th level.....	148
Figure 7.21	Acceleration PSD at the 16th level.....	149
Figure 7.22	Control force PSD.....	149
Figure 8.1	Experiment building and Active Mass Damper.....	153
Figure 8.2	PID design for shaking table.....	156
Figure 8.3	Shaking table response with step displacement command	157
Figure 8.4	Shaking table response with sinesoid wave displacement command	157
Figure 8.5	Shaking table transfer function: magnitude and phase plot.....	158
Figure 8.6	Diagram for shaking table design to get desired acceleration.....	158
Figure 8.7	Displacement command for El Centro earthquake ground acceleration	159
Figure 8.8	Measured shaking table acceleration simulating the 10% scaled El Centro earthquake using inverse transfer function	159
Figure 8.9	The 10% scaled El Centro earthquake (target)	160
Figure 8.10	Diagram for shaking table design using transfer function iteration	161
Figure 8.11	10% scaled El Centro earthquake signal and Simulated El Centro earthquake ground acceleration using transfer function iteration	161
Figure 8.12	Diagram of AMD, Structure and AMD-Structure interaction as a whole system.....	162
Figure 8.13	Transfer function from ground acceleration to the second floor acceleration.....	168
Figure 8.14	Transfer function from ground acceleration to the first floor acceleration	168
Figure 8.15	Transfer function from the AMD command to the second floor acceleration.....	169
Figure 8.16	Transfer function from the AMD command to its displacement.....	169
Figure 8.17	Transfer function from ground acceleration to the second floor acceleration.....	171
Figure 8.18	Transfer function from ground acceleration to the first floor acceleration	171
Figure 8.19	Comparison of uncontrolled and controlled second floor acceleration with acceleration FB ($R=2e5$)	172
Figure 8.20	Controlled second floor acceleration with	

	acceleration FB ($R=2e5$)	172
Figure 8.21	Comparison of uncontrolled and controlled first floor acceleration with acceleration FB ($R=2e5$).....	173
Figure 8.22	Controlled first floor acceleration with acceleration FB ($R=2e5$).....	173
Figure 8.23	Control command of AMD. ($R=2e5$)	174
Figure 8.24	Comparison of uncontrolled and controlled second floor acceleration with acceleration FB ($R=5000$).....	176
Figure 8.25	Controlled second floor acceleration with acceleration FB ($R=5000$)	177
Figure 8.26	Control command of AMD. ($R=5000$)	177
Figure 8.27	The second floor acceleration responses using MPC and MPC-AR schemes under scaled El Centro earthquake	181
Figure 8.28	The first floor acceleration responses using MPC and MPC-AR schemes under scaled El Centro earthquake	181
Figure 8.29	The control command using MPC and MPC-AR schemes under scaled El Centro earthquake	182
Figure 8.30	5% scaled Kobe earthquake signal and measured table acceleration.....	182
Figure 8.31	The second floor acceleration responses using MPC and MPC-AR schemes under scaled Kobe earthquake	184
Figure 8.32	The first floor acceleration responses using MPC and MPC-AR schemes under scaled Kobe earthquake.....	184
Figure 8.33	The control command using MPC and MPC-AR schemes under scaled Kobe earthquake.....	185
Figure 8.34	The second floor acceleration responses using constrained MPC scheme under scaled El Centro earthquake ($u \leq 0.4$) ..	186
Figure 8.35	The first floor acceleration responses using constrained MPC scheme under scaled El Centro earthquake ($u \leq 0.4$) ..	187
Figure 8.36	The control command using constrained MPC scheme under scaled El Centro earthquake ($u \leq 0.4$).....	187
Figure 8.37	The second floor acceleration using constrained MPC scheme under scaled Kobe earthquake ($u \leq 0.6$).....	188
Figure 8.38	The first floor acceleration using constrained MPC scheme under scaled Kobe earthquake ($u \leq 0.6$).....	188
Figure 8.39	The control command using constrained MPC scheme under scaled Kobe earthquake ($u \leq 0.6$).....	189
Figure 9.1	Comparison of sensitivities of different control schemes to the +15% change in stiffness	201
Figure 9.2	Comparison of sensitivities of different control schemes to the -15% change in stiffness	201

ACKNOWLEDGEMENTS

First, I would like to thank my advisor, Professor Ahsan Kareem, for his advice, encouragement, support and friendship throughout my five-year study at Notre Dame. His guidance has not only been restricted to academic matter, but also in real life experiences and general philosophy of life. His efforts to strength my communication skills through many presentations in front of TeamKareem has made a real difference for which I am deeply indebted to him. His hardworking style and serious scientific approach to problem solving has provided a good role model for me to follow in my professional career.

I would like to thank Professor Jeffrey Kantor, who introduced us to MPC and gave me advice and guidance even during his very busy schedule as Vice President and Associate Provost of the University of Notre Dame. I would also like to thank Professor Bill Spencer for his many helpful advice and guidance and Professor David Kirkner for serving as my committee and offering constructive comments. I am grateful for their efforts in reading this long dissertation despite their busy schedules.

In addition, I would like to thank my friends, Guangqiang Yang, Swaroop Yalla, Tracy Kijewski Correa, Gang Jin, Yun Chi, Dr. Yin Zhou, Dr. Xingzhong Chen, Dr. Fred Haan, Kenny Farrow, Richard Christenson, Limin Yuan, Qian Shen, Yong Gao, Hua Jiang, and many others who have helped me during the course of my study. I would also like to thank department secretaries, Tammy Youngs, Mollie Dash and Christina Negri, for their help during my stay at Notre Dame.

Finally, I would like to thank my dear wife, Aimei Zhong, for her many sacrifices. Without her love, understanding and support, this dream would not have materialized. I would also like to thank my parents, parent-in-law, brothers and all other family members for their love and support.

The financial support for this work was provided in part by the National Science Foundation Grants CMS-94-02196 and CMS-95-03779 under the NSF Structure Control Initiative. This support is gratefully acknowledged.

CHAPTER 1

INTRODUCTION

In recent years, an increasing number of high-rise buildings and long span bridges have been built to accommodate business, transportation and residential needs due to growing population. Unfortunately, the clusters of these structures are located in the regions of either high seismic activities or extreme winds. Public is becoming increasingly concerned about the safety and serviceability of structures which could be subjected to severe levels of structural motions induced by extreme events. Therefore, reducing structural load effects and structural motions due to earthquakes and strong winds is becoming a critical issue.

The concept of employing structural control to minimize structural vibration was first proposed in the 1960's and 1970's (Kobori, 1960 a, b and Yao, 1972). The collapse of buildings and bridges, and the loss of life during the Kobe, Japan (1995) and Northridge, CA (1994) earthquakes caught the attention of many researchers in civil engineering and other fields. Besides earthquakes structural control has received considerable attention in controlling motions of structures under extreme wind.

Structural control based on various passive, active, hybrid and semi-active control schemes offers attractive opportunities to mitigate damage and loss of serviceability caused by natural hazards such as earthquakes and hurricanes. In the past few decades,

passive control has gained popularity. This acceptance may be attributed to following reasons: (1) Simple operation; (2) Requirement of no external energy; (3) Stability (4) Reduction in response during most extreme events (Housner et al, 1997).

Due to the limited effectiveness in extreme events and the lack of adaptability of passive control schemes, active control devices effectively used in aerospace industry have been considered for structural applications. Numerous active and semi-active devices have been proposed and studied by researchers. Among these, the most common ones are the active bracing, active tuned mass damper, semi-active dampers including electrorheological (ER) or magnetorheological (MR) dampers (Soong, 1990; Housner et al, 1997; Spencer and Sain, 1997; Kareem et al, 1999).

Various control strategies have been formulated which include the optimal control, stochastic control, adaptive control, intelligent control, sliding mode control, robust control, and Model Predictive Control (MPC), etc. Among these schemes, MPC has been primarily used in chemical industry since 1960's, e.g., it has been used in controlling chemical reaction processes.

The advantage of using MPC lies in its ability to handle multivariable processes, input/output constraints and disturbances. MPC can simultaneously optimize the control effort and provide high-level performance with a minimum set of measurements of the system. It remains robust even in the presence of modeling errors and measurement noise.

The major objective of this dissertation is to study and develop new applications of MPC based schemes in civil engineering structures under earthquakes and winds. The MPC schemes are compared to H_2 control. Studies show that under the same performance criteria and conditions the MPC based approaches are equally effective as H_2 and LQG

methods with infinite prediction and control horizons. Next, constraints imposed on the actuator and structure are studied. MPC provides an optimal solution in the constrained space at each time instant. Then the MPC scheme is applied to a semi-actively controlled device. The acceleration feedback is used for both active tendon and active tuned mass dampers. Using both the MPC and AR models, a real-time optimization control strategy is formulated. The earthquake excitations are modeled and updated continuously in real-time based on the measured earthquake records by using an AR model. This information is used on-line in MPC to serve as the feedforward-feedback control strategy. The feedforward link is formed to add to the effectiveness of the control scheme for unusual earthquakes. Furthermore, a new numerical scheme is presented for modeling the Gaussian wind load processes through a state space representation. This method is then used in the feedforward-feedback control of structural response under wind loads. Experiment are conducted to validate the applicability of MPC scheme in scale models. In these studies, the controller-structure interaction is taken into account. Finally, A benchmark problem for the response control of wind-excited tall buildings is studied by using the MPC based schemes.

1.1 Literature Review

There are four basic kinds of structural control systems, i.e., passive control, active control, hybrid control, and semi-active control. The difference among these control systems lies in whether or not it uses an external power source to add or dissipate the energy of the structure.

Passive control does not require external power sources and cannot increase the energy of the system. The first such applied system was a base isolation system. In 1921, Frank Lloyd Wright designed the Imperial Hotel in Tokyo, which used an 8 ft. layer of soil on top of a layer of soft mud to float the building. It worked well during the 1923 Tokyo earthquake (Kelly, 1986). However, the isolation of earthquakes was not as important as the strength of the structure at that time. In the last several decades, cost and safety issues have required people to seriously consider base isolation as a way of reducing damage. One of the most common base isolation systems is the laminated rubber bearing (Kelly, 1982). This base isolation system has been used in a number of buildings in the US, Europe, Japan and New Zealand. Another kind of base isolation system involves a resilient-friction base isolation system (Mostaghel, 1987).

The Tuned Mass Damper (TMD) surfaced in the 1940's (Den Hartog, 1947), and has often been used to mitigate wind induced motion. Tuned liquid dampers have been developed and used in buildings to reduce overall response during strong wind conditions and earthquakes (Welt and Modi, 1989; Kareem, 1983,1994). Other important dampers such as the viscous fluid damper used in structural control were studied by Makris (1993), Arime (1988), Miyazaki and Mitsaaka (1992).

The energy dissipation devices have been implemented in buildings. For example, auxiliary viscoelastic dampers are introduced throughout the World Trade Center Towers in New York City and several other buildings in Seattle. TMDs have been installed in the John Hancock Tower in Boston, Citicorp Center in New York (Fig. 1.1 a) and National Memory Tower in Toronto.

However, a passive control system has limited ability because it is not able to adapt to structural changes or varying usage patterns and loading conditions. To overcome these shortcomings, active, hybrid and semi-active controls can be used. They can adapt to various operating conditions and apply external powers to generate control forces.

Active control promises to effectively minimize structural responses. It utilizes external power sources to operate actuators which generate control forces. A variety of active control devices have been discussed (Soong, 1990; Housner et al, 1990, 1993, 1994, 1997). The most commonly investigated ones are active tendon system (Roorda, 1975; Yang and Giannopoulos, 1978; Abdel-Rohman and Leipholz, 1978), active bracing system (Reinhorn et al, 1993), active tuned mass damper (Chang and Soong, 1980; Abdel-Rohman and Leipholz, 1983; Reinhorn et al, 1989), and active aerodynamic appendage mechanism (Soong and Skinner, 1981). Detailed experiments have been conducted to verify the effectiveness of these actuators (Chung, 1988, 1989; Reinhorn, 1989; Dyke, 1996). Dyke et al (1995) also considered the effects of Control-Structure-Interaction and actuator dynamics in their studies. The first application of active control system to a full-scale building was the Kyobashi Seiwa Building located in Tokyo in 1989 (Kobri, 1994). More than 20 buildings in Japan have since then been equipped with active control systems.

Since active control relies on external power, which requires routine maintenance and thus may become potentially unstable, hybrid control have been studied. It combines active and passive control systems and attempts to utilize the advantages of both methods to achieve better effects. One kind of hybrid control is Hybrid Mass Damper (HMD) which combines TMD and an active controlled actuator together. The force generated by the actuator is mainly to increase the efficiency of the TMD (Tanida, et al, 1991; Koike,

1994). A V-Shaped HMD was installed in the Shinjuka Park Tower (Fig. 1.1 (b))in Japan (Sakamoto et al, 1994). Another kind of hybrid control is in the base isolation area. An active control device is added to a base isolated structure. Better performance can thus be achieved with a small increase in cost (Reinhorn et al, 1987). Theoretical and experimental studies were performed by Kelly et al (1987), Schitendorf et al (1994), Yoshida and Wannabe (1994), Reinhorn and Riley (1994), Feng et al (1993), Yang et al (1994), etc.



Figure 1.1(a) Citicorp Center using TMD



Figure 1.1(b) Shinjuku Tower using HMD

Semi-active control devices provide some of the best features of both the passive and active control systems. Many of them can be operated by a battery, which is critical during the seismic events when the main power system fails. Semi-active control can achieve almost the same control effectiveness as the active control, and yet does not have the potential to destabilize the structure system under a variety of dynamics loading conditions (Housner et al, 1997; Dyke, 1996).

One of the semi-active devices involves the variable orifice damper (Hrovat et al, 1983; Mizuno et al, 1992; Sack et al, 1994). Another, more commonly used, semi-active device includes controllable fluid dampers. The controllable fluid can change from a free flowing linear viscous fluid to a semi-solid in milliseconds when exposed to electric (for Electrorheological (ER) fluids) or magnetic (for Magnetorheological (MR) fluids) fields. ER dampers were studied for civil engineering applications by Ehrgott and Masri (1992, 1994), Gavin et al (1994), Makris et al (1995), Masri et al (1995), etc. A MR damper was recently developed by Carlson(1994), Carlson and Weiss(1994), Spencer et al (1996, 1997), Dyke (1996) and Yang, et al. (2000 and 2001) .

Regardless of the choice of the control scheme, the system needs a certain control scheme to generate control forces which satisfy a prescribed optimization criteria. There are a variety of control schemes which are discussed below.

The linear quadratic regulator (LQR) is one of the most commonly used controller design techniques in civil engineering. An optimal controller for a deterministically excited system is generated by minimizing a quadratic performance index. By varying the weighting matrices in the performance index, a trade-off can be reached between the minimization of structural response and the minimization of control forces.

For random excitations, the counterpart of LQR is the LQG method. LQG combines LQR and optimal filtering via the Kalman-Bucy filter. In LQG control, an earthquake is assumed to be a zero mean white noise, and no ground acceleration measurement is used in structural control design. The LQG method for structural control was examined by Yang and Yao (1974). In their work, excitation was modeled as a filtered white noise. However in structural control, an earthquake is not known a priori. Suhardjo et al (1990)

used an earthquake signal with a given spectral model to formulate the so-called feedforward-feedback (FF-FB) control strategy. However, this only fits some earthquakes which have similar power spectral densities. Yamada and Kobori (1996) used the concept of on-line measurements of ground acceleration and fit them with an AR model. They employed the LQR control to obtain FF-FB gains. Their results demonstrated that the FF-FB strategy enhanced the performance of the LQR controller.

Doyle (1989) introduced the H_2 and H_∞ control methods. Suhardjo (1990) used these control methods in frequency domain design, which focused on the frequency domain characteristics of structural response. Dyke (1996) experimentally verified the H_2 method control scheme.

The sliding model control was developed by Utkin (1977) and Slotine (1984). A hyper surface, called the sliding surface, is defined in the state space. The error between the actual and desired response is zero when the state falls on the sliding surface. Different control rules are applied when the state is in a different region. Yang (1994a) showed application of the sliding model control for nonlinear and hysteretic structures. Yang (1994b) also applied it to hybrid systems and experimentally verified their effectiveness.

Intelligent controls, known as artificial neural network and fuzzy logic based control schemes, were used in structural control during the late 1980's. A neural network can model structure nonlinearity. This was investigated as an attractive option by Casciati et al (1993), Masri et al (1993) and Wen et al (1992). The effectiveness of neural network based control depends largely on the learning algorithm and the control architecture. Introduced in the 1960's, fuzzy logic control offers robustness and is capable of handling nonlinear systems. These methods require more investigations of multi-degree-of-freedom problems

because the effectiveness of the algorithm is strongly influenced by the nature of the problem. The degree of difficulty in applying the algorithm depends on the selected control strategy (Casciati and Yao, 1994).

Finally, MPC belongs to a class of algorithms that compute a sequence of manipulated variable adjustment in order to optimize the future behavior of a plant. An explicit model is used to predict the open-loop future behavior of the system over a finite time horizon from present states. The predicted behavior is then used to find a finite sequence of control actions which minimize a particular performance index within pre-specified constraints.

MPC was originally developed for process control of power plants and petroleum refineries. Now it is widely applied in chemical, food processing, automotive, aerospace and other industries. Two of the techniques used for the predictive control in MPC are the Model Algorithmic Control (MAC) and the Dynamics Matrix Control (DMC). MAC was developed by a French chemical engineer in the late 1960's, while DMC was developed by the Shell Oil Co. in the 1960's. Many improvements have subsequently been made to MAC, and this has led to a commercial package known as Identification and Command (IDCOM). Theoretical researches related to these techniques have been going on since the late 1970's (Richalet et al, 1978; Rouhani and Mehra, 1982; Cutler and Rouhani, 1980).

Garcia and Morari (1982) discussed the fundamental similarities of these algorithms for the single-input-single-output case and also noted their relationship to other forms of optimal control. They formed an overall structure for such algorithms, which they termed "Internal Model Control" (IMC), and extended it to multivariable cases (Garcia and Morari, 1985a, b).

The strength of these techniques lies in the simplicity of the algorithms and in the use of the impulse or step response model, which is usually preferred as it is more intuitive and requires less a priori information. However, these traditional MPC techniques have difficulty in handling more complex cases. These techniques contain more parameters than the state space or input-output domain because they were developed in an unconventional manner using step models. Recently, there have been efforts to interpret MPC in a state-space framework. This not only permits the use of well-known state-space theory, but also allows MPC to handle complex cases more easily. Li et al (1989) and Narratil et al (1988) showed that the step response model can be put into the general state space model structure. They presented an MPC technique using the tools available from the stochastic optimal control theory. Ricker (1990) showed how an MPC algorithm, similar to the conventional MPC techniques, can be developed based on a general state space model. Lee et al (1994), using state estimation techniques, developed an MPC based method without introducing significant additional numerical complexity.

Rodellar (1987, 1988) employed predictive control in civil engineering. In his experiment, he used a specific case of MPC which assumed the control horizon to be unity. Later Lopez-Almansa et al (1994a,b) used the predictive control in modal space and tried to control the first few mode shapes individually to reduce the overall structural response. Wang and Liu (1994) used Rodellar's predictive control method in hybrid control system which isolated the structure by frictional interface with the sliding base actively controlled by hydraulic actuators.

1.2 Overview of the Dissertation

In this dissertation, the MPC based schemes will be studied for the design of controllers for civil engineering structures.

As mentioned above, the MPC scheme is based on an explicit use of a prediction model of the system response to obtain the control action by minimizing an objective function. Optimization objectives include minimization of the difference between the predicted and reference response and minimization of the control effort subjected to certain constraints. In Chapter 2, the basic idea and formulation of MPC is presented. A single-story building and a three-story building are used as examples to demonstrate response reduction under earthquake excitation using MPC scheme. The effectiveness and convenience of the MPC scheme is compared to the H_2 based methods.

The most significant advantage of MPC lies in its ability to deal with hard constraints which is studied in Chapter 3. In reality, the control force and structure response have some limits. Beyond these limits, either the controller will not work or the structure will fail. In the MPC scheme, optimization of hard constraints is a quadratic programming problem. This allows us to simplify the constraint issue and to calculate the optimal control force in the presence of constraints.

Structural control using a semi-active device is then studied in Chapter 4. The semi-active mass damper and semi-active tuned liquid column damper are considered. The MPC scheme is employed to control the position of the valve to adjust the amount of the fluid passing by. Therefore, the damping force provided by the damper can be changed according to the changes in the external excitation.

In Chapter 5, accelerometer measurements are studied for the feedback link. However, with the exception of recent studies most civil engineering structural control schemes use state feedback because it is easy to use in the control design. In this study, an observer utilizing the Kalman-Bucy filter is designed to estimate the states of the structure and to obtain the estimator gains. The effects of sensor locations are also explored for the most effective control results.

In Chapter 6, two kinds of earthquake models are used in the feedforward-feedback control schemes. The first approach involves the use of the Kanai-Tajimi model in which a Gaussian white noise is passed through a second order digital filter to generate the ground motion. The second scheme to be considered entails real-time simulation of the ground motion. The ground motion is represented by an AR model which utilizes a previously measured ground motion record and the difference between the measured and the modeled output. It is a real-time simulation and is updated at each time increment. The earthquake model is expressed in terms of the state space representation and augmented to the equations of motion of the structure. The MPC-AR control performance index and the control force are updated at each time interval. As a result, a real-time feedforward link is added to the control scheme to develop predictive and adaptive feature to cater to seismic events with unusual and unexpected characteristics.

Besides earthquakes, wind can greatly influence the occupants' comfort, serviceability and safety of structures, especially for tall buildings and towers. Therefore, mitigating wind induced motions of structures is another important aspect of structural control. In Chapter 7, MPC is employed to reduce structural response under wind loads. A state space representation of wind velocity field is designed based on the Karhunen-Loeve eigen-

decomposition combined with an AR model. The state space description of wind is added to the equations of motion of the structure to implement the feedforward link in the feedback based MPC scheme.

In Chapter 8, experiments are conducted to validate the effectiveness of the MPC strategy using scale models. A shaking table is used to simulate a host of ground motion records. An active mass damper is adopted for this demonstration. Data acquisition and spectral analysis software toolboxes are used in the implementation of the controller. The inherent dynamic features of the actuator are considered in the control design including the controller structure interactions .

Finally, in Chapter 9, a benchmark problem of a tall building under wind excitation is studied using the MPC scheme. MPC with hard constraints is employed to simulate structural response with actuators subjected to the prescribed constraints. The MPC based schemes are tested for buildings with different stiffness to verify their robustness.

CHAPTER 2

MODEL PREDICTIVE CONTROL

Structural control is an attractive option for improving the performance of a variety of structures including bridges, tall buildings, and offshore structures. The performance of such systems under environmental loads has improved greatly as a result of theoretical and experimental research and related development efforts (Soong, 1990; Suhardjo *et al.*, 1992; Yang *et al.*, 1994; Spencer *et al.*, 1994; Suhardjo and Kareem, 1997; Kijewski *et al.*, 1998; Soong, 1998; Structural Control, 1994, 1998). A comprehensive review of theoretical developments in structural control design can be found in Housner *et al.* (1997). Details concerning their applications to real structures are reported in a recent publication (Kareem *et al.* 1999). Benchmark problems conducted to assess the performance of different control strategies can be found in Spencer *et al.* (1998). The most commonly used scheme in controller design is the Linear Quadratic Regulator (LQR). Other schemes like H_2 and H_∞ have been applied to civil engineering structures (Doyle *et al.*, 1989; Suhardjo *et al.*, 1990, 1992; Dyke, 1996; Wu *et al.*, 1998). The sliding mode control has been introduced by Utkin (1977) and its potential applications have been given by Slotine (1984) and Yang *et al.* (1994). Other schemes include the predictive control which has been used in structural applications (Rodellar *et al.* 1987). Lopez-Almansa *et al.* (1994a) employed a modal approach in which the first few modes were controlled to reduce the overall struc-

tural response. In a companion paper they presented this modal approach experimentally (Lopez-Almansa *et al.*, 1994b).

Model Predictive Control (MPC) has been effectively used in chemical, automotive, and aerospace industries (Ricker, 1990; Morari *et al.*, 1994; Qin and Badgwell, 1996; Camacho and Bordons, 1999). MPC has been shown to be feasible for structural control applications by Mei *et al.* (1998). The underlying concept of MPC is that the future behavior of a structure is predicted from its present response through a system dynamics model and control actions are determined so as to optimize future structural behavior over a prediction horizon. MPC offers a general framework of posing the control problem in the time domain and can be used to integrate issues of optimal control, stochastic control, and control of processes with time delays, and multivariable control. The concept is not limited to a particular system description, but the computation and implementation depend on the system model representation, e.g., state space, transfer matrix, etc. Inclusion of constraints is conceptually simple and can be systematically considered during the design and implementation of the controller.

In this chapter, MPC is investigated to reduce structural response under earthquake excitation. The general formulation of the non-constrained MPC scheme is discussed. A single-story and a three-story building example are used to demonstrate the methodology. The MPC controller is shown to be effective in reducing structural response under earthquakes. The results of the MPC analysis are also compared with the H_2 based control schemes. The effectiveness of MPC is demonstrated to be equivalent to that of the optimal control. This chapter lays a foundation for demonstrating the main strengths of MPC, i.e.,

computational expediency, real-time applications, intrinsic compensation for time delays, treatment of constraints, and potential for future extensions in structural control.

2.1 Problem Formulation

A building exposed to seismic excitation is modeled as an n -degree-of-freedom system:

$$\mathbf{M}\ddot{\mathbf{x}} + \mathbf{C}\dot{\mathbf{x}} + \mathbf{K}\mathbf{x} = \mathbf{F} - \mathbf{M}\mathbf{I}\ddot{x}_g \quad (2-1)$$

where \mathbf{M} , \mathbf{C} , and \mathbf{K} are the mass, damping, and stiffness matrices, respectively; \mathbf{x} , $\dot{\mathbf{x}}$, and $\ddot{\mathbf{x}}$ are the $n \times 1$ displacement, velocity and acceleration vectors relative to the ground; \mathbf{I} is the $n \times 1$ identity vector; \ddot{x}_g is the ground acceleration; and $\mathbf{F} = \mathbf{L}u$ is the $n \times 1$ control force vector generated by placing the actuator on different floors. \mathbf{L} is an $n \times m$ matrix with its elements equal to zero or one depending on the actuator placement on different floors, and u is a $m \times 1$ control force vector. Equation (2-1) is expressed in a state-space format as follows:

$$\begin{aligned} \dot{\mathbf{x}} = \begin{bmatrix} \dot{x} \\ \ddot{x} \end{bmatrix} &= \begin{bmatrix} 0 & \mathbf{I} \\ -\mathbf{M}^{-1}\mathbf{K} & -\mathbf{M}^{-1}\mathbf{C} \end{bmatrix} \begin{bmatrix} x \\ \dot{x} \end{bmatrix} + \begin{bmatrix} 0 \\ \mathbf{M}^{-1}\mathbf{L} \end{bmatrix} u + \begin{bmatrix} 0 \\ -\mathbf{I} \end{bmatrix} \ddot{x}_g \\ &= \mathbf{A}\mathbf{x} + \mathbf{B}u + \mathbf{G}\ddot{x}_g \end{aligned} \quad (2-2)$$

where \mathbf{G} is a vector that represents the seismic load distribution.

For digital implementation of a control strategy, Eq. (2-2) is expressed in discrete time as:

$$\mathbf{x}((k+1)\Delta t) = \Phi\mathbf{x}(k\Delta t) + \Gamma_u u(k\Delta t) + \Gamma_d \ddot{x}_g(k\Delta t) \quad (2-3)$$

where $\Phi = e^{A\Delta t}$ is a $2n \times 2n$ matrix; $\Gamma_u = \mathbf{P}_1 \mathbf{B}$ and $\Gamma_d = \mathbf{P}_1 \mathbf{G}$ are $2n \times m$ matrices for which $\mathbf{P}_1 = \int_0^{\Delta t} e^{A\tau} d\tau$ is a $2n \times 2n$ matrix; and Δt is the sampling time.

2.2 Model Predictive Control (MPC) Scheme

The MPC scheme is based on an explicit use of a prediction model of the system response to obtain the control actions by minimizing an objective function. Optimization objectives include minimization of the difference between the predicted and reference responses and minimization of the control effort subject to certain constraints such as limits on the control force magnitude. This concept is illustrated in Fig. 2.1 (a). First a reference trajectory, $y_r(k)$, is specified. The reference trajectory is the desired target trajectory for the process output. This is followed by an appropriate prediction model used to determine the future building responses, $\hat{y}(k)$. The prediction model must be able to include the dynamics of the system while remain simple enough for implementation and understanding. The prediction is made over a pre-established extended time horizon with the current time as the prediction origin. For a discrete time model, this means predicting $\hat{y}(k+1)$, $\hat{y}(k+2)$, ..., $\hat{y}(k+i)$ for i sample times in the future. This prediction is based on both actual past control inputs $u(k)$, $u(k-1)$, ..., $u(k-j)$ and the sequence of future control efforts that are needed to satisfy a prescribed optimization objective. The control signals that are determined by the prediction model are then applied to the structure, and the actual system output, $y(k)$, is found. Finally, the actual measurement, $y(k)$, is compared to the model prediction $\hat{y}(k)$ and the prediction error ($\hat{e}(k) = y(k) - \hat{y}(k)$) is utilized to update future predictions. The plant input can be of various types as shown in Fig. 2.1 (b).

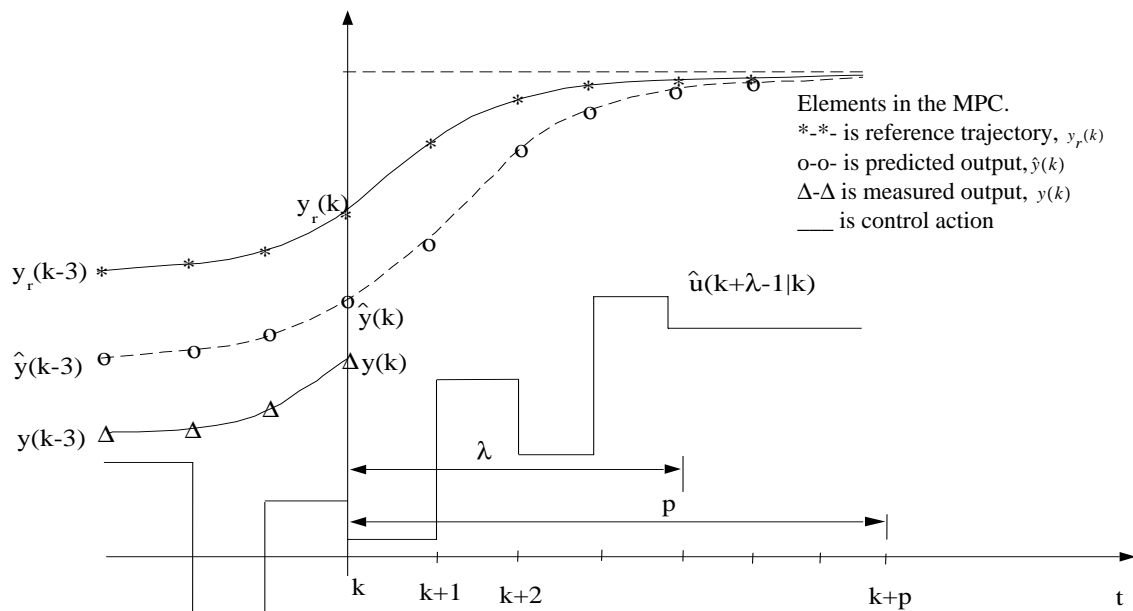


Figure 2.1(a) Basic MPC scheme

measured disturbances

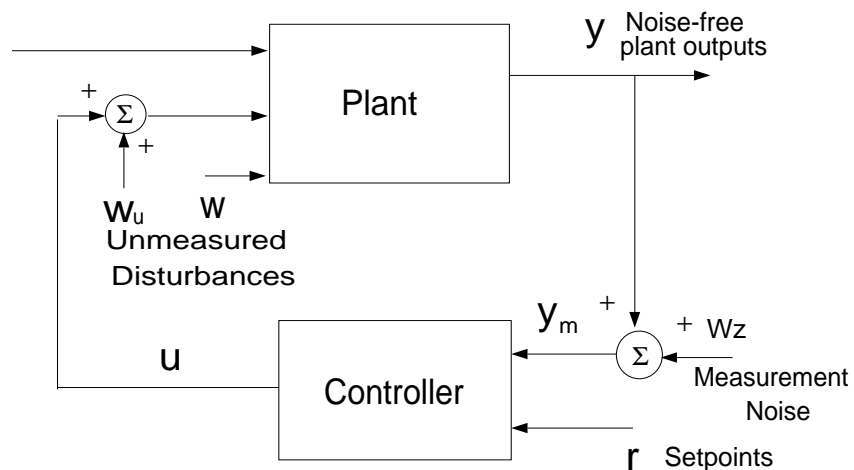


Figure 2.1 (b) FF-FB control system

In the general model predictive control, the discrete-time state-space equations of the system are expressed as:

$$\mathbf{x}(k+1) = \Phi \mathbf{x}(k) + \Gamma U(k)$$

$$\mathbf{y}(k) = C \mathbf{x}(k) + D U(k) \tag{2-4}$$

where $U(k) = \begin{bmatrix} u^T(k) & \ddot{x}_g^T(k) & w_u^T(k) & w^T(k) & w_z^T(k) \end{bmatrix}^T$; $w_u(k)$, $w(k)$, and $w_z(k)$ can be combined into a single unmeasured disturbance variable entering at the plant output. The unmeasured disturbance terms, $w_u(k)$, $w(k)$, and $w_z(k)$ are set equal to zero.

The prediction model is then expressed as:

$$\hat{x}(k+1|k) = \Phi\hat{z}(k|k-1) + \Gamma_u\hat{u}(k|k-1) + \Gamma_e\hat{e}(k|k) \quad (2-5)$$

$$\hat{y}(k|k-1) = C\hat{x}(k|k-1) \quad (2-6)$$

where $\hat{x}(k+1|k)$ estimates the state at a future sampling period, $k+1$, by using the information available at time step k ; $\hat{y}(k|k-1)$ estimates the structural output at time k based on the information at $k-1$; $C = \begin{bmatrix} I & 0 \end{bmatrix}$; Γ_e is a constant estimator gain matrix; and $\hat{e}(k|k)$ is the estimated error defined as $\hat{e}(k|k) = y(k) - \hat{y}(k|k-1)$.

Using Eq. (2-5), the process output predicted at the k -th and the subsequent time steps $k+j$, $j = 1, \dots, p$ can be expressed as a function of the current state vector $x(k)$ and the control vector $\mathbf{u}(k)$ as follows:

$$\Psi(k) = H\mathbf{u}(k) + Y_z\hat{x}(k|k-1) + Y_e\hat{e}(k|k) \quad (2-7)$$

$$\Psi(k) = \begin{bmatrix} \hat{y}^T(k+1|k) & \dots & \hat{y}^T(k+p|k) \end{bmatrix}^T, \quad \mathbf{u}(k) = \begin{bmatrix} \hat{u}(k|k) & \dots & \hat{u}(k+\lambda-1|k) \end{bmatrix}^T \quad (2-8)$$

The reference output can be written as $\Psi_r(k) = \begin{bmatrix} y_r^T(k+1|k) & \dots & y_r^T(k+p|k) \end{bmatrix}^T$, where p is the prediction horizon and λ is the control horizon.

The control objective function is given by:

$$J = \frac{1}{2}[\Psi(k) - \Psi_r(k)]^T \bar{Q}[\Psi(k) - \Psi_r(k)] + \frac{1}{2}\mathbf{u}^T(k) \bar{R}\mathbf{u}(k) \quad (2-9)$$

By minimizing J , the optimal predictive control force is given by

$$\mathbf{u} = [H^T \bar{Q} H + \bar{R}]^{-1} H^T \bar{Q} [Y_z \hat{x}(k|k-1) + Y_e \hat{e}(k|k)] \quad (2-10)$$

in which H , \bar{Q} , \bar{R} , Y_z , and Y_e are given as below:

$$H = \begin{bmatrix} H_1 & 0 & \dots & 0 \\ \dots & \dots & \dots & \dots \\ H_\lambda & H_{\lambda-1} & \dots & H_1 \\ H_{\lambda+1} & H_\lambda & \dots & H_1 + H_2 \\ \dots & \dots & \dots & \dots \\ H_p & H_{p-1} & \dots & H_1 + \dots + H_{p-\lambda} \end{bmatrix}, H_k = C \Phi^{k-1} \Gamma_u, \quad (2-11)$$

$$Y_z = [(C\Phi)^T (C\Phi^2)^T \dots (C\Phi^p)^T]^T \quad (2-12)$$

$$Y_e = \left[(C\Gamma_e)^T (C(I+\Phi)\Gamma_e)^T \dots \left(C \sum_{k=1}^p (\Phi^{k-1}) \Gamma_e \right)^T \right]^T, \quad (2-13)$$

$$\bar{Q} = \begin{bmatrix} Q & \dots & 0 \\ \dots & \dots & \dots \\ 0 & \dots & Q \end{bmatrix}, \bar{R} = \begin{bmatrix} R & \dots & 0 \\ \dots & \dots & \dots \\ 0 & \dots & R \end{bmatrix}, \quad Q = \begin{bmatrix} I & 0 \\ 0 & 0 \end{bmatrix}, \quad \text{and } R = I. \quad (2-14)$$

The MPC formulation presented in the preceding section is then utilized in the following examples to demonstrate its application to building structures.

2.3 Numerical Examples and Analysis

In this section, two examples are used to demonstrate the MPC scheme presented earlier. It is first applied to a single-story building with an active tendon system and compared

with an H_2 scheme. It is then applied to a three-story building with the active tendon system.

2.3.1 Analysis of a Single-Story Building Using the MPC Scheme

A single-story building is used here to demonstrate the MPC scheme. An active tendon system is used as the controller. The equation of motion for the single-degree-of-freedom system shown with cable bracings in Fig. 2.2 is given by:

$$\ddot{x}_0(t) + 2\zeta\omega_0\dot{x}_0(t) + \omega_0^2x_0(t) = -\ddot{x}_g(t) - \frac{4k_c \cos\alpha}{m}u_0(t) \quad (2-15)$$

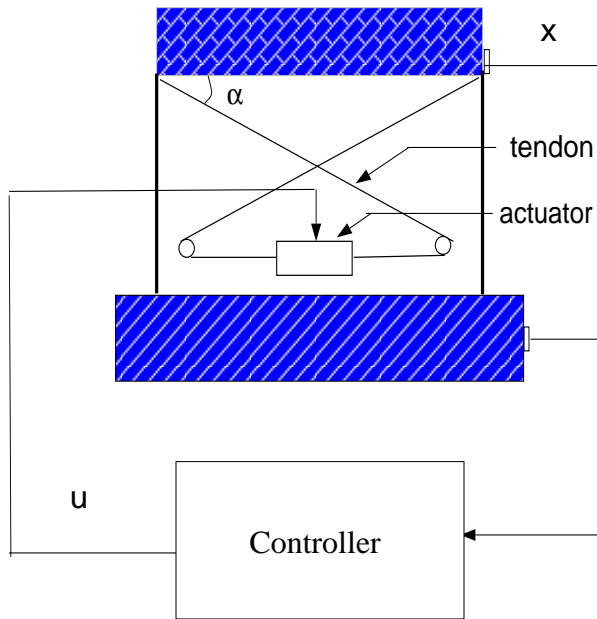


Figure 2.2 SDOF active tendon system

in which x_0 , \dot{x}_0 , and \ddot{x}_0 are the horizontal relative displacement, velocity and acceleration of the first floor; \ddot{x}_g is the ground acceleration; u_0 is the actuator displacement; m , ζ , and ω_0 are the mass, damping and angular frequency, respectively; k_c is the stiffness of the cable; and α is the cable angle. These parameters are defined as: $m = 2922.7$ kg, $\zeta = 0.0124$, $\omega_0 = 21.79$ rad/s, $k_c = 371950.8$

N/m, and $\alpha = 36^\circ$.

In this example, the 1940 El Centro earthquake record is scaled to 0.25 of its maximum intensity to excite the building. An actuator can be used to introduce tension in the cables

to meet the desired response control objective. Dynamic control-structure interaction is not considered here in this study. However, as shown in Dyke *et al.* (1995), it can be accounted for by including the dynamics of the actuator in the overall system model.

Figures 2.3 and 2.4 compare the displacement and acceleration responses obtained using MPC (solid line) with the uncontrolled response (dashed line). The corresponding control forces are shown in Fig. 2.5. Table 2.1 lists comparisons of the uncontrolled response with the controlled response using MPC based scheme. The root mean square (RMS) values of the building displacement and acceleration are reduced by 73% and 61%, respectively. The peak values of displacement and acceleration are reduced by 60% and 25%, respectively.

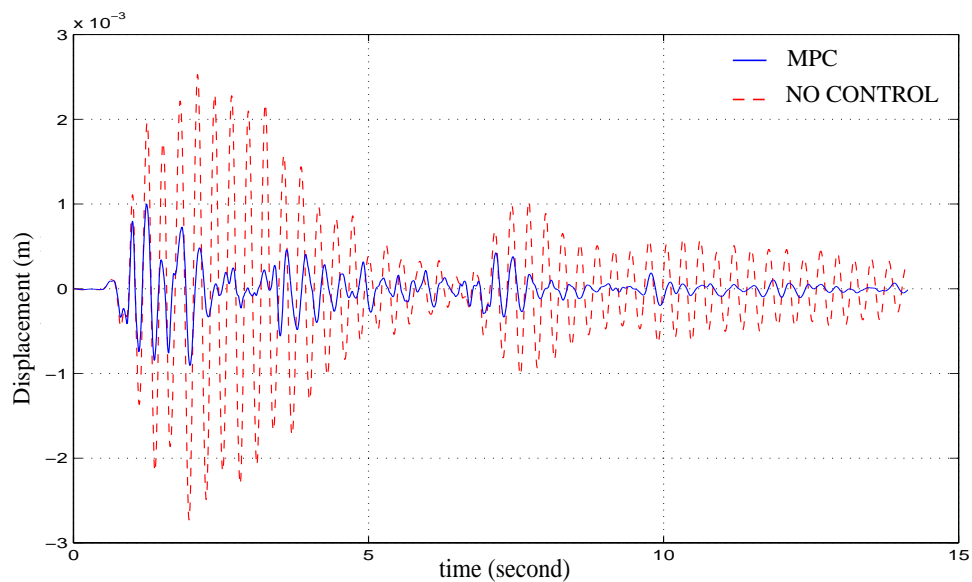


Figure 2.3 Comparison of uncontrolled building displacement with MPC scheme.

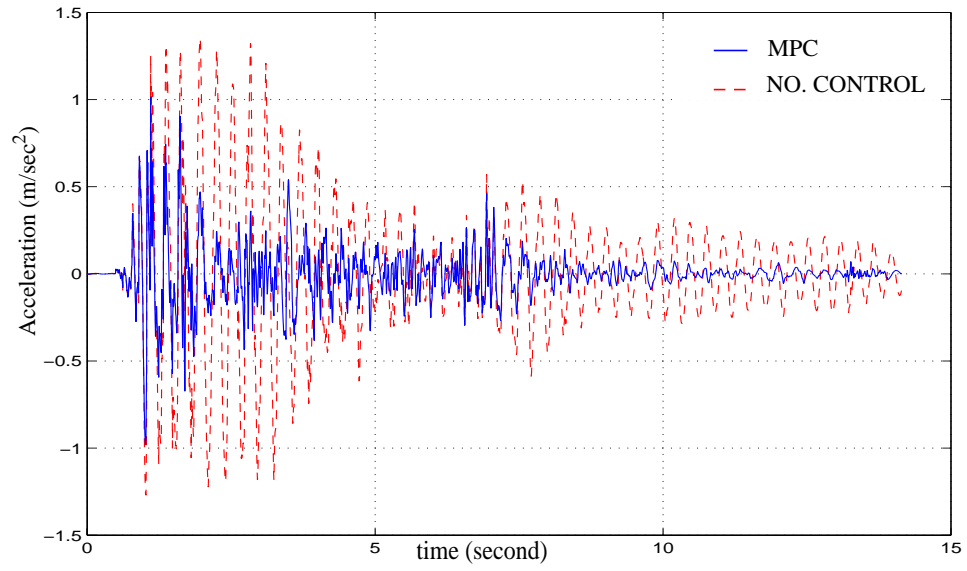


Figure 2.4 Comparison of uncontrolled building acceleration with MPC scheme.

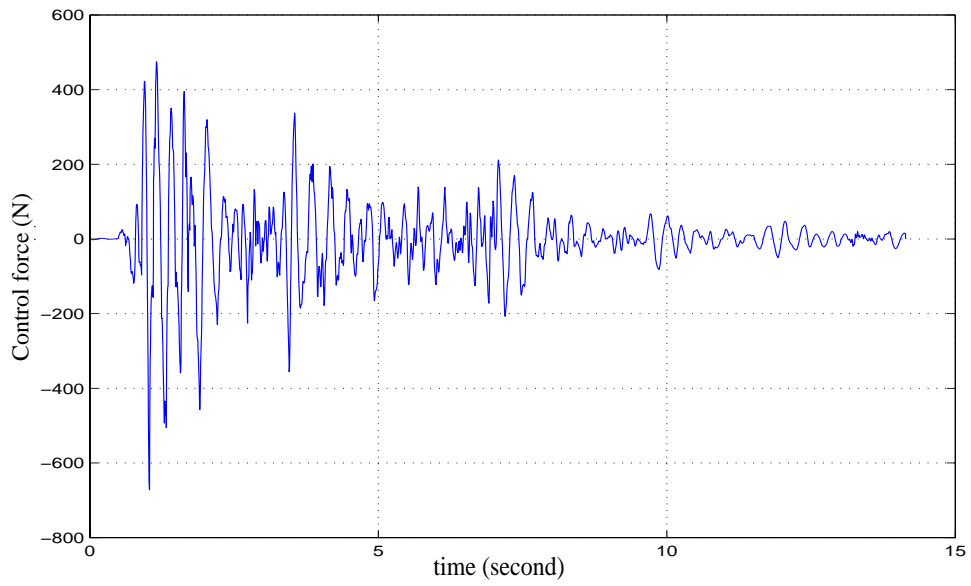


Figure 2.5 Control force using MRC scheme.

Table 2.1 Comparison between the uncontrolled response and MPC

	σ_x (cm)	$\sigma_{\dot{x}}$ (cm/s ²)	σ_u (kN)	x_{max} (cm)	\dot{x}_{max} (cm/s ²)	u_{max} (kN)
without control	7.53×10^{-2}	37.8	—	0.25	135.4	—
MPC	2.01×10^{-2}	14.6	0.099	0.10	101.5	0.672
Percentage change	73.3%	61.3%	—	60.0%	25.0%	—

The MPC scheme is also compared to the H_2 control strategies. In Fig. 2.6, the RMS values of the displacement and control force obtained by the MPC and H_2 control strategies are given as a function of the weighting parameter, R . In the MPC scheme, the value of the prediction horizon, p , is varied to be: 1, 5, 10, 15 and 20. The control horizon, λ , is kept smaller than the selected prediction horizon and chosen to be 1, 2, 2, 3 and 4 accordingly. Control forces are kept at a constant level between the end of the predictive and control horizons, i.e., $u(k + \lambda + i|k) = u(k + \lambda|k), \lambda + 1 \leq i \leq p$. Figure 2.6 shows that the control performance depends on both the value of the prediction horizon (p) and the weighting matrix (R). On one hand, the increase in R limits the control force, which results in less displacement reduction. On the other hand, an increase in the prediction horizon results in better control performance. The RMS value of the controlled displacement decreases as p increases although there is a corresponding increase in the control force. It is evident that the increase in the control force decreases the displacement response of the structure. Therefore, a better control performance is observed when the prediction horizon becomes longer.

As the prediction horizon approaches infinity, the cost function of the MPC strategy is close to the H_2 control scheme. Accordingly, the control performances of MPC and H_2 are nearly the same. Figure 2.6 shows that as the prediction horizon becomes longer, the

performance of MPC approaches that of the H_2 control scheme. Figure 2.7 shows the RMS values of control force verse displacement for the H_2 and MPC. The results demonstrate that the effectiveness of the H_2 and MPC schemes is equivalent. That is to say, by using the same control force, MPC reduces the displacement response to the same level as reached by the H_2 control scheme.

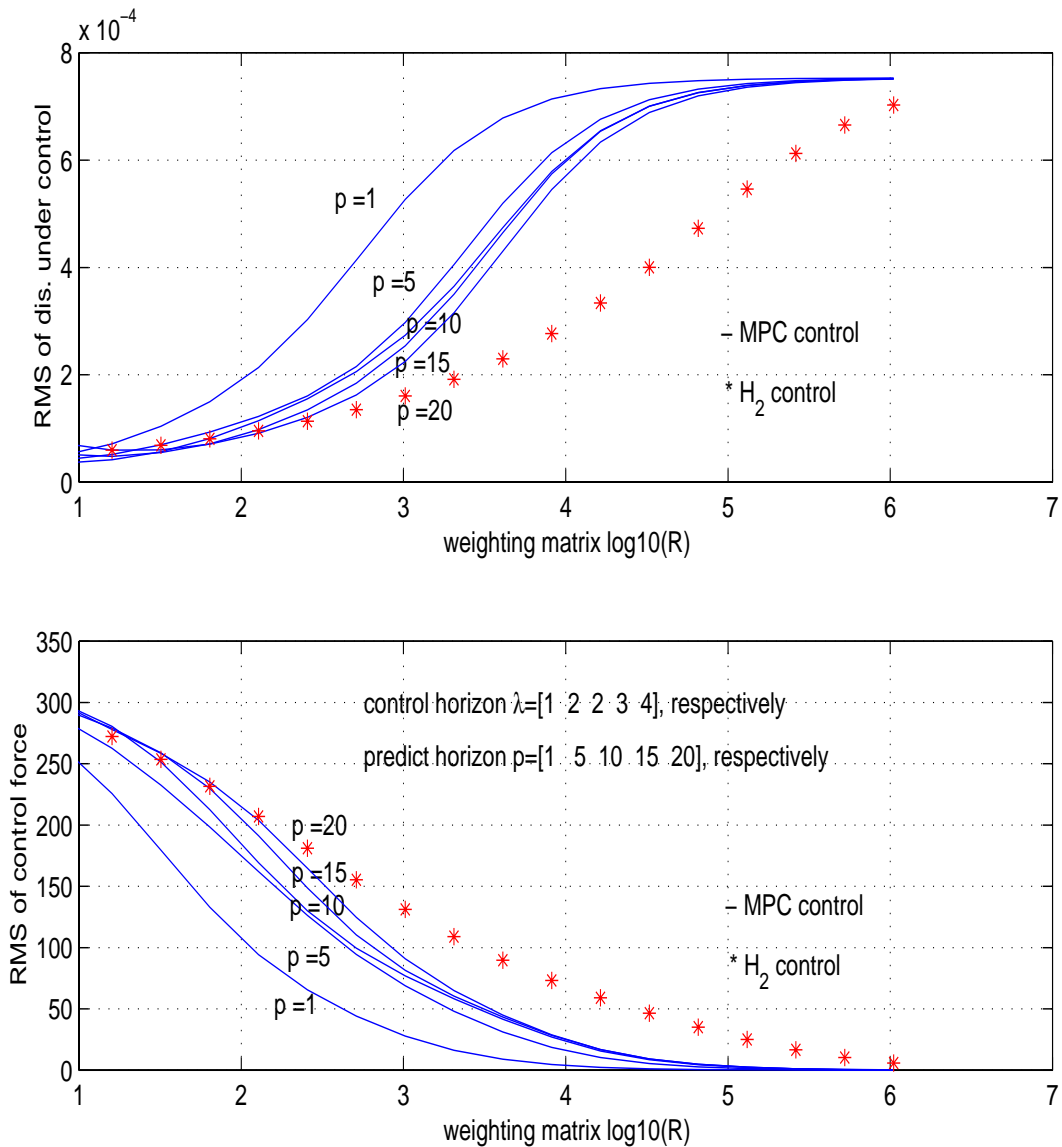


Figure 2.6 Comparison of RMS of displacement and control force between MPC and H_2 control

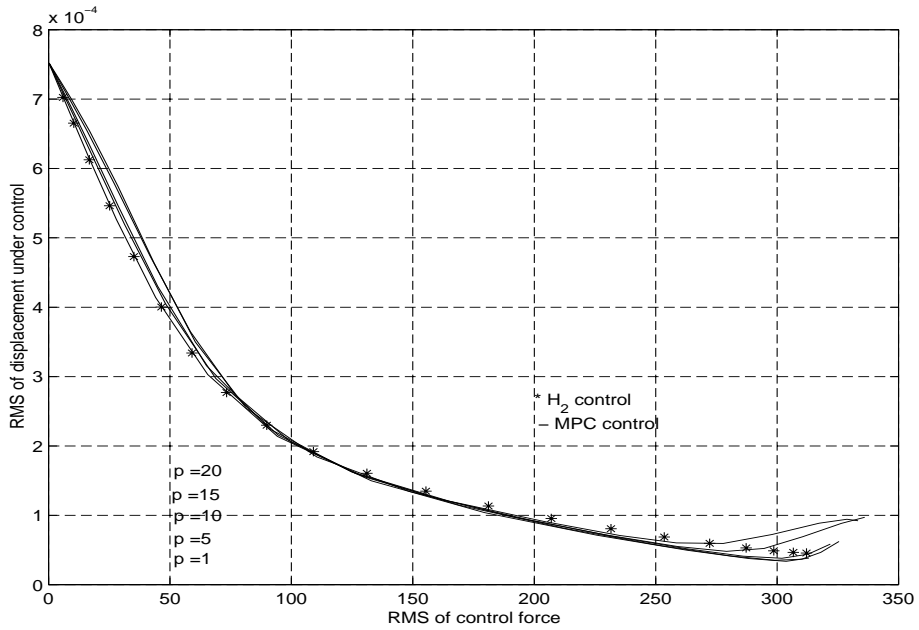


Figure 2.7 Comparison between MPC and H_2 control.

2.3.2 Analysis of A Three-Story Building Using the MPC Scheme

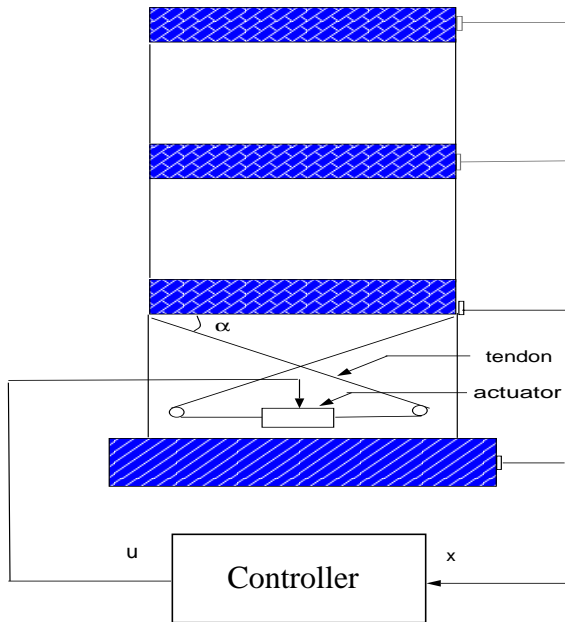


Figure 2.8 3-story building using active tendon control

In this example, a three-story building (Chung, *et al.* 1989) shown in Fig. 2.8 is used to demonstrate the MPC scheme using the state feedback obtained from each floor of the building. The mass, stiffness and damping matrices of the building are given in Table 2.2. The stiffness of the active tendon is $k_c = 3.7197 \times 10^5 (N/m)$ and $\alpha = 36^\circ$. The active tendon is installed at the first floor.

Table 2.2 Mass, Stiffness, and Damping Matrices of the Example Building

Parameters	Values
Mass Matrix M (kg)	$M = \begin{bmatrix} 974 & 0 & 0 \\ 0 & 974 & 0 \\ 0 & 0 & 974 \end{bmatrix}$
Stiffness Matrix K (N/m)	$K = \begin{bmatrix} 2.7405 & -1.6409 & 0.3690 \\ -1.6409 & 3.0209 & -1.6241 \\ 0.3690 & -1.6241 & 1.3331 \end{bmatrix} \times 10^6$
Damping Matrix C (N-sec/m)	$C = \begin{bmatrix} 382.65 & -57.27 & 61.64 \\ -57.27 & 456.73 & -2.63 \\ 61.64 & -2.63 & 437.29 \end{bmatrix}$

Table 2.3 lists the comparison between the uncontrolled and controlled structural responses. It provides both the RMS and maximum values of the displacement and acceleration of the top floor, and the control force.

Table 2.3 Response of a Three-Story Building using MPC Scheme

Third floor Response	σ_x (cm)	$\sigma_{\ddot{x}}$ (cm/s ²)	σ_f (kN)	x_{max} (cm)	\ddot{x}_{max} (cm/s ²)	f_{max} (kN)
Uncontrolled	0.16	46.5	---	0.38	154.6	---
MPC	0.060 (62.4%)	22.1 (52.4%)	0.106	0.26 (32.4%)	143.2 (7.4%)	0.517

The controlled response of the structure is shown in Figs. 2.9-2.10. Figure 2.9 shows the top floor displacement while Fig. 2.10 shows the top floor acceleration. The dashed lines represent the uncontrolled case, and the solid lines represent the controlled response under the MPC scheme. Figure 2.11 shows the control force needed in this example. Overall, this example has demonstrated the MPC based scheme can effectively reduce the response of multi-degree-of-freedom systems under earthquake loads.

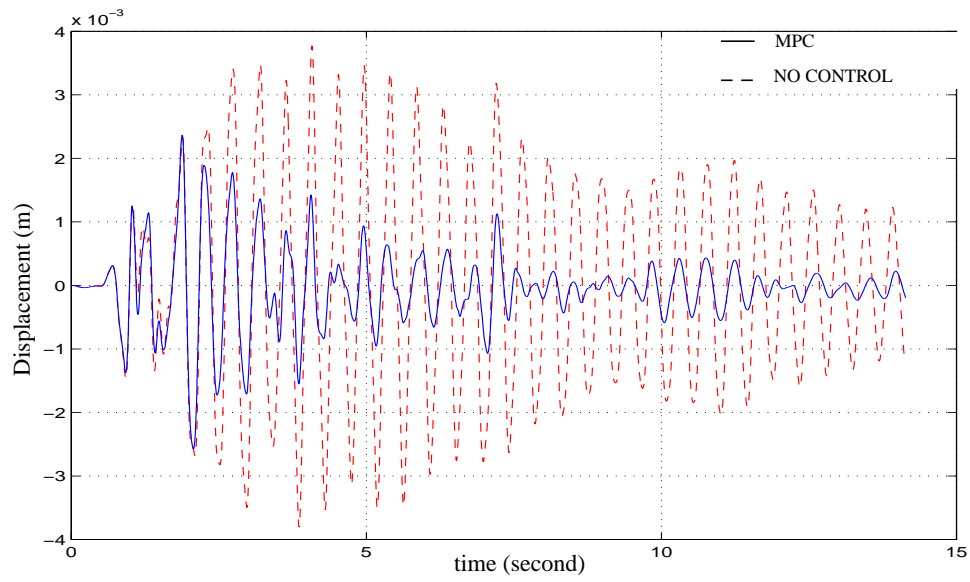


Figure 2.9 Comparison of uncontrolled top floor displacement with MPC scheme.

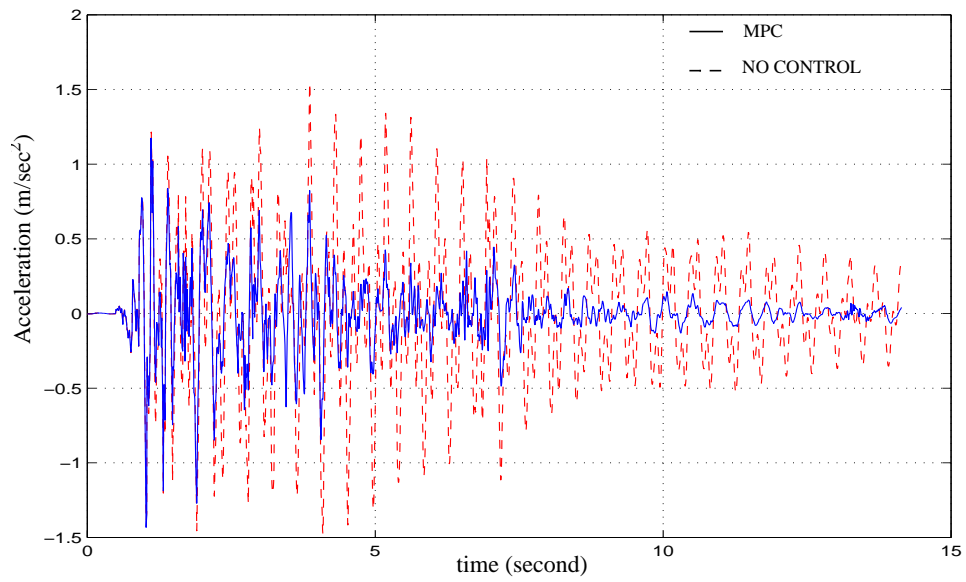


Figure 2.10 Comparison of uncontrolled top floor acceleration with MPC scheme.

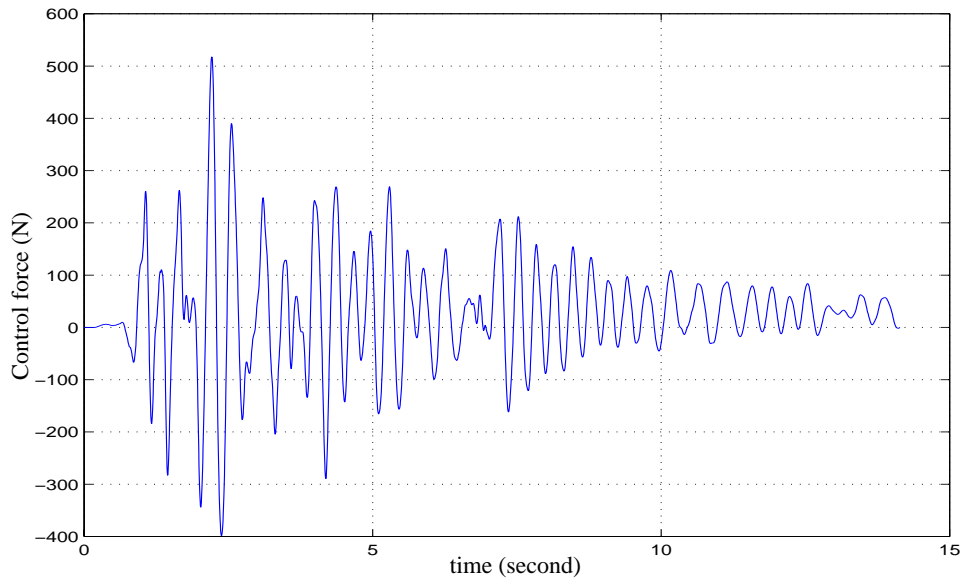


Figure 2.11 Control force using MPC scheme.

2.3 Summary

In this chapter, a general Model Predictive Control (MPC) was applied to reduce structural response under earthquake induced loads. MPC schemes were designed for a SDOF and a three-story building models using an active tendon system. A parameter study was conducted to delineate the influence of different weighting factors on the control force, and prediction and control horizons. This study clearly demonstrated the effectiveness of the general MPC strategy for reducing structural response under earthquake loads. Accordingly, the displacement and acceleration response of the building were reduced significantly. The performance of MPC in the infinite horizon case was shown to be comparable to the H_2 strategies. This chapter has demonstrated the effectiveness of MPC scheme in controlling structural motions under earthquakes and provided the framework for cap-

turing the attractive features of MPC, i.e., computational expediency and real-time applications. Another salient feature of MPC that concerns its intrinsic ability to include constraints in the design process for structural control applications will be discussed in next chapter.

CHAPTER 3

CONSTRAINTS STUDY IN STRUCTURAL CONTROL

A topic of significant practical importance, that has been studied sparingly, concerns the influence of physical constraints which are imposed on structures and control actuators. These constraints are referred to as hard constraints, and they must be satisfied because they reflect physical characteristics of the system. Correspondingly, another kind of constraint known as a soft constraint can be easily satisfied and is taken into account through the optimization criteria. These can often be satisfied through the trade-offs between the level of response and the applied force. In most structural control studies, hard constraints have been ignored or avoided by manipulating the weighting parameters in the objective function or by reducing the design loads. This is not very practical because all real life conditions impose hard constraints or offer a limited level of available energy. The intensity or magnitude of the natural events is random in nature and is treated in design in a probabilistic framework. Actuators, often employed in control devices, have limited strokes and associated control force that can be introduced. For example, active mass dampers (AMDs) are constrained by their strokes and their capacity to generate force which depend on damper size, power source, and the damper mass. The saturation method, which simply cuts off the force at a prescribed value, is often used as a way to deal with these constraints. However, if saturation is considered, the controller's stability

and optimization features are affected. In the literature, a variable feedback gain was applied to maintain an AMD's operation within the limits of its stroke and control input (Nitta and Nishitani, 1998). Johnson *et al.* (1998) studied a mixed-objective optimal control framework using l_1 and H_∞ constraints to improve the controller performance. D'Amato and Rotea (1998) used a general H_2 method to solve the optimal problem under stochastic hard constraints. The covariance control method was also proposed which searches an optimal controller that minimizes the output variance and at the same time places bounds on the output variance (Zhu and Skelton, 1998; Lu and Skelton, 1998). However, these methods are rather complicated and may not be easily implemented.

In this chapter, structural control problems that are subjected to input/output inequality constraints are studied using the MPC scheme. At each time step, the MPC scheme involves the solution of an optimal problem that is subjected to certain constraints on both the input and output. The problem is transformed into a quadratic programming framework with inequality constraints. A solution is then sought within the limits to obtain the optimal control forces that could be generated by actuators. Accordingly, the control command assures that the actuator works within the range of its prescribed capacity. This chapter first discusses the formulation of the MPC scheme with constraints. Then examples of buildings represented by a single (SDOF) and a multiple degree-of-freedom (MDOF) systems are employed to demonstrate the efficacy of this methodology. For the SDOF system, an active tendon is used as the control device. Three cases of the control design are considered, i.e., no constraints, weak constraints, and strict constraints. For the three story building, both the active tendon and active mass damper are used as control devices and cases involving no or weak constraints and strict constraints are compared.

Numerical examples are presented to demonstrate the effectiveness of the MPC scheme with constraints.

3.1 Constrained Model Predictive Control (MPC) Scheme

The basic ideas of Model Predictive Control (MPC) scheme with a structural model were described in Chapter 2. In this section, the constrained MPC scheme is discussed.

The discrete-time state-space equations of the prediction model are expressed as

$$\begin{aligned}\hat{x}(k+1|k) &= \Phi\hat{x}(k|k-1) + \Gamma_u\hat{u}(k|k-1) + \Gamma_e\hat{e}(k|k) \\ \hat{y}(k|k-1) &= C\hat{x}(k|k-1) + D_u\hat{u}(k|k-1)\end{aligned}\quad (3-1)$$

where $\hat{x}(k+1|k)$ represents the state at a future sampling time step, $k+1$, and uses the information available at time step k ; $\hat{y}(k|k-1)$ denotes estimate of the plant output at time step k based on information at time step $k-1$; $\Gamma_e = K$ is a constant estimator gain matrix; $\hat{e}(k|k)$ is the estimated error defined as $\hat{e}(k|k) = y(k) - \hat{y}(k|k-1)$.

Using Eq. (3-1), the process output predicted at step k for consecutive time steps $k+j$, $j = 1, \dots, p$ can be expressed as a function of the current state vector $x(k)$ and the control vector $\mathbf{u}(k) = [\hat{u}(k|k) \dots \hat{u}(k+\lambda-1|k)]^T$

$$\Psi(k) = H\mathbf{u}(k) + Y_z\hat{x}(k|k-1) + Y_e\hat{e}(k|k) \quad (3-2)$$

and $\Psi(k) = [\hat{y}^T(k+1|k) \dots \hat{y}^T(k+p|k)]^T$, where p is the prediction horizon and λ is the control horizon. The reference output can be written as $\Psi_r(k) = [y_r^T(k+1|k) \dots y_r^T(k+p|k)]^T$.

Accordingly, the objective function is given by

$$J = \min \left\{ \frac{1}{2} [\Psi(k) - \Psi_r(k)]^T \bar{Q} [\Psi(k) - \Psi_r(k)] + \frac{1}{2} \Delta \mathbf{u}^T(k) \bar{R} \Delta \mathbf{u}(k) \right\} \quad (3-3)$$

subjected to the following linear inequality constraints:

$$\mathbf{u}(k) \geq \mathbf{u}_{min}(k) \quad (3-4)$$

$$\mathbf{u}(k) \leq \mathbf{u}_{max}(k) \quad (3-5)$$

$$|\Delta \mathbf{u}(k)| \leq \Delta \mathbf{u}_{max}(k) \quad (3-6)$$

$$\Psi(k) \geq \Psi_{min}(k) \quad (3-7)$$

$$\Psi(k) \leq \Psi_{max}(k) \quad (3-8)$$

The quadratic programming approach is utilized here to solve this optimization problem. Using the transformation $\mathbf{v}(k) = \mathbf{u}(k) - \mathbf{u}_{min}(k)$, the optimization problem can be written as

$$J_q = \max \left\{ a^T(k) \mathbf{v}(k) - \frac{1}{2} \mathbf{v}^T(k) B \mathbf{v}(k) \right\} \quad (3-9)$$

which is subjected to the generalized inequality constraints:

$$A \mathbf{v}(k) \leq b(k) \quad (3-10)$$

where

$$a(k) = H^T \bar{Q} [\Psi_r(k) - Y_z \hat{x}(k|k-1) - Y_e \hat{e}(k|k)] + R_1^T \bar{R} \delta(k) - B^T \mathbf{u}_{min}(k) \quad (3-11)$$

$$B = H^T \bar{Q} H + R_1^T \bar{R} R_1 \quad (3-12)$$

$$A = \begin{bmatrix} -I \\ I \\ R_1 \\ -R_1 \\ -H \\ H \end{bmatrix}, \quad b(k) = \begin{bmatrix} 0 \\ \mathbf{u}_{max}(k) - \mathbf{u}_{min}(k) \\ \Delta \mathbf{u}_{max}(k) + \delta(k) - R_1 \mathbf{u}_{min}(k) \\ \Delta \mathbf{u}_{max}(k) - \delta(k) + R_1 \mathbf{u}_{min}(k) \\ -\Psi_{min}(k) + H \mathbf{u}_{min}(k) + Y_z \hat{x}(k|k-1) + Y_e \hat{e}(k|k) \\ \Psi_{max}(k) - H \mathbf{u}_{min}(k) - Y_z \hat{x}(k|k-1) - Y_e \hat{e}(k|k) \end{bmatrix} \quad (3-13)$$

$$H = \begin{bmatrix} H_1 & 0 & \dots & 0 \\ \dots & \dots & \dots & \dots \\ H_\lambda & H_{\lambda-1} & \dots & H_1 \\ H_{\lambda+1} & H_\lambda & \dots & H_1 + H_2 \\ \dots & \dots & \dots & \dots \\ H_p & H_{p-1} & \dots & H_1 + \dots + H_{p-\lambda} \end{bmatrix}, \quad H_k = C \Phi^{k-1} \Gamma_u, \quad (3-14)$$

$$Y_z = \left[(C \Phi)^T (C \Phi^2)^T \dots (C \Phi^p)^T \right]^T \quad (3-15)$$

$$Y_e = \left[(C \Gamma_e)^T (C(I + \Phi) \Gamma_e)^T \dots \left(C \sum_{k=1}^p (\Phi^{k-1}) \Gamma_e \right)^T \right]^T, \quad (3-16)$$

$$\bar{Q} = \begin{bmatrix} Q & \dots & 0 \\ \dots & \dots & \dots \\ 0 & \dots & Q \end{bmatrix}, \quad \bar{R} = \begin{bmatrix} R & \dots & 0 \\ \dots & \dots & \dots \\ 0 & \dots & R \end{bmatrix}. \quad (3-17)$$

$$R_1 = \begin{bmatrix} I & 0 & \dots & 0 & 0 \\ -I & I & \dots & 0 & 0 \\ \dots & \dots & \dots & \dots & \dots \\ 0 & 0 & \dots & I & 0 \\ 0 & 0 & \dots & -I & I \end{bmatrix} \quad (3-18)$$

$$\delta(k) = [u^T(k-1) \ 0 \ \dots \ 0]^T \quad (3-19)$$

This problem can be solved as a standard quadratic programming problem using *Matlab* (1998). The optimal solution is obtained in the constrained space. In order to accomplish this, the quadratic problem involving an active set strategy is utilized. A feasible solution is first obtained by solving a linear programming problem and then it is used as an initial point for the iterative solution involved in the quadratic programming problem. Then an iterative sequence of feasible points that converge to the desired solution are generated. The optimal point obtained in this manner is the optimal predictive control force in the constrained space which maximizes the objective function J_q . In the following section, examples are presented to demonstrate the constrained MPC scheme.

3.2 Numerical Examples and Analysis

In this section, a SDOF system represented by a single-story building with an active tendon system is used to demonstrate the constrained and unconstrained control. It is followed by a three-story building that uses an active tendon system and an active mass damper under the constrained and unconstrained MPC schemes.

3.2.1 SDOF Building using Active Tendon

The SDOF building with the active tendon shown in Fig. 2.2 of Chapter 2 is used here. The actuator introduces changes in the cable tension according to the MPC scheme. The 1940 El Centro earthquake record is scaled to 0.25 of its maximum intensity to excite the building for the analysis in this example.

First, the MPC scheme without constraints is compared to the MPC scheme with constraints. The constraints on the control force of the example structure are set much higher than the expected range so that the control force remain within the bounds. Such constraints are referred as weak constraints in this paper. According to the optimal control theory, this type of weak constrained case should provide results same as the unconstrained case. Accordingly, in this study, the following values were assigned to different parameters. $\mathbf{u}_{min}(k) = -1.2 \times 10^{-3} \text{ m}$, $\mathbf{u}_{max}(k) = 1.2 \times 10^{-3} \text{ m}$, $\Delta \mathbf{u}_{max}(k) = 4.15 \times 10^{-4} \text{ m}$, $x_{min}(k) = [-0.0026 \ -0.58]^T$ and $x_{max}(k) = [0.0026 \ 0.28]^T$. Multiply the limit of the control command, u , by $4k_c \cos \alpha / m$, which is given above for the tendon. The range of the control force is set between $[-1500N \ 1500N]$. In addition, an increase or decrease in the control force in one time step is restricted to 500N. In Figs. 3.1-3.4, the displacements, accelerations, control forces, and force increment at each time step for the MPC scheme without constraints and the MPC scheme with weak constraints are plotted, respectively. The results are also summarizes in Table 3.1. As seen clearly, the results of MPC without constraints and with the weak constraints are identical.

Table 3.1 Comparison between the MPC without Constraints and with Constraints

	without control	MPC without constraints	MPC with weak constraints	Percentage change	MPC with strict constraints	Percentage change
σ_x (cm)	0.075	0.016	0.016	78%	0.019	74%
$\sigma_{\dot{x}}$ (cm/s ²)	37.8	17.1	17.1	55%	18.2	52%
σ_f (N)	---	177.5	177.5	---	183.5	3%
x_{max} (cm)	0.25	0.081	0.081	68%	0.120	52%
\ddot{x}_{max} (cm/s ²)	135.4	114.9	114.9	15%	126.3	7%
f_{max} (N)	---	1205.5	1205.5	---	799.9	- 34%
Δf_{max}		210.5	210.5		99.9	-52%

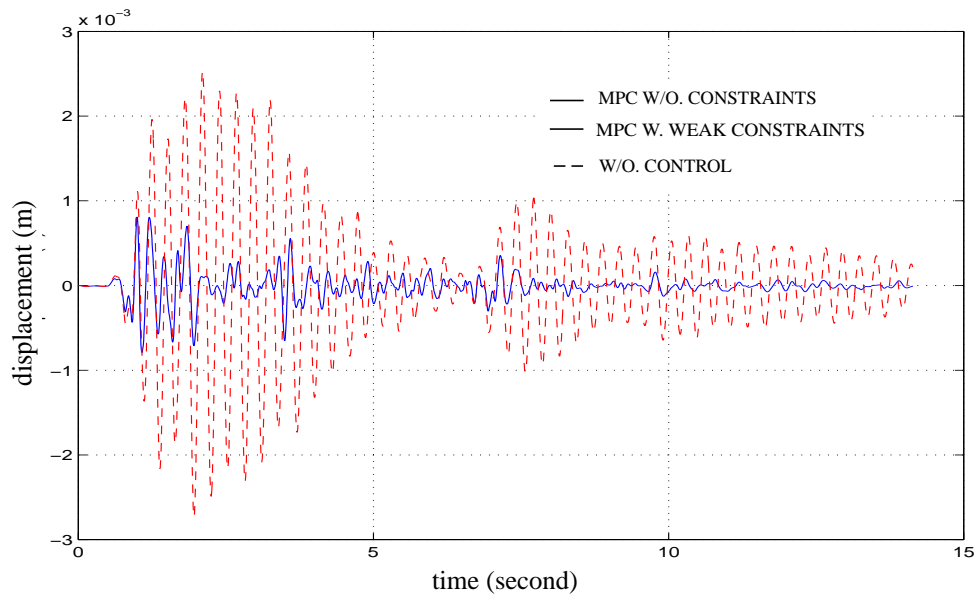


Figure 3.1 Building displacement under no control and under MPC with no constraints and weak constraints

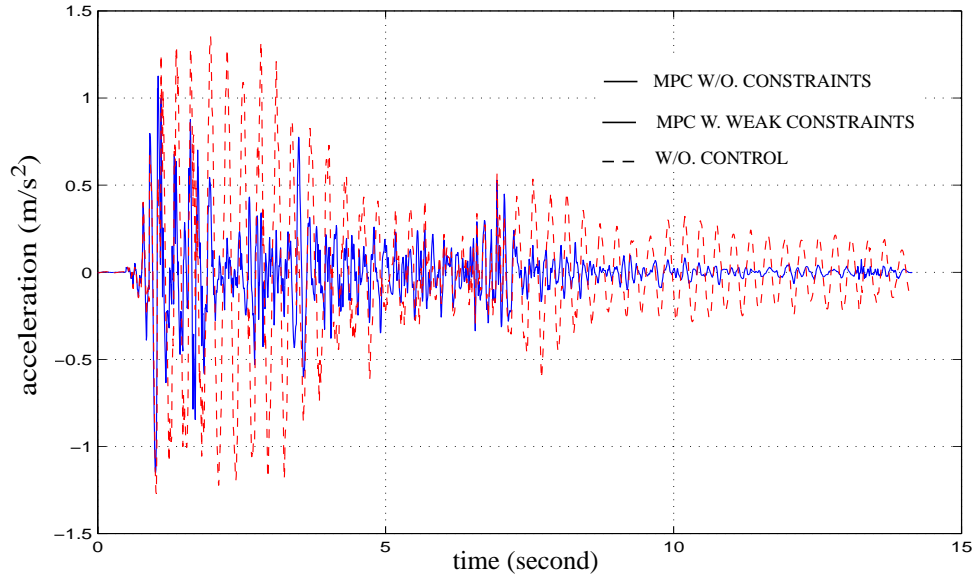


Figure 3.2 Building acceleration under no control and under MPC with no constraints and weak constraints

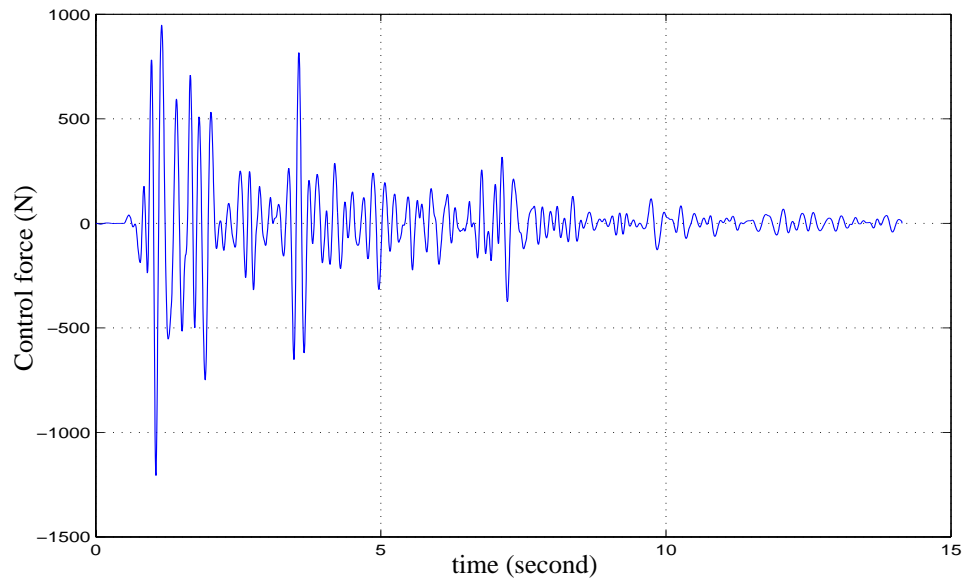


Figure 3.3 Control force under MPC (no constraints and weak constraints)

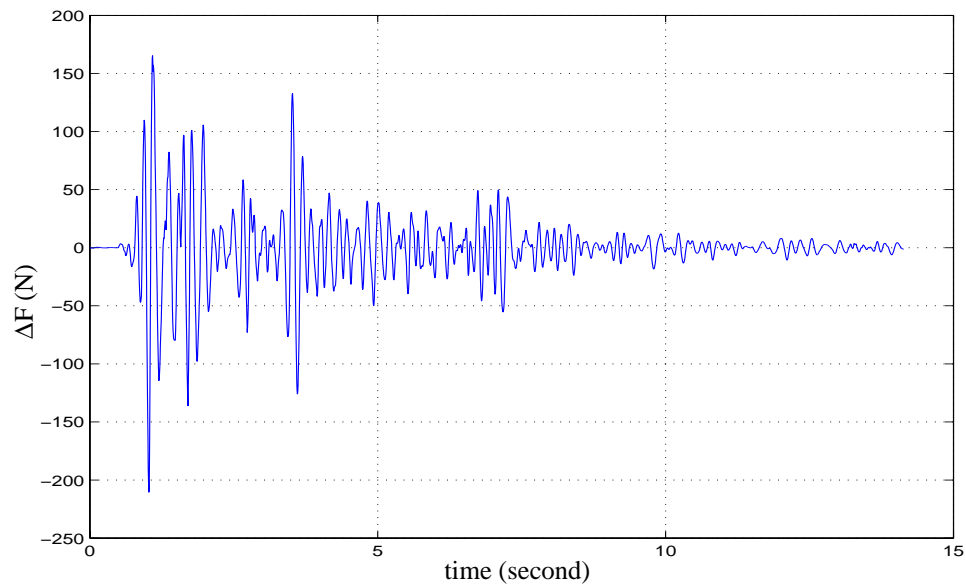


Figure 3.4 Increment of control force under MPC (no constraints and weak constraints)

The controlled responses under MPC with strict constraints are then calculated using the same example. The constraint on the control force is set as $[-800N \ 800N]$. An

increase or decrease in the control force at each time step is now constrained to 100N. Accordingly, the constraints on the inputs are: $\mathbf{u}_{min}(k) = -6.6464 \times 10^{-4}$, $\mathbf{u}_{max}(k) = 6.6464 \times 10^{-4}$, $\Delta\mathbf{u}_{max}(k) = 8.308 \times 10^{-5}$. Figures 3.5 and 3.6 show the displacement and acceleration under MPC with strict constraints. Figure 3.7 plots the corresponding control force, which does not exceed 800N, the upper limit of the constraint. Figure 3.8 displays the change in the control force at each time step. Again, the increment at each step does not exceed 100N as imposed by the constraint. Therefore, the constraints imposed in the MPC scheme to obtain the optimal control solution are faithfully maintained. The optimal control force is different from the control force obtained by using saturation. Rather, it is an optimal solution considering the limitations on the magnitude of the control force in which the maximum control force reached at a time instant would affect the future control force and response.

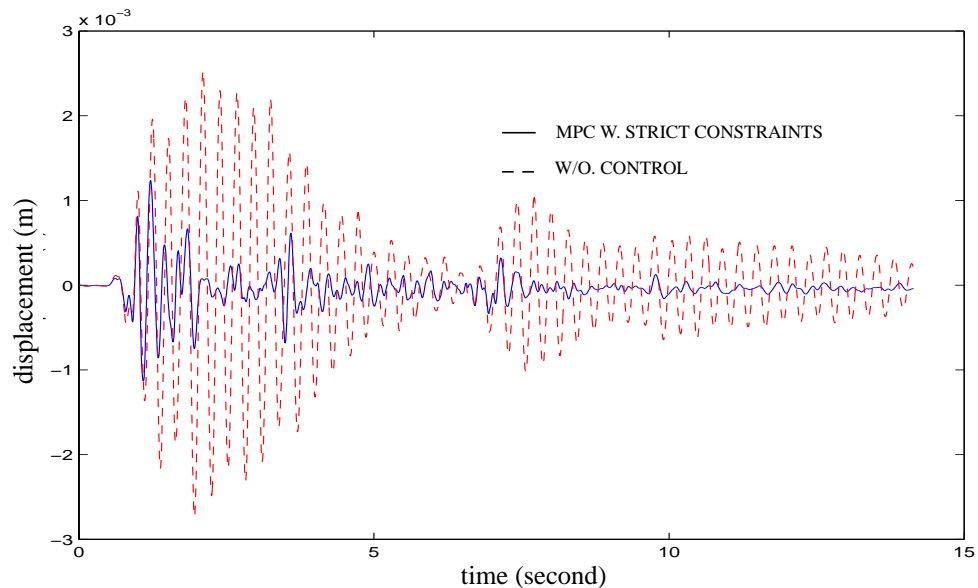


Figure 3.5 Building displacement under no control and under MPC with strict constraints.

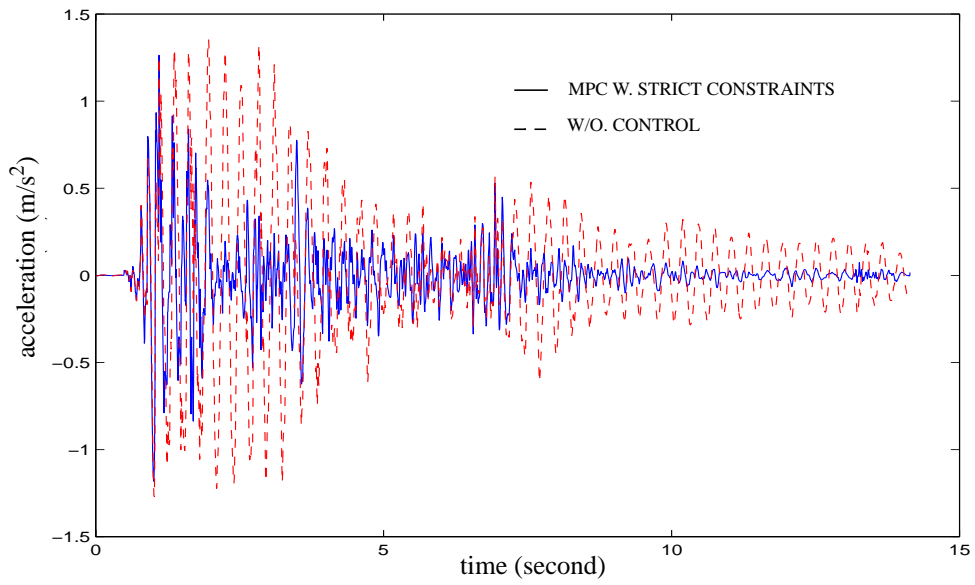


Figure 3.6 Building acceleration under no control and under MPC with strict constraints.

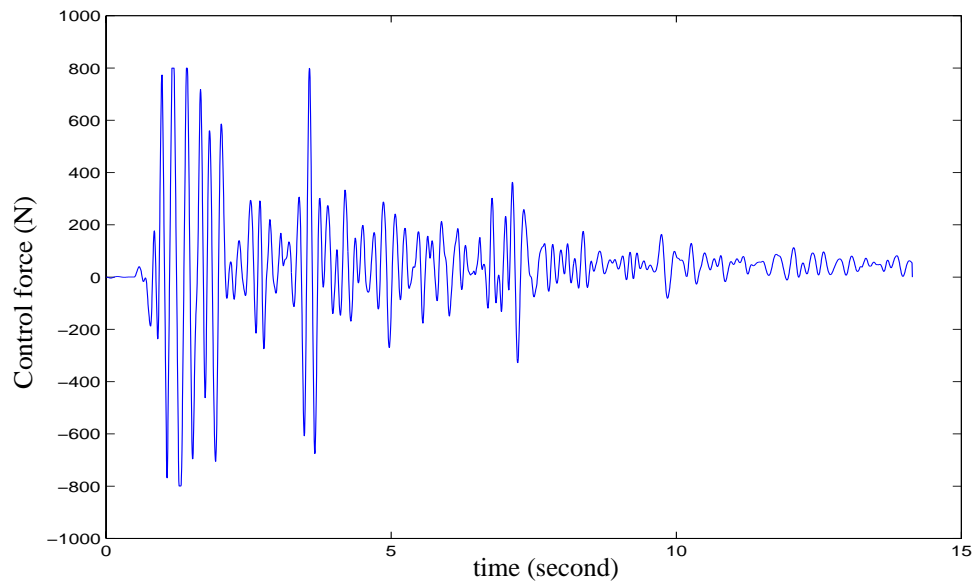


Figure 3.7 Control force under MPC with strict constraints

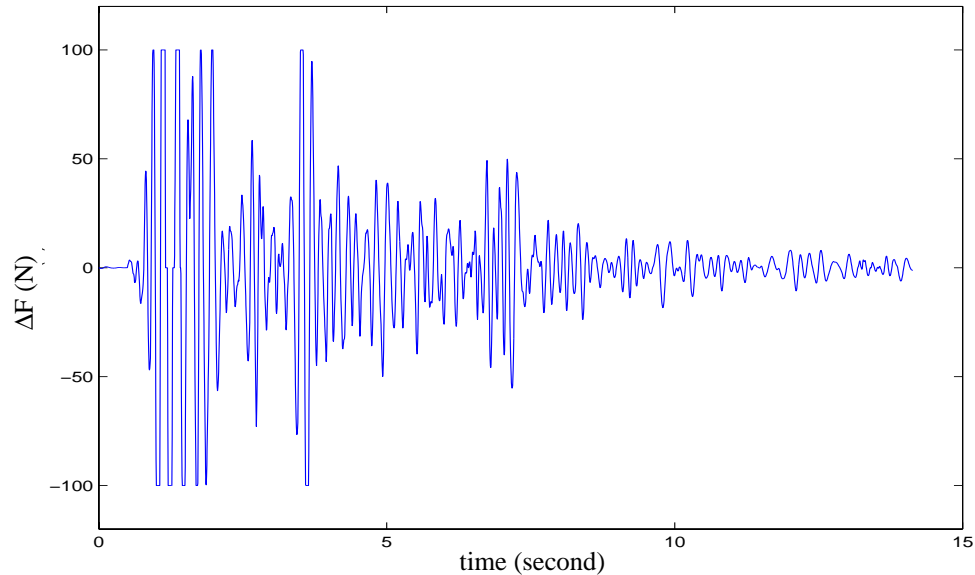


Figure 3.8 Increment of control force under MPC with strict constraints

The root mean square and maximum values of displacement, acceleration and control force under MPC with strict constraints are given in Table 3.1. As pointed out before, there is no difference in the response statistics between the MPC with no constraints and with weak constraints. Beside this, there are several other results noted in Table 3.1. While on one hand, once strict constraints are imposed, the response statistics are affected only slightly when compared to the unconstrained and weakly constrained cases. On the other hand, in the case of strict constraints, the maximum control force is 33% smaller, and the control force increment at each time step is 52.3% smaller. The root mean square value of the control force is slightly larger than that in the unconstrained case. This increase is introduced by the constraints, which make the control force change at a slower rate and thus introduce more time for the controller to work in its full capacity than in the unconstrained case. Although the control force is much smaller when the constraints are

imposed, the controlled responses change slightly, which is due to the action of an optimal controller despite the presence of imposed constraints. This also provides an economic control design for civil structures because the potential of the actuator is fully explored.

3.2.2 Three-story Building Using Active Tendon

In this example, the three-story building utilized in Chapter 2 (Fig. 2.8) is employed to demonstrate the effectiveness of the MPC scheme with constraints. The active tendon is installed on the first floor. The parameters are chosen as $Q = I_{3 \times 3}$, $R = 50000$, $p = 6$ and $\lambda = 2$.

The structural responses are obtained by using the MPC scheme without constraints, with weak constraints and with strict constraints. In the weak constraint case, the control force is limited between 400N and -400N, and the constraint on the increment of the control force at each time step is set at 100N. In the strict constraint case, the control force is limited between -300N and 300N and the constraint on the control force increment at each time step is set at 20N. Table 3.2 lists the structural responses obtained in these three cases. Similar to the results for a single-story building, the displacement, acceleration and control force are identical under the MPC scheme with weak or no constraints. The controlled responses under the MPC with strict constraints are at the same level as MPC with no constraints. However, its control force with the maximum value equal to its upper constraint limit is much smaller.

Table 3.2 Comparison between MPC with no or weak constraints and MPC with strict constraints for a 3-story building using active tendon

3rd floor response	uncontrolled	MPC with no or weak constraints	percent	MPC with strict constraints	percent
σ_x (cm)	0.16	0.077	52%	0.077	52%
$\sigma_{\ddot{x}}$ (cm/s ²)	46.5	25.0	46%	25.2	46%
σ_f (N)		84.9		80.5	-5%
x_{max} (m)	0.38	0.30	21%	0.30	21%
\ddot{x}_{max} (m/s ²)	154.6	143.9	7%	143.9	7%
f_{max} (N)		381.7		300.0	-21%
Δf_{max} (N)		24.7		19.9	-19%

Figures 3.9-3.12 graphically describe the displacement, acceleration, control force and the increment of the control force without control and under the MPC scheme with no or weak constraints. Figures 3.13-3.16 show the displacement, acceleration, control force and the increment of the control force under no control and under the MPC with strict constraints, respectively. These figures show that if no constraint or weak constraints are added, the peaks of the control force (Fig. 3.11) and the increment of the control force at each time step (Fig. 3.12) go beyond the 300N and 20N, respectively. This is different from that in the strict constraint case, where both of the control force and the increment of control force stay within the prescribed boundaries, [-300, 300] N (Fig. 3.15) and [-20, 20] N (Fig. 3.16), respectively. These results lead to the conclusion that the MPC based scheme that takes into account strict constraints can provide effective control with restrictions on the control devices.

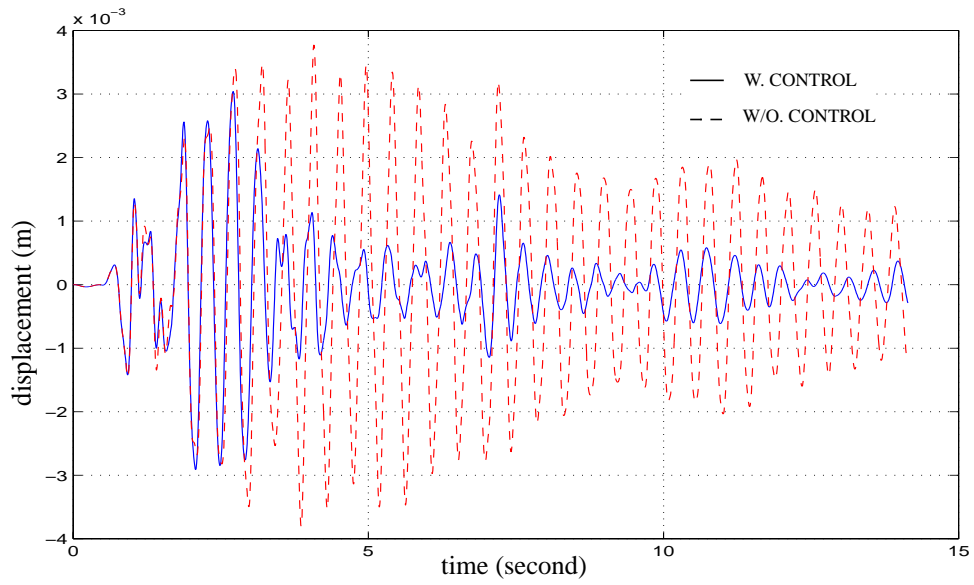


Figure 3.9 Building displacement under no control and under MPC with no/weak constraints

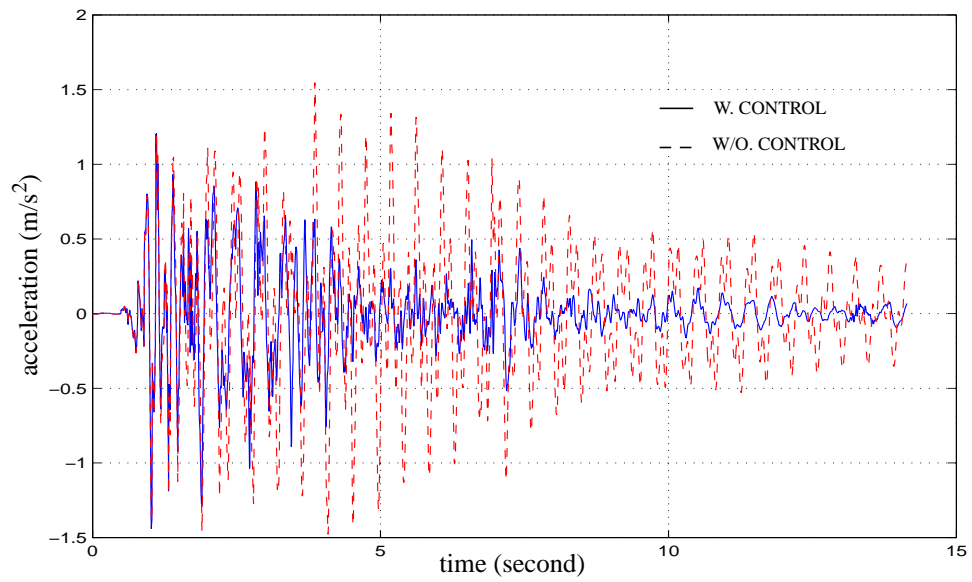


Figure 3.10 Building acceleration under no control and under MPC with no/weak constraints

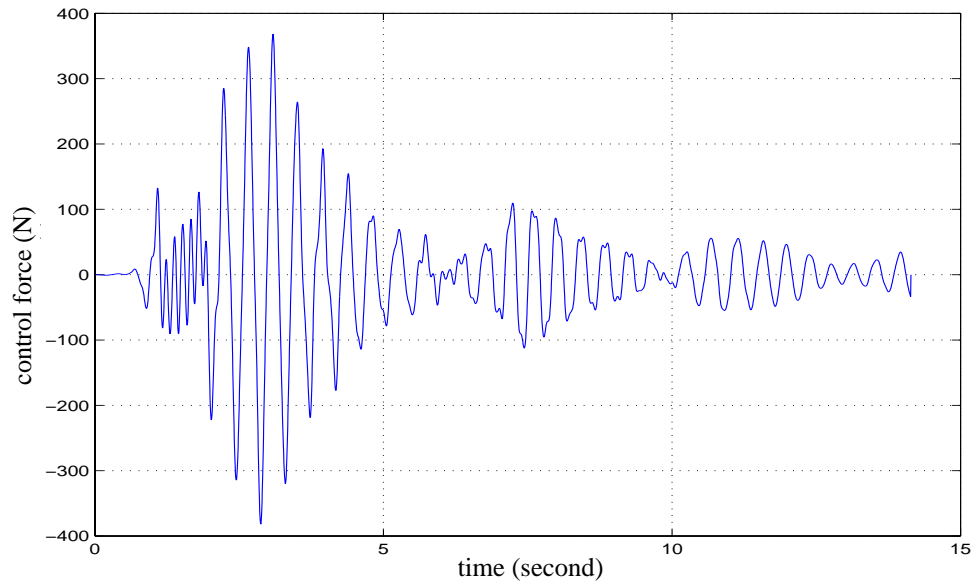


Figure 3.11 Control force under MPC with no/weak constraints

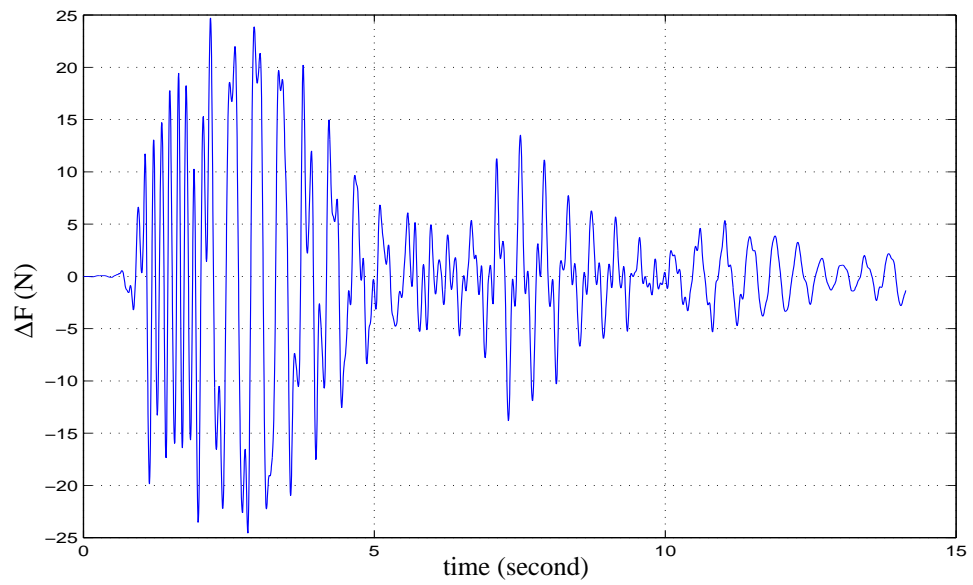


Figure 3.12 Increment of control force under MPC with no/weak constraints

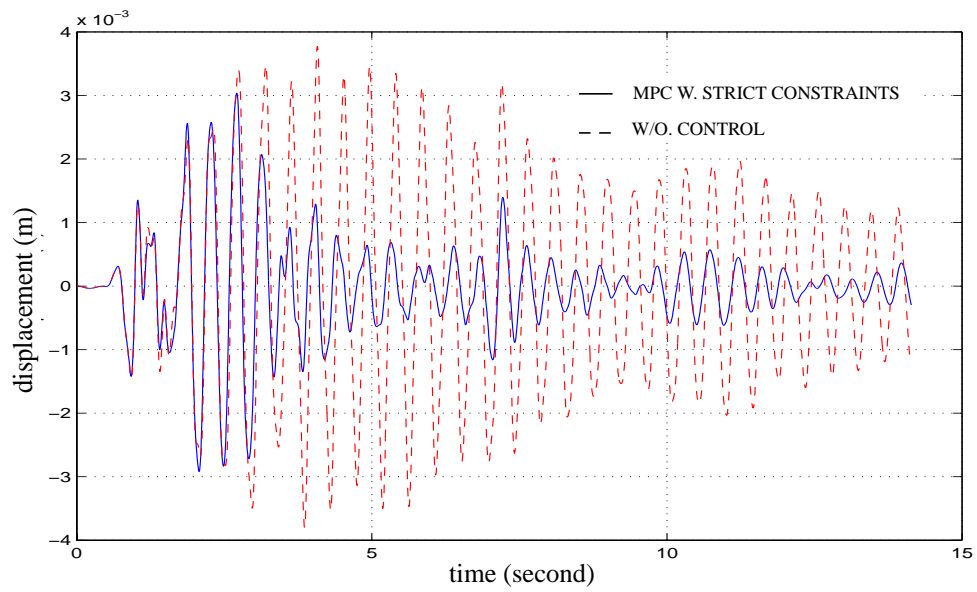


Figure 3.13 Building displacement under no control and under MPC with strict constraints

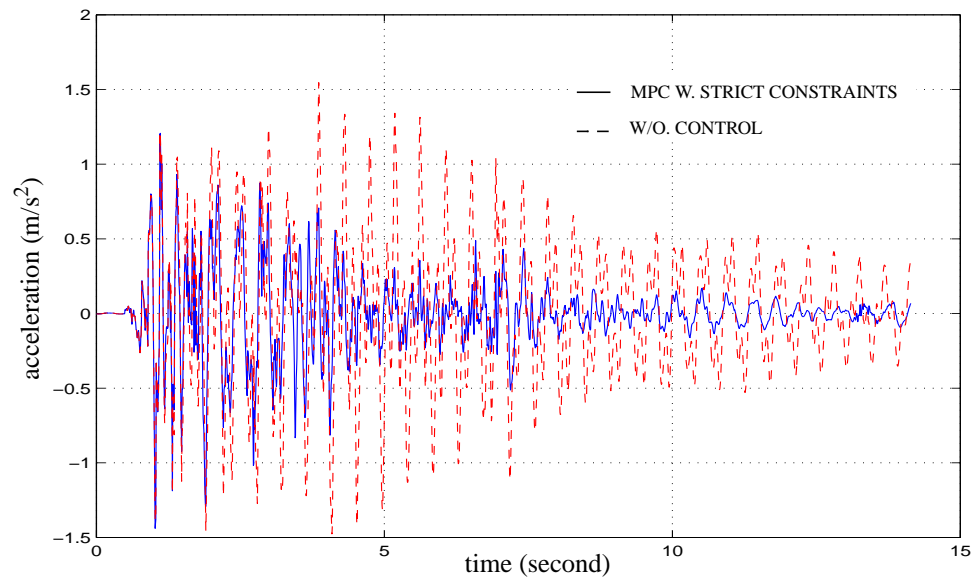


Figure 3.14 Building acceleration under no control and under MPC with strict constraints

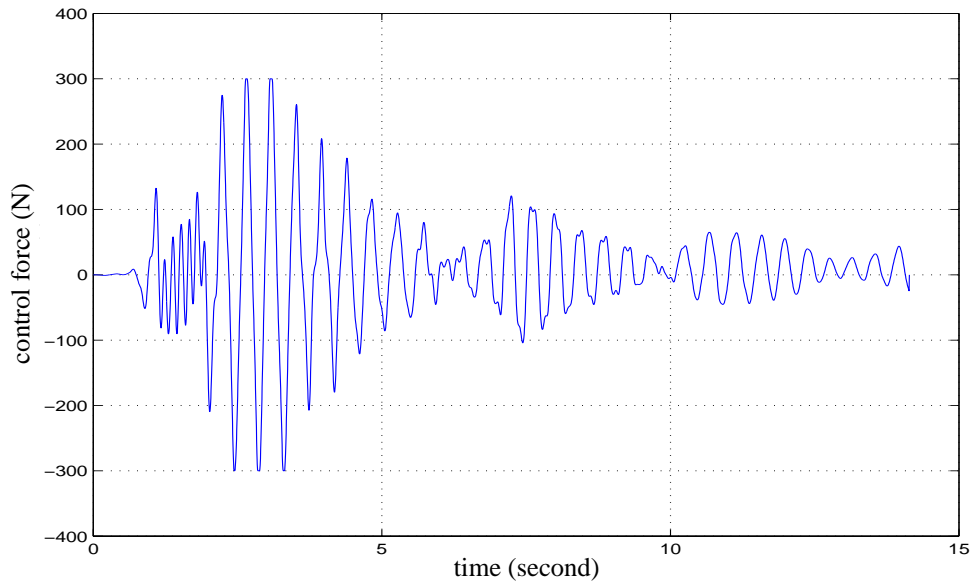


Figure 3.15 Control force under MPC with strict constraints

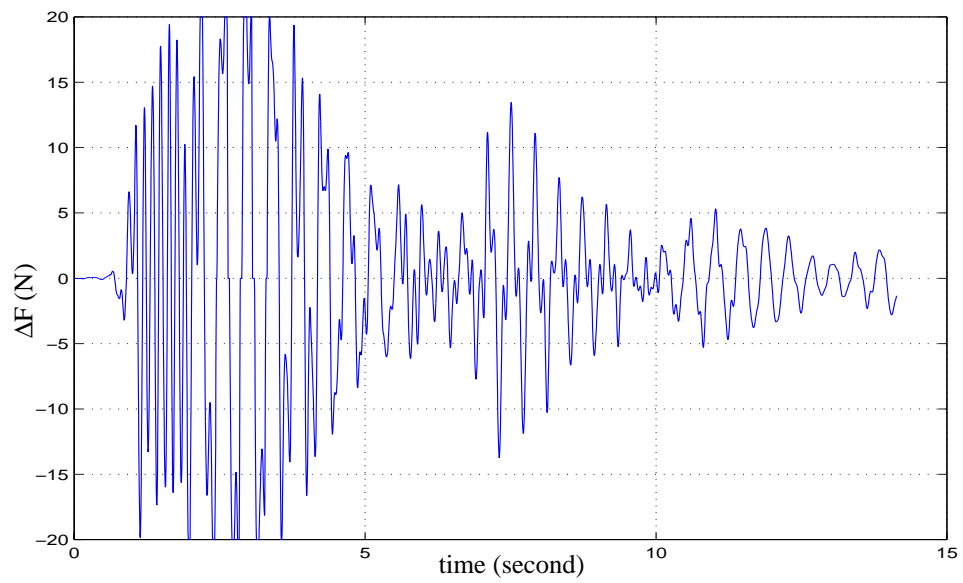


Figure 3.16 Increment of control force under MPC with strict constraints

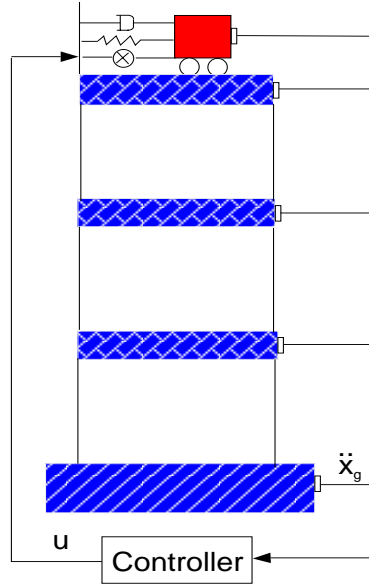


Figure 3.17 3-story building using AMD

3.2.3 Three-Story Building using AMD

In this section, the effectiveness of MPC scheme with strict constraints is further studied in an active mass damper controlled building as the one in section 3.2.2. But the controller is changed from the active tendon placed on the first floor to the active mass damper placed on the top floor. The natural frequency of the damper is tuned to the fundamental frequency of the building. The

mass, damping ratio, and natural frequency of the damper are: $m_2 = 0.02m_1$, $\zeta_2 = 0.2$ and $\omega_2 = 0.95\omega_1 rad/s$. In this example, $p = 8$, $\lambda = 2$, $R = 1$ and $Q = diag[100, 100, 1000, 1, 0, 0, 0, 0]$ are used.

As shown in the former sections, the weak constrained case is the same as no constraints. In this section, they are referred to as the MPC with no/weak constraints scheme. The building response under MPC with no/weak constraints is first simulated. In the case of strict constraints, the constraints are placed on the control force, the increment of the control force and the displacement of the damper mass. These are quite realistic constraints experienced by designers of such devices. The constraints for the control force is set as $[-500N, 500N]$. The maximum increment of the control force at each time step is 66 N and the maximum damper stroke is 7.5 cm. In Table 3.3, the root mean square and maximum values of the displacement, acceleration, and control force are given. It is noted that

once the strict constraints are implemented, the control performance is slightly affected but the damper always operates within the prescribed constraints.

Table 3.3 Comparison between MPC with no/weak Constraints and MPC with Constraints for a Building using AMD

3rd floor response	uncontrolled	MPC with no/weak constraints	Percentage	MPC with strict constraints	percentage
σ_x (cm)	0.16	0.079	50.4%	0.083	48.4%
$\sigma_{\ddot{x}}$ (cm/s ²)	46.5	23.8	48.7%	24.8	46.6%
σ_f (N)		190.9		215.8	13.3%
x_{max} (cm)	0.38	0.28	26.3%	0.27	29.0%
\ddot{x}_{max} (cm/s ²)	154.6	125.8	18.6%	125.5	18.9%
f_{max} (N)		566.9		500	-11.8%
Δf_{max} (N)		71.1		66	-7.2%

Figures 3.18 and 3.19 show the displacement and acceleration responses of the top floor of the building under the MPC with strict constraints, where the dashed lines represent the structural responses without control and the solid lines represent the responses of the system with strict constraints. Figures 3.20 and 3.21 show the control force and increment of the control force at each time step. The control force is shown to stay within the range of [-500 N, 500N] and the increment is limited between -66 N and 66N as prescribed in the constraints. There are a few time steps that control force reaches its maximum value. Figures 3.22 and 3.23 compare the displacement of the AMD mass with no constraints and with strict constraints. If no constraints are added, the displacement of the AMD can reach 8.4 cm. However, in the presence of constraints, the maximum displacement of the AMD

is limited to 7.5 cm. This displacement constraint is often very pivotal due to the limited space typically available for the movement of damper mass in actual structures.

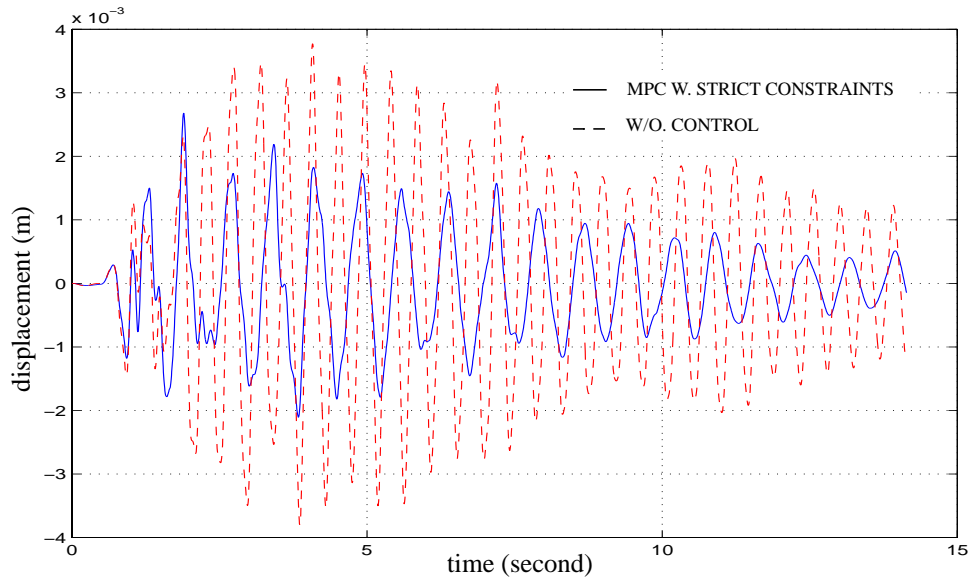


Figure 3.18 Building displacement under no control and under MPC with strict constraints

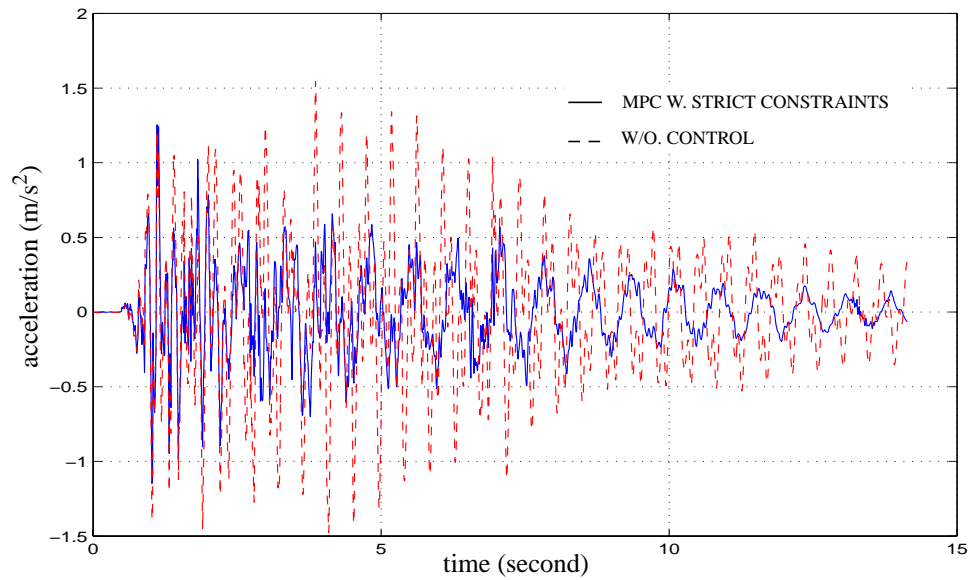


Figure 3.19 Building acceleration under no control and under MPC with strict constraints

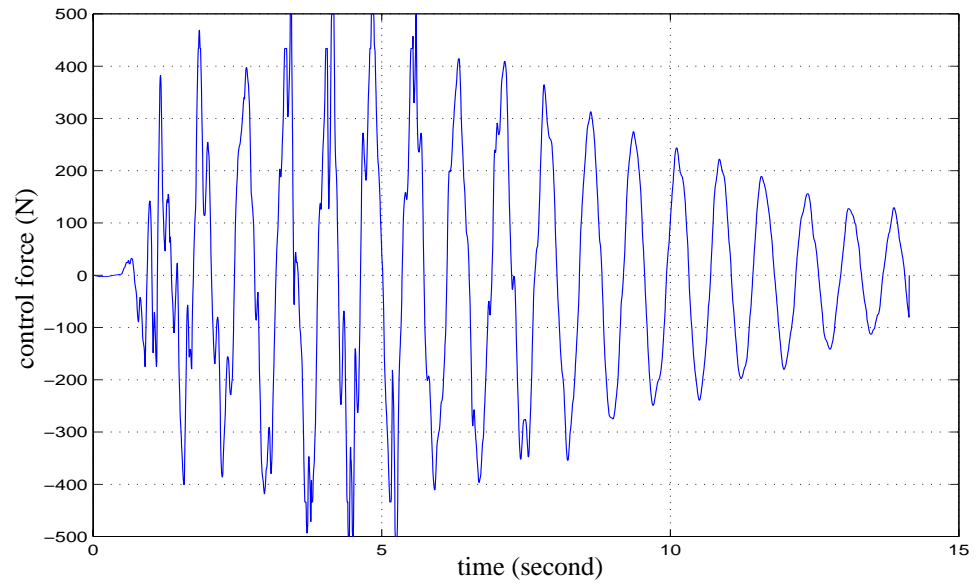


Figure 3.20 Control force under MPC with strict constraints

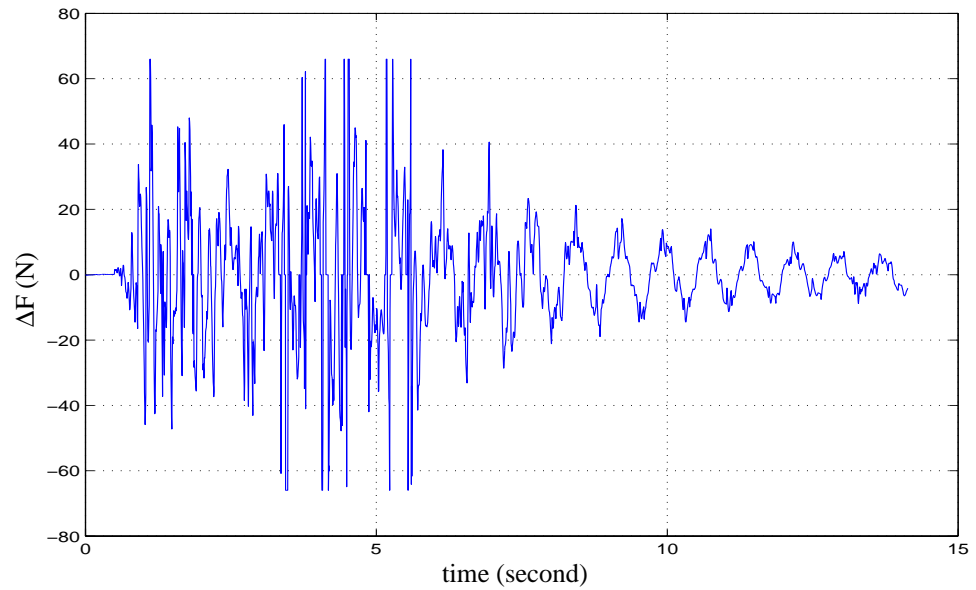


Figure 3.21 Increment of control force under MPC with strict constraints

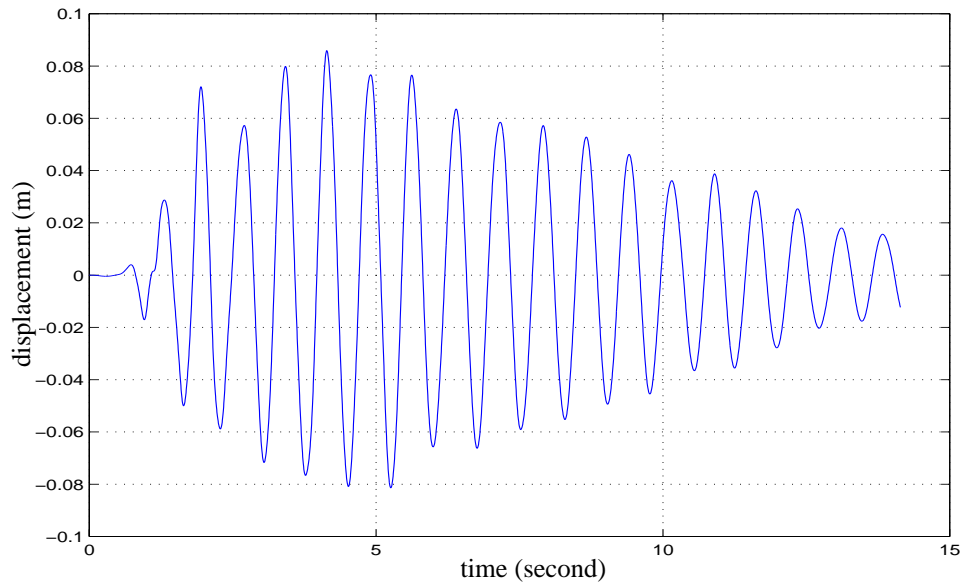


Figure 3.22 Displacement of AMD under MPC with no constraints

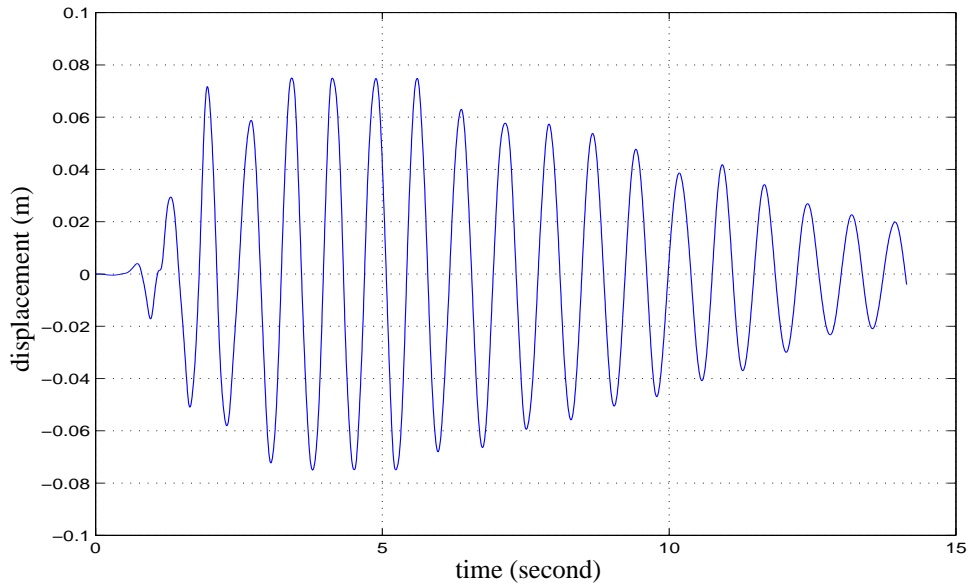


Figure 3.23 Displacement of AMD under MPC with strict constraints

In summary, the above numerical examples show that the MPC scheme can effectively incorporate constraints for structural control applications. Simulations show that for both the active tendon and AMD systems, the MPC scheme with strict constraints can perform at optimal level while maintaining the control force within the prescribed envelope and the change of control force at each time step within a pre-assigned value. For the AMD case, the damper displacement is restricted within a pre-defined upper limit. Above all, the MPC scheme with constraints attempts to solve actual engineering problems and provides an effective method for including the constraints that were ignored in previous studies.

3.3 Summary

In this chapter, the Model Predictive Control scheme was employed to reduce structural response under earthquake excitation while the structure and the control device were subjected to input/output inequality constraints. At each time step, the MPC scheme results in an optimization problem subjected to certain constraints on the input and output. This problem is then recast as a quadratic programming problem in a constrained space. The optimal solution is then found in this constrained space to obtain the optimal control forces.

Examples of buildings representing a single and multiple degree-of-freedom systems were presented to demonstrate the efficacy of this methodology. For the single degree-of-freedom system, the active tendon system was used as the control device. The analysis included cases of no constraints, weak constraints and strict constraints. For the three story building, both the active tendon system and the active mass damper were used as controllers and response levels under no constraints and strict constraints were compared.

Numerical examples demonstrated the effectiveness of the MPC scheme under strict constraints. For the active tendon system, the maximum control force and the force variation at each time step were considered as constraints. For the AMD system, the damper displacement, the maximum control force and the force variation at each time step were constraints considered. An optimal control design was obtained at each time step which satisfied the imposed conditions. Results show that the weak constrained case provides response reduction at the same level as unconstrained case. In the strict constraint case, the actuator capacity is exploited more effectively and the response reduction levels are similar to those in unconstrained case but with a smaller control force. Therefore, in the rest of this study, MPC with strict constraints will be referred as MPC with constraints.

The proposed MPC based method with constraints provides a reliable and convenient approach to study structural controls under constraints. This scheme can also enhance the efficiency and utilization of the actuator which makes the actuator design economically attractive. It is anticipated that with the availability of high speed actuators and fast digital processors and communication boards like processors on the chip, the MPC scheme with constraints will be conveniently implemented in real structures in the very near future.

CHAPTER 4

SEMI-ACTIVE CONTROL SYSTEM DESIGN

As discussed in Chapter 1, passive control devices have been used as energy dissipating systems in civil engineering structures. These systems do not require any external source of energy in their primary functions. On the contrary, active control devices utilize significant amount of external power to provide changeable control force actions under different loading conditions and structural behaviors. Semi-active control devices combine the advantages of both passive and active control system. These systems can offer effectiveness parallel to active systems and yet require much less external energy than a typical active control system.

Semi-active control systems were first studied in civil engineering structures by Hrovat et al. (1983) who proposed a semi-active tuned mass damper (SATMD) in structural control design. This SATMD involves a variable orifice damper which has a diameter-adjustable orifice. (Hrovat, 1983; Mizuno, 1992; Sack, 1994). Semi-active tuned liquid column dampers (SATLCD) are primarily a liquid mass version of SATMD and have been studied by Kareem (1994), and Haroun and Pires (1994). SATLCD relies on the liquid motion in a U-shaped tube to generate inertial force like the secondary mass of a TMD. The changeable orifice within the SATLCD acts as the active device for the alternation of the control force. Other semi-active devices include controllable fluid dampers. The controllable flu-

ids can alter their state in milliseconds like Electrorheological (ER) fluids and Magnetorheological (MR) fluids. ER dampers were studied for civil engineering applications by Ehrgott and Masri (1992, 1994), Gavin et al (1994), Makris et al (1995), Masri et al (1995), etc. MR dampers have been extensively studied by Carlson (1994), Carlson and Weiss (1994), Spencer et al. (1996, 1997) and Dyke (1996). The full-scale implementation of these controllable fluid damper, particularly MR dampers is currently underway (Yang, et al., 2000 and 2001).

For SATMD and SATLCD, usually the desired control force is formulated based on an optimal control law and then this desired control force is cut off at a level to obtain the final control force which is related to the directions of the damper's relative velocity and desired control force. This is known as clipped control force. However, the clipped control force is not optimal because it is an improvised version of the desired optimal control force.

This study models the variation of damping force in semi-active systems in term of time-varying constraints. An optimal control design is then achieved through the application of a constrained MPC scheme.

In an SATMD and SATLCD, variable damping serves the role of changes in the control force according to the changes in applied loading and associated structural response by means of a variable orifice system. The damping force is governed by the signs of the desired control force and the relative velocity. These limitations are then recast in terms of time-varying constraints on the control force. The constrained MPC scheme incorporates constraints on the control force and provides an optimal solution to the controlled system.

To demonstrate the effectiveness of the scheme, the constrained MPC scheme is employed to reduce the structural response under wind excitation by using SATMD and SATLCD in this chapter. First, SATMD and SATLCD are implemented in a single-degree-of-freedom (SDOF) building model and their performance is evaluated. An SATLCD is then employed in a building modeled as a five degree-of-freedom (DOF) system. The passive control, clipped-LQ control, and the constrained MPC scheme for semi-active devices are then investigated.

4.1 SATMD and SATLCD Models

This section discusses the basic modeling of semi-active tuned mass damper and semi-active tuned liquid column damper.

4.1.1 SATMD

Figure 4.1 represents the building to be controlled by an SATMD. The equations of motion describing the dynamics of an SDOF building and the SATMD can be represented by Eq. (2-1). The control force is governed by the semi-active device acting between the building and the damper mass.

The semi-active damper consists of a piston-cylinder combination supplemented by a control valve as shown in Fig. 4.2. The cylinder can be viewed as attached to the building and the piston to the mass damper. For the passive mode of operation, the valve is stationary and open, which corresponds to the standard passive damping scheme. In the semi-active control mode, the valve can be controlled to have upward or downward motions.

Accordingly, the different levels of damping force are thus introduced which depend on the valve position.

In an active control device, any desired control force, u_d , can be delivered. However, a semi-active device can only produce the desired force when feasible. This is because the damping force is always in a direction opposite to the relative velocity. Mathematically, the semi-active damper force is given by

$$u = u_d \frac{(1 - \text{sgn}(u_d \dot{z}))}{2}, \quad \text{sgn}(q) = \begin{cases} 1 (q \geq 0) \\ -1 (q < 0) \end{cases} \quad (4-1)$$

in which u_d is the desired control force which is obtained from optimal control scheme, \dot{z} is the relative velocity between the mass damper and the building (Hrovat et al, 1983).

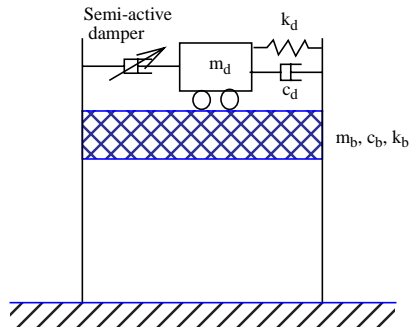


Figure 4.1 SDOF system with SATMD

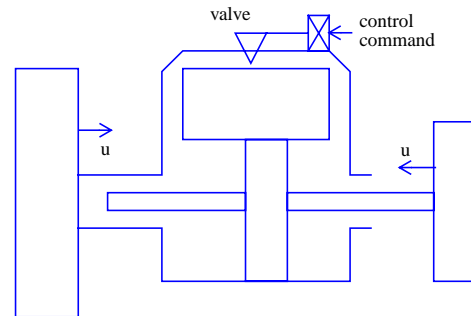


Figure 4.2 Semi-active actuator

4.1.2 SATLCD

SATLCD consists of liquid mass in a U-shaped container and an adjustable orifice as shown in Fig. 4.3. Like an SATMD, it is usually placed near the top of the building and takes advantage of the existing water storage of the building. The control force is derived from the inertia of the liquid mass and the damping effect of the hydrodynamic head loss. In this study, the valve dynamics of the adjustable orifice is assumed negligible.

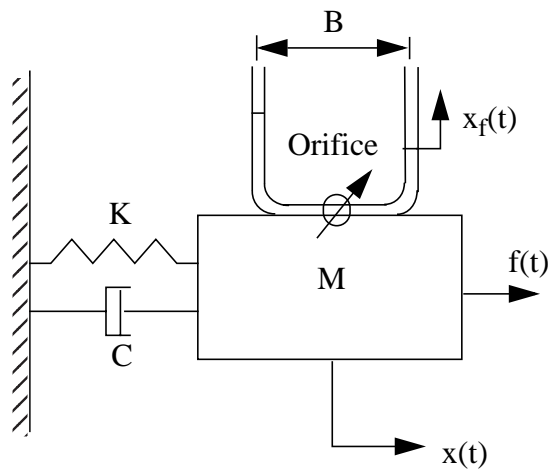


Figure 4.3 SDOF system with SATLCD

The dynamics of the coupled SATLCD and the structure system can be expressed as:

$$\begin{bmatrix} \rho AL & \rho AB \\ \rho AB & \rho AL + M \end{bmatrix} \begin{bmatrix} \ddot{x}_f(t) \\ \ddot{x}(t) \end{bmatrix} + \begin{bmatrix} (\rho A \xi |\dot{x}_f(t)|)/2 & 0 \\ 0 & C \end{bmatrix} \begin{bmatrix} \dot{x}_f(t) \\ \dot{x}(t) \end{bmatrix} + \begin{bmatrix} 2\rho Ag & 0 \\ 0 & K \end{bmatrix} \begin{bmatrix} x_f(t) \\ x(t) \end{bmatrix} = \begin{bmatrix} 0 \\ f(t) \end{bmatrix} \quad (4-2)$$

where M , K and C are the mass, damping and stiffness matrices of structure, respectively; x_f and x are the vertical elevation change of liquid surface and the lateral displacement of the structure; ρ , L , B and A are the density, length, width and cross-sectional area of the

liquid column; ξ is the coefficient of head loss governed by the orifice opening ratio; g is the acceleration of gravity; $f(t)$ is the external disturbance applied to the structure. The matrix equation (4-2) is nonlinear because of the nonlinear damping force generated by the loss of energy through the orifice. To make it simpler, the damping force is moved to the right hand side of the equation and is treated as the control force. As a result, Eq. (4-2) can be written as:

$$\begin{bmatrix} \rho AL & \rho AB \\ \rho AB & \rho AL + M \end{bmatrix} \begin{bmatrix} \ddot{x}_f(t) \\ \ddot{x}(t) \end{bmatrix} + \begin{bmatrix} 0 & 0 \\ 0 & C \end{bmatrix} \begin{bmatrix} \dot{x}_f(t) \\ \dot{x}(t) \end{bmatrix} + \begin{bmatrix} 2\rho Ag & 0 \\ 0 & K \end{bmatrix} \begin{bmatrix} x_f(t) \\ x(t) \end{bmatrix} = \begin{bmatrix} 0 \\ f(t) \end{bmatrix} + \begin{bmatrix} 1 \\ 0 \end{bmatrix} u(t) \quad (4-3)$$

where $u(t) = -(\rho A \xi |\dot{x}_f(t)| \dot{x}_f(t))/2$ is the damping force that can be adjusted by changing orifice opening ratio using different control schemes. For the active control system, the control force is realized by using an external actuator to pump the liquid to oscillate inside the U-tube which is not influenced by the direction of the liquid velocity. For the semi-active control, the variation of damping force is realized by altering the orifice opening which results in changes in the head loss coefficient. The change of the head loss coefficient is limited by the physical performance of the valve as follows

$$\begin{aligned} \xi(t) &= -2u(t)/(\rho A |\dot{x}_f(t)| \dot{x}_f(t)) && \text{if } u(t)\dot{x}_f(t) < 0 \\ \xi(t) &= \xi_{min} && \text{if } u(t)\dot{x}_f(t) \geq 0 \end{aligned} \quad (4-4)$$

The head loss coefficient ranges between 0 and ∞ , where $\xi = 0$ and $\xi = \infty$ representing the fully opened orifice and the completely closed orifice, respectively. $\xi \geq 0$ at all times,

which means $u(t)$ is always in the opposite direction of $\dot{x}_f(t)$. Usually an upper limit of ξ known as ξ_{max} is specified, which corresponds to the smallest orifice opening ratio. Therefore, the bounds for the supplied control force is ξ_{max} , where

$$0 \leq u(t) \leq -\rho A \xi_{max} |\dot{x}_f(t)| \dot{x}_f(t) / 2 \quad (4-5)$$

For the continuously-varying orifice control, ξ can change continuously between 0 and ξ_{max} . Rewriting Eq. (4-3) in the state space expression:

$$\begin{aligned} \dot{\mathbf{x}} = \begin{bmatrix} \dot{x}_1 \\ \dot{x}_2 \end{bmatrix} &= \begin{bmatrix} 0 & \mathbf{I} \\ -\mathbf{M}^{-1}\mathbf{K} & -\mathbf{M}^{-1}\mathbf{C} \end{bmatrix} \begin{bmatrix} x_1 \\ \dot{x}_2 \end{bmatrix} + \begin{bmatrix} 0 \\ \mathbf{M}^{-1}\mathbf{L} \end{bmatrix} u(t) + \begin{bmatrix} 0 \\ \mathbf{E} \end{bmatrix} f(t) \\ &= \mathbf{Ax} + \mathbf{Bu} + \mathbf{G}f(t) \end{aligned} \quad (4-6)$$

where \mathbf{I} is identity matrix; \mathbf{M} , \mathbf{K} , \mathbf{C} , \mathbf{L} , and \mathbf{E} are mass, stiffness, damping, control force location, and loading position matrices, respectively, which are given as:

$$\mathbf{M} = \begin{bmatrix} \rho AL & \rho AB \\ \rho AB & \rho AL + M \end{bmatrix}, \quad (4-7)$$

$$\mathbf{K} = \begin{bmatrix} 2\rho Ag & 0 \\ 0 & K \end{bmatrix}, \quad (4-8)$$

$$\mathbf{C} = \begin{bmatrix} 0 & 0 \\ 0 & C \end{bmatrix}, \quad \mathbf{L} = \begin{bmatrix} 1 \\ 0 \end{bmatrix}, \quad \text{and} \quad \mathbf{E} = \begin{bmatrix} 0 \\ 1 \end{bmatrix} \quad (4-9)$$

For real-time digital implementation of MPC control, Eq. (4-3) is expressed in discrete time as

$$\mathbf{x}((k+1)\Delta t) = \Phi \mathbf{x}(k\Delta t) + \Gamma_u u(k\Delta t) + \Gamma_d \ddot{x}_g(k\Delta t) \quad (4-10)$$

where Φ , \mathbf{P}_1 are $2n \times 2n$ matrices and Γ_u is $2n \times m$ matrix defined by: $\Phi = e^{A\Delta t}$, $\mathbf{P}_1 = \int_0^{\Delta t} e^{A\tau} d\tau$, $\Gamma_u = \mathbf{P}_1 \mathbf{B}$, and $\Gamma_d = \mathbf{P}_1 \mathbf{G}$. Δt is the sampling time. The output measurement is

$$y(k) = C_y x(k) + D_y u(k) + F_y f(k) \quad (4-11)$$

where $C_y = I$, $D_y = 0$, and $F_y = 0$ in the case of state feedback; $C_y = [-\mathbf{M}^{-1} \mathbf{K} \quad -\mathbf{M}^{-1} \mathbf{C}]$, $D_y = \mathbf{M}^{-1} \mathbf{L}$, and $F_y = \mathbf{E}$ in the case of acceleration feedback.

For SATMD and SATLCD, the desired control force is generally formulated according to a control law and then this desired control force is trimmed according to Eq. (4-1) and (4-5) to obtain the final control force, which is the clipped optimal control force. This study simplifies the damping force generating mechanism in semi-active systems by interpreting it in terms of time-varying constraints. An optimal control design is directly achieved through the application of an MPC scheme subjected to constraints.

4.2 Examples

In order to demonstrate MPC based semi-active control, two examples are used in the following analysis. In the first, a single-degree-of-freedom system (SDOF) is studied by employing SATMD and SATLCD. The second example analyzes a five degree-of-freedom building equipped with an SATLCD.

4.2.1 SDOF System

First, a SDOF system with a semi-active tuned mass damper proposed by Hrovat et al. (1983) is studied. The semi-active tuned liquid column damper presented by Haroun and Pires (1994) is then used on the same structure to demonstrate the control efficiency. The parameters of the systems studied are given in Table 4.1 (Haroun and Pires, 1994).

Table 4.1 Data for the SDOF, TMD and TLCD

Building Data	TMD Data	TLCD Data
$m_b = 1.04 \times 10^2$ kip.sec ² /in $k_b = 1.04 \times 10^2$ kip/in $c_b = 2.08$ kip.sec/in $\zeta_b = 0.01$ $\omega_b = 1.0$ rad/sec	$m_d = 2.8$ kip.sec ² /in $k_d = 1.73$ kip/in $c_d = 0.137$ kip.sec/in $\zeta_d = 0.036$ $\omega_d = 0.912$ rad/sec	$L = 65.7$ ft $B = 46.0$ ft $A = 194.9$ ft ² $\xi_{opt} = 1.5$ $\omega_{tlcd} = 0.99$ rad/sec

For simplicity, the wind load is modeled by:

$$f(t) = p(3 \sin \omega t + 7 \sin 2\omega t + 5 \sin 3\omega t + 4 \sin 4\omega t) \quad (4-12)$$

where $p = 9.75$ kips, and $\omega = 1.0$ rad/sec, which is the same as the natural frequency of the structure. For the SATMD, the control force is generated according to Eq. (4-1). Hrovat et al. (1983) used clipped semi-active optimal control to limit the maximum semi-active force to a reasonable value, i.e. 7 kips. Here a time varying constrained MPC scheme is applied to make the control force stay within the damper capability. Therefore, the following limits can be derived from Eq. (4-1):

$$\text{Case One: if } \dot{z} \leq 0, \quad \begin{cases} \max(u) = 7 \\ \min(u) = 0 \end{cases} \quad (4-13)$$

$$\text{Case two: if } \dot{z} > 0, \quad \begin{cases} \max(u) = 0 \\ \min(u) = -7 \end{cases} \quad (4-14)$$

The above constraints switch between the two cases according to the direction of the relative velocity, which changes with time as shown in Fig 4.4. These constraints are time-varying and updated at each time step. The MPC constrained scheme provides an optimal solution within these time-varying constraints. The control results using the SATMD are shown in Table 4.2. The performance of the different control schemes are measured by root mean square (RMS) values of displacement and acceleration. As show in Table 4.2, y_{rms} , \ddot{y}_{rms} and u_{rms} are RMS values of the displacement, acceleration of the structure, and the control force, respectively.

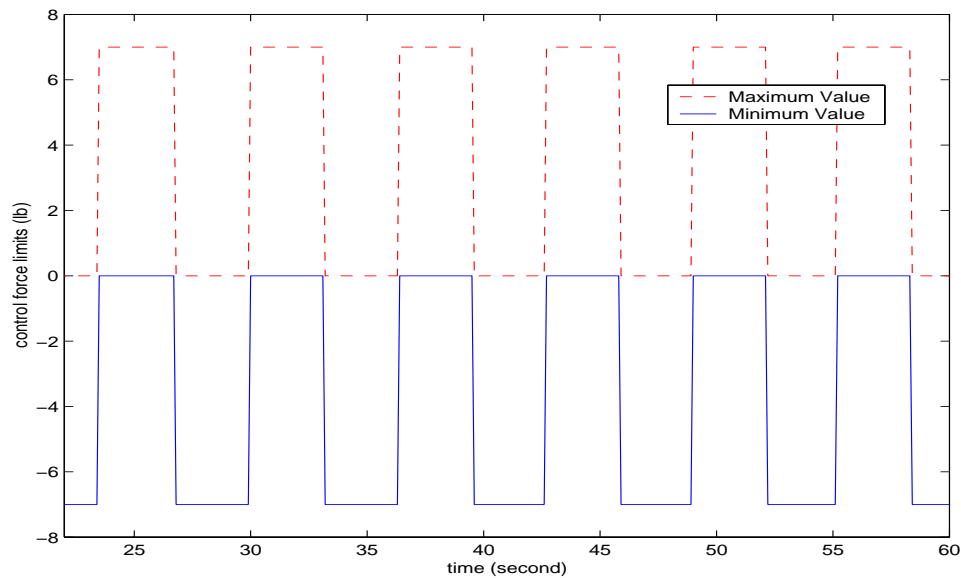


Figure 4.4 Time-varying constraints using SATMD.

Table 4.2 Summary of Main Results using SATMD

Type of control	y_{rms} (in)	\dot{y}_{rms} (in/sec ²)	u_{rms} (lb)
No control	4.5	4.5	-
Passive TMD	2.0	2.1	-
SA-clipped TMD(LQ)	1.3	1.5	3.3
SATMD (MPC constrained)	1.2	1.4	3.3
ATMD (MPC constrained)	0.77	1.1	3.3

In Table 4.2, the results of five cases are listed. The results of the first three cases, i.e., no control, passive TMD and SA-clipped TMD are obtained from Hrovat et al. (1983). The last two cases are SATMD and active TMD using constrained MPC. Apparently, the results of the last two cases are better than those in the first three cases. SATMD based on MPC scheme gives 7% more reduction on the displacement and acceleration with the same damping force. The constrained case of actively controlled TMD performs 30% better in displacement reduction and 21% better in acceleration reduction than the SATMD using MPC constrained. Figure 4.5 shows building displacement responses under passive control, semi-active control and active control based on MPC constrained scheme, respectively. Figure 4.6 shows that the control force using ATMD remains within ± 7 kips with a RMS value of 3.3N. The semi-active control force is shown in Fig. 4.7 which has a RMS value of 3.3N. It changes between either 0 and 7 kips or -7 and 0 kips depending on the sign of relative velocity.

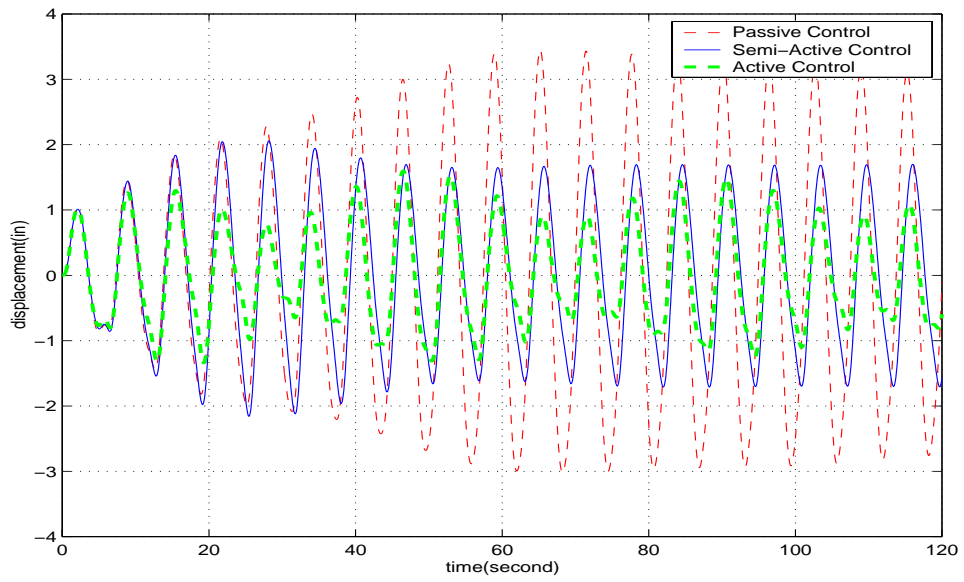


Figure 4.5 Building displacement vs. time using active and SATMD control based on MPC constrained scheme.

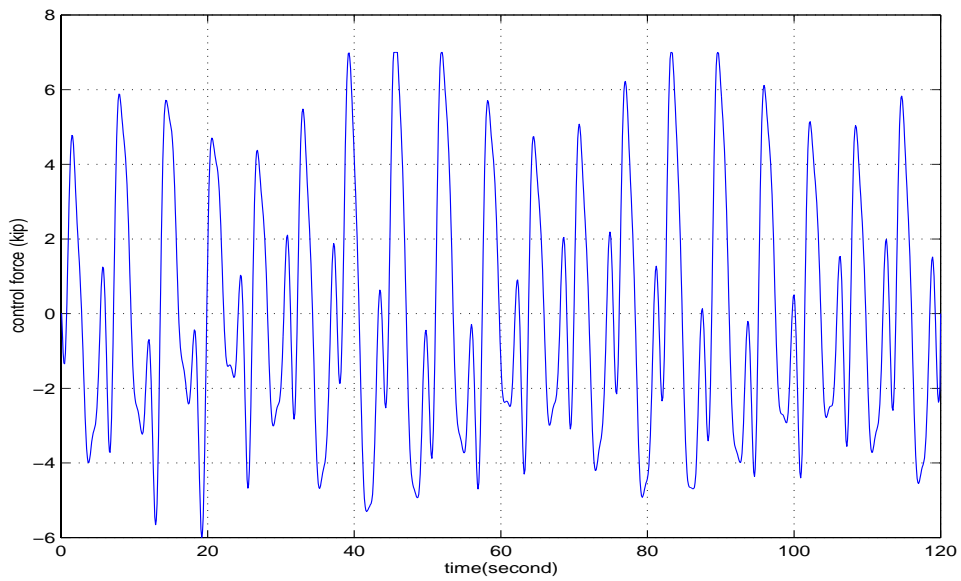


Figure 4.6 Control force vs. time: Active Control force based on MPC constrained scheme

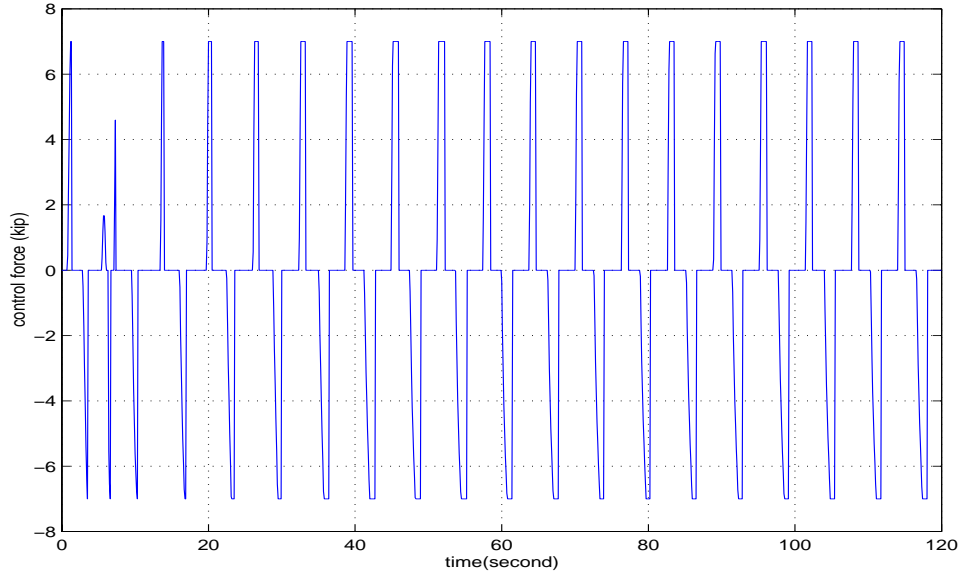


Figure 4.7 SA Control force based on MPC constrained scheme

The same SDOF building is used in the following example which employs SATLCD as a controller device. Here SATLCD control force is generated based on the MPC scheme. The salient features of the TLCD are given in Table 4.1. According to Eq. (4-4)-(4-5), the control force is given by the following rules:

$$u = \begin{cases} 0 \\ -\rho A \xi |\dot{x}_f(t)| \dot{x}_f(t) / 2 \\ -\rho A \xi_{max} |\dot{x}_f(t)| \dot{x}_f(t) / 2 \end{cases}, \text{ if } \begin{cases} \xi < 0 \\ 0 \leq \xi \leq \xi_{max} \\ \xi > \xi_{max} \end{cases} . \quad (4-15)$$

Accordingly, it can be shown that the control force is constrained within the following limits which are time-varying.

$$\text{if } \dot{x}_f < 0, \quad \begin{cases} \max(u) = -\rho A \xi_{max} |\dot{x}_f(t)| \dot{x}_f(t) / 2 \\ \min(u) = 0 \end{cases} \quad (4-16)$$

$$\text{if } \dot{x}_f \geq 0, \quad \begin{cases} \max(u) = 0 \\ \min(u) = -\rho A \xi_{\max} |\dot{x}_f(t)| \dot{x}_f(t) / 2 \end{cases} \quad (4-17)$$

SATLCD with MPC constrained scheme considers the orifice operating strategy as constraints on the control force, which has limitations expressed by Eqs. (4-16) and (4-17). Figure 4.8 shows the time-varying constraints. It can be seen that the non-zero maximum and minimum values of constraint are modulated by the liquid relative velocity and the maximum head loss coefficient.

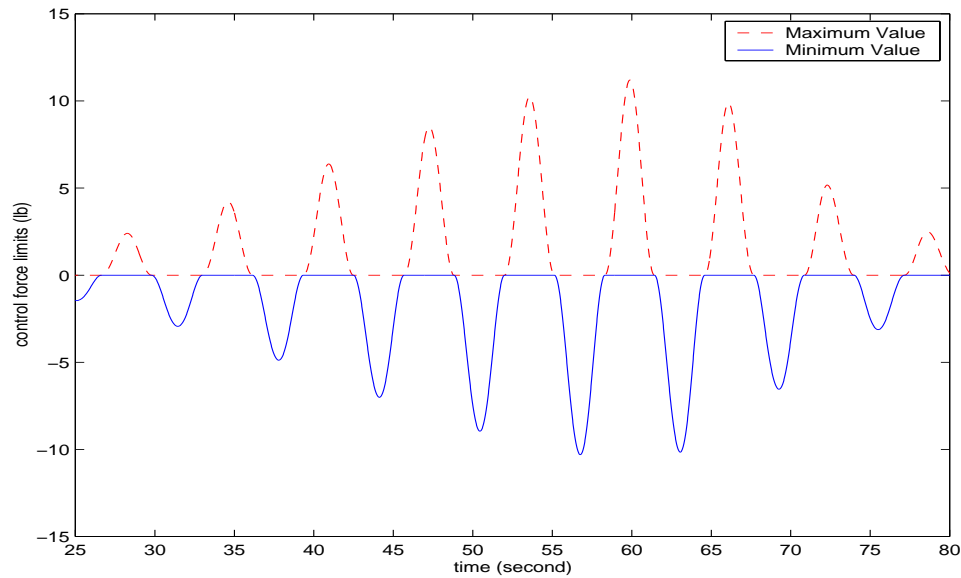


Figure 4.8 Time-varying constraint using SATLCD.

RMS values of the displacement and acceleration response in four cases (no control, SATLCD using clipped LQR, and SATLCD using MPC constrained) are shown in Table 4.3. SATLCD represents semi-active controlled TLCD. It shows that the constrained MPC provides better displacement reduction than the clipped LQR control. The SATLCD based on the constrained MPC scheme gives 20% more reduction in the displacement and uses 33% smaller damping force. If the orifice control strategy described by Eqs. (4-4) and (4-

5) is expressed in terms of bounds as in Eqs. (4-16) and (4-17), the performance of the controller is improved. Figure 4.9 shows the controlled displacement response under the clipped-LQR and MPC constrained schemes, respectively. The head loss under the MPC scheme is plotted in Fig. 4.10. The control forces in the SATLCD case using clipped LQR and MPC constrained schemes are shown in Fig. 4.11. From the figures and Table 4.3, it can be concluded that SATLCD provides a better control performance than the clipped LQR control.

Table 4.3 Summary of Main Results using SATLCD

Type of control	y_{rms} (in)	\ddot{y}_{rms} (in/sec ²)	u_{rms} (lb)
No Control	4.5	4.5	-
SATLCD (Clipped LQR)	1.00	1.24	1.223
SATLCD (MPC constrained)	0.801	1.09	0.813

In order to examine the influence of the maximum head loss, ξ_{max} , on the control performance, three performance criteria are defined:

$$J_1 = \frac{y_{urms} - y_{rms}}{y_{urms}} ; J_2 = \frac{\ddot{y}_{urms} - \ddot{y}_{rms}}{\ddot{y}_{urms}} ; J_3 = u_{rms} \quad (4-18)$$

where y_{urms} and \ddot{y}_{urms} are the uncontrolled RMS values of building displacement and acceleration, respectively. The upper limit of the coefficient of head loss, ξ_{max} , is related to the smallest orifice opening ratio that is needed to maintain the liquid oscillations for control action. For different ξ_{max} values, the controller performance varies (Fig. 4.12) and it influences the level of control force and the correspondingly controlled response. A smaller value of ξ_{max} limits the control force to a relatively small value and results in lower reduction of structural response. As ξ_{max} increases, there is a concomitant increase

in J_1 , J_2 and J_3 up to $\xi_{max} = 10$ and after that either these measures remain unchanged or are slightly changed (Fig. 4.12).

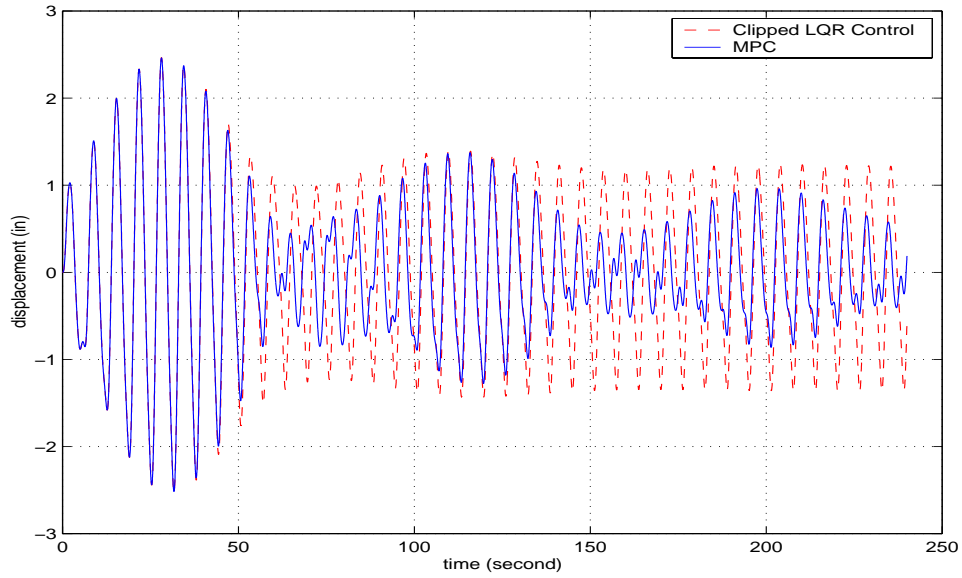


Figure 4.9 Displacement of SATLCD using Clipped-LQR and MPC with constraints

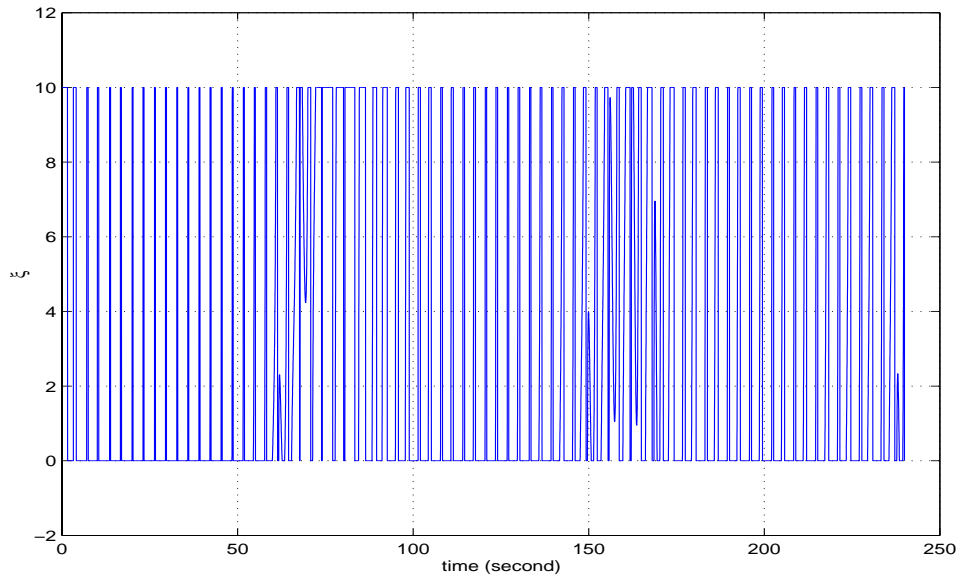


Figure 4.10 Head loss ξ verses time

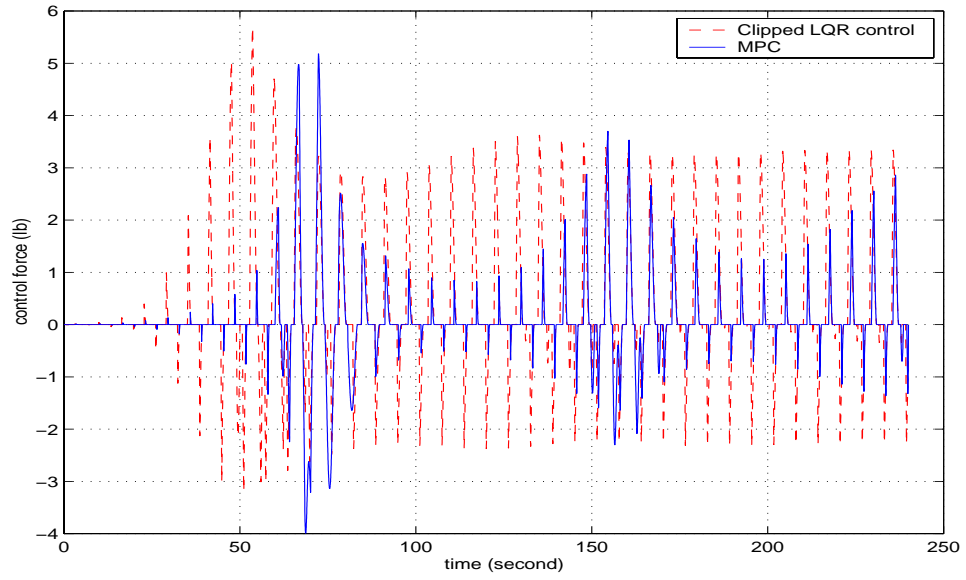


Figure 4.11 Control force of SATLCD using Clipped-LQR and MPC scheme consider constraints

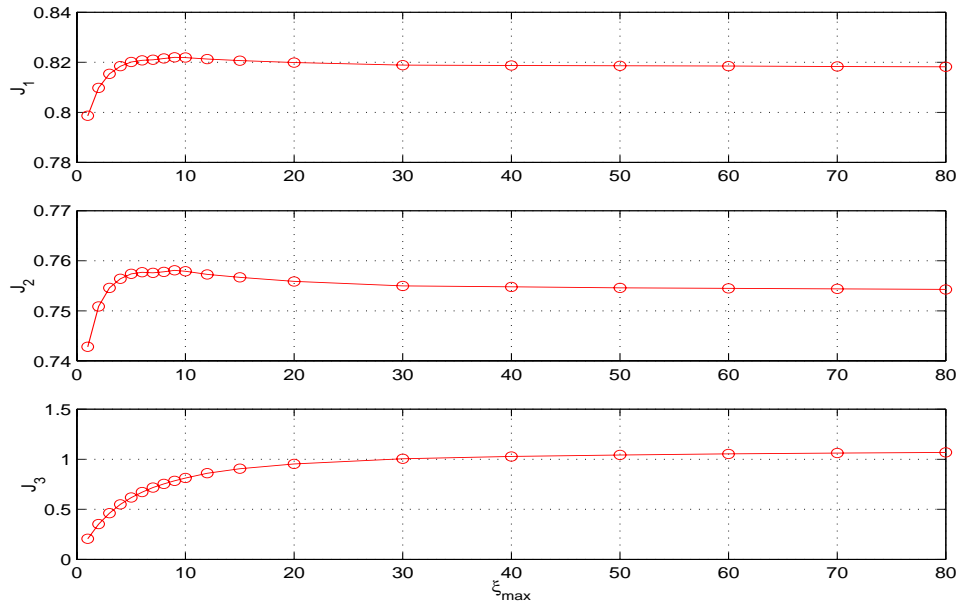


Figure 4.12 Performance index vs. ξ_{max} using

4.2.2 Multi-Story Building

In this example, a multi-story building subjected to the along-wind aerodynamic excitation is used to illustrate the MPC based scheme. The building dimensions are 31m square in plan and 183m in height. The structural system is lumped at five levels and the associated mass, stiffness and damping matrices are listed below (Kareem, 1981):

$$M = \begin{bmatrix} 4.5e5 & 0 & 0 & 0 & 0 \\ 0 & 4.5e5 & 0 & 0 & 0 \\ 0 & 0 & 4.5e5 & 0 & 0 \\ 0 & 0 & 0 & 4.5e5 & 0 \\ 0 & 0 & 0 & 0 & 4.5e5 \end{bmatrix} \text{ slug} \quad (4-19)$$

$$K = \begin{bmatrix} 8.77e6 & -8.77e6 & 0 & 0 & 0 \\ -8.77e6 & 1.75e7 & -8.77e6 & 0 & 0 \\ 0 & -8.77e6 & 1.75e7 & -8.77e6 & 0 \\ 0 & 0 & -8.77e6 & 1.75e7 & -8.77e6 \\ 0 & 0 & 0 & -8.77e6 & 1.75e7 \end{bmatrix} \text{ slug/s}^2 \quad (4-20)$$

$$C = \begin{bmatrix} 3.41e4 & -1.99e4 & -4.40e3 & -1.75e3 & -6.80e2 \\ -1.99e4 & 4.96e4 & -1.72e4 & -3.33e3 & -1.07e3 \\ -4.40e3 & -1.72e4 & 5.05e4 & -1.66e4 & 2.65e3 \\ -1.75e3 & -3.33e3 & -1.66e4 & 5.15e4 & -1.55e4 \\ -6.80e2 & -1.07e3 & -2.65e3 & -1.55e4 & 5.40e4 \end{bmatrix} \text{ slug/s} \quad (4-21)$$

The five natural frequencies of this building are 0.20, 0.583, 0.921, 1.182 and 1.348 *Hz*, respectively. The corresponding modal damping ratios are 1%, 1.57%, 2.14%, 2.52%, and 2.9%. The alongwind aerodynamics loading model used to generate wind excitation is based on the quasi-steady and strip theories. Its details will be discussed in Chapter 7. Figure 4.13 shows the power spectral density of the modeled wind velocity and the prescribed spectrum. It can be seen that the target and the simulated spectra have a good agreement. Figure 4.14 shows a sample time history of wind velocity at the top level of the building.

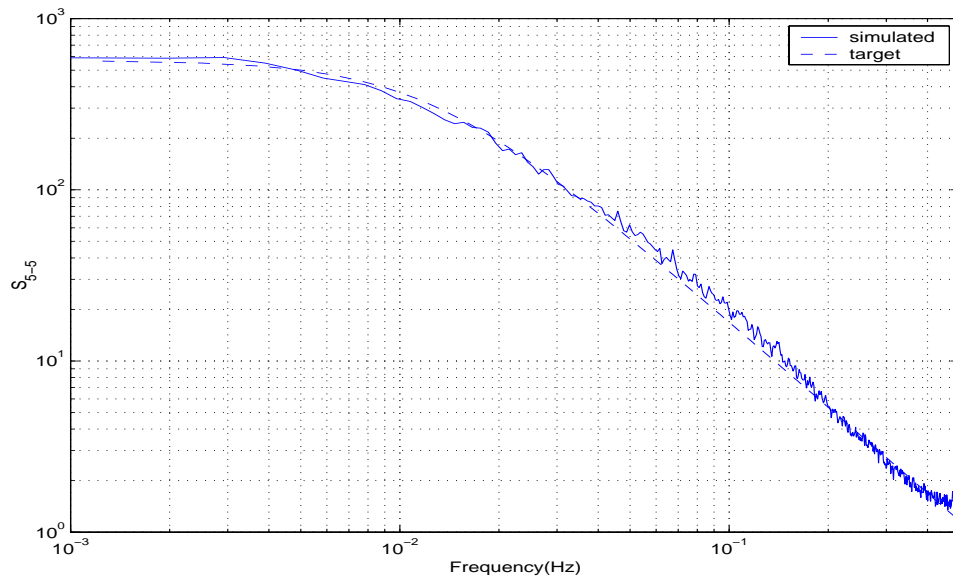


Figure 4.13 Comparison of the simulated and target PSD of wind velocity at 5-th level.

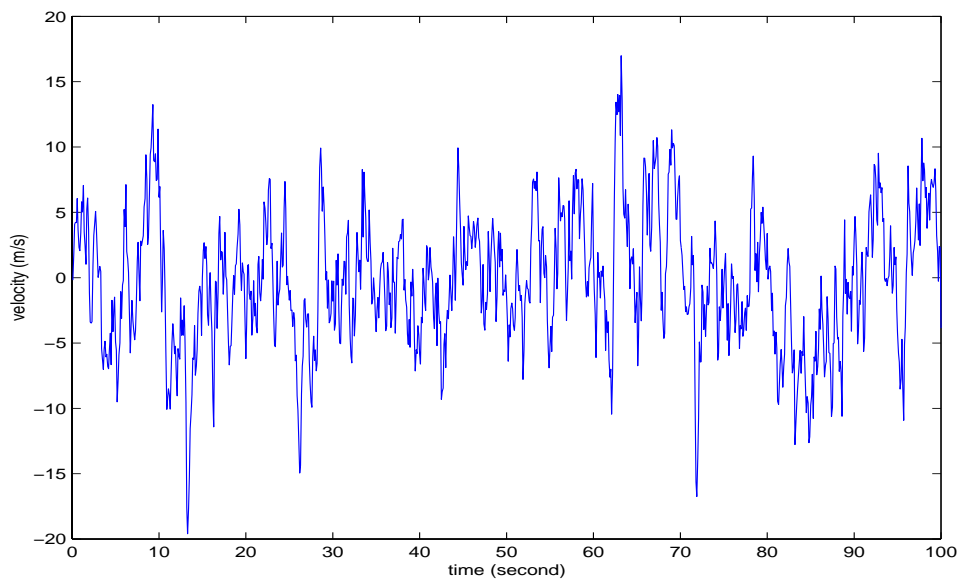


Figure 4.14 Time history of wind velocity at 5-th level

The semi-active TLCD is set up on the top level and the MPC with constrained scheme is employed to reduce the building motion in the alongwind direction. The structural response under different control schemes are listed in Table 4.4. The results of no control, passive TLCD, SATLCD using MPC constrained scheme, and semi-active TLCD using LQR are compared. On the one hand, SATLCD using MPC constrained scheme results in 17% and 14% more reduction in displacement and acceleration, respectively, than the passive control. On the other hand, it utilizes a 16% smaller damping force while reducing the displacement 5% more than the clipped LQR scheme. In conclusion, the SATLCD using MPC constrained scheme can deliver better performance for the multi-story building like the SDOF examples.

Table 4.4 Responses of the five-story building

Control Scheme	y_{rms} (cm)	\ddot{y}_{rms} (cm/s ²)	u_{rms} (kN)
Uncontrolled	15.21	25.62	
Passive Control	11.22	20.18	
Clipped LQR	9.15	17.17	90.3
SATLCD (MPC constrained)	8.74	16.72	74.5

Figure 4.15 shows the displacement response of the top level under passive control, clipped LQR and SATLCD using MPC constrained scheme. The damping forces generated by the clipped LQR and the SATLCD using MPC scheme are displayed in Fig. 4.16. The difference between the two control forces is clear as noted in Table 4.4.

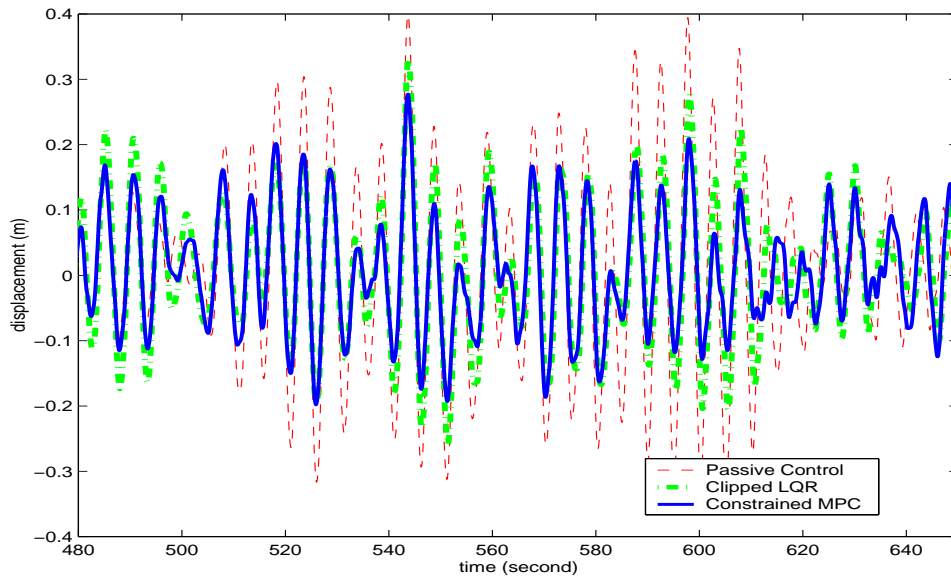


Figure 4.15 Comparison of displacement responses under passive control, clipped LQR, and constrained MPC

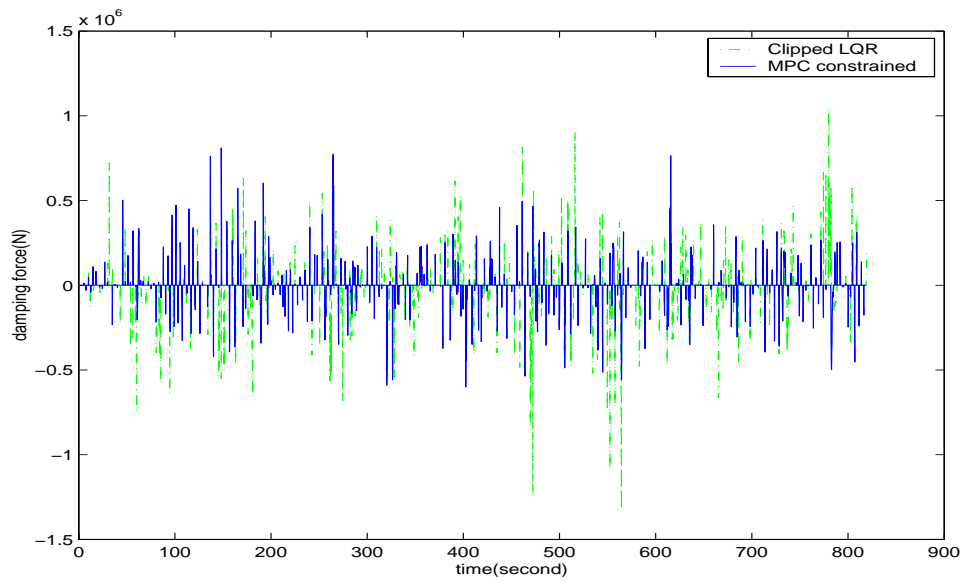


Figure 4.16 Control forces under clipped LQR and constrained MPC scheme

To sum up, SATLCD based on the MPC constrained scheme shows good performance and provides an optimal solution to the semi-active controlled tuned liquid column dampers. This control scheme considers the limits on the head loss of the orifice, which are due to the physical limitation of the valve opening, and converts these to the constraints on the control force. By using MPC with time-varying constraints on the control force, an optimal control force is generated and good control effects are obtained.

4.3 Summary

In this chapter, the MPC constrained scheme was studied for application to the semi-active control devices. The damping force variation mechanism in the semi-active systems was simplified and expressed in terms of time-varying constraints. An optimal control design was achieved through the application of an MPC scheme subjected to constraints. An SATMD and SATLCD were implemented in a single-degree-of-freedom (SDOF) building model and their performances were evaluated. An SATLCD was then employed in a building modeled as a five degree-of-freedom (DOF) system. From the SDOF building study, it can be seen that there is an optimal value of the maximum head loss coefficient that results in the best control performance. However, the changes in the maximum value of head loss coefficient does not have a dramatic improvement on the control performance. In both building models, the semi-active device based on the constrained MPC delivered better performance than the clipped LQR scheme. It shows that the constrained MPC offers more effective control design strategy for the semi-active systems with restrained damping force.

CHAPTER 5

MPC USING ACCELERATION FEEDBACK

Most of the control strategies utilize displacement and/or velocity response measurements of the structure as a feedback. However, directly measuring these response components can be quite difficult because the displacement and velocity are not absolute measurements, i.e. they need a fixed reference frame. In addition, during an earthquake, a structure's foundation moves with the ground, and thus does not provide a convenient fixed reference coordinate system. Therefore, control algorithms based on such measurements are impracticable for full-scale implementation. As a result, the acceleration response feedback becomes an attractive option. Furthermore, measuring the earthquake-induced acceleration response at different locations in the structure by means of accelerometers is relatively convenient (Spencer et al, 1991, 1992; Dyke et al, 1996).

This chapter employs the MPC scheme to reduce structural response of buildings under earthquakes by using acceleration response feedback. The Kalman-Bucy filter in the state observer is used to estimate the system states from the acceleration output feedback. Four different examples are employed to demonstrate the effectiveness of the acceleration feedback methodology. The first two examples analyze buildings using active tendon devices, and the second set of examples using active mass dampers (AMDs). In each case, the first building is a single-degree-of-freedom (SDOF) system and the second building is a three-

story one. For the SDOF system, the analysis results of the acceleration feedback are compared to those obtained from the state feedback. Furthermore, the influence of accelerometer locations on the effectiveness of the controller is also examined in the three-story building example.

5.1 Problem Formulation

In Chapter 2 the equations of the motion are presented. In this Chapter, acceleration is the measured output. An overall system model is listed below.

$$\begin{aligned}\mathbf{x}(k+1) &= \Phi(k)\mathbf{x}(k) + \Gamma_u(k)u(k) + \Gamma_d(k)\ddot{x}_g(k) \\ \mathbf{y}(k) &= C\mathbf{x}(k) + D_u u(k) + D_d \ddot{x}_g + v\end{aligned}\quad (5-1)$$

in which $\mathbf{y}(k)$ is the measured acceleration output; v is the measurement noise and

$$C = \begin{bmatrix} -\mathbf{M}^{-1}\mathbf{K} & -\mathbf{M}^{-1}\mathbf{C} \end{bmatrix}\quad (5-2)$$

$$D_u = -\mathbf{M}^{-1}\mathbf{L}, \quad D_d = 0\quad (5-3)$$

5.2 Acceleration Feedback and State Estimator

As stated earlier, acceleration measurements are more straightforward and convenient than the displacement and velocity responses, which define the states of the system. The main assumption for using the Kalman-Bucy filter in the MPC scheme is that the input and output disturbances are random with zero mean values (Ricker, 1990). According to the separation principle (Kailath, 1980), the control and estimation problems can be consid-

ered separately. Therefore, the estimator gain can be obtained independently of the feedback gain. The full state vector, $\mathbf{x}(k)$, is reconstructed by using an observer to obtain the estimate of the state vector, $\hat{\mathbf{x}}(k)$. It can be constructed in the following manner

$$\hat{\mathbf{x}}(k+1) = \Phi\hat{\mathbf{x}}(k) + \Gamma_u u(k) + \Gamma_e(\mathbf{y}(k) - \hat{\mathbf{y}}(k)) \quad (5-4)$$

where $\hat{\mathbf{y}}(k) = C\hat{\mathbf{x}}(k) + Du(k)$ and Γ_e is related to the Kalman-Bucy filter:

$$\Gamma_e = PC^T(CPC^T + V)^{-1} \quad (5-5)$$

where P is the unique, symmetric, and positive definite solution of the Riccati equation:

$$P = \Phi[P - PC^T(CPC^T + V)^{-1}CP]\Phi^T + \Gamma_d W \Gamma_d^T \quad (5-6)$$

where $W = E[\ddot{x}_g \ddot{x}_g^T]$; $V = E[vv^T]$; $W = W^T$ when $W > 0$; and $V = V^T$ when $V > 0$. It is assumed that \ddot{x}_g and v are uncorrelated to each other, i.e. $E[\ddot{x}_g v^T] = 0$.

5.3 MPC Using Acceleration Feedback

For the acceleration feedback problem, the prediction model can be expressed as:

$$\hat{\mathbf{x}}(k+1|k) = \Phi\hat{\mathbf{x}}(k|k-1) + \Gamma_u \hat{u}(k|k-1) + \Gamma_e \hat{e}(k|k)$$

$$\hat{\mathbf{z}}(k|k-1) = C_z \hat{\mathbf{x}}(k|k-1)$$

$$\hat{\mathbf{y}}(k|k-1) = C\hat{\mathbf{x}}(k|k-1) + D_u \hat{u}(k|k-1) \quad (5-7)$$

where $\hat{\mathbf{x}}(k+1|k)$ estimates the state at the future sampling period $k+1$ based on the information available at k ; $\hat{\mathbf{y}}(k|k-1)$ estimates the plant output at period k based on the infor-

mation available at period $k-1$; $\hat{\mathbf{z}}(k|k-1)$ estimates control output vector; $C_z = I$; Γ_e is the Kalman-Bucy estimator gain matrix; and $\hat{e}(k|k)$ is the estimated error, i.e., $\hat{e}(k|k) = \mathbf{y}(k) - \hat{\mathbf{y}}(k|k-1)$.

Using Eq. (5-7), the process output predicted at the k -th time step and at subsequent time steps $k+j$, $j = 1, \dots, p$ can be expressed as a function of the current state vector $\mathbf{x}(k)$ and the control vector $\mathbf{u}(k) = [\hat{u}^T(k|k) \dots \hat{u}^T(k+\lambda-1|k)]^T$ as follows:

$$\Psi(k) = H\mathbf{u}(k) + Y_z \hat{\mathbf{x}}(k|k-1) + Y_e \hat{e}(k|k) \quad (5-8)$$

and $\Psi(k) = [\hat{\mathbf{z}}^T(k+1|k) \dots \hat{\mathbf{z}}^T(k+p|k)]^T$, where p is the prediction horizon and λ is the control horizon. The reference output can be written as $\Psi_r(k) = [\mathbf{z}_r^T(k+1|k) \dots \mathbf{z}_r^T(k+p|k)]^T$.

Therefore, the objective function is given by:

$$J = \frac{1}{2}[\Psi(k) - \Psi_r(k)]^T \bar{Q} [\Psi(k) - \Psi_r(k)] + \frac{1}{2} \mathbf{u}^T(k) \bar{R} \mathbf{u}(k). \quad (5-9)$$

By minimizing J , the optimal predictive control force is given by

$$\mathbf{u} = [H^T \bar{Q} H + \bar{R}]^{-1} H^T \bar{Q} [Y_z \hat{\mathbf{x}}(k|k-1) + Y_e \hat{e}(k|k)] \quad (5-10)$$

in which

$$H = \begin{bmatrix} H_1 & 0 & \dots & 0 \\ \dots & \dots & \dots & \dots \\ H_\lambda & H_{\lambda-1} & \dots & H_1 \\ H_{\lambda+1} & H_\lambda & \dots & H_1 + H_2 \\ \dots & \dots & \dots & \dots \\ H_p & H_{p-1} & \dots & H_1 + \dots + H_{p-\lambda} \end{bmatrix}, H_k = C_z \Phi^{k-1} \Gamma_u, \quad (5-11)$$

$$Y_z = \left[(C_z \Phi)^T (C_z \Phi^2)^T \dots (C_z \Phi^p)^T \right]^T, \quad (5-12)$$

$$Y_e = \left[(C_z \Gamma_e)^T (C_z (I + \Phi) \Gamma_e)^T \dots \left(C_z \sum_{k=1}^p (\Phi^{k-1}) \Gamma_e \right)^T \right]^T, \quad (5-13)$$

$$\bar{Q} = \begin{bmatrix} Q & \dots & 0 \\ \dots & \dots & \dots \\ 0 & \dots & Q \end{bmatrix}, \bar{R} = \begin{bmatrix} R & \dots & 0 \\ \dots & \dots & \dots \\ 0 & \dots & R \end{bmatrix}. \quad (5-14)$$

The control variable taken at each time step is $u(k) = \hat{u}(k|k)$. It can be expressed as:

$$u(k) = K_1 \hat{\mathbf{x}}(k|k-1) + K_2 e(k|k) \quad (5-15)$$

where K_1 is the first row of matrix $[H^T \bar{Q} H + \bar{R}]^{-1} H^T \bar{Q} Y_z$ and K_2 is the first row of matrix $[H^T \bar{Q} H + \bar{R}]^{-1} H^T \bar{Q} Y_e$.

The system and the observer can then be expressed in state-space equations as shown below:

$$\begin{bmatrix} \mathbf{x}(k+1) \\ \hat{\mathbf{x}}(k+1|k) \end{bmatrix} = \begin{bmatrix} \Phi + \Gamma_u K_2 C & \Gamma_u K_1 - \Gamma_u K_2 C \\ (\Gamma_u K_2 + \Gamma_e) C & \Phi + \Gamma_u K_1 - (\Gamma_u K_2 + \Gamma_e) C \end{bmatrix} \begin{bmatrix} \mathbf{x}(k) \\ \hat{\mathbf{x}}(k|k-1) \end{bmatrix} + \begin{bmatrix} \Gamma_u K_2 D_d + \Gamma_d \\ (\Gamma_u K_2 + \Gamma_e) D_d \end{bmatrix} \ddot{x}_g(k) \quad (5-16)$$

$$\mathbf{y}(k) = \begin{bmatrix} C + D_u K_2 C & D_u K_1 - D_u K_2 C \end{bmatrix} \begin{bmatrix} \mathbf{x}(k) \\ \hat{\mathbf{x}}(k|k-1) \end{bmatrix} + \begin{bmatrix} D_d + D_u K_2 D_d \end{bmatrix} \ddot{x}_g(k) \quad (5-17)$$

In the following example, MPC formulation presented in the preceding section is utilized to demonstrate its applications to building structures.

5.4 Numerical Examples

Four numerical examples are presented below to demonstrate the acceleration feedback scheme presented earlier. This scheme is first applied to two buildings, each utilizing an active tendon device. It is then applied to the same two buildings, each equipped with an AMD. The 1940 El Centro earthquake record is scaled to 0.25 of its maximum intensity and used in this analysis as the input ground motion.

5.4.1 Active Tendon System

The first example below analyzes a building modeled as a single-degree-of-freedom (SDOF) system, and the second example analyzes a three-story building.

5.4.1.1 SDOF Building

The SDOF building with the active tendon used in Chapter 2 and shown in Fig. 2.2 is used here. In this example, $Q = I$, $R = 460$, $p = 5$ and $\lambda = 2$.

The analysis of the SDOF system using MPC with the acceleration feedback is compared to that using MPC with the state (i.e. displacement and velocity) feedback. In the former case, an observer is used to estimate the states of the system through the measured acceleration output, and the estimator gain is obtained by the Kalman-Bucy filter as described in Section 5.3. Table 5.1 lists the comparison results. Using almost the same control force (the difference is 0.05% in RMS value and 1.2% in the maximum value), these two schemes deliver similar control performance. The magnitude and phase plot of the transfer function for the acceleration feedback are shown in Fig. 5.1. The peak values of the system bode plot show a significant increase in damping after the control force is included. The damping ratio with and without control is found to be 0.182 and 0.01, respectively. Figures 5.2 and 5.3 show the time histories of the displacement and acceleration responses of the building with and without the control action, respectively. Figure 5.4 shows the variation in control force for this example.

Table 5.1 Comparison Between MPC with State FB and MPC with Acceleration FB

$p=5, \lambda=2$	without control	MPC with state feedback	Percentage change	MPC with acceleration feedback	Percentage change
σ_x (cm)	0.075	0.0201	73.3	0.0202	73.2
$\sigma_{\dot{x}}$ (cm/s ²)	37.8	14.6	61.3	14.7	61.2
σ_f (N)	—	99.2	—	99.1	- 0.05
x_{max} (cm)	0.25	0.10	60.0	0.10	60.0
\ddot{x}_{max} (cm/s ²)	135.4	101.5	25.0	101.4	25.1
f_{max} (N)	—	672.0	—	663.7	- 1.2

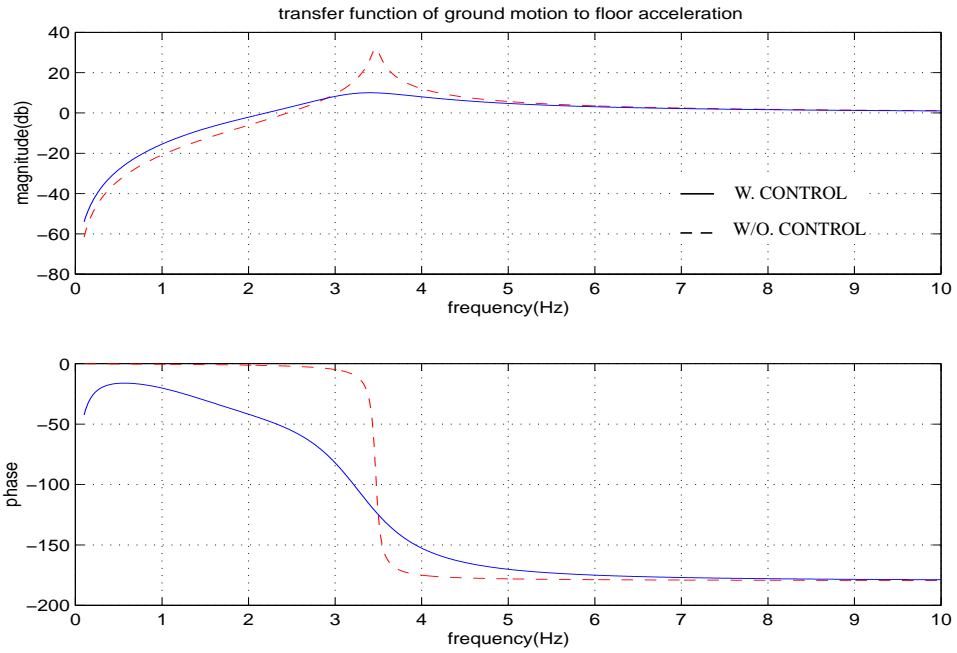


Figure 5.1 Transfer function from ground acceleration to floor acceleration

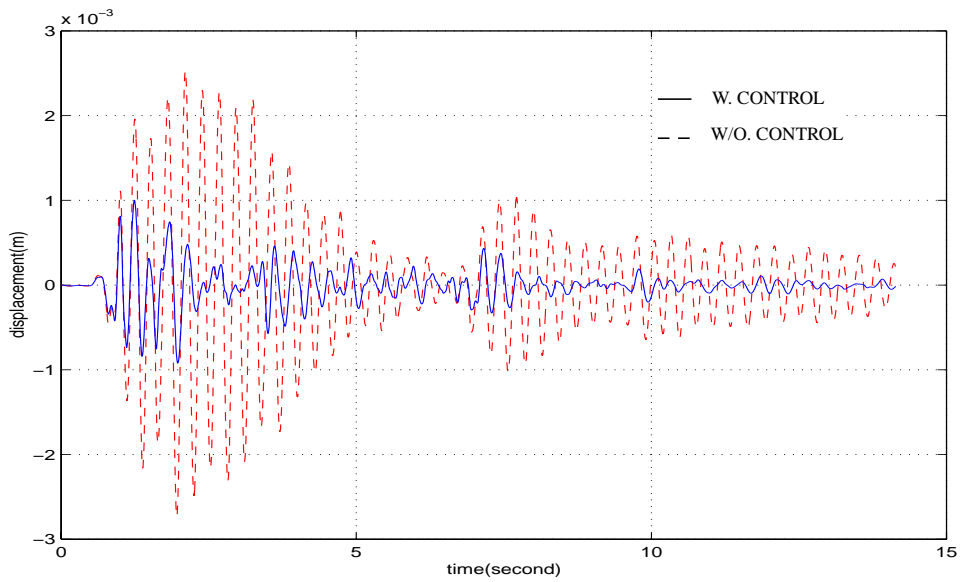


Figure 5.2 Comparison of uncontrolled and controlled displacement with acceleration FB.

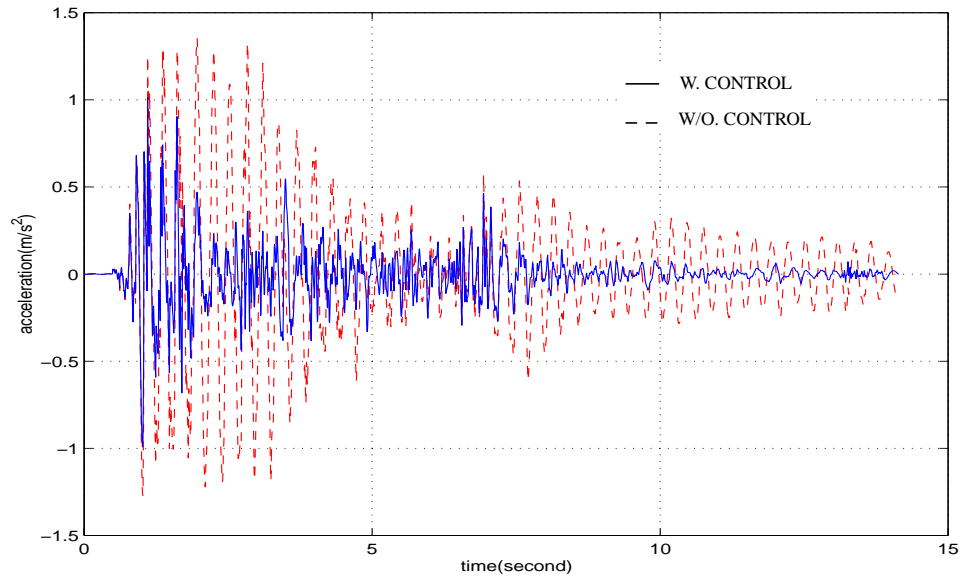


Figure 5.3 Comparison of uncontrolled and controlled acceleration with acceleration FB.

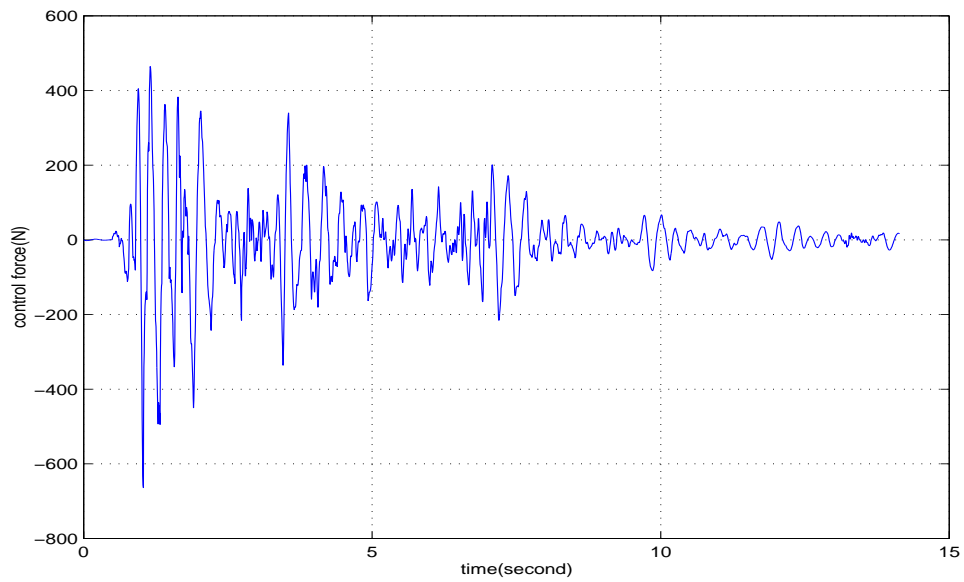


Figure 5.4 Control force for MPC acceleration FB.

5.4.1.2 Three-Story Building

In the following example, a three-story building with the active tendon system shown in Chapter 2 (Fig. 2.8) is used to implement the MPC scheme using the acceleration feedback obtained from different locations. The mass, stiffness, and damping matrices of the building are given in Table 2.4.

In this example four cases are considered. In the first case, the accelerometer is placed at each floor. Then these acceleration outputs are fed back to the observer, which estimates the states of the system. In the other three cases, the accelerometer is placed at one floor at a time. Therefore, only one acceleration output is known, which is used as an input into the observer to estimate the system states.

Table 5.2 lists the comparison of the top floor acceleration responses. Under these four feedback configurations, results reveal that if the acceleration feedback is obtained from the first floor, the control force is the lowest. The maximum top floor acceleration obtained from the first floor feedback is slightly higher than that from the third floor feedback but lower than those from the other two cases. Although the observed differences in the top floor acceleration response in the studied cases are small, the control force in each case is notably different.

In addition, Table 5.2 also shows that if the accelerometer is placed on the third floor, the control force is the largest and the observed value of the maximum acceleration is the lowest. If the accelerometer is placed on the second floor, the control force value is in between those in the above two cases. The control performance for this configuration is not as good as in the other cases. If the all-floor acceleration feedback is used, the RMS

values of acceleration and displacement are found to be smaller than those in the other three cases, but the control force becomes larger. This is because the acceleration feedbacks of all three floors contain more information of all three modes of the building. The controller tries to control all three modes. It requires more efforts which leads to the increase in the control force.

Table 5.2 Comparison of Results Obtained from Various Accelerometer Layouts

3rd floor response	uncontrolled	3-floor feedback	1st floor FB	2nd floor FB	3rd floor FB
σ_x (cm)	0.162	0.085	0.091	0.087	0.087
$\sigma_{\ddot{x}}$ (cm/s ²)	46.5	22.5	23.6	23.3	23.6
σ_f (N)		51.6	47.0	49.2	50.4
x_{max} (cm)	0.38	0.29	0.31	0.29	0.29
\ddot{x}_{max} (cm/s ²)	154.6	137.0	136.8	141.2	136.1
f_{max} (N)		173.4	156.7	159.1	183.9

In Figs. 5.5 and 5.6, the magnitude and phase plot of the transfer functions from the ground motion to the first and third floor accelerations are shown. Three peaks occur at the first three natural frequencies of the structure, which represent the first three modes. After the control action is included, the contribution of these modes are reduced. Figure 5.7 gives the time history of the third floor acceleration and Fig. 5.8 shows the control force generated by the active tendons.

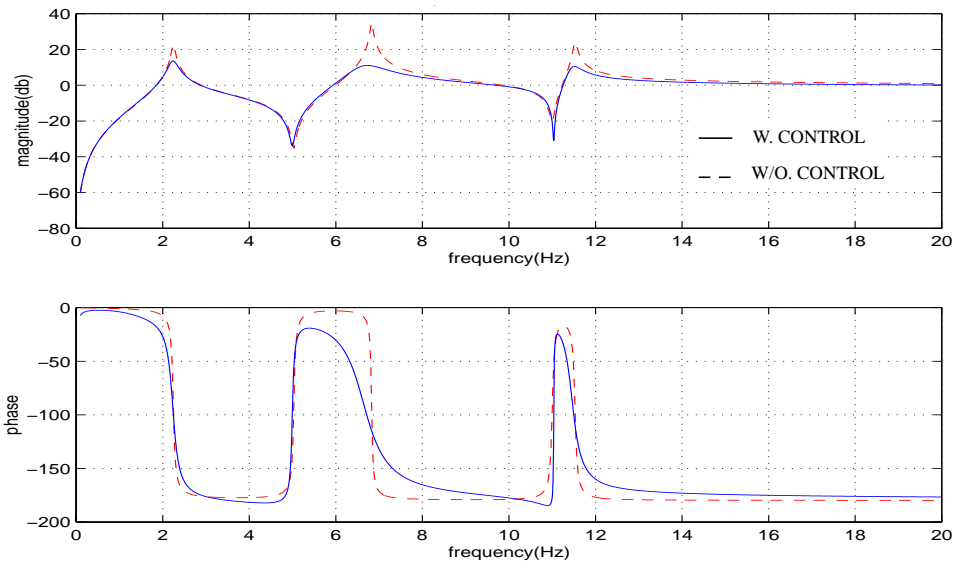


Figure 5.5 Bode plot of ground motion to the 1st floor acceleration (All floor feedback).

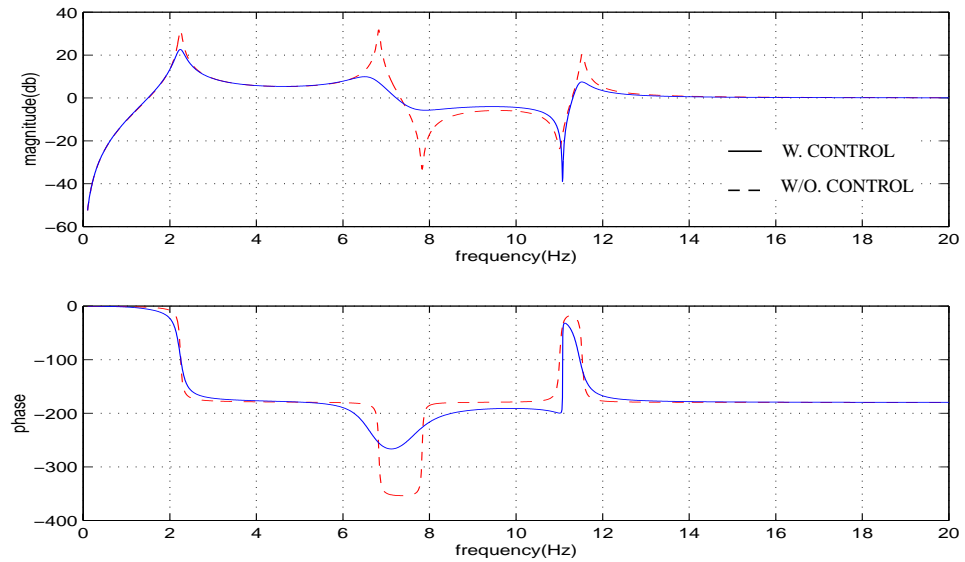


Figure 5.6 Bode plot of ground motion to 3rd floor acceleration (All floor feedback).

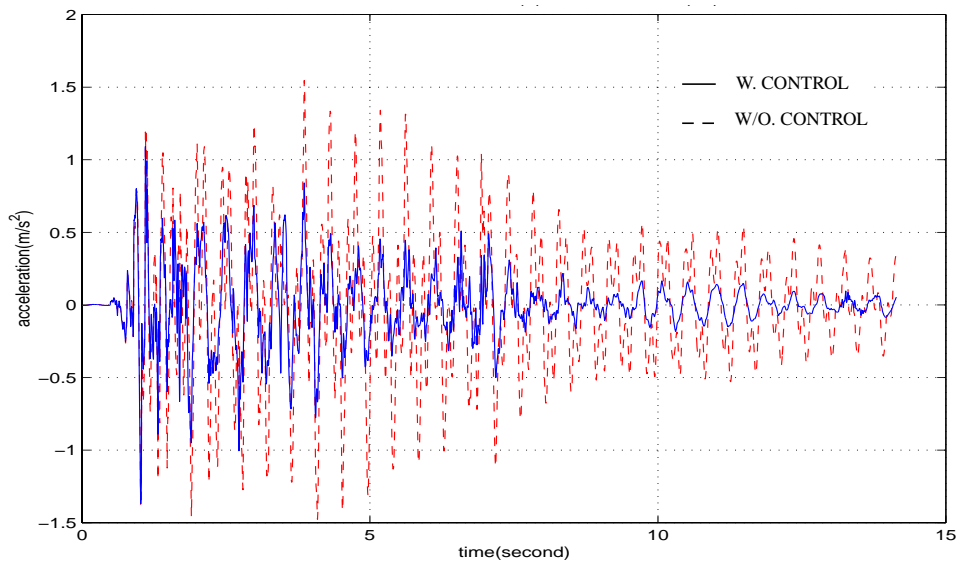


Figure 5.7 Uncontrolled and controlled third floor acceleration.

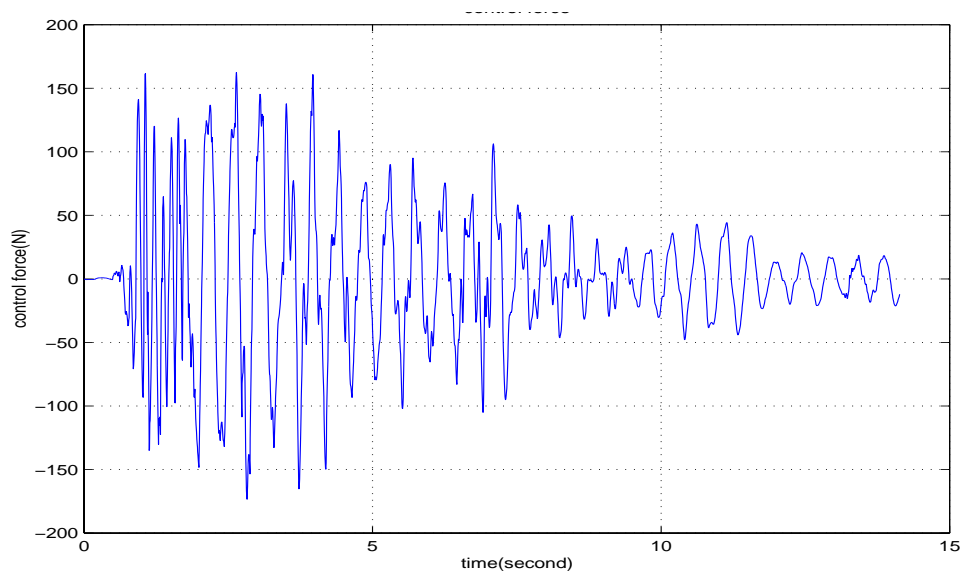


Figure 5.8 Control force using active tendon.

5.4.2 Active Mass Damper

In the following examples, a SDOF and a three-story building each equipped with an active mass damper (AMD) are studied.

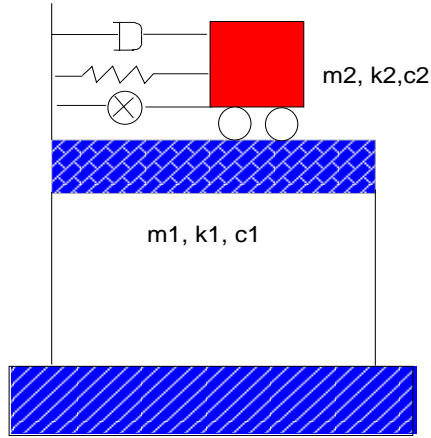


Figure 5.9 SDOF building using AMD

5.4.2.1 SDOF System

In this example, the building from Section 5.4.1.1 is analyzed again by putting an active mass damper (AMD) on the top of the building instead of the active tendon system. The mass, damping ratio, and natural frequency of the AMD are chosen as $m_2 = 0.02m_1$, $\omega_2 = 21.6\text{rad/s}$ and $\zeta_2 = 0.1$. As in Sec-

tion 5.1.1, MPC schemes using both the state feedback and the acceleration feedback are employed. The parameters are chosen as $R = 1$, $Q = \text{diag}[500000, 10, 0, 0]$, $p = 5$ and $\lambda = 2$.

Table 5.3 shows the results. It can be seen that both the state and acceleration feedback schemes perform similarly. The maximum and RMS values of the displacement, acceleration and control force are comparable. However, the maximum control force demanded by the acceleration feedback scheme is significantly larger than that of the state feedback scheme.

The transfer function relating the ground motion to the building acceleration is plotted in Fig. 5.10. The response is greatly reduced around the structure's natural frequency. If the excitation frequency is far from the system's natural frequency, the control system is least effective. In addition, the damping ratio is increased from 1.24×10^{-2} in an uncontrolled case to 0.176 in the controlled case. Accordingly, the response of the system is sig-

nificantly reduced. The time histories of the uncontrolled and controlled building displacements are given in Fig. 5.11.

Table 5.3 Comparison between the MPC with state FB and acceleration FB (AMD)

	without control	MPC with state feedback	Percentage change	MPC with acceleration feedback	Percentage change
σ_x (cm)	0.08	0.031	59.4	0.034	55.3
$\sigma_{\ddot{x}}$ (cm/s ²)	37.8	20.0	47.2	20.6	45.6
σ_u (N)	---	144.7	---	152.8	5.52
x_{max} (cm)	0.27	0.15	44.4	0.16	40.7
\ddot{x}_{max} (cm/s ²)	135.4	126.5	6.6	126.8	6.4
u_{max} (N)	---	483.8	---	820.7	69.6

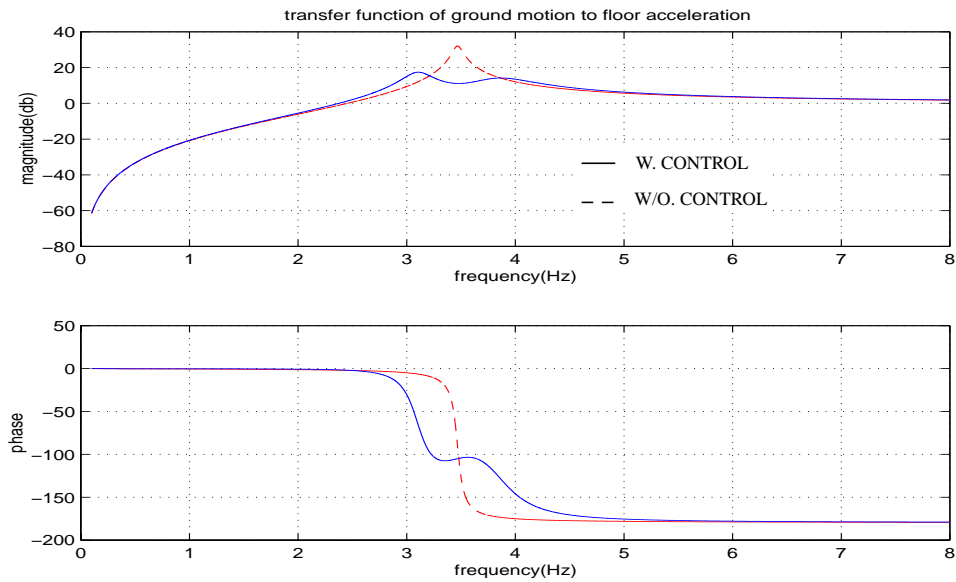


Figure 5.10 Bode plot of ground motion to floor acceleration using AMD

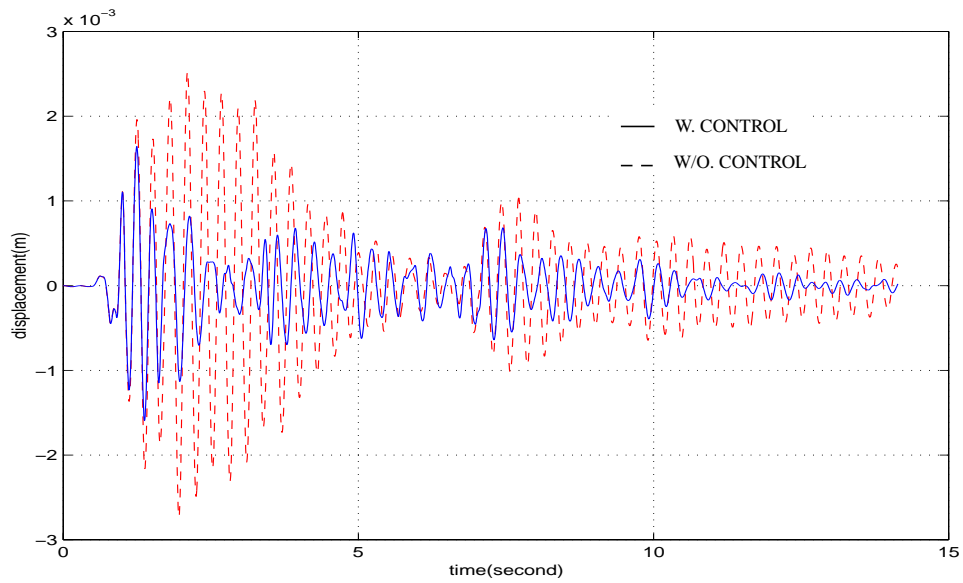


Figure 5.11 Uncontrolled and controlled floor acceleration using AMD

5.4.2.2 Three-Story Building

The building analyzed in Chapter 3 Section 3.2.3 is used here with an active mass damper placed on top of the third floor. The mass, damping ratio, and natural frequency of the AMD are chosen as $m_2 = 0.02m_1$, $\zeta_2 = 0.2$, and $\omega_2 = 0.95\omega_1 rad/s$, respectively. Here, $p = 5$, $\lambda = 2$, $R = 0.03$, and $Q = diag[10000, 10000, 50000, 10, 0, 0, 0, 0]$.

The transfer functions that relate ground motion to the first and third floor acceleration response are shown in Figs. 5.12 and 5.13. As shown in these two figures, the first mode response is greatly reduced due to the combined effect of the active control force and the tuning of the AMD to the first natural frequency of the building. The response in the second and third modes is slightly reduced as a result of the active controlled mass damper.

In Table 5.4, the performance of the controller is observed for different configurations of the acceleration feedback as in the active tendon example. In the four cases examined, the best control effect can be achieved if the acceleration is measured at all three floors. If

only one acceleration feedback is employed, almost the same control effect can be obtained regardless of the location of the acceleration measurement. However, the control force is the lowest when the acceleration is monitored at the first floor. Therefore, placing the accelerometers on the first floor is more effective than placing them at other locations if only one accelerometer is employed.

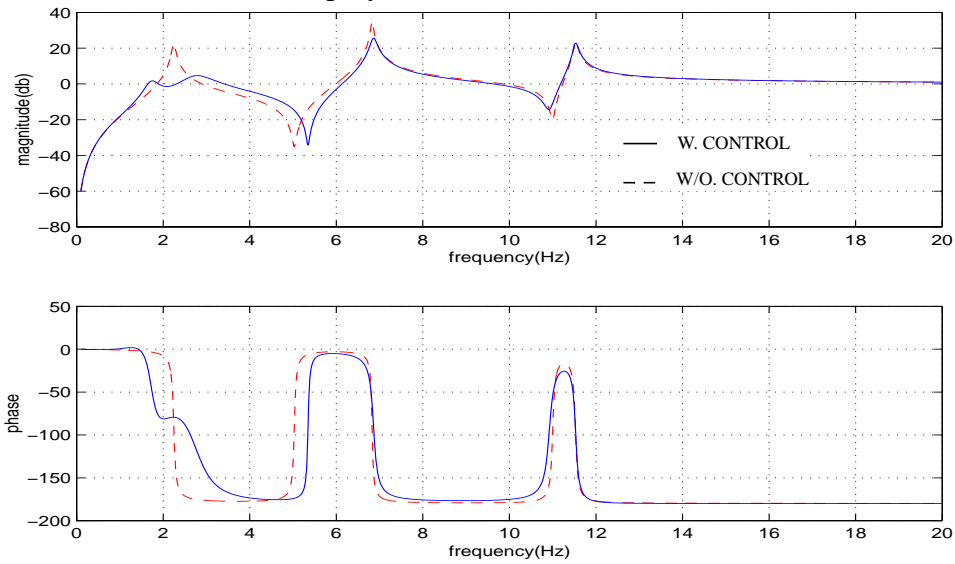


Figure 5.12 Bode plot of ground motion to the 1st floor acceleration (All floor feedback using AMD).

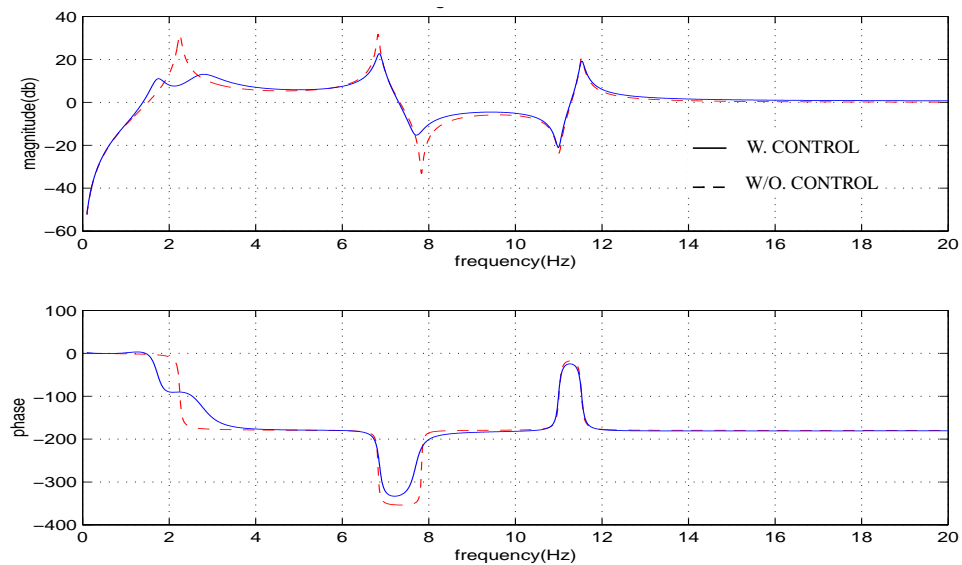


Figure 5.13 Bode plot of ground motion to the 3rd floor acceleration (All floor feedback using AMD).

Table 5.4 Comparison of Results Obtained Using Various Accelerometer Layouts

3rd floor response	uncontrolled	3-floor FB	1st floor FB	2nd floor FB	3rd floor FB
σ_x (cm)	0.162	0.049	0.050	0.050	0.051
$\sigma_{\ddot{x}}$ (cm/s ²)	46.5	24.2	24.5	24.4	25.8
σ_u (N)		32.6	21.2	28.7	42.5
x_{max} (cm)	0.38	0.29	0.26	0.27	0.28
\dot{x}_{max} (cm/s ²)	154.6	136.1	136.4	139.0	140.6
u_{max} (N)		180.2	116.1	159.7	171.8

Figures. 5.12 and 5.13 show that the overall building performance with an AMD is similar to those obtained using an active tendon. They also demonstrate that the second and third modes contribute more to the first floor acceleration than to the third floor acceleration. Therefore, the first floor acceleration feedback more effectively reduces the acceleration response using a smaller level of control force. However, the relative improvement of one over the other is small.

From above discussing, it is noted that the performance of the proposed MPC scheme using the acceleration feedback is shown to be equally effective as that of the MPC scheme using the state (displacement and velocity) feedback for the same objective function. Changing the location of the acceleration feedback has some subtle influence on the controlled response and the control force. Similar trends are noted for both the active tendon device and the active tuned mass damper.

5.5 Summary

In this chapter, an MPC based scheme using the acceleration response feedback was presented for controlling structural response to earthquake induced motions. An observer

employing the Kalman-Bucy filter was utilized to estimate the system states from the measured acceleration output. The performances of a single-story and a three-story building equipped with an active tendon and AMD systems were analyzed. In these examples, the MPC scheme that utilized the acceleration feedback was compared to the MPC scheme with the state feedback. The results suggested that the acceleration feedback scheme is comparable to the state feedback approach and at the same time offers convenience in measurements. Furthermore, the acceleration feedback from different floors resulted in a rather similar response reduction, but the feedback from the first floor required the least control force.

CHAPTER 6

REAL-TIME STRUCTURAL CONTROL

Most of the control strategies reported in the literature have been based only on the feedback (FB) control. However, some studies also utilized a feedforward (FF) compensator which works in conjunction with a FB loop (e.g., Suhardjo *et al.*, 1990 and 1992; Yamada and Kobori, 1996; Mei *et al.*, 1998; Wu, *et al.*, 1998, Yoshida *et al.*, 1998). In this FF-FB scheme, the equations of structural motion are augmented with an appropriate state-space excitation model that is based on a filtered Gaussian white noise process. The FF loops can be formulated with two types of inputs. First, the FF loops can be based on established spectral characteristics of the excitation (e.g., earthquakes, wind, and waves). Second, the FF loops can be based on actual measurements and on-line models fitted to the data (e.g., the auto-regressive (AR) model). These loops are then used in conjunction with the equations of motion to determine both FF and FB gains. Suhardjo *et al.* (1990,1992), and Suhardjo and Kareem (1997) presented the frequency domain optimal control of earthquake, wind, and wave excited structures using FF-FB control schemes. Yamada and Kobori (1996) used an AR model to fit on-line measurements of ground acceleration into a state-space excitation model and used the LQR control to obtain the FF-FB gains. Their results demonstrated that the FF-FB strategy enhanced the performance of the controller.

In this chapter, MPC is employed in conjunction with the FF-FB strategy to reduce structural response under earthquake excitation. First, the Kanai-Tajimi earthquake model is used for the FF component of the FF-FB control. Next, a formulation of MPC with an AR model embedded in the FF loop is presented. In this manner, a real-time FF link is included to introduce predictive and adaptive features to account for seismic events with unusual dynamic features. The AR model in the FF loop is based on initial observations of the ground motion. The model is constantly updated with new information. The time series based model is then used to represent the state equations of the excitation. Finally the structural system equations are augmented with the excitation model to include real-time earthquake input.

A single-story and a three-story building examples are used to demonstrate the methodology. The MPC-AR controller is shown to be effective in reducing structural response under a host of earthquakes that contain distinct spectral and transient features. The results of the MPC analysis are also compared with those of the LQG based control schemes.

6.1 Feedforward Model

6.1.1 Pre-Established Earthquake Model: Kanai-Tajimi

The earthquake signal can be modeled as filtered white noise process. The filter design is based on a prescribed spectrum of ground motion, e.g., the Kanai-Tajimi model (Clough and Penzien, 1993). In this discussion, the Kanai-Tajimi spectral description of the ground motion is used as:

$$S(\omega) = S_0 \left[\frac{\omega_g^4 + 4\omega_g^2 \zeta_g^2 \omega^2}{(\omega^2 - \omega_g^2)^2 + 4\omega_g^2 \zeta_g^2 \omega^2} \right] \quad (6-16)$$

where ζ_g , ω_g and S_0 are parameters which depend on the site soil characteristics and seismic intensity. The transient or non-stationary feature of the earthquake is introduced through an amplitude modulating function (Deodatis and Shinozuka, 1988).

The transfer function is then decomposed to get the state-space realization of the earthquake signal. The state-space representation can be expressed as:

$$\begin{aligned} r(k+1) &= A_r r(k) + B_r e_r(k) \\ d(k) &= C_r(k) r(k) \end{aligned} \quad (6-17)$$

where $r(k)$ is a two-dimensional vector containing the states of the seismic excitation model; $e_r(k)$ is a stationary Gaussian vector white noise process; and $C_r(k)$ is a time-varying vector that includes non-stationary excitation in this model. The matrices in the excitation model are given by:

$$A_r = \begin{bmatrix} 0 & 1 \\ -\omega_g^2 & -2\zeta_g \omega_g \end{bmatrix}, \quad B_r = \begin{bmatrix} 0 \\ 1 \end{bmatrix}, \quad C_r(k) = g(k) \begin{bmatrix} -\omega_g^2 & -2\zeta_g \omega_g \end{bmatrix}. \quad (6-18)$$

where $g(k)$ is a modulating function chosen to reflect the transient nature of the time-dependent ground acceleration. This dynamic earthquake model can then be combined with the state-space model of the structure to derive an augmented state-space equation, which is used to perform FF-FB control.

6.1.2 Real-time Model of Earthquake

The ground acceleration time history can be introduced through a time-varying autoregressive (AR) model to reflect the non-stationary features of ground motion. At each time instant $t_k = k\Delta t$, a q -dimensional AR model is formulated by the Yule-Walker equation. The simulated seismic excitation at time t_k is defined as $d(k)$. The error between the measured and the modeled excitation, $e_r(k)$, is then obtained at each step. The AR model is expressed in the state-space form and is subsequently embedded into the overall system state-space equations as follows:

$$\begin{aligned} r(k+1) &= A_r(k)r(k) + B_r(k)e_r(k) \\ d(k) &= C_r(k)r(k) + D_r(k)e_r(k) \end{aligned} \quad (6-19)$$

where

$$r(k) = \left[d^T(k-q) \ d^T(k-q+1) \ \dots \ d^T(k-2) \ d^T(k-1) \right]^T \quad (6-20)$$

$$A_r(k) = \begin{bmatrix} 0 & 1 & \dots & 0 \\ \dots & \dots & \dots & \dots \\ 0 & 0 & \dots & 1 \\ -a_q(k) & \dots & \dots & -a_1(k) \end{bmatrix}, \quad B_r(k) = \begin{bmatrix} 0 & \dots & 1 \end{bmatrix},$$

$$C_r(k) = -b_0(k) \begin{bmatrix} a_q(k) & \dots & a_1(k) \end{bmatrix}, \quad D_r(k) = b_0(k) \quad (6-21)$$

$a_q(k), a_{q-1}(k), \dots, a_1(k), b_0(k)$ are obtained from the AR model at time t_k .

6.2 Structure-Excitation Model

The building model described in Chapter 2 and the earthquake model given in the previous section are then combined to establish an augmented overall system model. From Eqs. (2-3) and (6-19), the following augmented state-space representation is obtained:

$$z(k+1) = \hat{\Phi}(k)z(k) + \hat{\Gamma}_u(k)u(k) + \hat{\Gamma}_d(k)e_r(k) \quad (6-22)$$

in which

$$z(k+1) = \begin{bmatrix} x(k+1) \\ r(k+1) \end{bmatrix}, \hat{\Phi}(k) = \begin{bmatrix} \Phi & \Gamma_d C_r(k) \\ 0 & A_r(k) \end{bmatrix}, \hat{\Gamma}_u(k) = \begin{bmatrix} \Gamma_u \\ 0 \end{bmatrix}, \hat{\Gamma}_d(k) = \begin{bmatrix} \Gamma_d D_r(k) \\ B_r(k) \end{bmatrix} \quad (6-23)$$

For the Kanai-Tajimi model $D_r(k) = 0$.

6.3 Model Predictive Control Scheme with Feedforward-Feedback Link

As illustrated in Chapter 2, the MPC scheme is based on an explicit use of a prediction model of the system response to obtain the control action by minimizing an objective function. For the FF-FB control, an earthquake model is formulated. The information obtained from this model is forwarded to the controller and the measured outputs are fed back to the controller as shown in Fig. 6.1. Both of them are included in the prediction model for the MPC based control design.

As described in Chapter 2, the state-space equations of the system are expressed as:

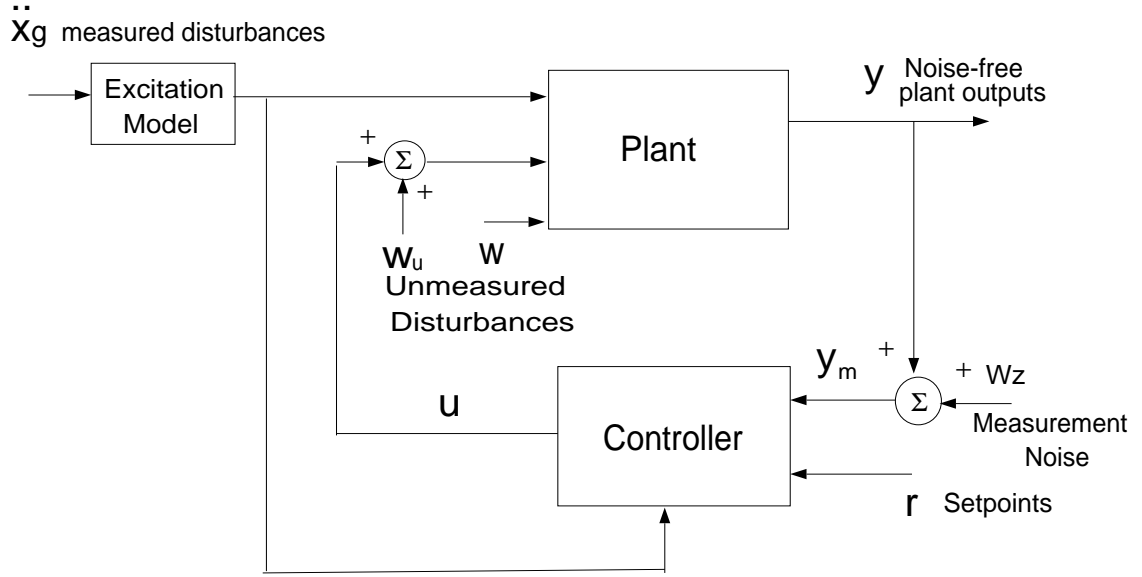


Figure 6.1 FF-FB control system

$$\mathbf{x}(k+1) = \Phi \mathbf{x}(k) + \Gamma U(k)$$

$$\mathbf{y}(k) = C \mathbf{x}(k) + D U(k) \quad (6-24)$$

where $U(k) = \begin{bmatrix} u^T(k) & \ddot{x}_g^T(k) & w_u^T(k) & w^T(k) & w_z^T(k) \end{bmatrix}^T$; $w_u(k)$, $w(k)$, and $w_z(k)$ could be combined into a single unmeasured disturbance variable entering at the plant output. The unmeasured disturbance terms, $w_u(k)$, $w(k)$, and $w_z(k)$ are set equal to zero.

When a structure-excitation model with an embedded AR model is used, the overall system states are increased. The prediction model is then expressed as:

$$\hat{\mathbf{z}}(k+1|k) = \hat{\Phi} \hat{\mathbf{z}}(k|k-1) + \hat{\Gamma}_u \hat{u}(k|k-1) + \hat{\Gamma}_d e_r(k|k) + \hat{\Gamma}_e \hat{\boldsymbol{\epsilon}}(k|k) \quad (6-25)$$

$$\hat{\mathbf{y}}(k|k-1) = C \hat{\mathbf{z}}(k|k-1) \quad (6-26)$$

where $\hat{\mathbf{z}}(k+1|k)$ estimates the state at a future sampling period, $k+1$, by using the information available at time step k ; $\hat{\mathbf{y}}(k|k-1)$ estimates the structural output at time k based

on the information at $k-1$; $C = [I \ 0]$; $\hat{\Gamma}_e$ is a constant estimator gain matrix; and $\hat{e}(k|k)$ is the estimated error defined as $\hat{e}(k|k) = y(k) - \hat{y}(k|k-1)$.

Using Eq. (6-22), the process output predicted at the k -th and the subsequent time steps $k+j$, $j = 1, \dots, p$ can be expressed as a function of the current state vector $z(k)$ and the control vector $u(k)$ as follows:

$$\Psi(k) = H\mathbf{u}(k) + Y_z \hat{z}(k|k-1) + Y_d e_r(k) + Y_e \hat{e}(k|k) \quad (6-27)$$

$$\Psi(k) = [\hat{y}^T(k+1|k) \dots \hat{y}^T(k+p|k)]^T, \quad \mathbf{u}(k) = [\hat{u}(k|k) \dots \hat{u}(k+\lambda-1|k)]^T \quad (6-28)$$

The reference output can be written as $\Psi_r(k) = [y_r^T(k+1|k) \dots y_r^T(k+p|k)]^T$, where p is the prediction horizon and λ is the control horizon.

The control objective function is given by:

$$J = \frac{1}{2} [\Psi(k) - \Psi_r(k)]^T \bar{Q} [\Psi(k) - \Psi_r(k)] + \frac{1}{2} \mathbf{u}^T(k) \bar{R} \mathbf{u}(k) \quad (6-29)$$

By minimizing J , the optimal predictive control force is given by

$$\mathbf{u} = [H^T \bar{Q} H + \bar{R}]^{-1} H^T \bar{Q} [Y_z \hat{z}(k|k-1) + Y_d e_r(k) + Y_e \hat{e}(k|k)] \quad (6-30)$$

in which H , \bar{Q} , \bar{R} , Y_z , Y_d and Y_e are given as follows:

$$H = \begin{bmatrix} H_1 & 0 & \dots & 0 \\ \dots & \dots & \dots & \dots \\ H_\lambda & H_{\lambda-1} & \dots & H_1 \\ H_{\lambda+1} & H_\lambda & \dots & H_1 + H_2 \\ \dots & \dots & \dots & \dots \\ H_p & H_{p-1} & \dots & H_1 + \dots + H_{p-\lambda} \end{bmatrix}, \quad H_k = C \hat{\Phi}^{k-1} \hat{\Gamma}_u, \quad (6-31)$$

$$Y_z = \left[(C\hat{\Phi})^T (C\hat{\Phi}^2)^T \dots (C\hat{\Phi}^p)^T \right]^T \quad (6-32)$$

$$Y_e = \left[(C\hat{\Gamma}_e)^T (C(I + \hat{\Phi})\hat{\Gamma}_e)^T \dots \left(C \sum_{k=1}^p (\hat{\Phi}^{k-1})\hat{\Gamma}_e \right)^T \right]^T, \quad (6-33)$$

$$Y_d = \left[H_{v1}^T \ H_{v1}^T + H_{v2}^T \ \dots \ \sum_{k=1}^p H_{vk}^T \right]^T, \ H_{vk} = C\hat{\Phi}^{k-1}\hat{\Gamma}_d, \text{ and} \quad (6-34)$$

$$\bar{Q} = \begin{bmatrix} Q & \dots & 0 \\ \dots & \dots & \dots \\ 0 & \dots & Q \end{bmatrix}, \bar{R} = \begin{bmatrix} R & \dots & 0 \\ \dots & \dots & \dots \\ 0 & \dots & R \end{bmatrix}, \quad Q = \begin{bmatrix} I & 0 \\ 0 & 0 \end{bmatrix}, \quad R = I. \quad (6-35)$$

The MPC formulation presented above is then utilized in the following examples to demonstrate its application to building structures.

6.4 Numerical Examples and Analysis

The SDOF building with the active tendon used in Chapter 2 shown in Fig. 2.2 is used here. An actuator can be used to introduce tension in cables to obtain the desired control force. The earthquake input to the building can be formulated in two ways. One approach involves modeling earthquake using the Kanai-Tajimi spectral model. The other utilizes the actual measurements to model the real-time excitation through an AR model. Details of both are discussed in the following sections.

6.4.1 MPC/Kanai-Tajimi Control Scheme

In this section, the kanai-Tajimi spectral model is applied to generate the earthquake excitation and used in the MPC scheme to reduce structural response. Details are given in

previous sections. The prediction and control horizons are chosen to be 5 and 2, respectively. The weighting matrices are $Q = I_{(2 \times 2)}$ and $R = 100$.

Figure 6.2 compares the displacement responses without control (dashed line) and with MPC control using the Kanai-Tajimi model (solid line). Figures 6.3, 6.4 and 6.5 compare the displacement, acceleration, and control force using MPC control alone (dashed line) and MPC control using the Kanai-Tajimi model (solid line). It is noted that the FF-FB case (MPC plus Kanai-Tajimi) performs better than the FB case (MPC alone). Table 6.1 lists numerical values obtained by the MPC FB and MPC FF-FB schemes. Apparently the FF-FB control of MPC is better than the FB control alone. Using almost the same control force, the MPC FF-FB control produces a higher response reduction than the MPC FB control.

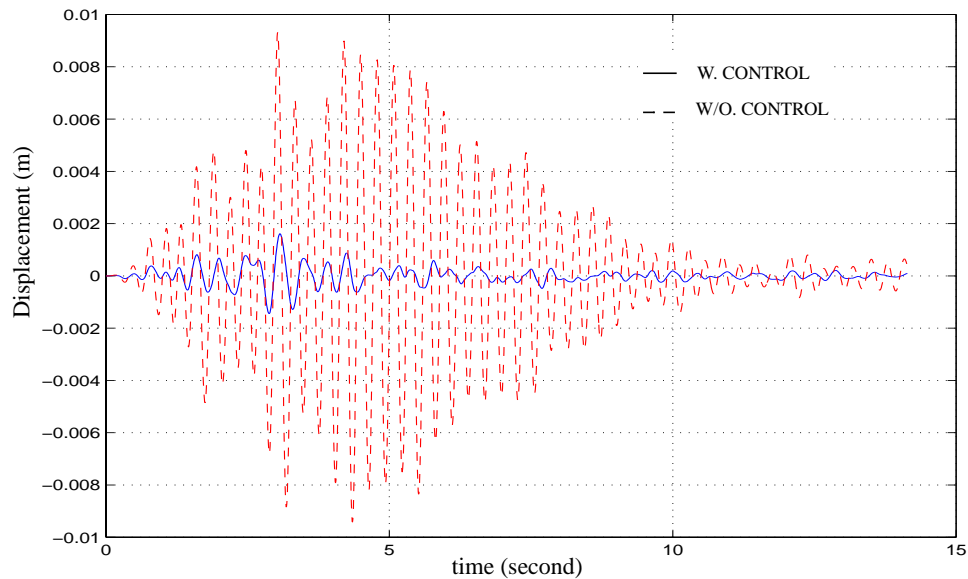


Figure 6.2 Displacement response without control and with MPC/Kanai-Tajimi scheme.

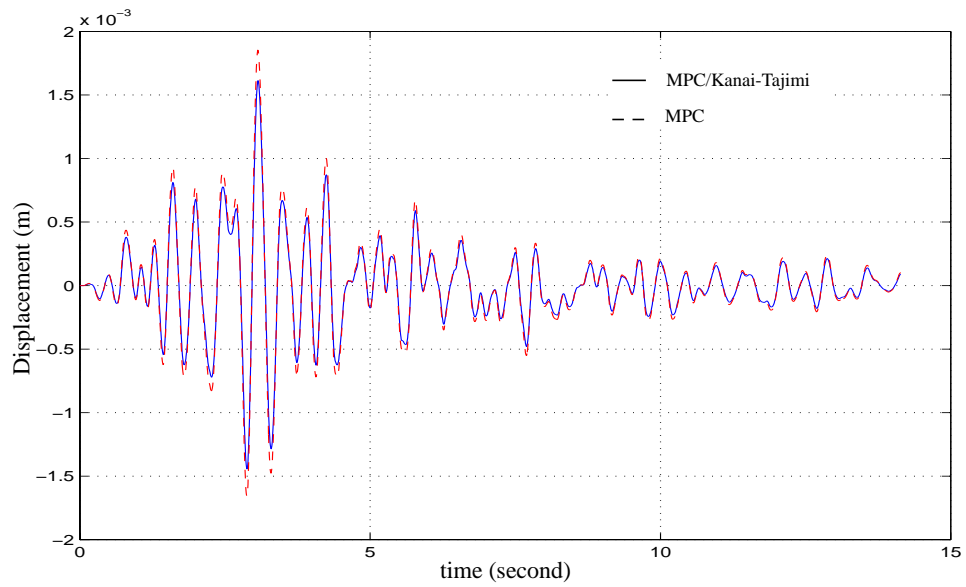


Figure 6.3 Displacement response using MPC/Kanai-Tajimi and MPC schemes.

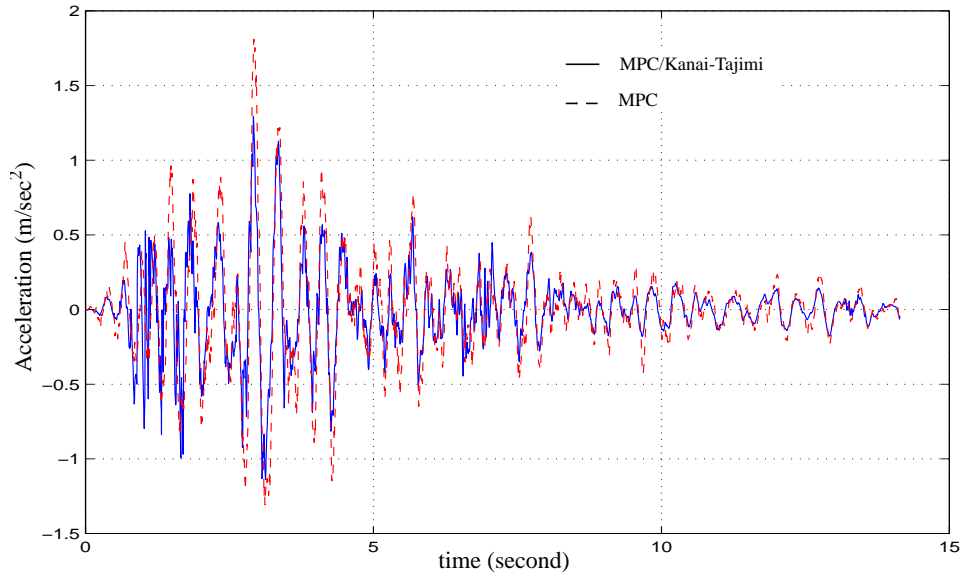


Figure 6.4 Acceleration using MPC/Kanai-Tajimi model and MPC schemes.

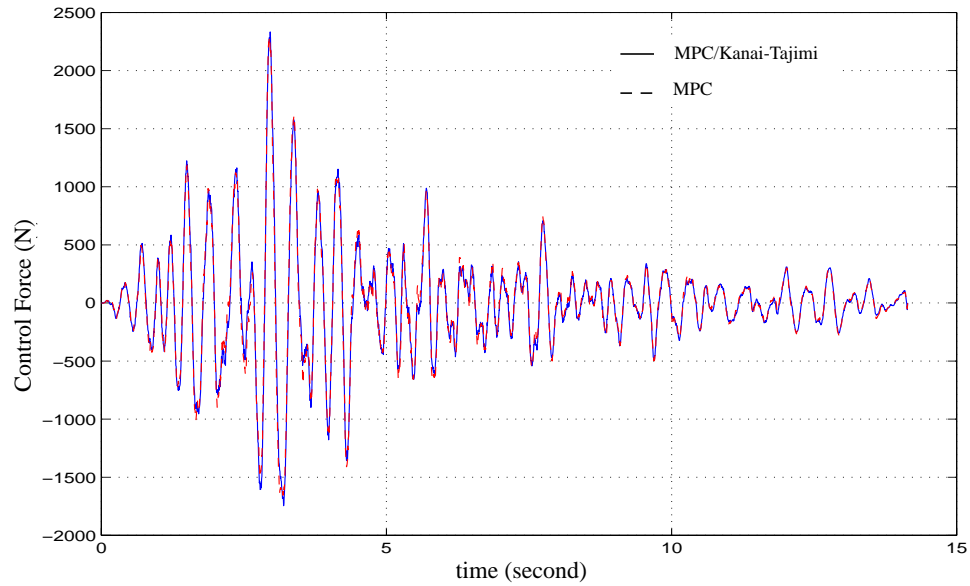


Figure 6.5 Control forces using MPC/Kanai-Tajimi model and MPC schemes.

Table 6.1 Comparison between the MPC/Kanai-Tajimi model and MPC

	σ_x (cm)	$\sigma_{\ddot{x}}$ (cm/s ²)	σ_u (kN)	x_{max} (cm)	\dot{x}_{max} (cm/s ²)	u_{max} (kN)
Without control	0.31	141.5	---	0.94	447.7	---
MPC	3.77×10^{-2}	35.4	0.453	0.19	181.1	2.297
Percentage change	88%	75%	—	80%	60%	—
MPC/ Kanai-Tajimi	3.28×10^{-2}	25.8	0.455	0.16	129.3	2.334
Percentage change	90%	82%	0.38%	93%	71%	1.6%

The prescribed spectral model can be implemented either off-line or on-line, which requires that the spectral density of the earthquake excitation be known a priori. This is not practical, and may only be effective in cases where the earthquake characteristics match the prescribed spectral model, e.g., the Kanai-Tajimi model. The effectiveness of the con-

trol action could be reduced if the earthquake characteristics either differ from the Kanai-Tajimi model or change rapidly. In order to overcome this shortcoming, a real-time model based on actual measurements is utilized in the following case.

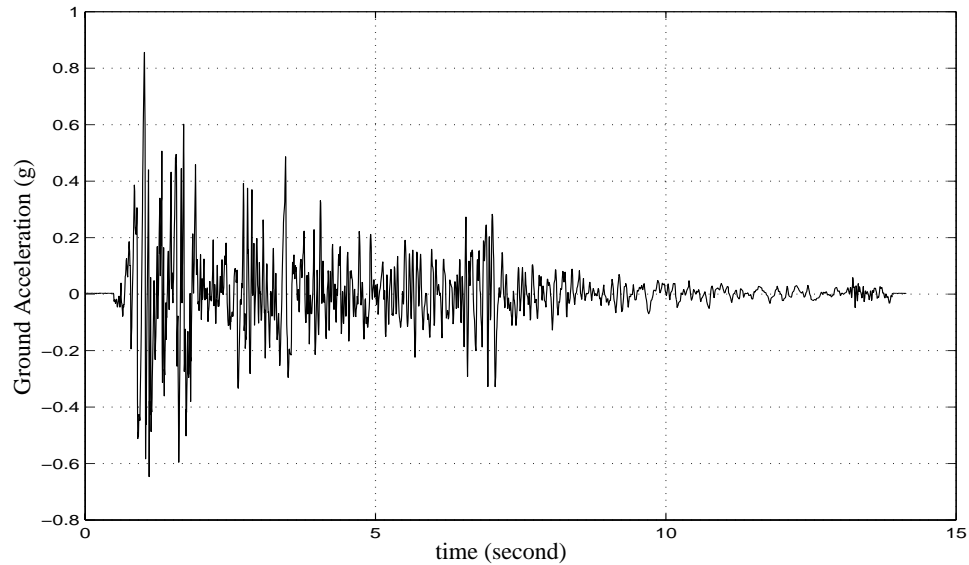


Figure 6.6 1940 El Centro earthquake

6.4.2 MPC-AR Control Scheme

The FF based on AR modeling provides a practical way to apply the FF-FB control scheme more effectively. The 1940 El Centro earthquake record (Fig. 6.6) is scaled to 0.25 of its maximum intensity and used in this analysis to excite the example building. Figures 6.7 and 6.8 show the displacement and acceleration without control (dashed line) and those using the MPC-AR model (solid line). Both the displacement and acceleration responses are significantly reduced in the presence of the controller.

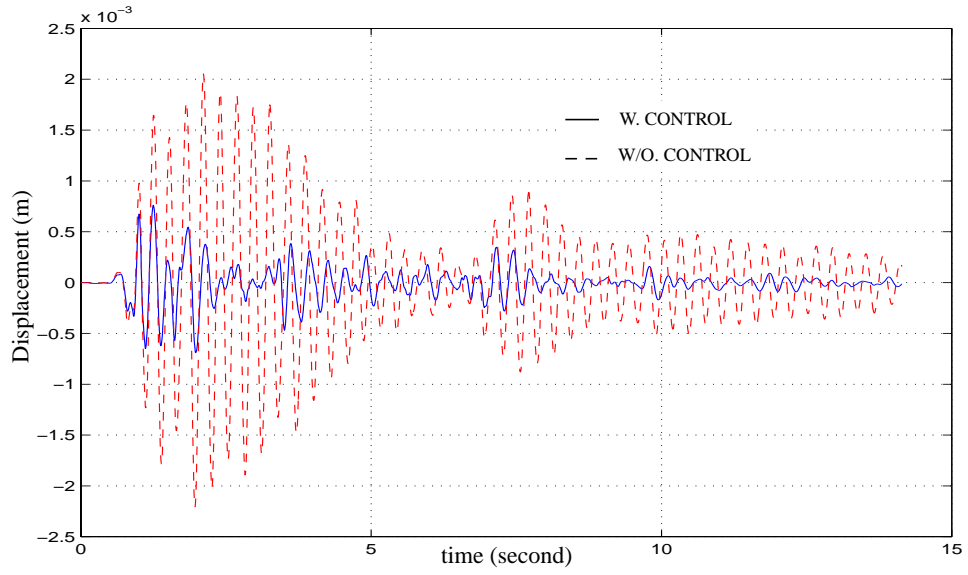


Figure 6.7 Comparison of displacement response without control and with MPC-AR scheme.

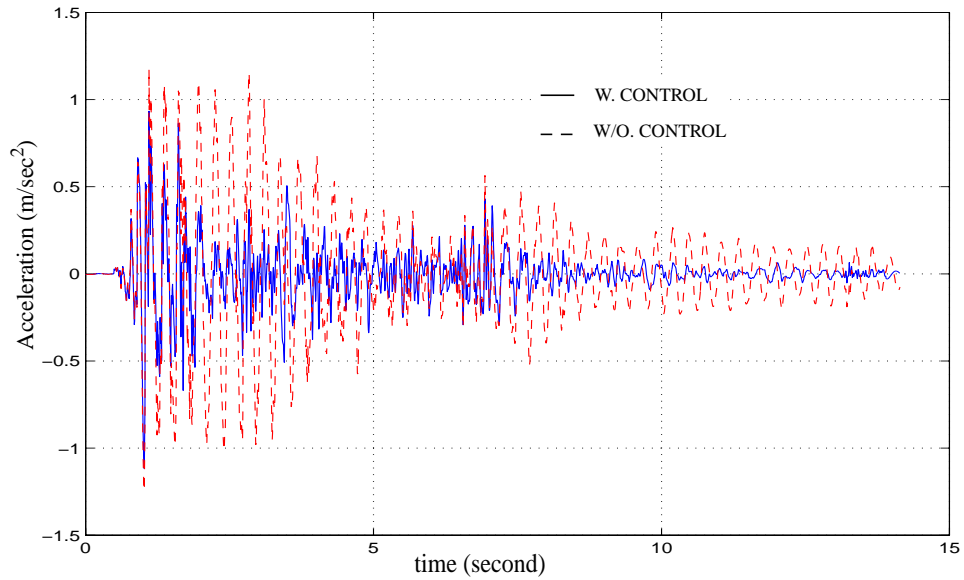


Figure 6.8 Comparison of acceleration response without control and with MPC-AR scheme.

Figures 6.9 and 6.10 compare the displacement and acceleration response obtained using MPC alone (dashed line) with those obtained using MPC-AR (solid line). The corre-

sponding control forces are given in Fig. 6.11. Table 6.2 lists comparisons of the responses under no control, MPC alone, and MPC-AR schemes. The results show that when the MPC-AR model is used, the control performance is better than that using MPC alone and furthermore, the control force is smaller. Clearly, the FF-FB control is more effective than the FB control scheme

Table 6.2 Comparison between the MPC-AR model and MPC

	σ_x (cm)	$\sigma_{\ddot{x}}$ (cm/s ²)	σ_u (kN)	x_{max} (cm)	\ddot{x}_{max} (cm/s ²)	u_{max} (kN)
without control	7.53×10^{-2}	37.8	—	0.25	135.4	—
MPC	2.01×10^{-2}	14.6	0.099	0.10	101.5	0.672
Percentage change	73.3%	61.3%	—	60.0%	25.0%	—
MPC-AR	1.60×10^{-2}	13.4	0.083	7.80×10^{-2}	95.1	0.622
Percentage change	78.3%	64.4%	-15.6%	68.8%	29.7%	-7.37%

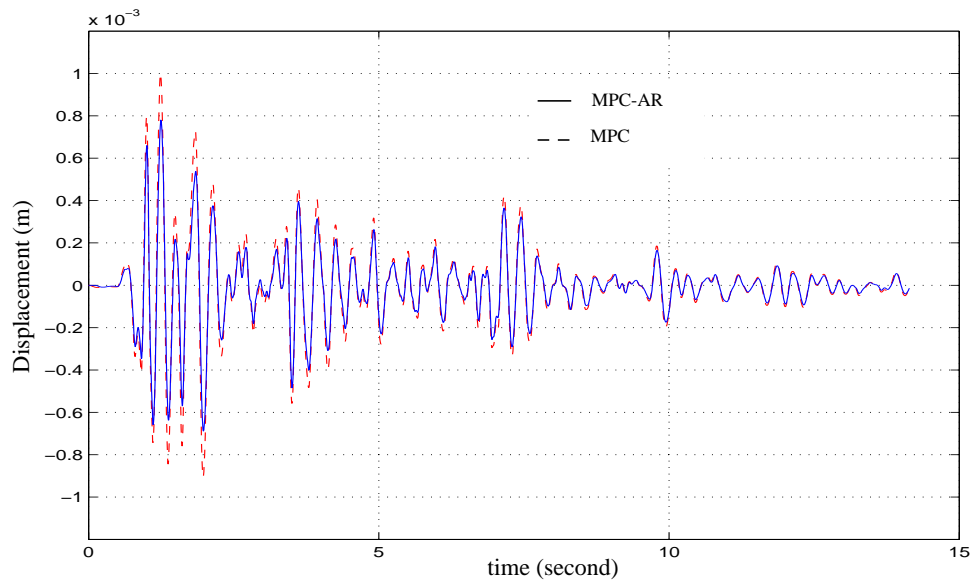


Figure 6.9 Comparison of displacement response between MPC-AR and MPC schemes.

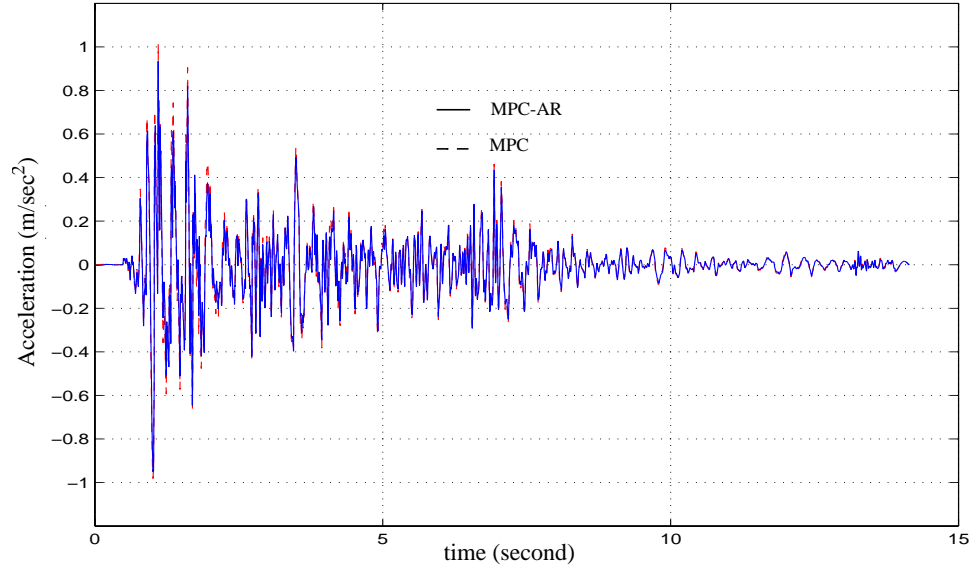


Figure 6.10 Comparison of acceleration response between MPC-AR and MPC schemes.

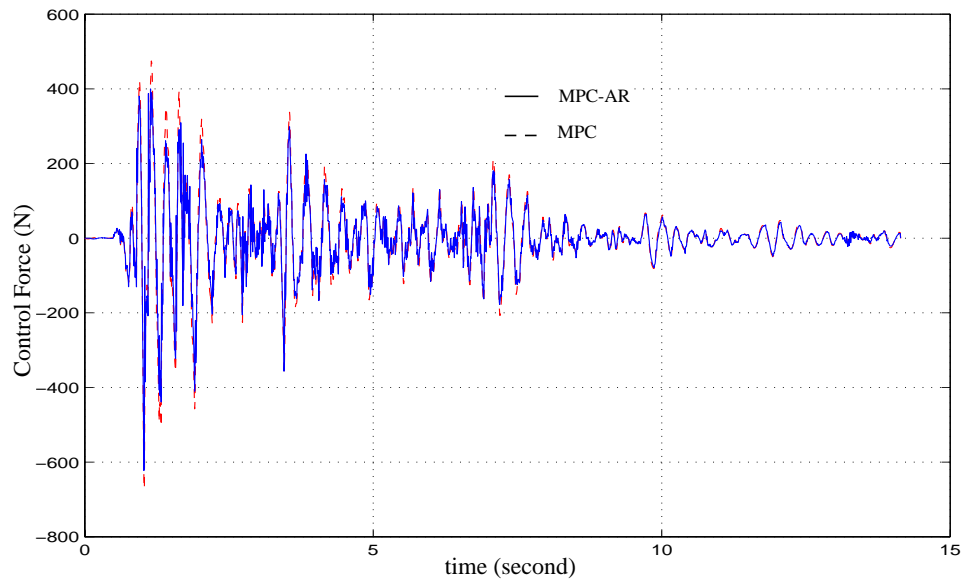


Figure 6.11 Comparison of control forces between MPC-AR and MPC schemes.

In addition, the performance of MPC-AR scheme is compared to that of the LQG-AR control strategies. As shown in Fig. 6.12, the MPC-AR scheme shows a slightly better performance than LQG-AR. On a Sun UltraSparc-30 workstation, the computational time for the MPC-AR scheme is 0.015 seconds per time step and for the LQG-AR scheme it is 0.060 seconds per time step. For the AR model system identification, 0.011 seconds per time step are needed. For the MPC-AR scheme, most of the time is consumed in identifying AR model from the ground motion. However, for the LQG-AR model, most time is used in solving the Riccati equation.

Finally, the Kobe and Hachinohe earthquake acceleration time histories are used as inputs to assess the effectiveness and robustness of the MPC-AR control scheme. As shown in Table 6.3, Figs. 6.13 and 6.14, the structural responses are significantly reduced when the MPC-AR scheme is employed. These results suggest that the MPC-AR model is effective in controlling a wide range of ground accelerations with their own distinct features.

Table 6.3 Performance of MPC-AR scheme under Kobe and Hachinohe earthquakes

		σ_x (cm)	$\sigma_{\dot{x}}$ (cm/s ²)	σ_u (kN)	x_{max} (cm)	\ddot{x}_{max} (cm/s ²)	u_{max} (kN)
Kobe earthquake	without control	0.13	68.8		0.67	466.9	
	MPC-AR	0.054	40.4	0.28	0.35	307.5	2.3
	Percentage change	56.9%	41.3%		47.8%	34.1%	
Hachinohe earthquake	without control	0.09	45.8		0.21	106.3	
	MPC-AR	0.03	16.7	0.07	0.10	71.2	0.28
	Percentage change	69.6%	63.6%		52.4%	33.0%	

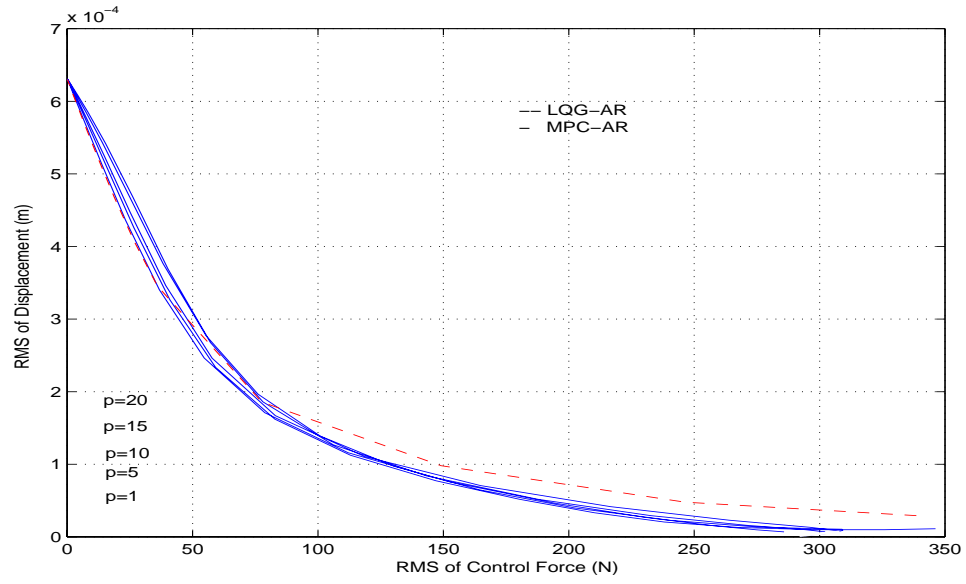


Figure 6.12 Control performance of LQG-AR and MPC-AR with different prediction and control horizons.

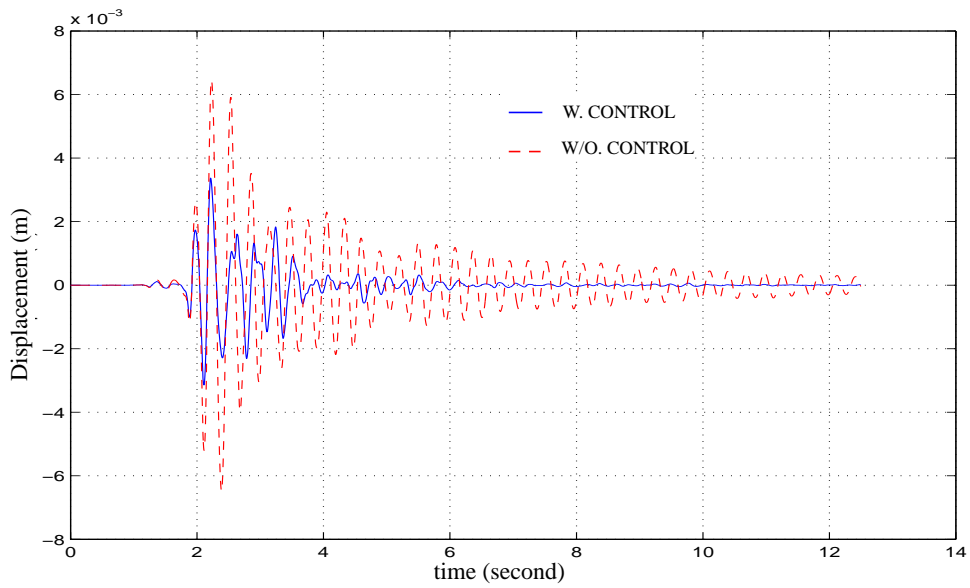


Figure 6.13 Displacement under Kobe earthquake without control and with MPC-AR scheme.

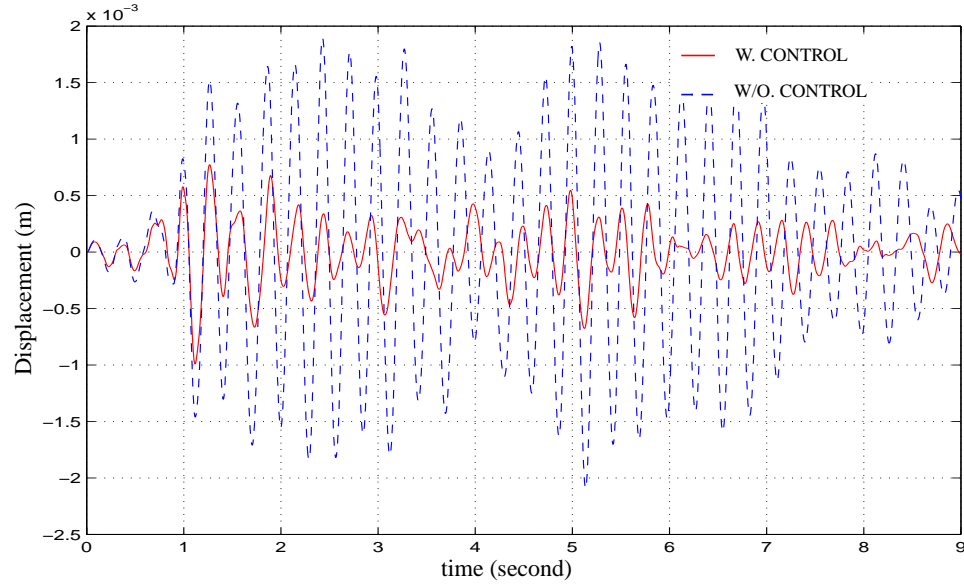


Figure 6.14 Displacement under Hachinohe earthquake without control and with MPC-AR scheme.

6.4.3 Analysis of A Three-Story Building Using the MPC-AR Model

In this example, the three-story building in Chapter 2 (Fig. 2.8) is used to demonstrate the MPC-AR scheme using the state feedback obtained from each floor of the building. The mass, stiffness and damping matrices of the building are given in Chapter 2. In this example, the stiffness of the active tendon is $k_c = 3.7197 \times 10^5 (N/m)$ and $\alpha = 36^\circ$. The active tendon is installed at the first floor. In this example, $Q = I_{(3 \times 3)}$, $p = 5$ and $\lambda = 2$.

The comparison between the MPC and MPC-AR schemes is listed in Table 6.4 which shows both the RMS and maximum values of the displacement and acceleration of the top floor, and the control force. The weighting matrix is chosen as $R = 5$ for the MPC and $R = 800$ for the MPC-AR model. Different values of R are used to ensure that a comparable control force is generated in both cases. Table 6.4 shows that with a smaller control force, the MPC-AR scheme offers a better control action than MPC alone. Both the RMS and maximum response values obtained using MPC-AR are lower than those obtained

using MPC alone. This further points to the superiority of the FF-FB control using MPC-AR over MPC with FB only.

Table 6.4 Comparison of MPC-AR and MPC Schemes Using a Three-Story Building

Third floor Response	σ_x (cm)	$\sigma_{\ddot{x}}$ (cm/s ²)	σ_f (kN)	x_{max} (cm)	\ddot{x}_{max} (cm/s ²)	f_{max} (kN)
Uncontrolled	0.16	46.5	—	0.38	154.6	—
MPC	0.060 (62.4%)	22.1 (52.4%)	0.106	0.26 (32.4%)	143.2 (7.4%)	0.52
MPC-AR	0.052 (67.6%)	17.7 (61.9%)	0.092 (-14.3%)	0.22 (43.0%)	138.4 (10.5%)	0.44 (-14.7%)

The controlled responses of the structure are shown in Figs. 6.15-6.18. Figures 6.15 and 6.16 show the displacement of the first and top floors of the building, respectively, whereas, Figs. 6.17 and 6.18 show the acceleration of the first and top floors of the building, respectively. The dashed lines represent the uncontrolled case, and the solid lines represent the controlled response using the MPC-AR scheme. Figure 6.19 shows the control force needed in this example.

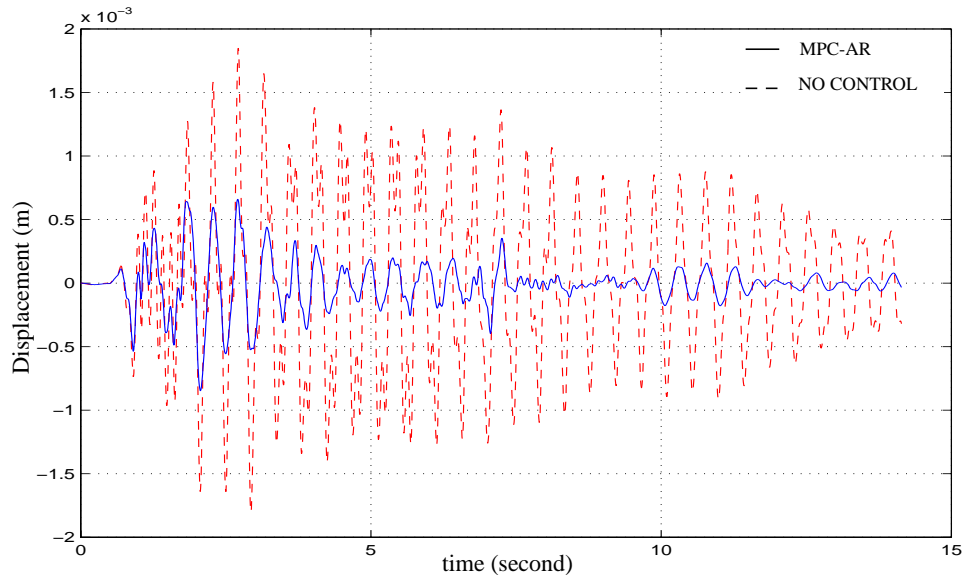


Figure 6.15 Comparison of first floor displacement between no control and MPC-AR scheme.

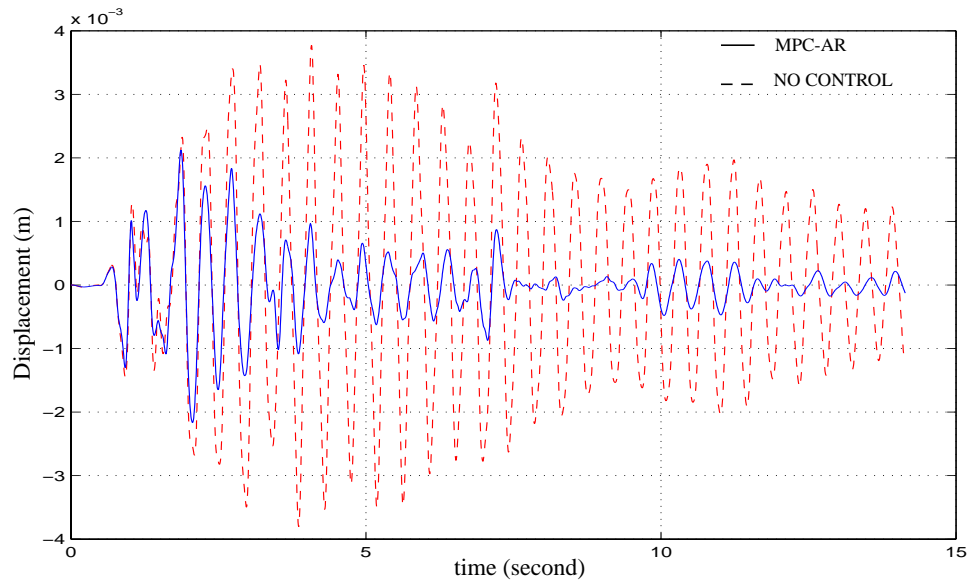


Figure 6.16 Comparison of top floor displacement between no control and MPC-AR scheme.

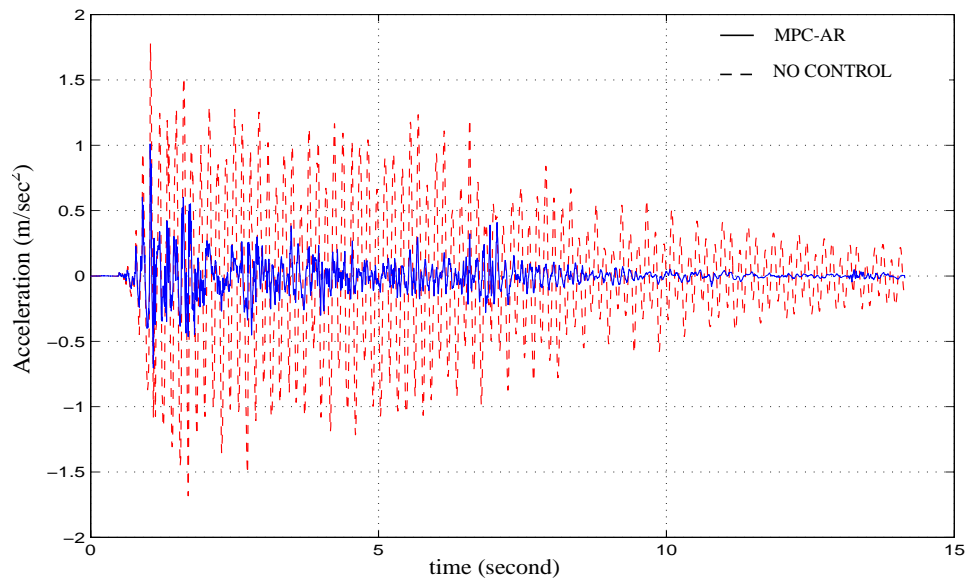


Figure 6.17 Comparison of first floor acceleration between no control and MPC-AR scheme.

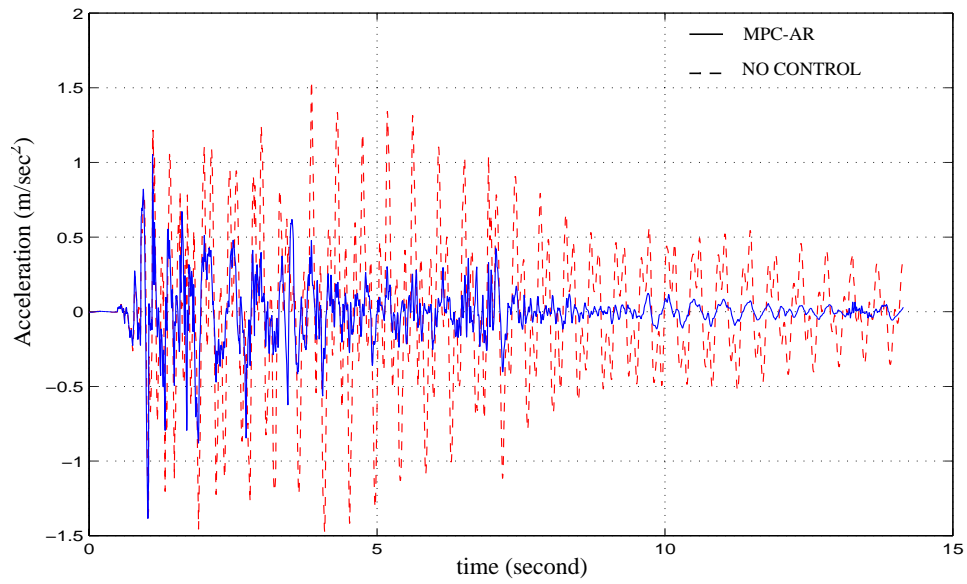


Figure 6.18 Comparison of top floor acceleration between no control and MPC-AR scheme.

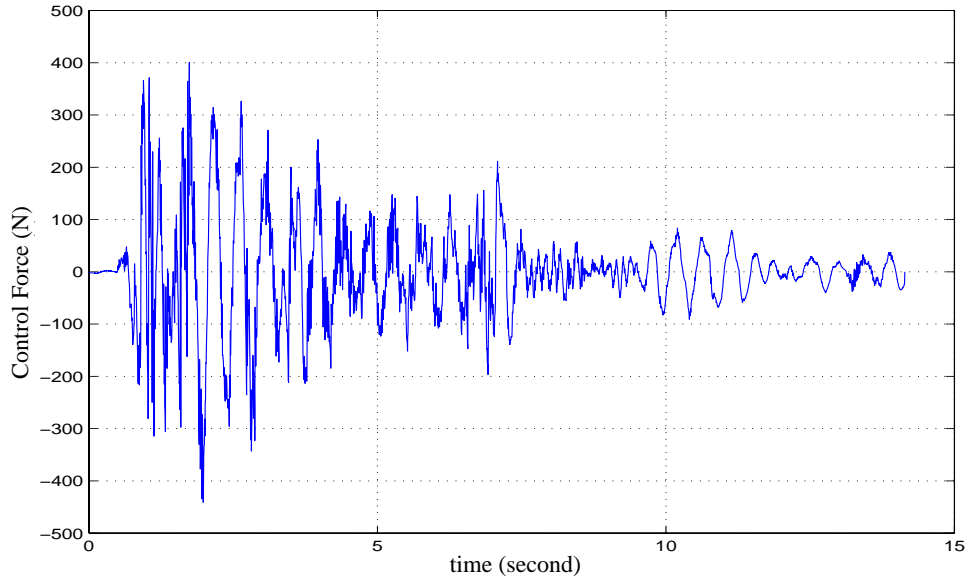


Figure 6.19 Control force using MPC-AR scheme.

This example has demonstrated how the MPC-AR model can effectively control multi-degree-of-freedom systems. On a Sun UltraSparc-30 workstation, the three-story building

took 0.002 seconds for each time step if MPC was used alone and 0.019 seconds for each time step for MPC-AR model. Because the AR model is estimated at each time step, most of the time is taken up by the identification of the ground motion model. More efficient AR identification schemes need to be considered to further reduce the computational efforts for the digital experimental implementation. The availability of high speed actuators and computers has made it possible to explore the potentials of MPC scheme which promises to enhance our ability in improving the performance of structure under extreme loads.

6.5 Summary

In this chapter, a real-time Model Predictive Control with feedforward linkage was applied to reduce structural response under earthquake induced loads. The MPC scheme including both the FB and FF was formulated. Two types of inputs were used to represent the FF loop in this study. First, the Kanai-Tajimi model was used, which represented the FF loop based on the established earthquake spectral characteristics. Second, the MPC-AR scheme was introduced in which actual real-time measurements obtained on-line were utilized to model the FF component. The FF model using these two methodologies was then augmented with the equations of motion of the structure to determine the FF-FB gains.

This study clearly demonstrated the effectiveness of the MPC-AR strategy for reducing structural response and associated load effects under earthquake loads. MPC with the FF-FB components clearly enhanced the performance of the controller, e. g., the Kanai-Tajimi model provided an improved reduction in the response when compared to MPC with FB

only. However, since this method depends on a prescribed spectral model of earthquake, it may not always yield satisfactory performance results for earthquakes with features that differ from those captured in this model. This shortcoming can be alleviated by an MPC-AR based FF-FB scheme, which can be employed in real-time for any earthquake inputs. The results obtained using the MPC-AR scheme showed further improvement over MPC with only FB.

CHAPTER 7

FEEDFORWARD-FEEDBACK CONTROL OF WIND-EXCITED STRUCTURES

Wind loads play an important role in the design of tall buildings and other flexible structures. Strong winds can result in occupant discomfort and even may cause local or overall failure of structures. Therefore, reduction of structural response under wind loads is a major structural design issue.

This chapter presents the development and application of the stochastic decomposition approach to the simulation of random processes and modal space reduction of wind loading. The concept of stochastic decomposition as applied to probabilistic dynamics and digital simulation of multivariate random processes was advanced in Kareem and Li (1988), and Li and Kareem (1993 and 1995). This approach is theoretically based on the Karhunen-Loeve expansion which is also known as proper orthogonal decomposition (POD), or principal component analysis (PCA). Central to this technique is the decomposition of a set of correlated random processes into a number of component random sub-processes. Statistically, any two decomposed processes are either fully coherent or non-coherent. Hence, each process is viewed as a summation of mutually non-coherent component sub-processes. Each random sub-process is characterized by a decomposed spectrum that is related to conventional spectral description, e.g., the power spectral density function (PSD), or cross-power spectral density function (XPSD). Any linear transformation

that relates a set of random processes also describes the corresponding decomposed spectral descriptions of these processes. In this study, this concept has been extended to a state-space realization of excitation which can be used for direct simulation of wind-related processes or to model wind excitation in a state-space format needed for structural control problems involving a feedforward link. The decomposed spectral matrix is used to model component processes as auto-regressive (AR) models, which are then expressed in a state space format (Kareem and Mei, 1999).

This wind velocity description is then employed in structure control design to add a feedforward link to the MPC approach discussed in Chapter 2 for earthquake response control. A model reduction technique is employed for the wind state-space model for computational efficiency. In this chapter, the wind description is combined with MPC to reduce the response of a TV tower under wind excitation. The MPC based feedforward-feedback (MPC/FF-FB) control scheme is then compared with passive control and MPC without the feedforward link.

7.1 Proper Orthogonal Decomposition of Wind Loading

Fluctuating wind velocity is generally modeled as a stationary Gaussian process. A cross spectral density function related to the fluctuating wind velocity at different heights is defined as $S(f)$. The (i, j) th element of $S(f)$ can be expressed as:

$$S_{ij} = 4K_0V_r^2 \frac{\chi}{nf(1+\chi^2)^{5/6}} \exp\left(-\frac{2c_1|f||h_i-h_j|}{V_i+V_j}\right) \quad , \quad \chi = \frac{1700f}{V_r} \quad (7-1)$$

where K_0 is a constant that depends on the surface roughness of the ground; V_r is the reference mean wind velocity at 10 m above the ground; c_1 is an experimental constant coefficient; n is a nominal constant; f is the frequency in Hz; h_i and h_j are the heights of floors i and j , respectively; V_i and V_j are mean wind velocities at the corresponding floors which can be obtained by:

$$V_i = V_r \left(\frac{h_i}{h_r} \right)^\alpha \quad (7-2)$$

where α is a constant value; and h_r is the reference height.

The PSD matrix $S(f)$ can be decomposed utilizing a modal or Schur type decomposition at each frequency f .

$$S(f) = \Psi^T(f) \Lambda(f) \Psi(f) \quad (7-3)$$

where $\Psi(f)$ is a matrix whose i -th column is the i -th eigenvector of $S(f)$ and $\Lambda(f)$ is a diagonal matrix whose elements are the eigenvalues of $S(f)$.

For this study, a correlated wind field for a four story building is employed as an example. The parameters in Eq. (7-1) are characterized as $V_r = 30\text{m/s}$, $K_0 = 0.04$, $c_1 = 8$, $\alpha = 0.3$, $n = 2.065$, and $h = [0 \ 5 \ 10 \ 15]$. The dependence of eigenvectors and eigenvalues on frequency is shown in Figs. 7.1 and 7.2. Figure 7.1 details the elements of the first eigenvectors of the power spectral density at different frequencies. It indicates that the eigenvectors of the PSD of the wind velocity change slowly with respect to the frequency. Figure 7.2 describes the eigenvalues of the wind velocity power spectral density at different frequencies. It also reveals that the first eigenvalue is the dominant one, especially at lower frequencies. Similar observation have been made by Paola (1998). From these

results, a method for simplifying the simulation of the wind load using state-space representation can be derived.

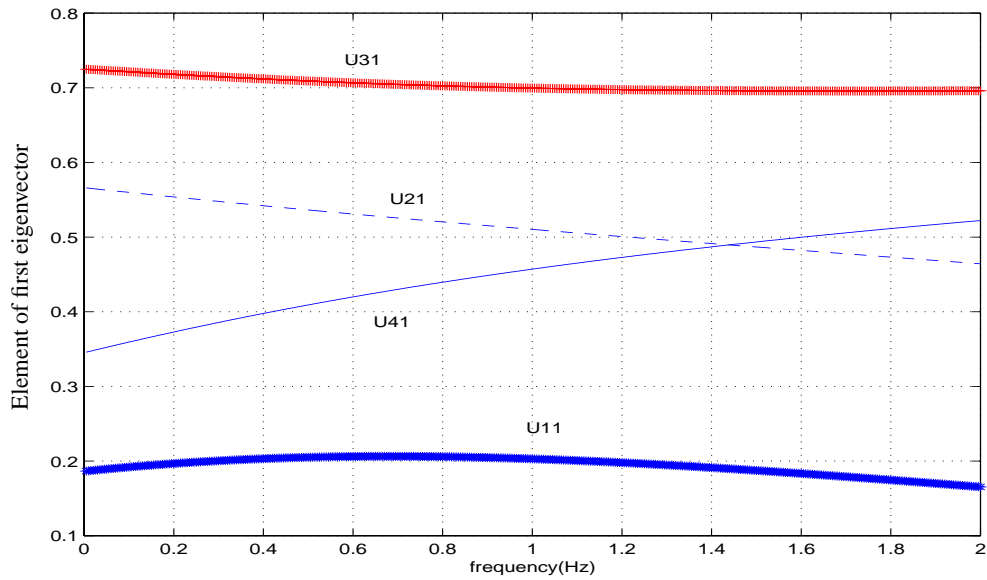


Figure 7.1 Elements of first eigenvector at different frequencies

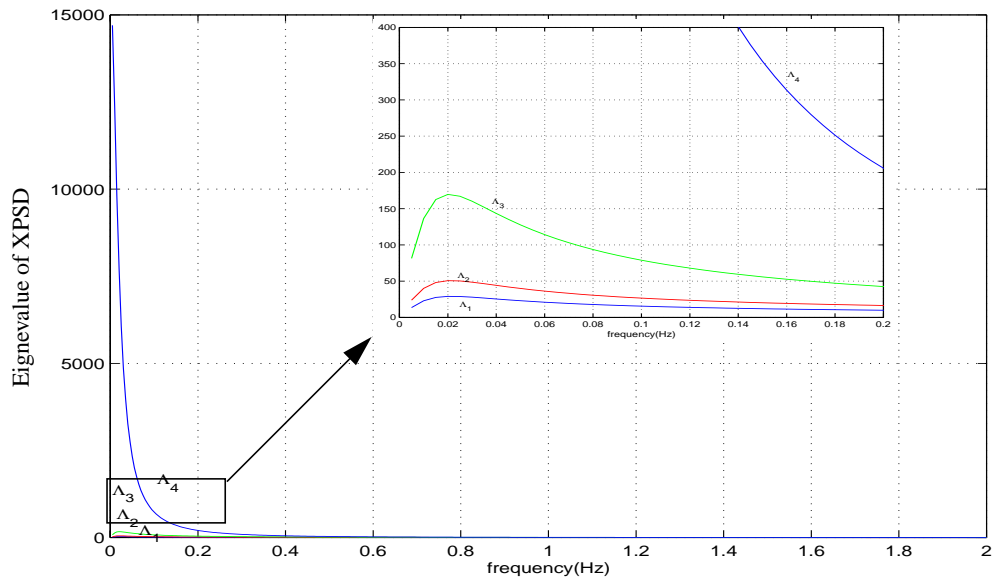


Figure 7.2 Eigenvalues of XPSD at different frequencies

7.2 Autoregressive (AR) Model

An autoregressive (AR) model of order q can generate a random process $y(k\Delta t)$ at time $k\Delta t$ from its previous time history and corresponding excitation as follows:

$$y(k) = - \sum_{i=1}^q a_i y(k-i) + b_0 w(k) \quad (7-4)$$

where a_1, a_2, \dots, a_q and b_0 are the coefficients of the AR process, and $w(k)$ is a white noise process.

If the power spectral density (PSD) of the stochastic process $y(t)$ is known, the auto-correlation function can be derived from:

$$R(\tau) = \int_{-f_c}^{f_c} S(f) \exp(2\pi f\tau) df \quad (7-5)$$

where f_c is the cut off frequency and τ is the time difference. For one-side PSD, Eq. (7-5) can be recast as:

$$R(\tau) = \int_0^{f_c} S(f) \cos(2\pi f\tau) df \quad (7-6)$$

Using the Yule-walker equation, the coefficients of the AR model can be obtained from the following

$$\begin{bmatrix} R(0) & R(1) & \dots & R(q-1) \\ R(1) & R(0) & \dots & R(q-2) \\ \dots & \dots & \dots & \dots \\ R(q-1) & R(q-2) & \dots & R(0) \end{bmatrix} \begin{bmatrix} a_1 \\ a_2 \\ \dots \\ a_q \end{bmatrix} = \begin{bmatrix} R(1) \\ R(2) \\ \dots \\ R(q) \end{bmatrix} \quad (7-7)$$

where $R(i)$ is the auto-correlation function at time instant $i\Delta t$, and

$$b_0 = R(0) + \sum_{i=1}^q a_i R(i) \quad (7-8)$$

For the single-input-single-output (SISO) process, the AR model can be expressed in the state-space form as follows (Kay, 1993)

$$\begin{aligned} r(k+1) &= A_r r(k) + B_r w(k) \\ y(k) &= C_r r(k) + D_r w(k) \end{aligned} \quad (7-9)$$

where

$$r(k) = \left[y^T(k-q) \ y^T(k-q+1) \ \dots \ y^T(k-2) \ y^T(k-1) \right]^T \quad (7-10)$$

$$A_r = \begin{bmatrix} 0 & 1 & 0 & \dots & 0 \\ \dots & \dots & \dots & \dots & \dots \\ 0 & 0 & \dots & 0 & 1 \\ -a_q & \dots & \dots & -a_2 & -a_1 \end{bmatrix}, \quad B_r = \begin{bmatrix} 0 & \dots & 0 & 1 \end{bmatrix},$$

$$C_r = -b_0 \begin{bmatrix} a_q & \dots & a_1 \end{bmatrix}, \quad D_r = b_0 \quad (7-11)$$

7.3 State-Space Model of the Wind Field

In Eq. (7-3), the eigenvalue matrix, $\Lambda(f)$, is a diagonal matrix which can be expressed as:

$$\Lambda(f) = \begin{bmatrix} \Lambda_1(f) & 0 & \dots & 0 \\ 0 & \Lambda_2(f) & \dots & 0 \\ \dots & \dots & \dots & \dots \\ 0 & 0 & \dots & \Lambda_n(f) \end{bmatrix} \quad (7-12)$$

Each diagonal element of the matrix is a function of frequency and can be treated as a PSD of a stationary autoregressive process. Therefore, by using the method described in Section 7.2, a state-space model for $\Lambda_i(f)$, $i = 1, 2, \dots, n$ can be obtained. These state-space models are defined by A_i, B_i, C_i, D_i , $i = 1, 2, \dots, n$. By replacing these matrices as the i -th diagonal sub-matrix of matrices A_v, B_v, C_v, D_v , respectively, the state-space model of the eigenvalue matrix $\Lambda(f)$ can be obtained:

$$\begin{aligned} x(k+1) &= A_v x(k) + B_v V(k), \\ v(k) &= C_v x(k) + D_v V(k) \end{aligned} \quad (7-13)$$

in which

$$V(k) = \begin{bmatrix} w_1^T(k) & w_2^T(k) & \dots & w_n^T(k) \end{bmatrix}^T \quad (7-14)$$

$$A_v = \text{diag}(A_1, A_2, \dots, A_n), \quad B_v = \text{diag}(B_1, B_2, \dots, B_n) \quad (7-15)$$

$$C_v = \text{diag}(C_1, C_2, \dots, C_n), \quad D_v = \text{diag}(D_1, D_2, \dots, D_n) \quad (7-16)$$

w_i , $i = 1, \dots, n$ are independent Gaussian white noise generated by *Matlab 5.2* (1998).

The eigenvalue matrix $\Lambda(f)$ can also be expressed as a product of the transfer function of the modeled system

$$\Lambda(f) = HH^T \quad (7-17)$$

in which $H = C_v(sI - A_v)^{-1}B_v + D_v$ is the transfer function of the wind model and $s = j\omega$.

Generally the eigenvectors of the XPSD change very slowly with respect to the frequency. Therefore, an eigenvector matrix $\Psi_0(f_0)$ at a certain frequency f_0 is chosen for

further consideration. By multiplying this eigenvector matrix at the left side of the C_v and D_v matrices, the new matrices for the wind velocity can be obtained.

$$C_{new} = \Psi_0^T(f_0)C_v, \quad D_{new} = \Psi_0^T(f_0)D_v \quad (7-18)$$

The XPSD of the wind velocity field $S(f)$ can then be approximated as:

$$S(f) = \Psi_0^T(f_0)\Lambda(f)\Psi(f_0) \quad (7-19)$$

7.4 Wind Field For a Four-Story Building

The four-story building example used in Section 7.1 is employed here using the preceding method. The A_v , B_v , C_{new} and D_{new} matrices of the state-space representation are obtained as below:

$$A_v = \begin{bmatrix} 0.5800 & 0.0606 & 0 & 0 & 0 & 0 & 0 & 0 \\ -0.0606 & -0.0882 & 0 & 0 & 0 & 0 & 0 & 0 \\ 0 & 0 & 0.6126 & -0.0156 & 0 & 0 & 0 & 0 \\ 0 & 0 & 0.0156 & -0.0248 & 0 & 0 & 0 & 0 \\ 0 & 0 & 0 & 0 & 0.7242 & -0.0310 & 0 & 0 \\ 0 & 0 & 0 & 0 & 0.0310 & 0.0667 & 0 & 0 \\ 0 & 0 & 0 & 0 & 0 & 0 & 0.9545 & -0.0193 \\ 0 & 0 & 0 & 0 & 0 & 0 & 0.0193 & 0.2204 \end{bmatrix}, \quad (7-20)$$

$$B_v = \begin{bmatrix} 0.9518 & 0 & 0 & 0 \\ 0.0505 & 0 & 0 & 0 \\ 0 & 1.1178 & 0 & 0 \\ 0 & -0.0171 & 0 & 0 \\ 0 & 0 & 1.4446 & 0 \\ 0 & 0 & -0.0683 & 0 \\ 0 & 0 & 0 & 2.1122 \\ 0 & 0 & 0 & -0.4363 \end{bmatrix}, \quad (7-21)$$

$$C_{new} = \begin{bmatrix} 0.1908 & -0.0101 & -0.5983 & -0.0092 & -1.0003 & -0.0473 & 0.9300 & 0.19921 \\ -0.5214 & 0.0277 & 0.6522 & 0.0100 & -0.3885 & -0.0184 & 1.1318 & 0.2338 \\ 0.6804 & -0.0361 & 0.3520 & 0.0054 & 0.4459 & 0.0211 & 1.1464 & 0.2368 \\ -0.3671 & 0.0195 & -0.5850 & -0.0090 & 0.8583 & 0.0406 & 1.0006 & 0.2067 \end{bmatrix}, \quad (7-22)$$

$$D_{new} = \begin{bmatrix} 0.3682 & -1.1375 & -1.8230 & 1.6006 \\ -1.0062 & 1.2400 & -0.7080 & 1.9478 \\ 1.3129 & 0.6693 & 0.8126 & 1.9731 \\ -0.7084 & -1.1121 & 1.5642 & 1.7220 \end{bmatrix}. \quad (7-23)$$

Figure 7.3 gives the time history of the processes whose spectral matrix $\Lambda(f)$ is the eigenvalue matrix of the XPSD $S(f)$. The magnitude of the time history associated with the fourth eigenvalue is much larger than the others. After the eigenvectors at frequency f_0 is multiplied to generate C_{new} and D_{new} , the time histories of the wind velocity are shown in Fig. 7.4, whose XPSD is described by $S(f)$. The simulated XPSD $S_{ww}(f)$ can be obtained from the time history using *Matlab (1998)*. In Fig. 7.5 (a), (b), (c) and (d), the XPSD of the first row of the matrices $S(f)$ and $S_{ww}(f)$ are compared. The dashed line is for the target XPSD, $S(f)$ and the solid line represents the simulated XPSD, $S_{ww}(f)$. It is apparent that the simulated XPSD matches the target XPSD.

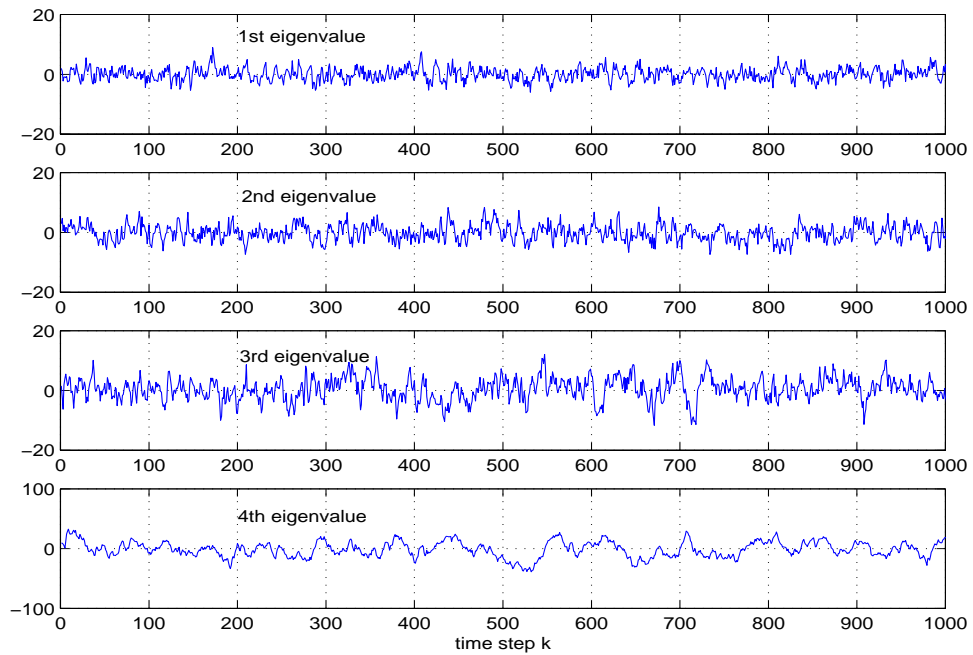


Figure 7.3 Time histories of the processes whose PSDs are the eigenvalues of the wind velocity XPSD, $S(f)$

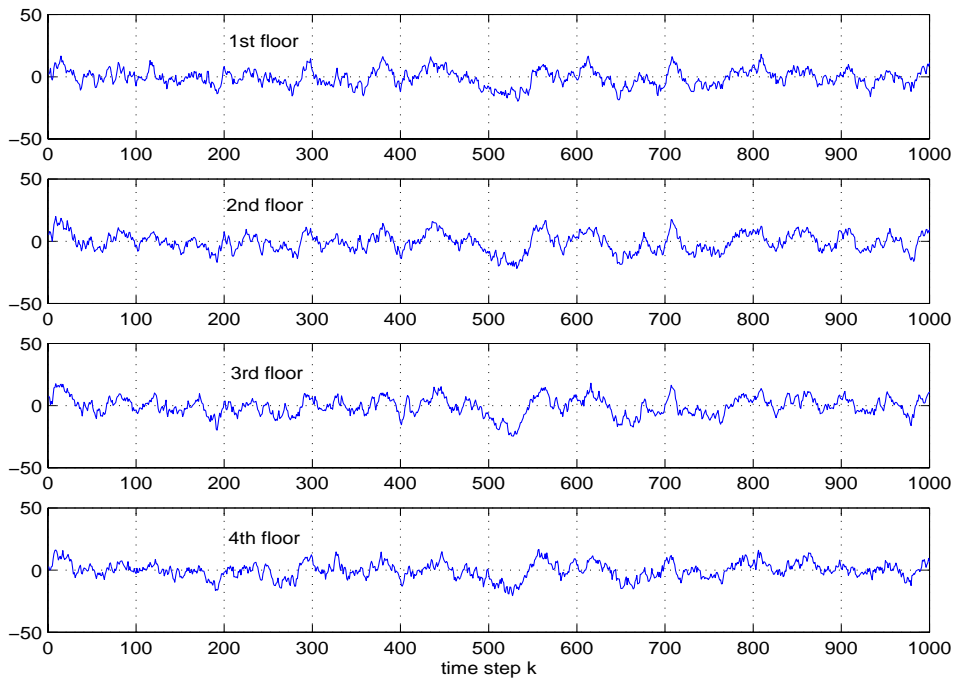


Figure 7.4 Time histories of wind velocity at 1st, 2nd, 3rd and 4th floors generated by the state-space approach.

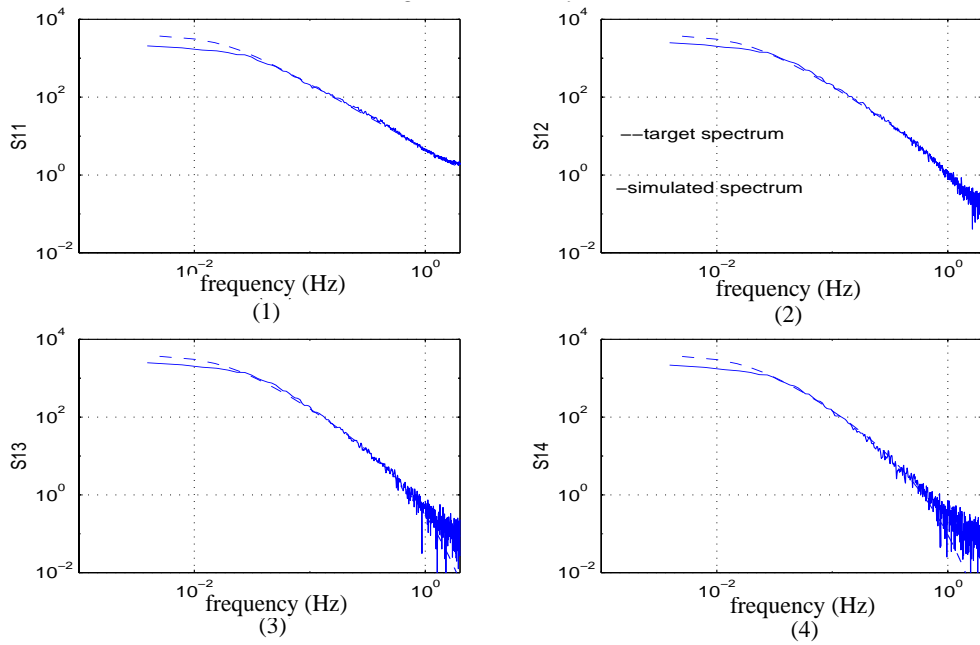


Figure 7.5 XPSDs of the target and the simulated velocities. (1) 1-1 floor XPSD. (2) 1-2 floor XPSD. (3) 1-3 floor XPSD. (4) 1-4 floor XPSD.

To measure the accuracy of the approach, the variance of the wind velocity at each floor is obtained using three approaches. The first approach comes from the the integration of the wind spectral density function:

$$\sigma^2 = R(0) = \int_0^{\infty} S(f)df \quad (7-24)$$

The second method employs the simulated power spectral density as follows

$$\sigma_w^2 = R_{ww}(0) = \int_0^{f_c} S_{ww}(f)df \quad (7-25)$$

The third method is to obtain the covariance using the time history of wind velocity as follows

$$\sigma_{xy} = \frac{1}{N-1} \sum_1^N (x_i - \bar{x})(y_i - \bar{y}) \quad (7-26)$$

The σ values generated by these three methods are listed in Table 7.1.

Table 7.1 Comparison of σ values Using Different Estimation Methods

Methods	σ_1	σ_2	σ_3	σ_4	$\sqrt{\sigma_{12}}$	$\sqrt{\sigma_{14}}$
1st	12.00	12.00	12.00	12.00	11.08	10.41
2nd	10.72 (10.66%)	12.27 (2.25%)	12.38 (3.15%)	11.22 (6.5%)	10.78 (2.7%)	9.59 (7.9%)
3rd	10.69 (10.94%)	11.98 (0.17%)	12.03 (0.28%)	10.86 (9.5%)	10.66 (3.8%)	9.41 (9.6%)

The results show good comparison between the simulated signals obtained from state-space representation and those from the target spectral density.

7.5 Wind Load Model For Nanjing Tower

This example analyzes the wind field around the Nanjing Tower. It is a 310-meter high TV tower built in 1993 in Nanjing, China. The tower is described in Fig. 7.6. The wind model described earlier is also used here. A simplified model of the tower consisting of sixteen lumped masses at different levels is used. The height of each level is at 10.1, 32.2, 58.6, 80.2, 101.8, 119.8, 137.8, 158.6, 171.8, 185.8, 199.2, 240.4, 270.1, 286.1, 299.1 and 310.1 meters, respectively. The following parameters for the wind field in Eq. (7-1) are used: $K_0 = 0.008$, $V_r = 20.7m/s$, $\alpha = 0.16$, $n = 1.976$, and $c_1 = 7.7$.

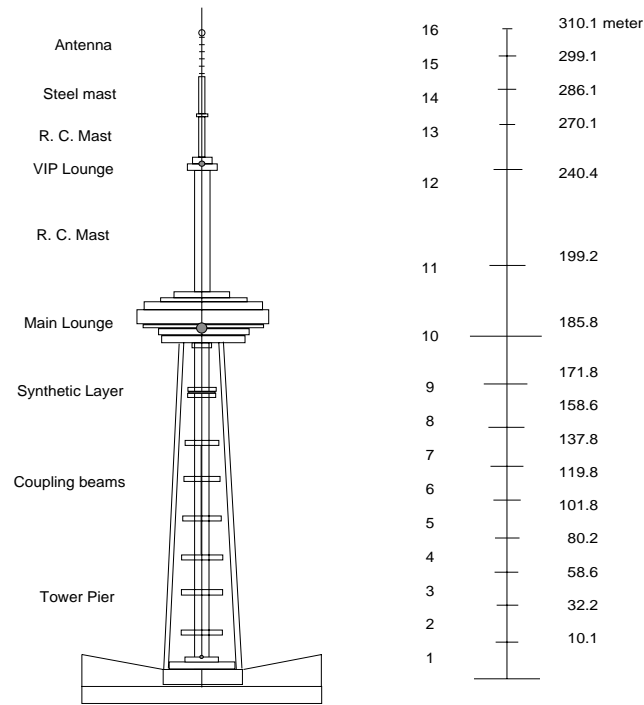


Figure 7.6 Nanjing Tower --- lumped 16 degree of freedom representation.

The elements in the first row of the cross-power spectral density matrix of the wind velocity are plotted in Fig. 7.7. This figure shows that the diagonal elements of the XPSD are much larger than the off-diagonal elements, especially at higher frequencies. The farther the elements are from the diagonal, the smaller is the magnitude of the cross-power spectrum. Element S_{1-16} , which is the XPSD of wind velocity at the first and the sixteenth level, is much smaller than S_{1-1} , the PSD of wind velocity at the first level only. This difference occurs because the first and sixteenth levels are so far apart that the wind at the first level is much less correlated with the wind at the sixteenth level than with the wind at the lower levels, especially at higher frequencies. Therefore, the higher the structure is, the less is the correlation of the wind at the first and top levels. As shown in the Fig

7.7, the XPSD approaches zero above 0.1 Hz for s_{1-16} and above 0.5 Hz for s_{1-2} . At lower frequencies, the magnitude of the XPSDs is in the order of 10^3 . This means that most of the wind loading energy lies in the lower frequencies. Furthermore, the dominant frequency of the tall, flexible structures is in the low frequency range, therefore, matching of the model in the lower frequency range is the primary focus of this exercise.

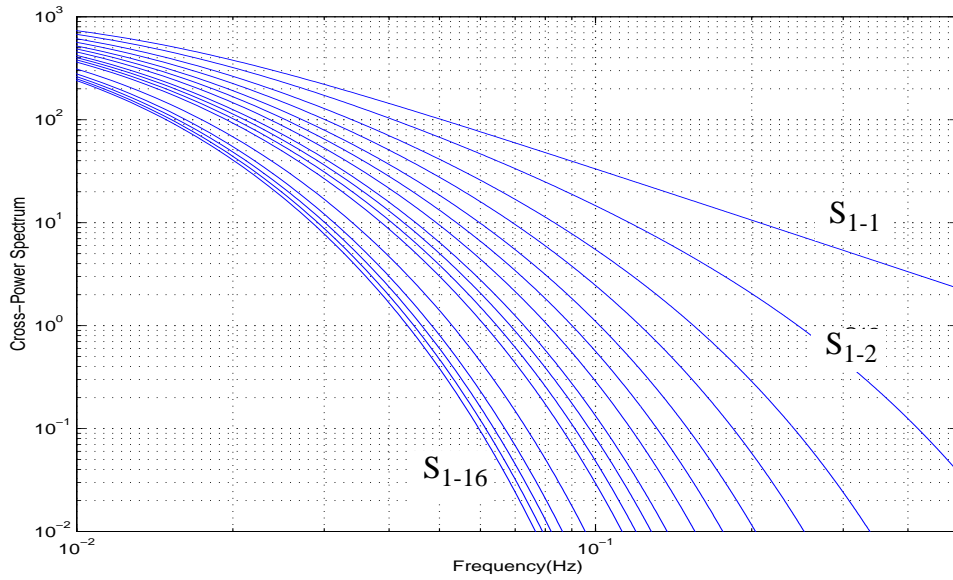


Figure 7.7 First row of XPSD, $S(f)$.

7.5.1 State-Space Realization of Wind Velocity

The POD and state-space methods discussed in Section 7.2 and 7.3 are used here to model wind fluctuations. A state-space realization with 32 states is obtained for the along-wind velocity. Sixteen independent white noise processes are generated as the inputs to the state-space equation. The XPSDs of the system outputs under these white noise inputs are then obtained. The simulated XPSDs of the wind velocity for the Nanjing Tower are shown in Figs. 7.8-7.11, which are the (i, i) -th ($i= 3, 6, 14, 16$) element of the cross power

spectral density matrix, respectively. The dashed lines represent the target spectra calculated from Eq. (7-1) and are the diagonal elements of the matrix $S(f)$. The solid lines represent the simulated spectra which match the target XPSD quite well.

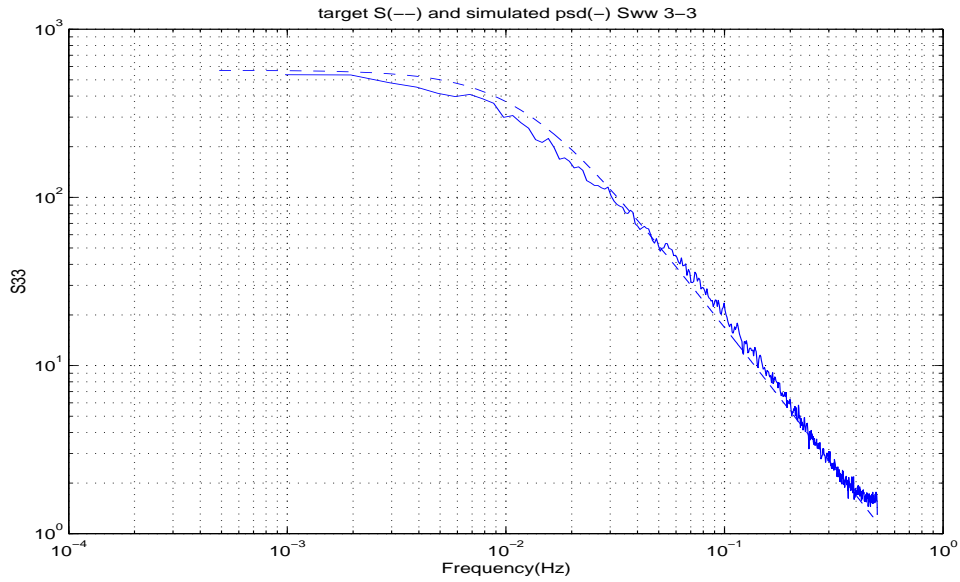


Figure 7.8 Comparison between the target XPSD $S_{3-3}(f)$ (dashed line) and the simulated XPSD $S_{ww3-3}(f)$ (solid line).

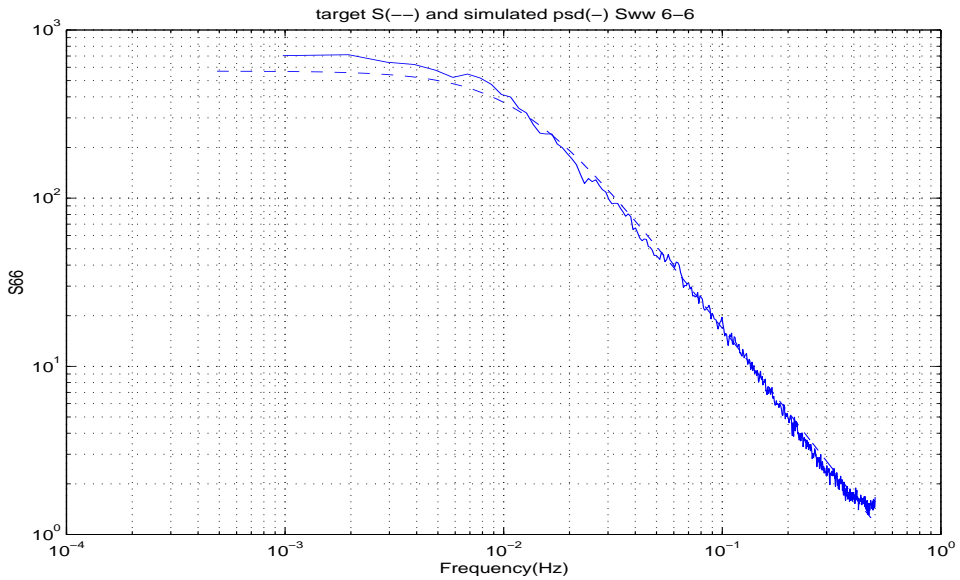


Figure 7.9 Comparison between the target XPSD $S_{6-6}(f)$ (dashed line) and the simulated XPSD $S_{ww6-6}(f)$ (solid line).

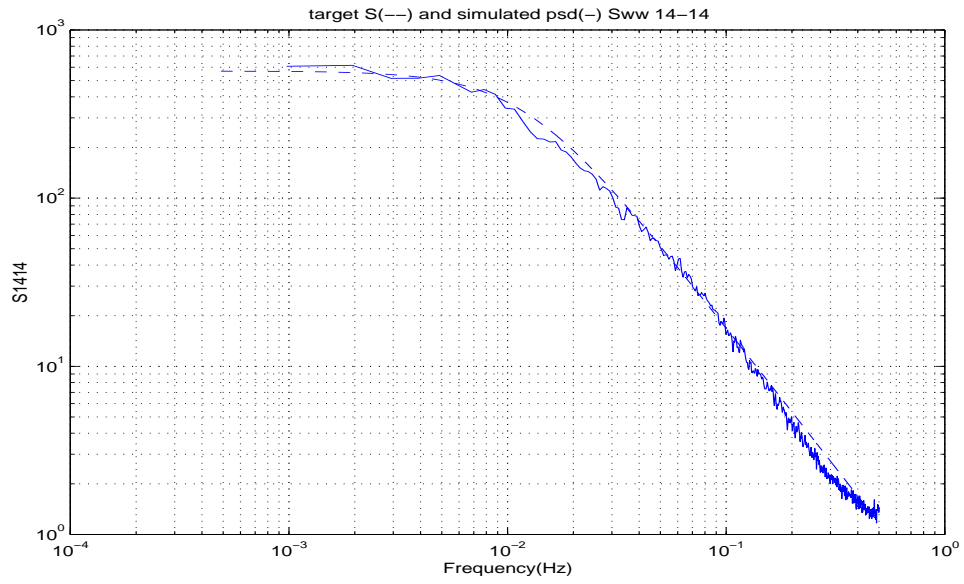


Figure 7.10 Comparison between the target XPSD $S_{14-14}(f)$ (dashed line) and the simulated XPSD $S_{\text{ww}14-14}(f)$ (solid line).

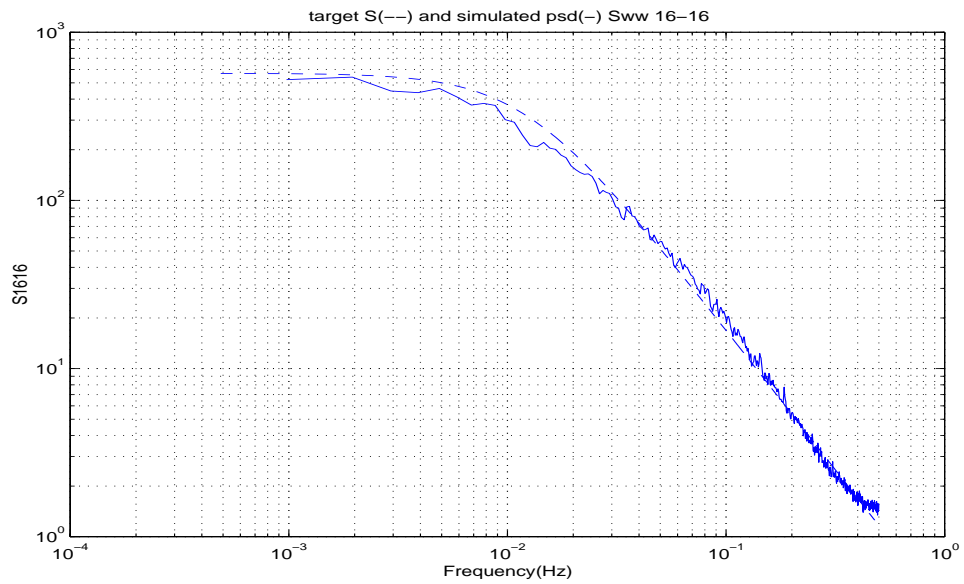


Figure 7.11 Comparison between the target XPSD $S_{16-16}(f)$ (dashed line) and the simulated XPSD $S_{\text{ww}16-16}(f)$ (solid line).

Some off-diagonal elements of the matrix $S(f)$ are shown in Figs. 7.12-7.16. In these figures, the dashed lines are the target cross spectra S_{1-2} , S_{1-3} , S_{2-3} , S_{5-10} , and S_{1-16} . The solid lines are the simulated cross-power spectral densities S_{ww1-2} , S_{ww1-3} , S_{ww2-3} , S_{ww5-10} , and S_{ww1-16} . Here $i-j$ means the i -th row and j -th column of the matrices $S(f)$ and $S_{ww}(f)$, which represent the XPSDs of wind velocities at the i -th and j -th levels. The simulated XPSDs of wind velocities show a good agreement with the target spectral densities. The XPSD of the first and the sixteenth levels S_{ww1-16} matches S_{1-16} at lower frequencies. At higher frequencies, S_{1-16} approaches to zero, while S_{ww1-16} goes to a very small number close to zero. Therefore, the log-log plot in Fig. 7.16 shows a larger difference than the linear coordinate plots (Fig. 7.17). However, S_{1-16} and S_{ww1-16} match each other in linear coordinates. In fact, all values are close to zero at higher frequencies. The results show that when the distance between the levels is large, the simulation at higher frequencies is not as good as when the distance between the levels is small. This is due to the exponential term in the wind velocity model $\exp(-2c_1|f|(|h_i - h_j|/(V_i + V_j)))$. If $|h_i - h_j|$ and $|f|$ become large, the exponential term becomes very small. For example, if $i = 1$, $j = 16$, and $f = 0.5\text{Hz}$, this term is 3.7928×10^{-17} and the target cross-power spectrum is 4.4202×10^{-17} , which for all practical purpose can be treated as zero. The corresponding simulated cross-power spectrum is 1.682×10^{-1} . These numbers are almost negligible since both the target and simulated spectra are on the order of 10^2 at lower frequencies.

As mentioned before, sixteen independent white noise processes are used as input to the state-space equation system. The output consists of sixteen wind velocity time histories at sixteen levels. Figure 7.18 shows the time histories of the wind velocity fluctuations at the first, fifth, tenth and sixteenth levels.

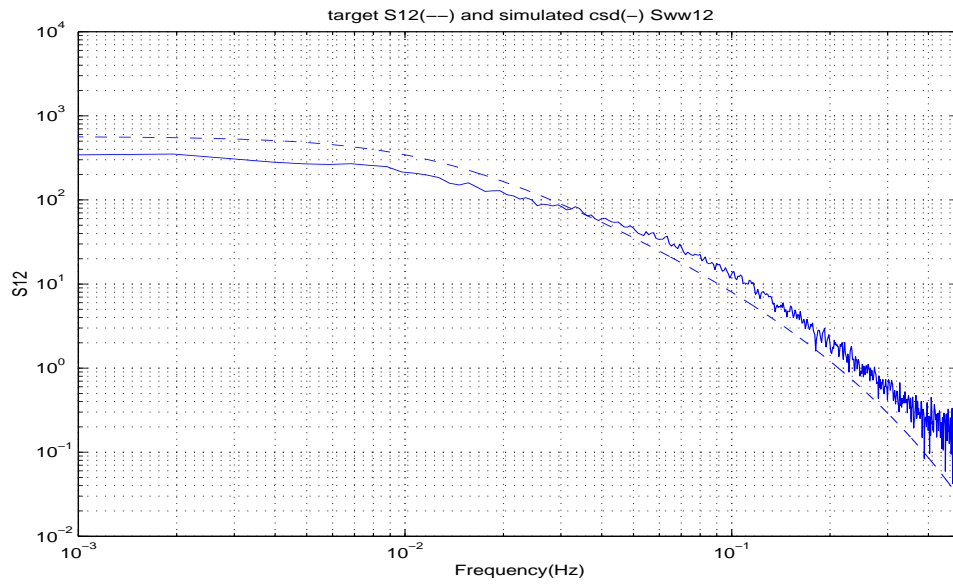


Figure 7.12 Comparison between the target XPSD $S_{1-2}(f)$ (dashed line) and simulated PSD $S_{ww1-2}(f)$ (solid line).

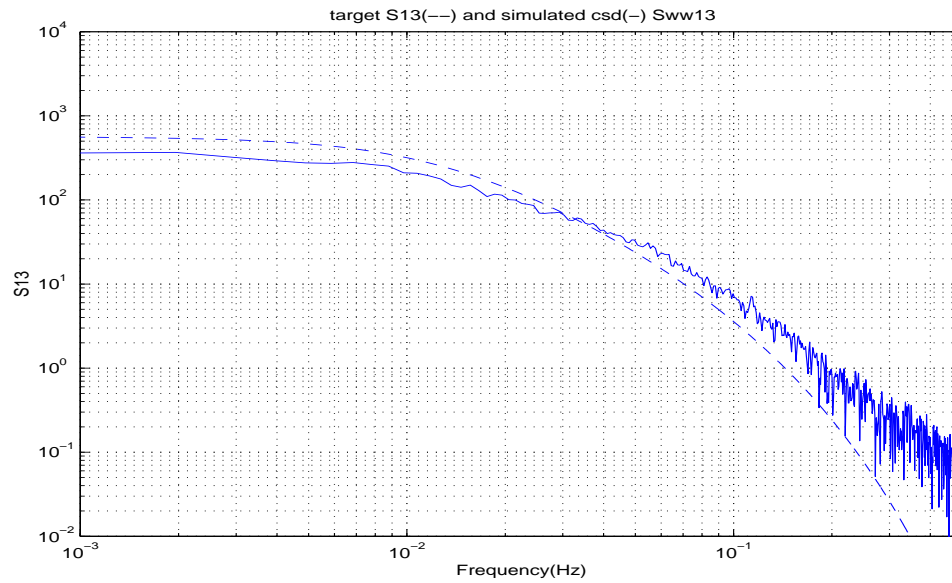


Figure 7.13 Comparison between the target XPSD $S_{1-3}(f)$ (dashed line) and simulated PSD $S_{ww1-3}(f)$ (solid line).

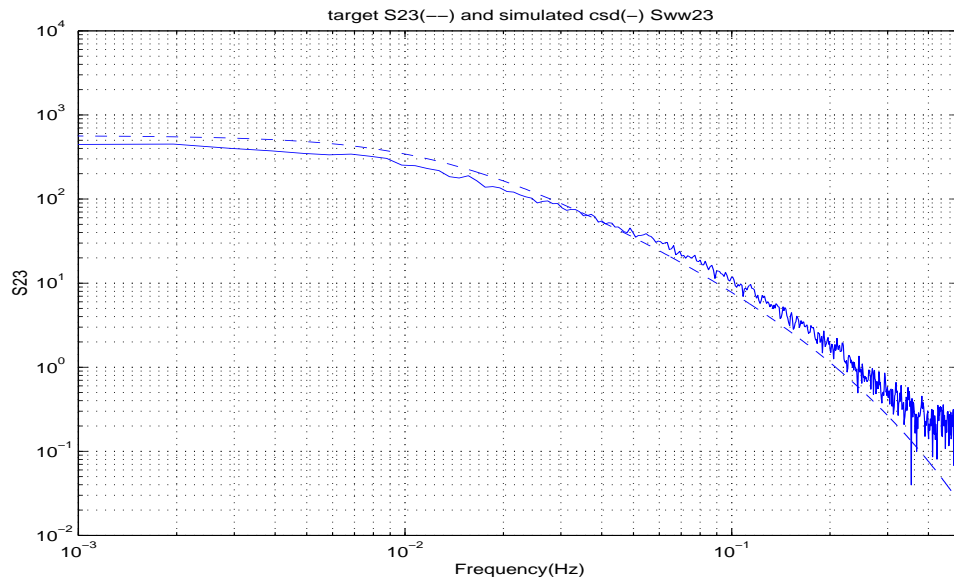


Figure 7.14 Comparison between the target XPSD $S_{2-3}(f)$ (dashed line) and simulated PSD $S_{ww2-3}(f)$ (solid line).

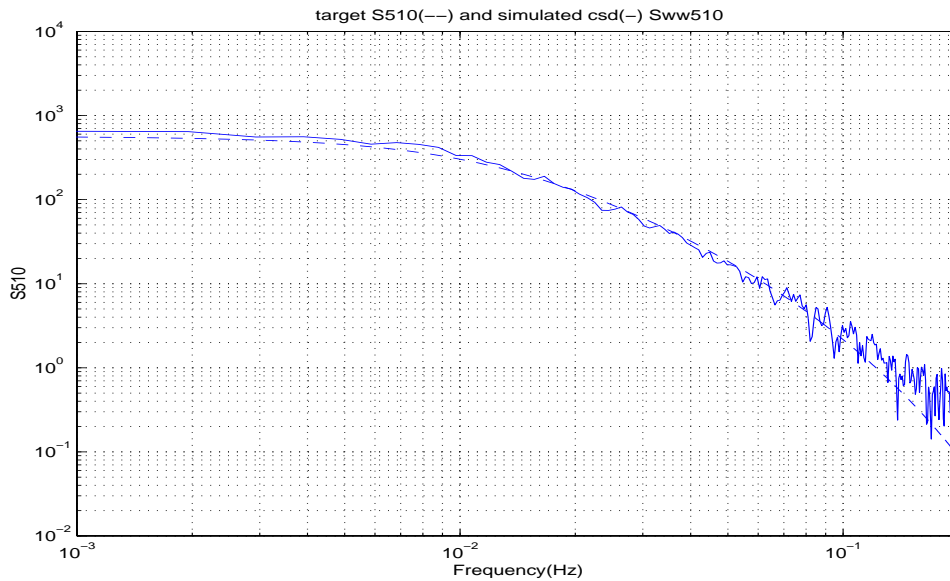


Figure 7.15 Comparison between the target XPSD $S_{5-10}(f)$ (dashed line) and simulated PSD $S_{ww5-10}(f)$ (solid line).

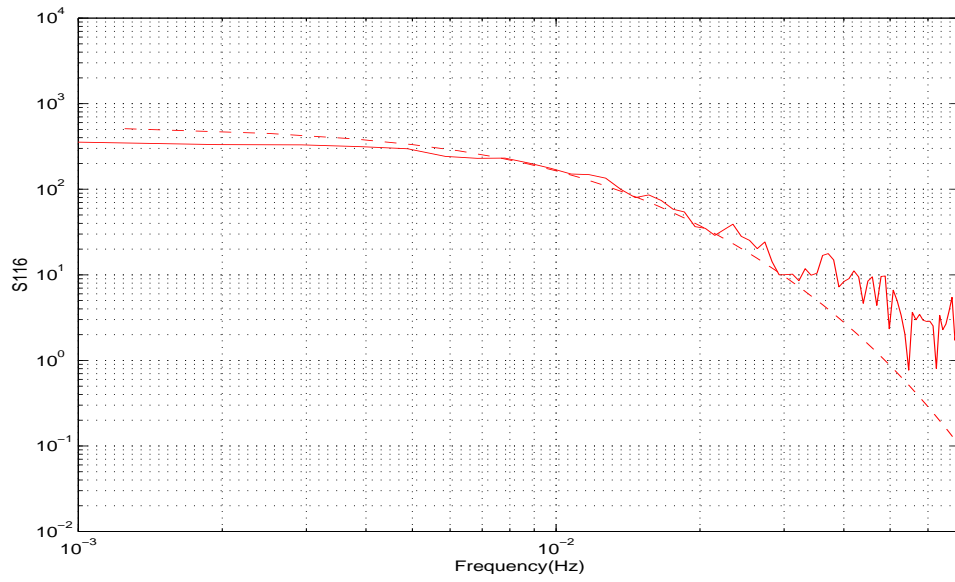


Figure 7.16 Comparison between the target XPSD $S_{1-16}(f)$ (dashed line) and simulated XPSD $S_{ww1-16}(f)$ (solid line) in log-log coordinate.

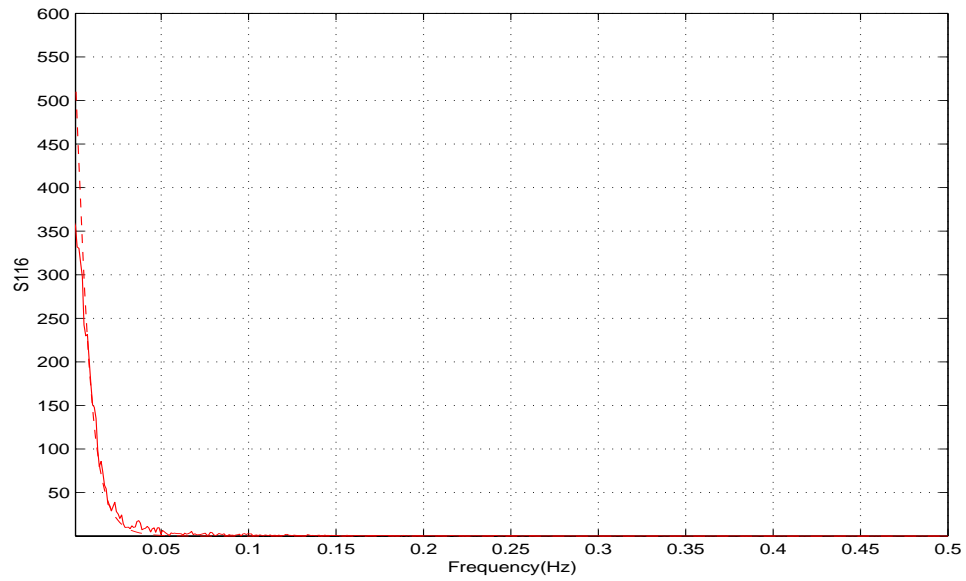


Figure 7.17 Comparison between the target XPSD $S_{1-16}(f)$ (dashed line) and simulated XPSD $S_{ww1-16}(f)$ (solid line) in linear coordinate.

Table 7.2 lists the σ values of wind velocity. Three different approaches mentioned in Section 7.3 are used. The simulation results use the full state-space representation which has 32 states. The RMS value of the target spectral density using Eq. (7-24) is calculated as, $\sigma = \sqrt{4K_0V_r^2} = 3.685$ for the Nanjing Tower. Using Eq. (7-25) and the simulated spectral density, the RMS values are calculated and listed in Table 7.2. The difference between target and simulated values varies between 0.41% and 3.29%. The RMS values calculated using Eq. (7-26) are also listed in Table 7.2. The difference between the target and simulated values varies between 0.01% and 3.75%.

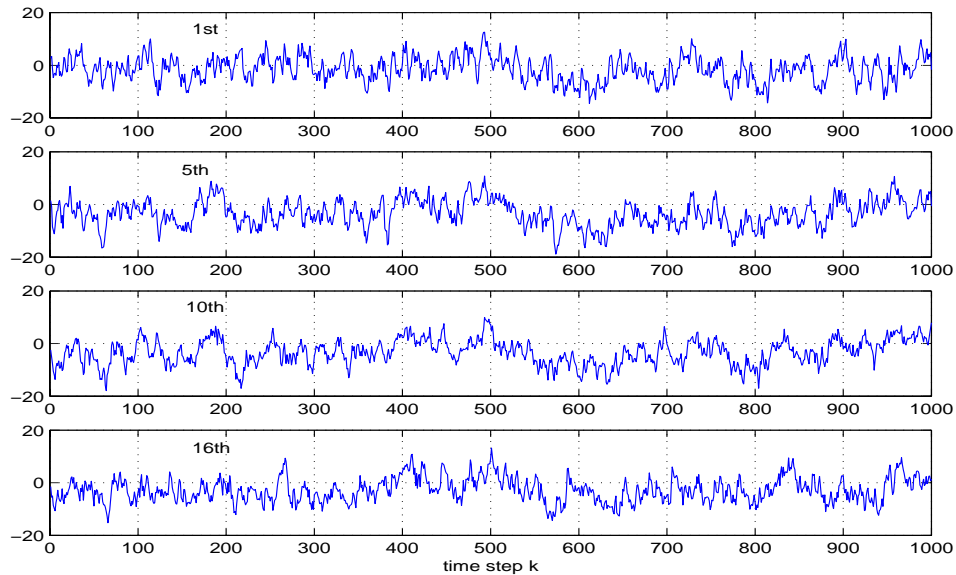


Figure 7.18 Time histories of wind velocity at 1st, 5th, 10th and 16th levels of Nanjing Tower generated by state-space representation.

Table 7.2 σ Values of Wind Velocity Using Full State-Space Representation (32 States)

	Eq. (7-24)	Eq. (7-25)	Diff. %	Eq. (7-26)	Diff. %		Eq. (7-24)	Eq. (7-25)	Diff. %	Eq. (7-26)	Diff. %
σ_1	3.685	3.670	0.41	3.643	1.16						
σ_2	3.685	3.658	0.75	3.625	1.63	$\sqrt{\sigma_{1-2}}$	3.267	3.199	2.09	3.419	4.65
σ_3	3.685	3.693	0.20	3.651	0.93	$\sqrt{\sigma_{1-3}}$	3.010	2.940	2.31	3.269	8.63
σ_4	3.685	3.734	1.32	3.686	0.01	$\sqrt{\sigma_{1-4}}$	2.861	2.796	2.24	3.152	10.19
σ_5	3.685	3.775	2.42	3.720	0.93	$\sqrt{\sigma_{1-5}}$	2.740	2.687	1.93	2.994	9.28
σ_6	3.685	3.796	2.99	3.739	1.45	$\sqrt{\sigma_{1-6}}$	2.655	2.611	1.64	2.808	5.79
σ_7	3.685	3.808	3.32	3.750	1.75	$\sqrt{\sigma_{1-7}}$	2.579	2.529	1.95	2.749	6.61
σ_8	3.685	3.805	3.25	3.747	1.67	$\sqrt{\sigma_{1-8}}$	2.501	2.452	1.95	2.690	7.56
σ_9	3.685	3.778	2.52	3.722	1.00	$\sqrt{\sigma_{1-9}}$	2.456	2.402	2.19	2.636	7.34
σ_{10}	3.685	3.784	2.68	3.732	1.25	$\sqrt{\sigma_{1-10}}$	2.411	2.360	2.13	2.540	5.33
σ_{11}	3.685	3.807	3.29	3.753	1.83	$\sqrt{\sigma_{1-11}}$	2.371	2.318	2.25	2.469	4.11
σ_{12}	3.685	3.788	2.80	3.737	1.39	$\sqrt{\sigma_{1-12}}$	2.261	2.171	4.00	2.392	5.81
σ_{13}	3.685	3.699	0.37	3.649	0.97	$\sqrt{\sigma_{1-13}}$	2.192	2.074	5.36	2.288	4.38
σ_{14}	3.685	3.641	1.21	3.591	2.55	$\sqrt{\sigma_{1-14}}$	2.157	2.025	6.13	2.169	0.55
σ_{15}	3.685	3.619	1.81	3.574	3.01	$\sqrt{\sigma_{1-15}}$	2.130	1.983	6.93	2.005	5.90
σ_{16}	3.685	3.664	0.58	3.623	1.68	$\sqrt{\sigma_{1-16}}$	2.109	1.948	7.64	1.830	13.2

In addition, the square root of covariance between the wind velocity at the first and the 2nd level is 3.267, and the simulated value using Eq. (7-25) is 3.199 which results in a difference of 2.09%. Using the time history method the simulated value is 3.419 with a difference of 4.65%. The square root of covariance between the wind velocity at the first and

the sixteenth level is 2.11. For the simulated spectrum using Eq. (7-25) it is 1.948 with a difference of 7.64%. Using the time history method it is 1.83 with a difference of 13.2%. It is noted that the difference between the target and simulated values increases with an increase in the distance between the two location. This may be attributed to numerical errors or the truncation introduced in the modeling of off-diagonal terms.

7.5.2 Model Reduction of State-Space Representation

In Fig. 7.2 the eigenvalues of the XPSD matrix were presented. It was noted that the first several eigenvalues were much larger than the others. These eigenvalues are the dominant factors of the XPSD matrix. This suggests a model reduction technique. If only the first six eigenvalues are considered in the Nanjing Tower wind velocity XPSD matrix, the total number of states in the state-space representation would be reduced to 12 from 32 states. This would significantly simplify the computation effort. Table 7.3 lists the results of this model reduction technique using the largest 6 eigenvalues in the state-space representation, and the RMS values of wind velocity fluctuations using different calculation procedures. Note, the number of states is reduced from 32 to 12. This simplifies the calculation significantly and makes the applications using this model more conveniently realizable. Furthermore, Table 7.3 also demonstrates that the simulated wind velocity obtained from the reduced state-space representation provides a good approximation of the actual wind velocity with prescribed wind velocity XPSD.

Table 7.3 σ Values of Wind Velocity Using Six-Eigenvalue State-Space Representation (12 States)

	Eq. (7-24)	Eq. (7-25)	Diff. %	Eq. (7-26)	Diff. %		Eq. (7-24)	Eq. (7-25)	Diff. %	Eq. (7-26)	Diff. %
σ_1	3.685	3.531	4.19	3.497	5.12						
σ_2	3.685	3.401	7.70	3.359	8.87	$\sqrt{\sigma_{1-2}}$	3.267	3.357	2.77	3.479	6.47
σ_3	3.685	3.503	4.95	3.452	6.33	$\sqrt{\sigma_{1-3}}$	3.010	2.946	2.10	3.388	12.6
σ_4	3.685	3.552	3.63	3.494	5.19	$\sqrt{\sigma_{1-4}}$	2.861	2.724	4.79	3.220	12.6
σ_5	3.685	3.564	3.28	3.501	5.01	$\sqrt{\sigma_{1-5}}$	2.740	2.630	4.03	2.928	6.85
σ_6	3.685	3.637	1.30	3.571	3.10	$\sqrt{\sigma_{1-6}}$	2.655	2.612	1.60	2.783	4.83
σ_7	3.685	3.633	1.41	3.565	3.26	$\sqrt{\sigma_{1-7}}$	2.579	2.577	0.08	2.764	7.18
σ_8	3.685	3.618	1.83	3.551	3.66	$\sqrt{\sigma_{1-8}}$	2.501	2.473	1.14	2.739	9.53
σ_9	3.685	3.650	0.98	3.585	2.74	$\sqrt{\sigma_{1-9}}$	2.456	2.393	2.54	2.689	9.49
σ_{10}	3.685	3.661	0.67	3.600	2.32	$\sqrt{\sigma_{1-10}}$	2.411	2.330	3.36	2.562	6.27
σ_{11}	3.685	3.621	1.74	3.564	3.30	$\sqrt{\sigma_{1-11}}$	2.371	2.280	3.83	2.447	3.20
σ_{12}	3.685	3.649	0.99	3.603	2.23	$\sqrt{\sigma_{1-12}}$	2.261	2.164	4.27	2.358	4.28
σ_{13}	3.685	3.517	4.58	3.474	5.75	$\sqrt{\sigma_{1-13}}$	2.192	2.068	5.63	2.286	4.32
σ_{14}	3.685	3.481	5.53	3.438	6.70	$\sqrt{\sigma_{1-14}}$	2.157	2.000	7.28	2.202	2.06
σ_{15}	3.685	3.531	4.20	3.488	5.36	$\sqrt{\sigma_{1-15}}$	2.130	1.952	8.40	2.016	5.39
σ_{16}	3.685	3.527	4.31	3.485	5.43	$\sqrt{\sigma_{1-16}}$	2.109	1.913	9.26	1.776	15.8

Once the wind velocity is obtained from the state-space representation, the wind loading can be derived according to the strip and quasi-steady theories (Simiu and Scanlan 1985; Kareem, 1987). The alongwind force on a structure per unit height is given as below

$$F_{wh} = \frac{1}{2}\rho C_d B(\bar{V} + v)^2 \quad (7-27)$$

where ρ is air density, C_d is drag coefficient, B is width of the building, \bar{V} is mean wind velocity, and v is the fluctuation of wind velocity. Usually the fluctuation of wind velocity is relatively very small compared to the mean wind velocity. Therefore, the fluctuating along-wind force at each level is then given by:

$$F_w = \rho C_d B h \bar{V} v \quad (7-28)$$

where h is level height. The wind load can be generated from the state-space representation of wind velocity as given below:

$$\begin{aligned} \mathbf{x}_w(k+1) &= A_w \mathbf{x}_w(k) + B_w V(k), \\ \mathbf{y}_w(k) &= C_w \mathbf{x}_w(k) + D_w V(k) \end{aligned} \quad (7-29)$$

where $A_w = A_v$, $B_w = B_v$, $C_w = \rho C_d B h \bar{V} C_{new}$, $D_w = \rho C_d B h \bar{V} D_{new}$, and $y_w(k)$ represents the fluctuation wind load.

7.6 Feedforward-Feedback Based Controller Design for Nanjing Tower

The following example compares the MPC based feedforward-feedback control with a passive control and feedback based MPC (MPC/FB) scheme. In this example, the Nanjing tower is modeled as a lumped mass MDOF system (Kareem et al, 1998). The AMD is attached at the VIP lounge on the 12th level. The structural properties are listed in Table 7.4. The natural frequencies of the tower are 0.20, 0.62, 1.26, 1.83, 2.51, 4.71, 5.03, 8.86,

9.40, 14.21, 20.25, 26.20, 36.20, 47.60, 53.40, and 64.18 Hz, respectively. The damping ratio in each mode has been estimated by using:

$$\zeta_n = \min\left(0.01, \zeta_1\left(1 + 0.38\left(\frac{\omega_n}{\omega_1} - 1\right)\right)\right) \quad (7-30)$$

(Kareem, 1981) and the stiffness matrix has been given by Reinhorn et al. (1995).

Table 7.4 Geometric Properties of Nanjing Tower

Level	Mass(t)	Elevation (m)	Story Height (m)	Width (m)	Area (m ²)
1	3992.9	10.1	10.1	28.56	413.24
2	3186.7	32.2	22.1	24.35	536.02
3	2820.1	58.6	26.4	20.23	469.50
4	2319.8	80.2	21.6	18.75	387.18
5	1917.9	101.8	21.6	17.10	323.73
6	1624.5	119.8	18.0	15.45	271.35
7	1628.1	137.8	18.0	14.70	277.38
8	1322.3	158.6	20.8	13.95	233.65
9	3395.3	171.8	13.2	13.42	182.51
10	5678.6	185.5	14.0	13.42	183.85
11	1512.4	199.2	13.4	13.42	213.51
12	1254	240.4	41.2	6.0	175.58
13	165.1	270.1	29.7	3.5	66.38
14	18.7	286.1	16.0	1.8	21.55
15	12	299.1	13.0	1.1	11.28
16	4	310.1	12.0	0.75	4.13

The equations of motion are expressed in the following:

$$M\ddot{x}(t) + C\dot{x}(t) + Kx(t) = F_w(z, t) + Lf(t) \quad (7-31)$$

where M , C , K are the mass, damping and stiffness matrices including tower and AMD, $F_w(z, t)$ is the wind load at different levels, $f(t)$ is the control force due to AMD, and L is the matrix representing the AMD location

Equation (7-31) can be reformulated in the state-space form as:

$$\dot{X}(t) = AX(t) + BU(t) + EW(t) \quad (7-32)$$

where A is the system matrix, B is the control location matrix, E is the excitation influence matrix, W is the wind load, and U is the control force. The control output vector z and measured output vector y can be expressed as:

$$z = C_z X + D_z U + F_z W \quad (7-33)$$

$$y = C_y X + D_y U + F_y W \quad (7-34)$$

By assuming $W = y_w$, the wind load state-space model (Eq. (7-29)) and the structural model (Eq. (7-32), (7-34)) are combined to form the augmented state-space system.

$$\begin{bmatrix} \dot{X}(t) \\ \dot{x}_w(t) \end{bmatrix} = \begin{bmatrix} A & EC_w \\ 0 & A_w \end{bmatrix} \begin{bmatrix} X(t) \\ x_w(t) \end{bmatrix} + \begin{bmatrix} B \\ 0 \end{bmatrix} U(t) + \begin{bmatrix} ED_w \\ B_w \end{bmatrix} w(t)$$

$$\begin{bmatrix} y(t) \\ y_w(t) \end{bmatrix} = \begin{bmatrix} C & F_y C_w \\ 0 & C_w \end{bmatrix} \begin{bmatrix} X(t) \\ x_w(t) \end{bmatrix} + \begin{bmatrix} D_y \\ 0 \end{bmatrix} U(t) + \begin{bmatrix} F_y D_w \\ D_w \end{bmatrix} w(t) \quad (7-35)$$

Then MPC scheme is implemented on this augmented system. The designed control force includes the wind load information in the feedforward loop and the structural response in the feedback loop. A TMD and a MPC/FB scheme using Eq. (7-32) are also applied to control the tower response. Figures 7.19-7.21 show the power spectral density

function of the acceleration at the 10th, 12th and 16th levels, respectively. There are four types of lines used in these figures. The dotted line represents the uncontrolled case, the dash-dot line denotes the passive control case, the dashed line is MPC/FB scheme, and the solid line describes the MPC/FF-FB case. Figure 7.22 shows the power spectral density function of the control force using MPC/FB and the MPC/FF-FB schemes.

The RMS values of the displacement, velocity and acceleration at levels 10, 12, 16 and the active mass damper from different control schemes are listed in Table 7.5. The RMS values of control force are also given in Table 7.5. The passive control using a TMD helps to reduce the acceleration of level 12 by over 20%. The active mass damper using MPC/FB scheme reduces the acceleration of the same level by 34% with the RMS value of control force of 121.89 kN. The MPC/FF-FB scheme further improves the active control performance. The acceleration of the 12th level in this case is reduced by over 36% while the control force is only 96.55 kN, which is 21% smaller than that for the MPC/FB scheme. In addition, the MPC/FF-FB scheme is also effective in reducing the displacement, velocity and acceleration responses at the other levels. The displacement of AMD using MPC/FB scheme is 185.54 cm while it is only 132.92 cm using the MPC/FF-FB scheme, which is 28% smaller.

To sum up, MPC/FF-FB control is relatively more effective than the passive control and MPC/FB scheme. With a smaller control force, it can reduce the tower response more than the MPC/FB scheme. Its superior effectiveness results from its feedforward-feedback based information which improves the efficiency of the control design.

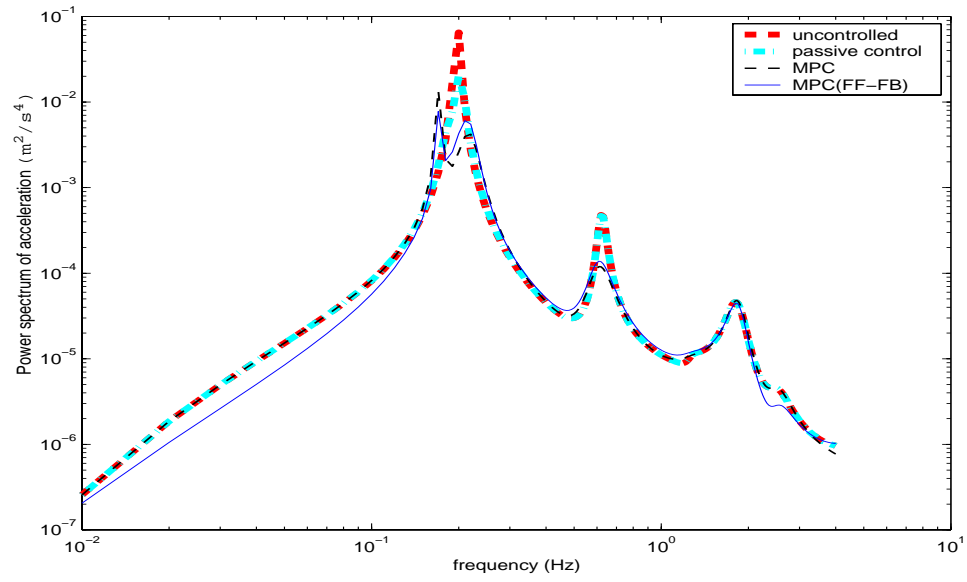


Figure 7.19 Acceleration PSD at the 10th level.

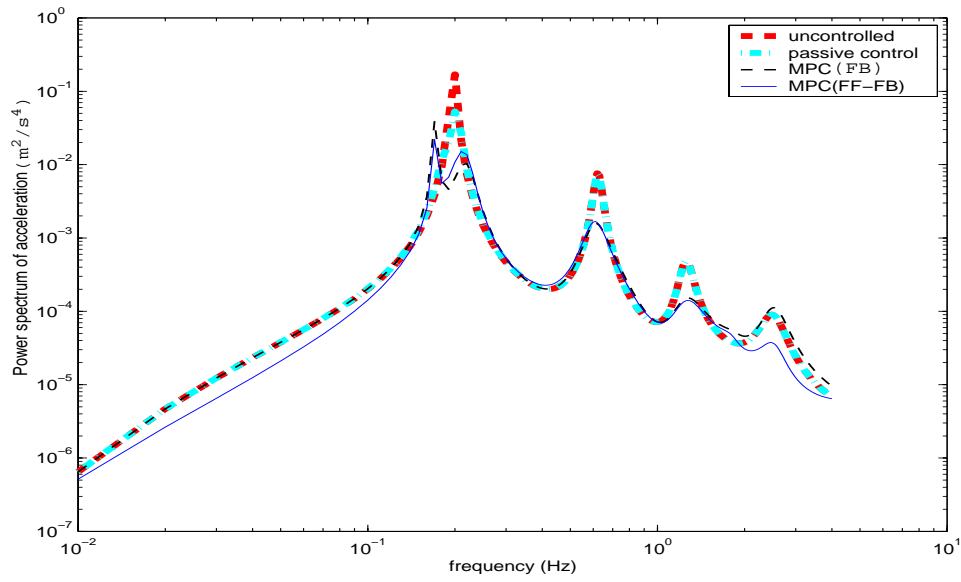


Figure 7.20 Acceleration PSD at the 12th level.

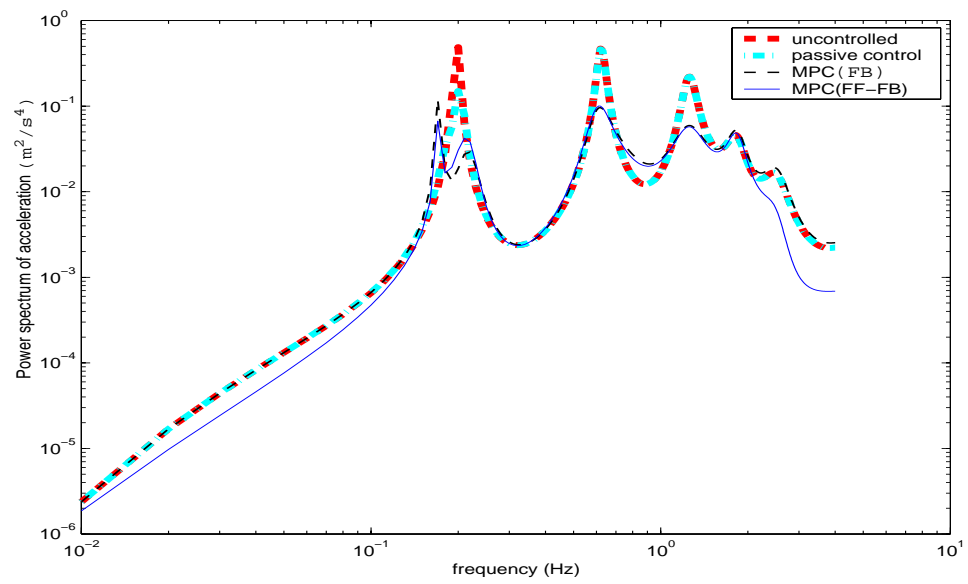


Figure 7.21 Acceleration PSD at the 16th level.

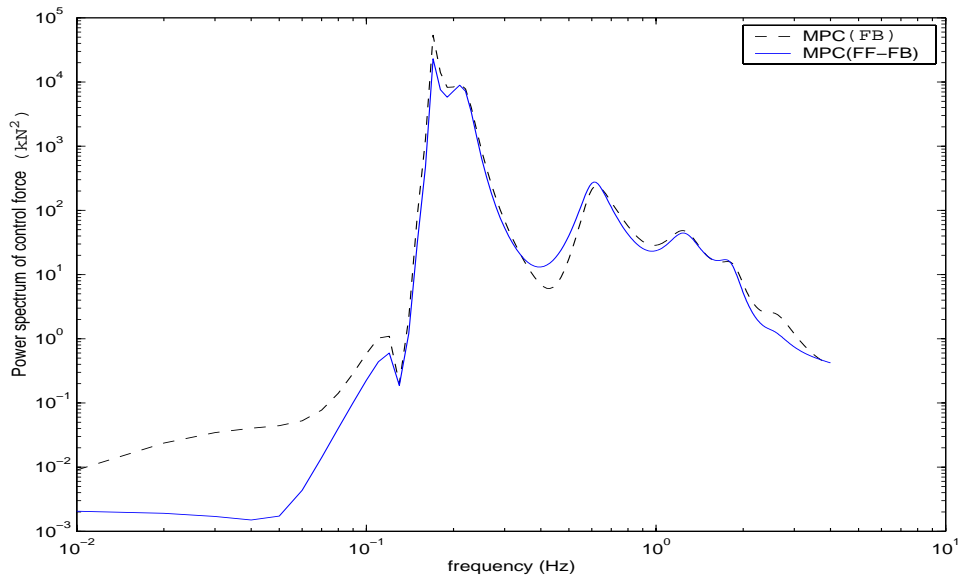


Figure 7.22 Control force PSD.

Table 7.5 Tower Response Under Different Control Schemes

	uncontrolled	TMD (passive Control)	MPC	MPC(FF-FB)
$\sigma_{x_{10}}$ (cm)	9.55	8.10	7.84	6.69
$\sigma_{x_{12}}$ (cm)	15.31	12.93	12.62	10.73
$\sigma_{x_{16}}$ (cm)	27.54	23.75	23.26	19.73
σ_{x_m} (cm)		46.28	185.54	132.92
$\sigma_{\dot{x}_{10}}$ (cm)	9.34	6.89	6.04	5.73
$\sigma_{\dot{x}_{12}}$ (cm)	15.21	11.26	9.99	9.38
$\sigma_{\dot{x}_{16}}$ (cm)	32.58	22.97	22.93	21.87
$\sigma_{\dot{x}_m}$ (cm)		56.66	207.23	152.55
$\sigma_{\ddot{x}_{10}}$ (cm/s ²)	11.86	8.88	7.47	7.45
$\sigma_{\ddot{x}_{12}}$ (cm/s ²)	20.97	16.64	13.76	13.34
$\sigma_{\ddot{x}_{16}}$ (cm/s ²)	124.77	122.68	102.54	94.24
$\sigma_{\ddot{x}_m}$ (cm/s ²)		70.56	241.02	185.92
σ_u (kN)			121.89	96.55

7.7 Summary

This chapter presented the formulation and application of stochastic decomposition for the simulation of multi-variate processes, e.g., wind velocity fluctuations, and modal space reduction in the wind-induced response analysis of structures. The proposed state-space wind model provides an accurate description of wind velocity, especially for correlated wind processes. This is very important for designing high-performance controllers. The state-space based simulation describing the fluctuating nature of wind loading was imple-

mented in the MPC/FF-FB control scheme to effectively reduce the response of structure under wind excitations. The numerical example using Nanjing Tower in China demonstrated the effectiveness of the MPC/FB and MPC/FF-FB schemes. This also showed that the MPC/FF-FB scheme could effectively deliver a better control performance than the passive control and the MPC/FB scheme. In summary, the wind loading state-space realization and MPC based schemes provide a reliable and convenient strategy to control structural motions under wind excitation.

CHAPTER 8

EXPERIMENTAL VERIFICATION OF MODEL PREDICTIVE CONTROL

MPC based schemes have been shown to be effective in structural response control by computer simulations in previous chapters. In this chapter, MPC based schemes are employed experimentally to reduce response of buildings under earthquake excitation using acceleration feedback. A Kalman-Bucy filter is used in the state observer to estimate the state of the system from the acceleration feedback. The operations of a small-scale shaking table are tailored to simulate different ground motions. Scaled El Centro and Kobe earthquakes are used as the input ground motions. A two-story flexible building is used as the experimental model. A DC motor-driven moving cart acts as the AMD actuator. The control force is implemented in real-time using Matlab Real-Time Workshop and WinCon software and MultiQ data control board. The MPC using acceleration feedback is first verified experimentally for different weighting matrices. Then the effect of accelerometer locations is studied. Finally, the real-time MPC-AR and constrained MPC schemes (Chapter 3 and 6) are verified by means of a pseudo real-time control approach.

8.1 Experimental Setup

The tests are conducted in the NatHaz Modeling Laboratory, University of Notre Dame. The test equipment includes a small-scale shaking table, a steel column building model, an

active mass damper (AMD), a MultiQ data acquisition I/O board, a signal spectrum analyzer, accelerometers, and a computer.

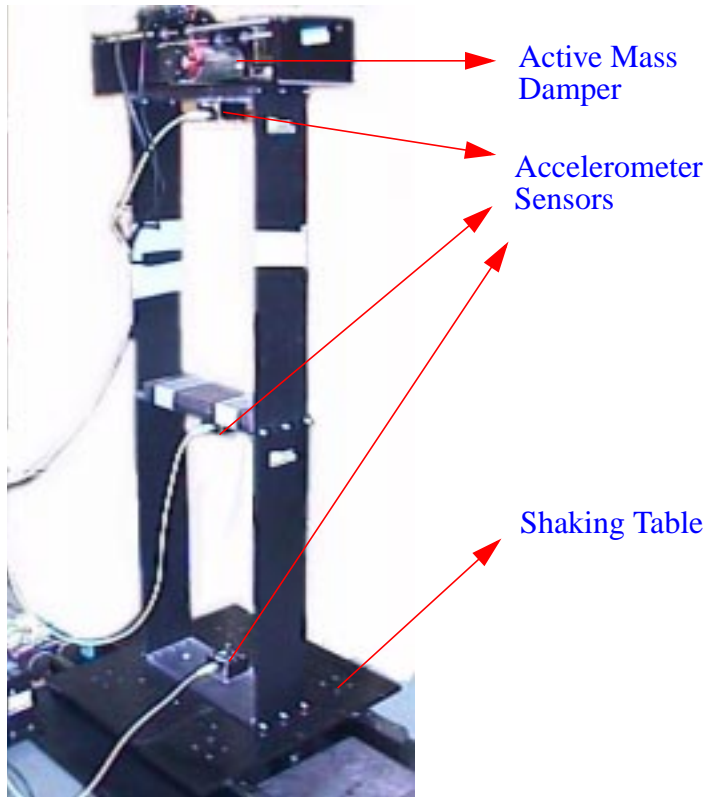


Figure 8.1 Experiment building and Active Mass Damper

The small-scale shaking table built by SMI technologies Inc. is used for simulating ground excitation. It consists of an electric powered servo motor at a maximum capacity of 6000 RPM. A flat table ($46\text{cm} \times 46\text{cm}$) is mounted on a linear high-accuracy driving shaft and two 64cm-long sliding tracks. A standard encoder at a resolution of 1000 count/rev. and $2.6667\text{e-}4$ cm/count measures the displacement of the table.

The test building employed in the experiment is a flexible small-scaled model. This structure is configured to have 2 floors. Each floor is 490mm high and has two steel columns with the dimension of $2 \times 108 \times 490$ mm³. The mass of each column is 0.227kg. The mass of the first floor is 4.8kg, and the mass of the second floor including AMD is 5.0 kg. An accelerometer with the sensitivity of 1.96 (m/sec²)/V and the bandwidth of 50 Hz is installed at each floor.

The AMD is a direct drive linear motion cart operated by a high torque DC motor. The cart position is measured by an encoder with a resolution of 2048 counts/rev. and 4.8704e-4 cm/count.

A MultiQ-3 I/O board is used for data acquisition and conversion. The terminal control board has 8 single ended analog inputs (13-bit A/D), 8 analog outputs (12-bit D/A), 16 bits of digital inputs and outputs, and 8 encoder inputs, etc. It is used to obtain the measured responses from sensors and to send control signals to the shaking table and AMD.

The MPC scheme based controller is first designed by Simulink (1998). Then the Simulink program is converted into C code through Matlab's Real-time Workshop and Quanser's WinCon software. Through WinCon server-client interface, the control schemes are realized and the measured data and control commands are transferred through the MultiQ-3 I/O board.

In addition, Siglab 3.0 package is applied as the spectrum analyzer. This PC-based 2 input/2 output Siglab package has a Matlab interface and is used in system identification and response analysis. All these devices are run by a 200 Mhz Pentium Gateway-2000 computer with 32 Mb RAM.

8.2 Design of Shaking Table Operations

A closed-loop PID controller is designed for displacement controlled small-scale shaking table used in the experiment (Fig. 8.2). The desired displacement is sent to the AC motor as a voltage change of current. The PID controller generates control signals and makes the actual displacement of the table track the desired displacement signal. A second-order system model is used for the shaking table. The pole placement technique is

applied to design the closed-loop displacement controller. Assume the desired performance of the shaking table specifies a peak time t_p and a damping ratio ζ , and then the natural frequency of the desired system can be calculated by:

$$\omega_0 = \frac{\pi}{t_p \sqrt{1 - \zeta^2}} \quad (8-1)$$

and the characteristic polynomial is equal to $s^2 + 2\zeta\omega_0s + \omega_0^2$. A peak time of 0.03 seconds and a damping ratio of 0.7 are selected. Then using the pole-placement method, the state-feedback matrix k is obtained such that the shaking table system's poles are set as the roots of the characteristic polynomial.

As shown in Figs. 8.3 and 8.4, a test for the shaking table is done. A step function and a sinusoid wave function are chosen as the desired displacements. The dashed lines represent the measured table displacement, which follows the desired displacement in solid lines with satisfactory dynamic features.

However, for the earthquake, ground acceleration is usually measured by accelerograph. For the shaking table, the displacement control method cannot employ the desired ground acceleration directly. Therefore, an inverse transfer function method is used to obtain the desired ground acceleration signals. Assuming that the shaking table can be modeled as a linear system over the frequency range of interest. This system identification test is carried out by Siglab 3.0 spectrum analyzer. The shaking table transfer function, H_{au} , from the control command to the table acceleration is obtained and shown in Fig. 8.5 as the magnitude and phase plots. The dashed line is for the transfer function obtained experimentally. The solid line is for the analytical model obtained by curve-fitting. Once the transfer func-

tion is established, it can be written in the numerator and denominator form and the inverse, H_{au}^{-1} , can be easily derived.

The concept of inverse transfer function strategy is demonstrated in Fig. 8.6, which demonstrates that a simulated earthquake signal can be generated. Figure 8.7 shows the displacement command for a 10% scaled El Centro earthquake signal and Fig. 8.8 displays the corresponding El Centro simulated earthquake signal which is the measured table acceleration. The original 10% scaled ground motion shown in Fig 8.9 has a RMS value of 0.0449, and the simulated one has a RMS value of 0.0569. The difference between the two is 26%, which is relatively large.

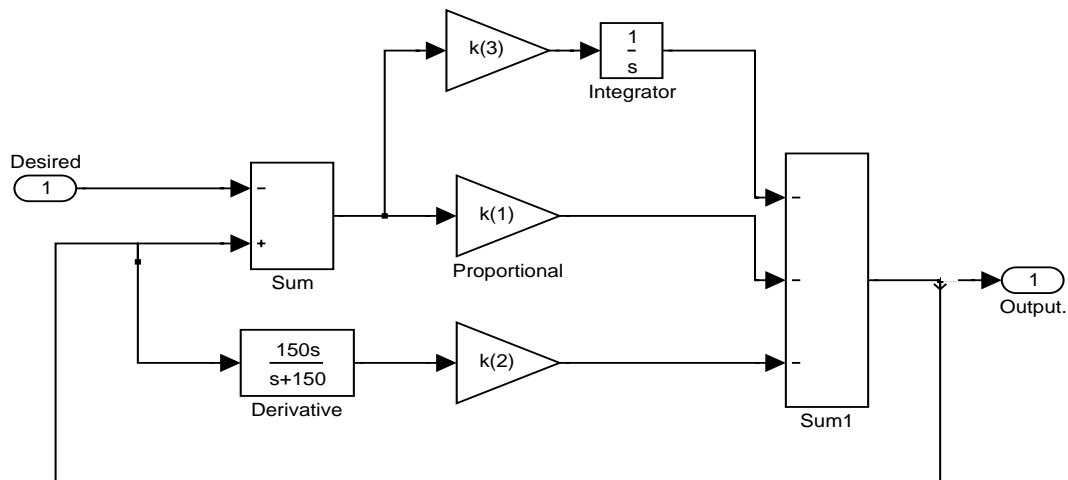


Figure 8.2 PID design for shaking table

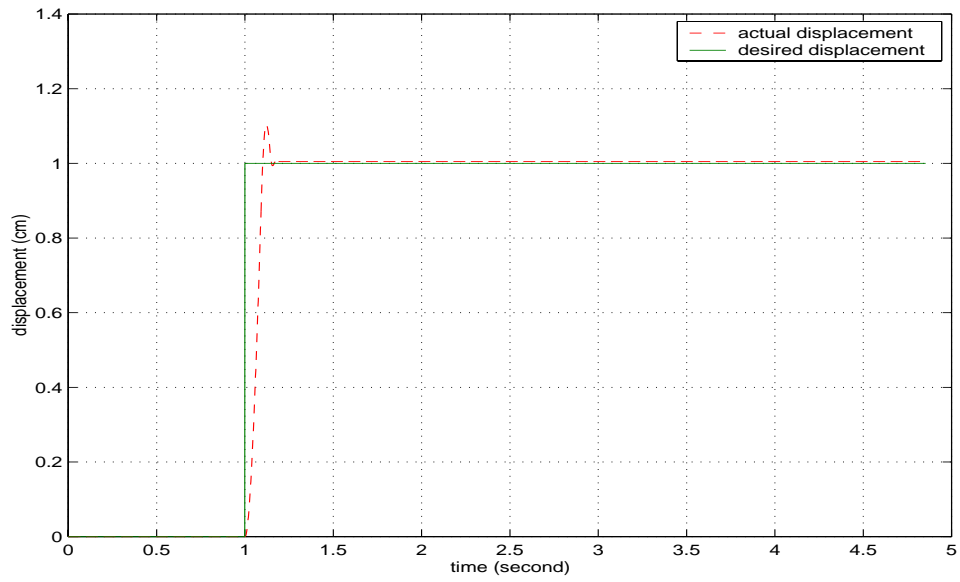


Figure 8.3 Shaking table response with step displacement command

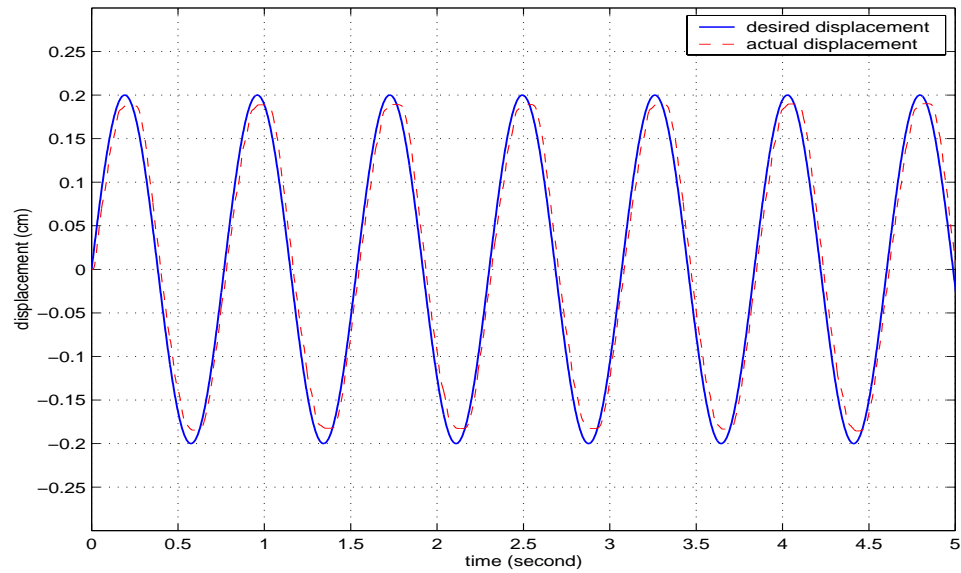


Figure 8.4 Shaking table response with sinewave displacement command

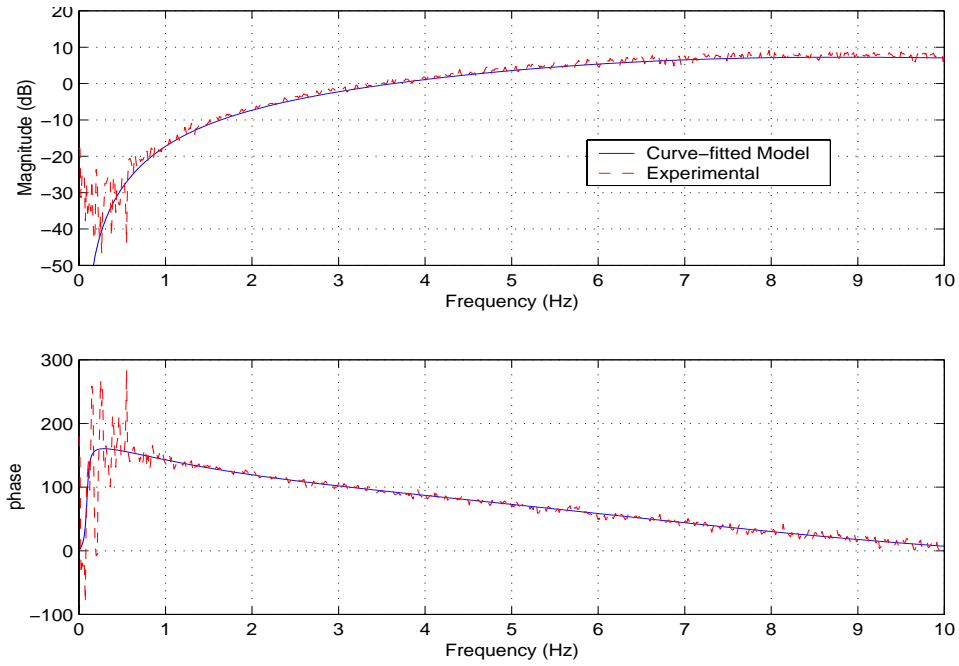


Figure 8.5 Shaking table transfer function: magnitude and phase plot

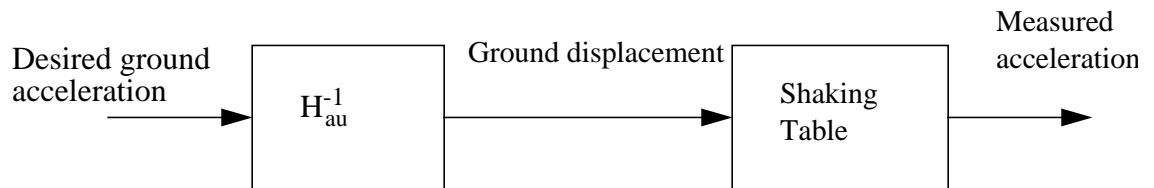


Figure 8.6 Diagram for shaking table design to get desired acceleration

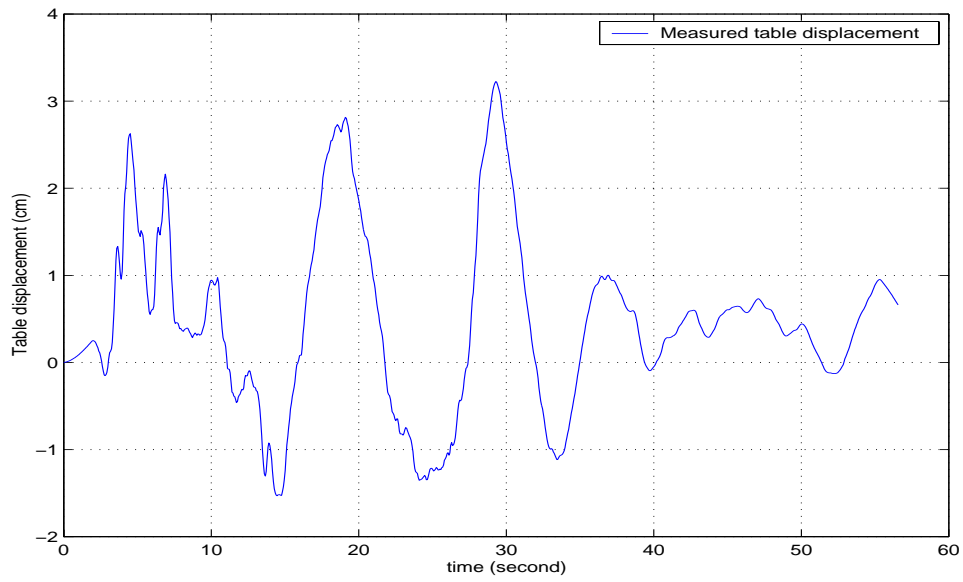


Figure 8.7 Displacement command for El Centro earthquake ground acceleration

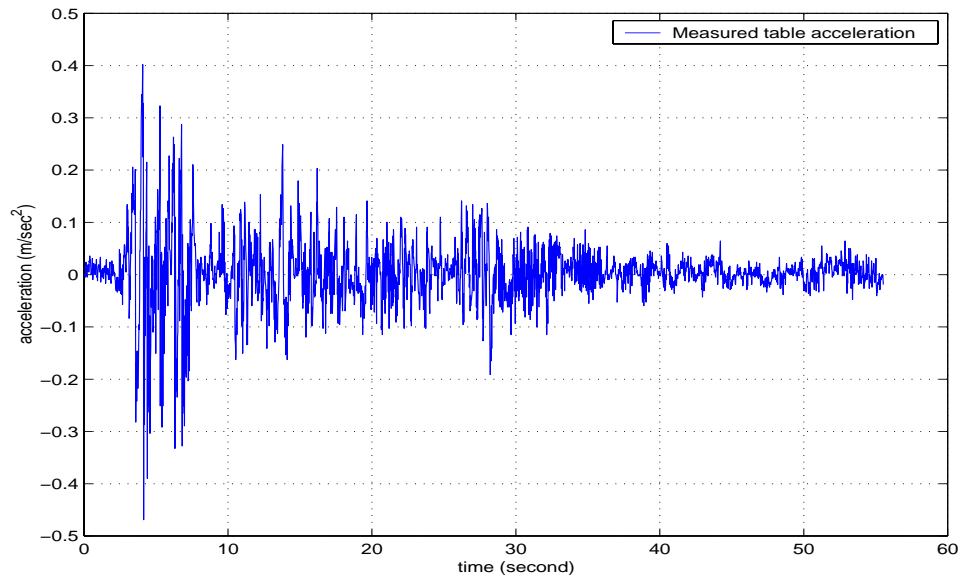


Figure 8.8 Measured shaking table acceleration simulating the 10% scaled El Centro earthquake using inverse transfer function

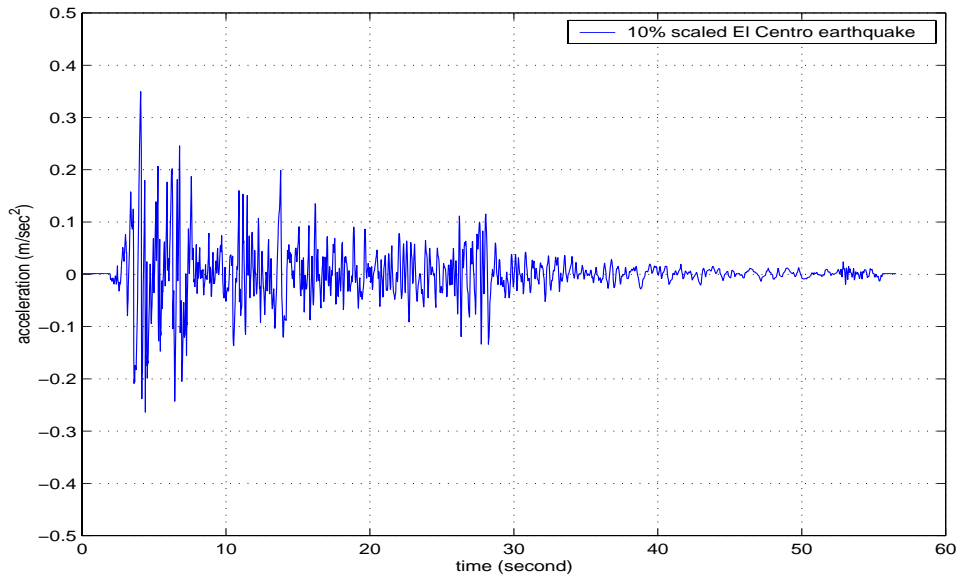


Figure 8.9 The 10% scaled El Centro earthquake (target)

In order to increase the tracking accuracy of the shaking table, a transfer function iteration approach (Spencer and Yang, 1998), which is based on the inverse transfer function method, is used. The iteration is employed because the shaking table is not a completely linear system. According to the transfer function iteration an initial command signal is first calculated as a fraction of the command signal. After the initial command signal is sent to the shaking table, the response can be measured. Then the error signal is obtained to generate the differential signal. The sum of weighted initial command and the differential signal makes up the updated command signal to the shaking table. This process is repeated until the satisfactory result is achieved. Figure 8.10 describes the transfer function iteration procedure.

Figure 8.11 shows the scaled El Centro earthquake acceleration record (dashed line) and the measured acceleration of the shaking table (solid line). The RMS value of the scaled El Centro is 0.062 and the RMS value of the measured acceleration of shaking table

is 0.064. Using this scheme, the difference is only 3%, which is much smaller than that of the inverse transfer function approach.

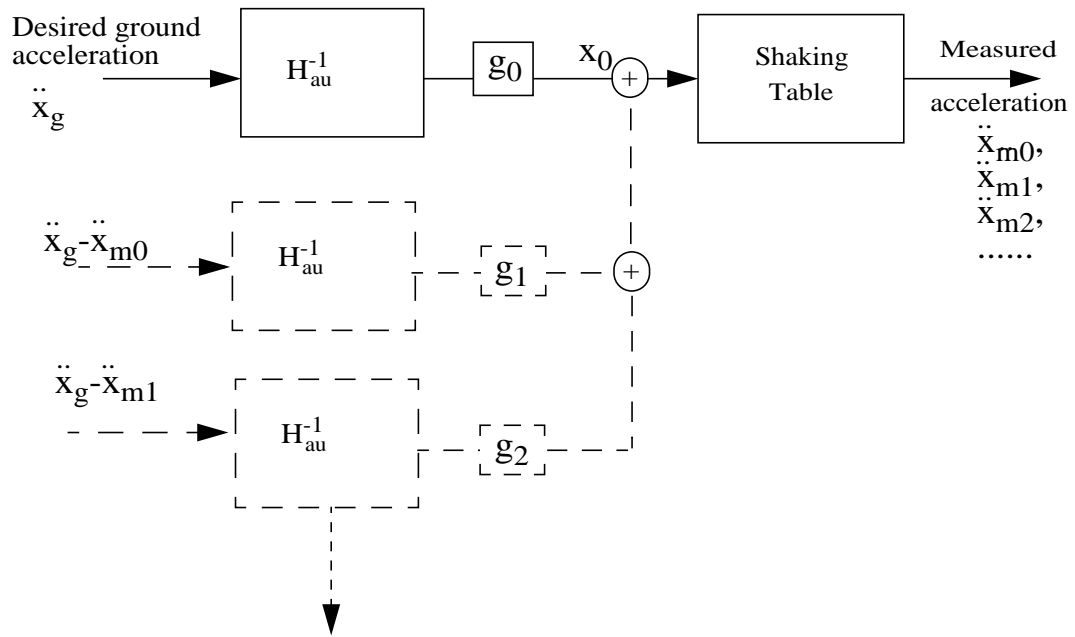


Figure 8.10 Diagram for shaking table design using transfer function iteration

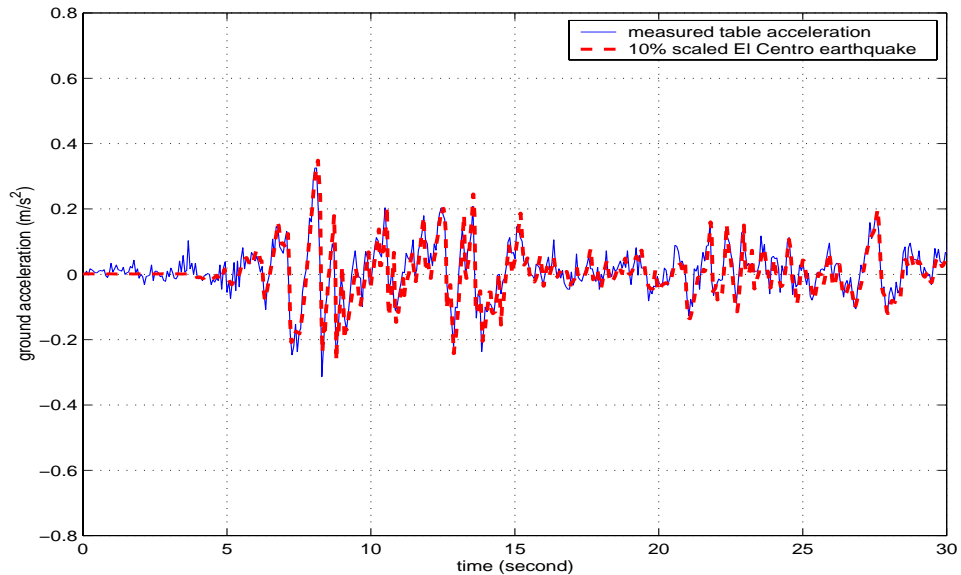


Figure 8.11 10% scaled El Centro earthquake signal and Simulated El Centro earthquake ground acceleration using transfer function iteration

8.3 System Identification

An important dynamic feature in structural control problems concerns control-structure interaction (CSI), which is often neglected by most researchers. Dyke et al. (1995) noted that CSI is a critical factor in design and application of high performance controllers. For the flexible building used in our experiments, AMD is set up on the top of the building which has its own dynamic features (Battaini et al. 2000). A PID controller is designed to drive the AMD to the desired positions. Therefore, it is important that the dynamics of this PID close-loop controller are taken into consideration. The entire system consists of the AMD, building and AMD-building interaction as displayed in Fig. 8.12.

To obtain an accurate mathematical model for this system, the input-output responses are measured and used in system identification. This input-output model has been shown to be effective for the design of high performance controllers that include control-structure interaction (Dyke et al, 1995; Battaini et al, 2000).

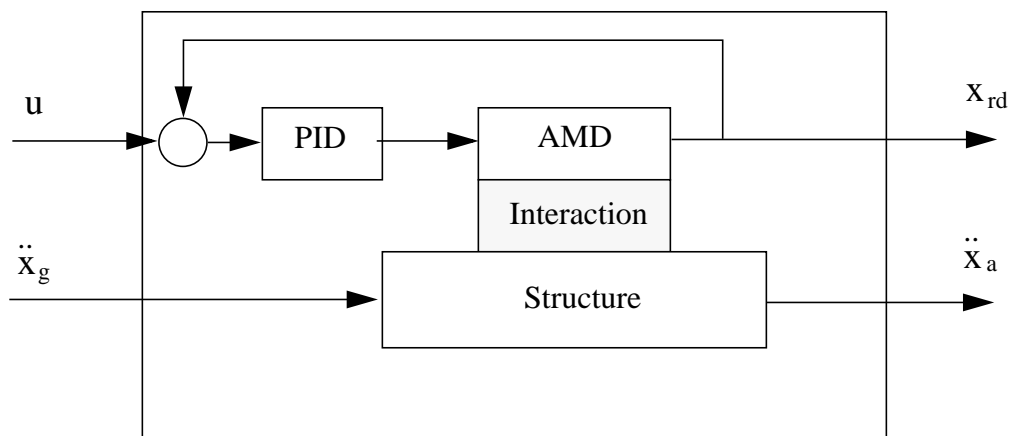


Figure 8.12 Diagram of AMD, Structure and AMD-Structure interaction as a whole system

The transfer functions from the system's inputs to outputs are experimentally determined as shown in Fig. 8.12. The two inputs include the ground acceleration \ddot{x}_g and the command signal u . The outputs are the measured acceleration of the structure \ddot{x}_a and the relative displacement of AMD with respect to the top floor. The number of measured acceleration outputs depends on the number of accelerometers installed. For this 2-DOF building, accelerometers are placed at each floor for acceleration measurements. Therefore, the transfer function for the system is described by a 2×3 matrix.

The Siglab's Spectrum analyzer is utilized to obtain the experimental transfer functions. Each of the transfer function is curve-fitted and modeled by a Laplace function in the following form.

$$H(s) = \frac{N(s)}{D(s)} \quad (8-2)$$

where s is Laplace variable and $s = i\omega$; ω is frequency; $N(s)$ is the numerator polynomial; and $D(s)$ is the denominator polynomial. This system is a multi-input and multi-output system (MIMO). As a result, the MIMO state space realization is needed for the transformation from the Laplace formed transfer function to the state space representation. This realization process is accomplished by curve-fitting (Dyke, 1996), left matrix fraction, and eigen-system realization algorithm (Juang, 1994) as explained below.

The first step to get the analytical state space representation of the system from the experimentally obtained transfer function is curve-fitting. A Matlab function *invfreq* is used to curve-fit each individual term of the transfer function matrix $H(s)$. For the MIMO system, two separate systems are first formed as a result of two inputs. Each of these corresponds to a single-input-multi-output system. Subsequently, both are realized in a state-

space representation and are stacked together to frame the state-space representation of the MIMO system. However, both sub-systems contain some common dynamic features of the structure, thus, simply stacking these together introduces redundancy in this regard. Therefore, the following scheme is introduced to arrive at the needed minimal realization of the system.

Once curve-fitting is completed, the left matrix-fraction method is used to obtain the Markov parameters, which are commonly used as the basis for identifying mathematical models for linear dynamic systems (Juang, 1994). The Markov parameters, Y_k , are defined as:

$$Y_0 = D, \quad Y_1 = CB, \quad Y_2 = CAB, \dots, \quad Y_k = CA^{k-1}B \quad (8-3)$$

where A , B , and C are matrices for the state space representation. The left matrix-fraction assumes that the transfer function matrix can be expressed as:

$$H(s) = Q^{-1}(s)R(s), \quad (8-4)$$

where $Q(s)$ and $R(s)$ are polynomials with matrix coefficients.

$$Q(s) = I_m + Q_1s^{-1} + \dots + Q_p s^{-p}, \quad (8-5)$$

$$R(s) = R_0 + R_1s^{-1} + \dots + R_p s^{-p} \quad (8-6)$$

By multiplying $Q(s)$ on both sides of Eq. (8-4) and re-arranging

$$H(s) = -Q_1H(s)s^{-1} - \dots - Q_pH(s)s^{-p} + R_0 + R_1s^{-1} + \dots + R_p s^{-p}. \quad (8-7)$$

With $H(s)$, Eq. (8-7) becomes a linear equation. $H(s_k)$ is obtained from the curve-fitting model when $s_k = j\omega_k$ ($k = 0, \dots, n-1$). Now, there are n linear equations available. This yields,

$$\Pi = \Theta\Omega \quad (8-8)$$

where

$$\Omega = \begin{bmatrix} H(s_0)s_0^{-1} & H(s_1)s_1^{-1} & \dots & H(s_{n-1})s_{n-1}^{-1} \\ \dots & \dots & \dots & \dots \\ H(s_0)s_0^{-p} & H(s_1)s_1^{-p} & \dots & H(s_{n-1})s_{n-1}^{-p} \\ I_m & I_m & \dots & I_m \\ s_0^{-1}I_m & s_1^{-1}I_m & \dots & s_{n-1}^{-1}I_m \\ \dots & \dots & \dots & \dots \\ s_0^{-p}I_m & s_1^{-p}I_m & \dots & s_{n-1}^{-p}I_m \end{bmatrix} \quad (8-9)$$

$$\Theta = \begin{bmatrix} -Q_1 & \dots & -Q_p & R_0 & \dots & R_p \end{bmatrix} \quad (8-10)$$

$$\Pi = \begin{bmatrix} H(s_0) & H(s_1) & \dots & H(s_{n-1}) \end{bmatrix} \quad (8-11)$$

Eq. (8-8) is a linear algebraic equation from which an estimated real value of Θ can be obtained by:

$$\tilde{\Theta} = \begin{bmatrix} \text{real}(\Pi) \\ \text{imag}(\Pi) \end{bmatrix} \begin{bmatrix} \text{real}(\Omega) \\ \text{imag}(\Omega) \end{bmatrix}^{\perp} \quad (8-12)$$

where \perp denotes pseudo-inverse and $\tilde{}$ indicates the estimated value.

By comparing similar terms, Q_i and R_i ($i = 0, \dots, p$) can be obtained from $\tilde{\Theta}$. It is known that

$$H(s) = Y_0 + Y_1s^{-1} + Y_2s^{-2} + \dots \quad (8-13)$$

Eq. (8-4) can be written as:

$$\left(\sum_{i=0}^p Q_i s^{-i} \right) \left(\sum_{i=0}^{\infty} Y_i s^{-i} \right) = \sum_{i=0}^p R_i s^{-i} \quad (8-14)$$

Therefore, the Markov parameters can be obtained as:

$$Y_0 = D = R_0 \quad (8-15)$$

$$Y_k = R_k - \sum_{i=1}^k Q_i Y_{k-i}, \quad k = 1, \dots, p \quad (8-16)$$

$$Y_k = - \sum_{i=1}^p Q_i Y_{k-i}, \quad k = p+1, \dots, \infty \quad (8-17)$$

In order to obtain a minimal state-space realization of the transfer function matrix, eigen-system realization algorithm (ERA) is applied here (Juang, 1994). Hankel matrices T and \hat{T} are defined as:

$$T = \begin{bmatrix} Y_1 & \dots & Y_r \\ \dots & \dots & \dots \\ Y_r & \dots & Y_{2r-1} \end{bmatrix}, \quad \hat{T} = \begin{bmatrix} Y_2 & \dots & Y_{r+1} \\ \dots & \dots & \dots \\ Y_{r+1} & \dots & Y_{2r} \end{bmatrix} \quad (8-18)$$

where r is the degree of the least common denominator of all nonzero entries of the $l \times m$ matrix $H(s)$. Then using singular value decomposition, T is written as:

$$T = K \begin{bmatrix} \Sigma & 0 \\ 0 & 0 \end{bmatrix} L = K_1 \Sigma L_1 = (K_1 \Sigma^{1/2})(\Sigma^{1/2} L_1) = VU \quad (8-19)$$

where $\Sigma = \text{diag}(\lambda_1, \dots, \lambda_q)$ are the singular value matrix of T , K_1 denotes the first q columns of K , L_1 denotes the first q rows of L , $K_1^T K_1 = I_q$, and $L_1 L_1^T = I_q$. Let V^\perp and U^\perp denote pseudo-inverses of V and U as:

$$V^\perp = \Sigma^{-1/2} K_1^T, U^\perp = L_1^T \Sigma^{-1/2} \quad (8-20)$$

Accordingly, the state space matrices of the system can be obtained as:

$$A = V^\perp \hat{T} U^\perp, B = U I_{m, mr}^T, C = I_{l, lr} V, D = Y_0 \quad (8-21)$$

Here B is defined as the first m columns of U , and C is defined as the first l rows of V which yields a minimal realization of $H(s)$ (Antsaklis and Michel, 1997).

An expression for the transfer function can be obtained from $H(s) = C(sI - A)^{-1}B + D$. The experimental (dashed lines) and analytical (solid lines) transfer functions are shown in Figs. 8.13-8.16. Figure 8.13 shows the transfer function from the ground acceleration to the second floor acceleration. Figure 8.14 shows the transfer function from the ground acceleration to the first floor acceleration. The transfer function from the actuator command to the second floor acceleration is displayed in Fig. 8.15. In Fig. 8.16, the transfer function from the actuator command to the relative displacement of AMD is plotted. All these figures show that the structural model obtained using preceding approach agrees well with the experimental data.

The final state space realization including the structure and AMD is expressed as:

$$\dot{x} = Ax + Bu + E\ddot{x}_g \quad (8-22)$$

$$y = Cx + Du + F\ddot{x}_g + v \quad (8-23)$$

where x is the state vector of the system; $y = [\ddot{x}_{a2} \ddot{x}_{a1} x_{rd}]^T$, which is the vector of measured responses; matrices A , B , C , D , E , and F are the realized state space matrices, and v is the noise in the measured signals.

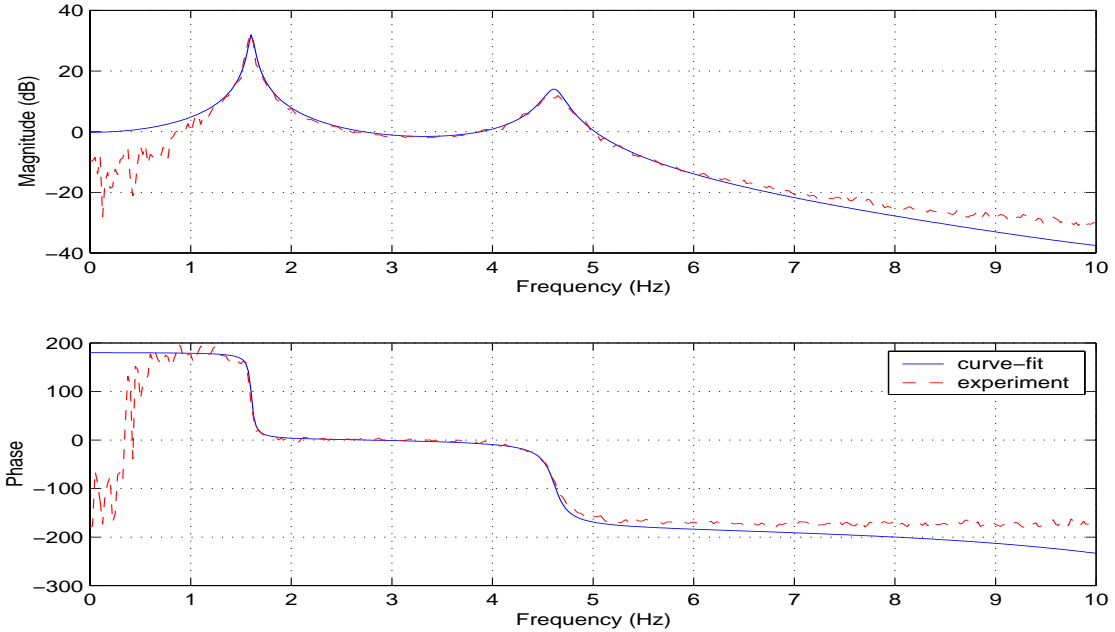


Figure 8.13 Transfer function from ground acceleration to the second floor acceleration

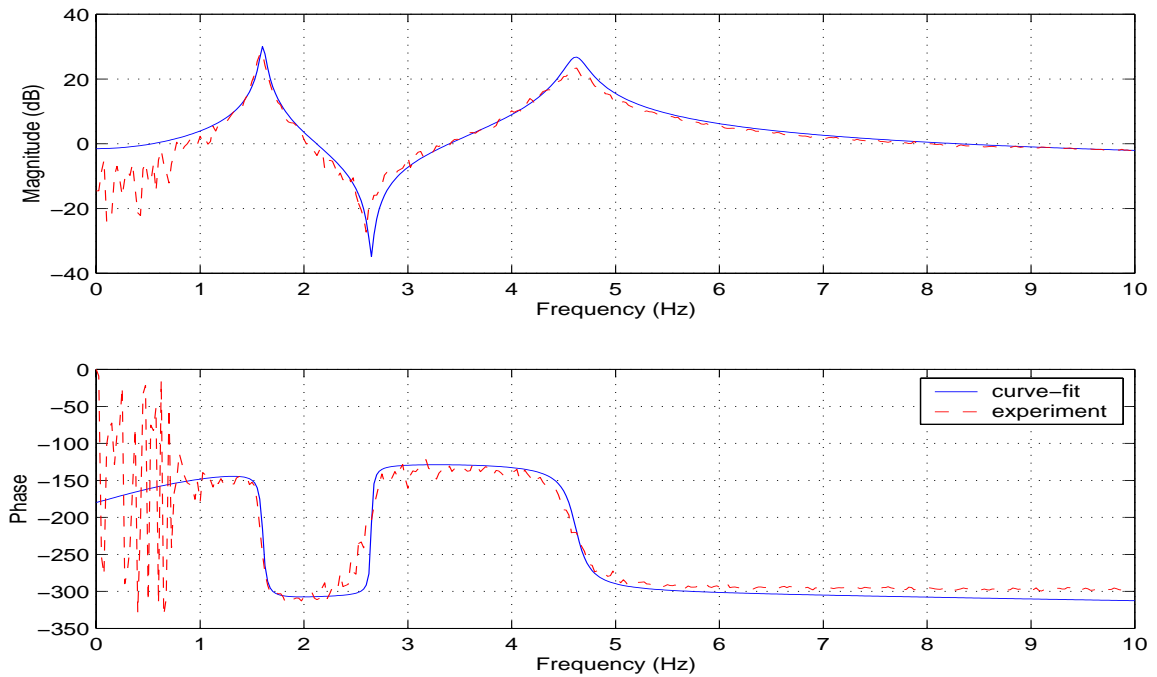


Figure 8.14 Transfer function from ground acceleration to the first floor acceleration

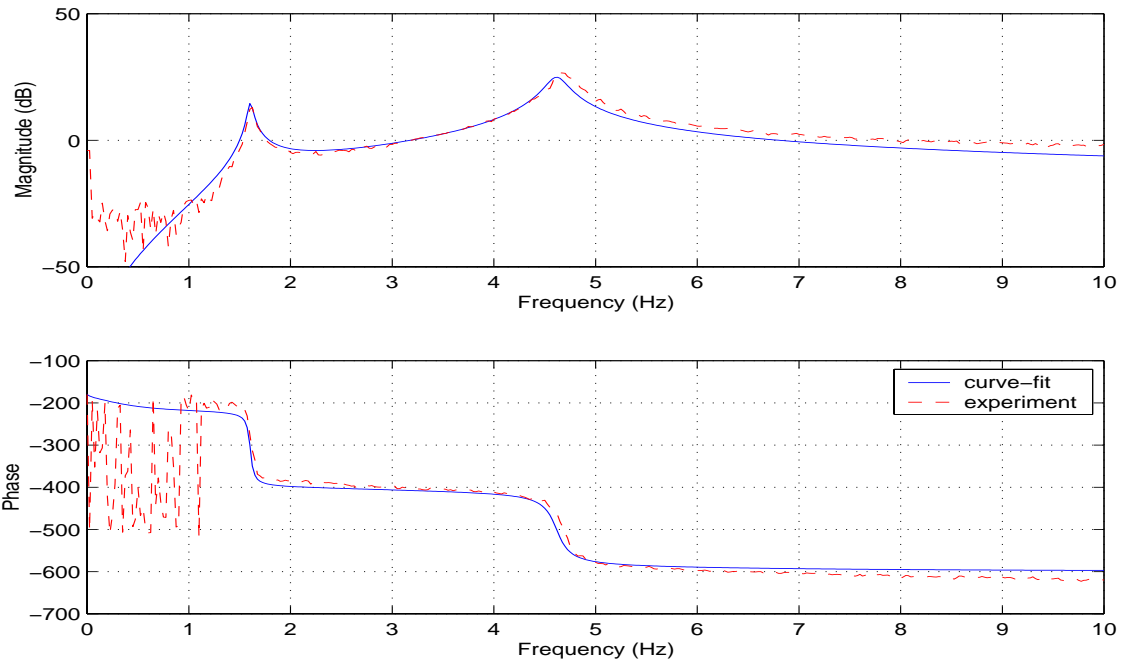


Figure 8.15 Transfer function from the AMD command to the second floor acceleration

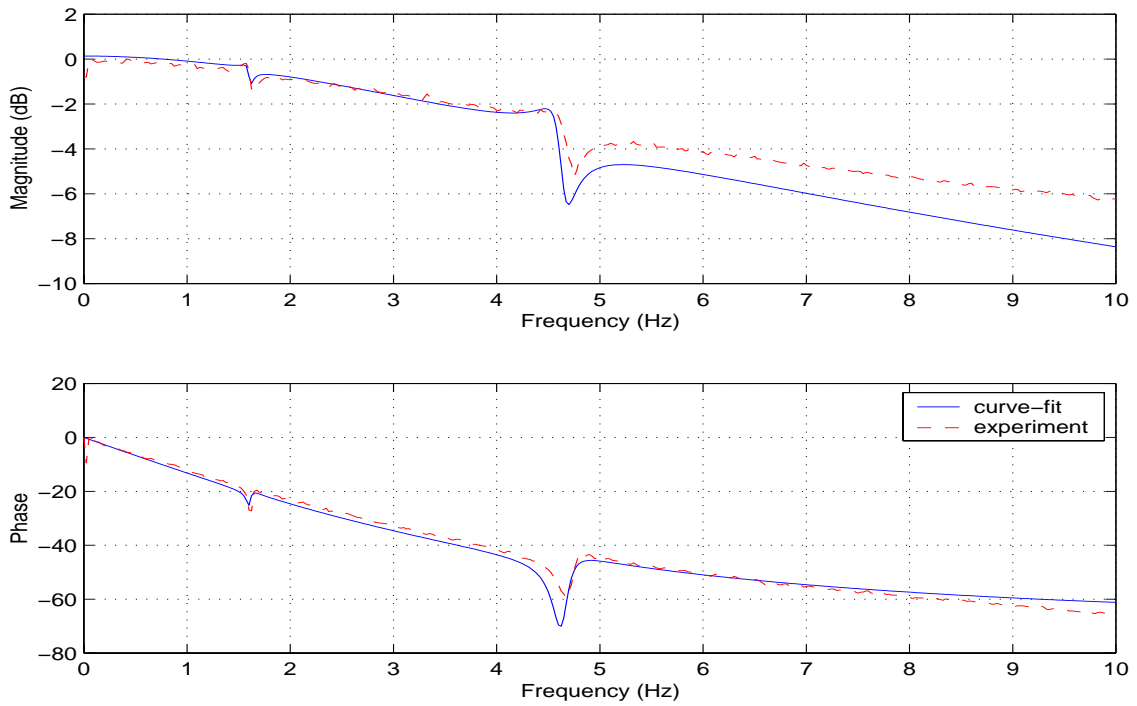


Figure 8.16 Transfer function from the AMD command to its displacement

8.4 MPC Using Acceleration Feedback

A control system is designed for the combined AMD and the structure system by using MPC scheme discussed in previous chapters. It is first modeled in Simulink, and then transformed to a C code by Quanser's WinCon software and Matlab's Real-Time Workshop. A MultiQ control board is used for finalizing the real-time control operations. The sampling time is fixed at 0.001 seconds using MultiQ board's digital timer.

The MPC based control scheme discussed in Chapter 5 is used in this experiment. First the transfer functions are measured in the frequency domain. Figure 8.17 shows the transfer function from the ground acceleration to the second floor acceleration. In Fig. 8.18, the transfer function from the ground acceleration to the first floor acceleration is presented. Three versions of transfer functions, i.e., uncontrolled, experimentally controlled, and simulation based controlled are displayed. As shown in these two figures, the response in first and second modes is greatly reduced and the simulated and experimental results show a good agreement.

In the following, typical time histories obtained experimentally are presented. The model building is subjected to the El Centro earthquake (10% scaled) with weighting matrices $Q = [1.8e6 \ 4e5 \ 0]$ and $R = 2e5$. Figure 8.19 shows the time histories of the uncontrolled and controlled second floor acceleration. The dashed and solid lines represent the response of the uncontrolled system and controlled system, respectively. Figure 8.20 compares the experimental and simulated acceleration of the second floor. Similarly, Fig. 8.21 displays experimental time histories of the first floor acceleration under El centro earthquake with and without control. Figure 8.22 compares experimental and simulated

acceleration of the first floor of the controlled system. The control forces generated in both the experiment study and the simulation by MPC are shown in Fig. 8.23.

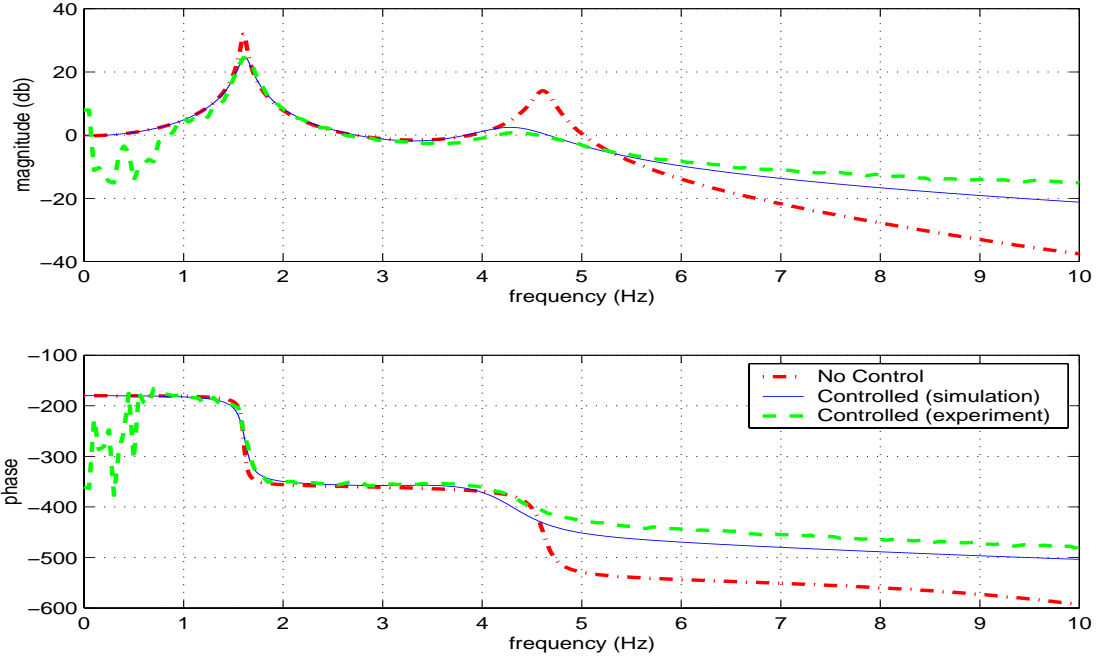


Figure 8.17 Transfer function from ground acceleration to the second floor acceleration

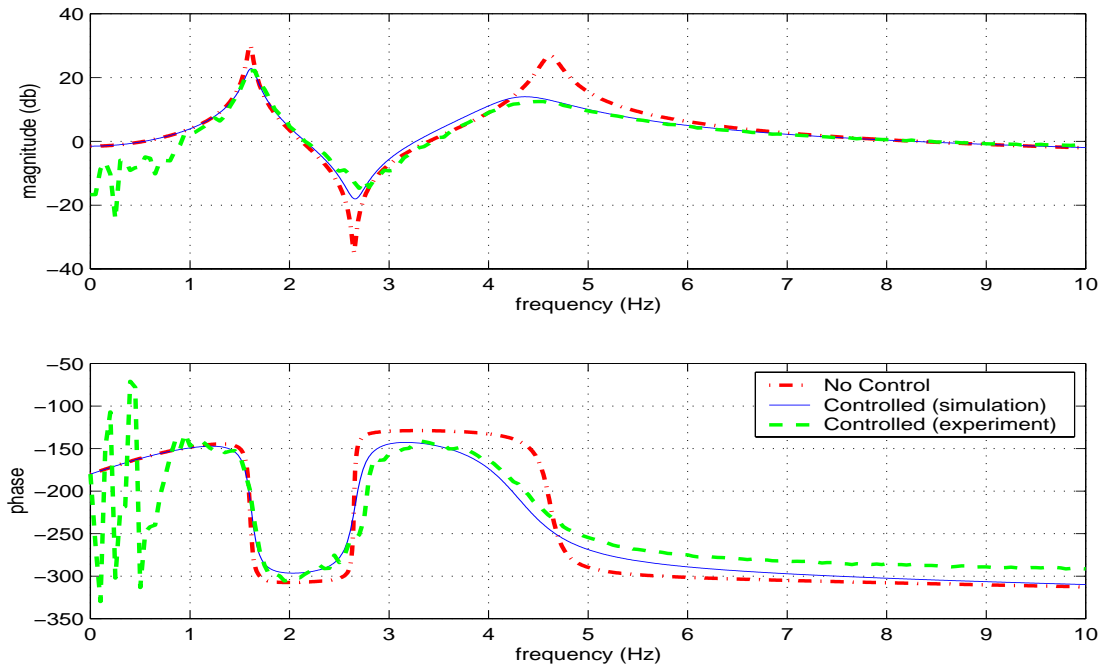


Figure 8.18 Transfer function from ground acceleration to the first floor acceleration

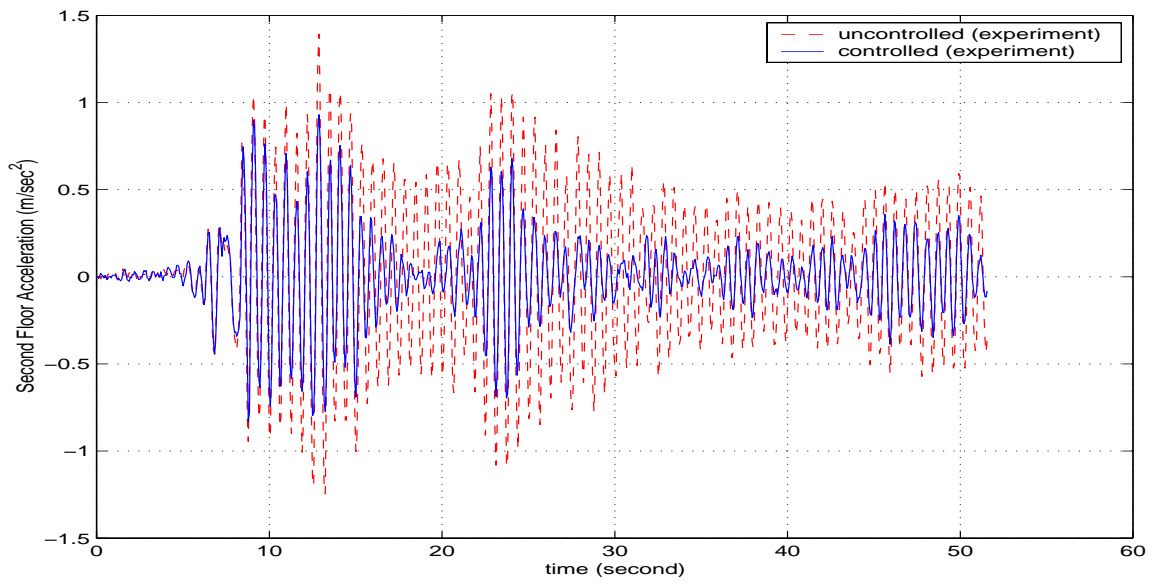


Figure 8.19 Comparison of uncontrolled and controlled second floor acceleration with acceleration FB ($R=2e5$)

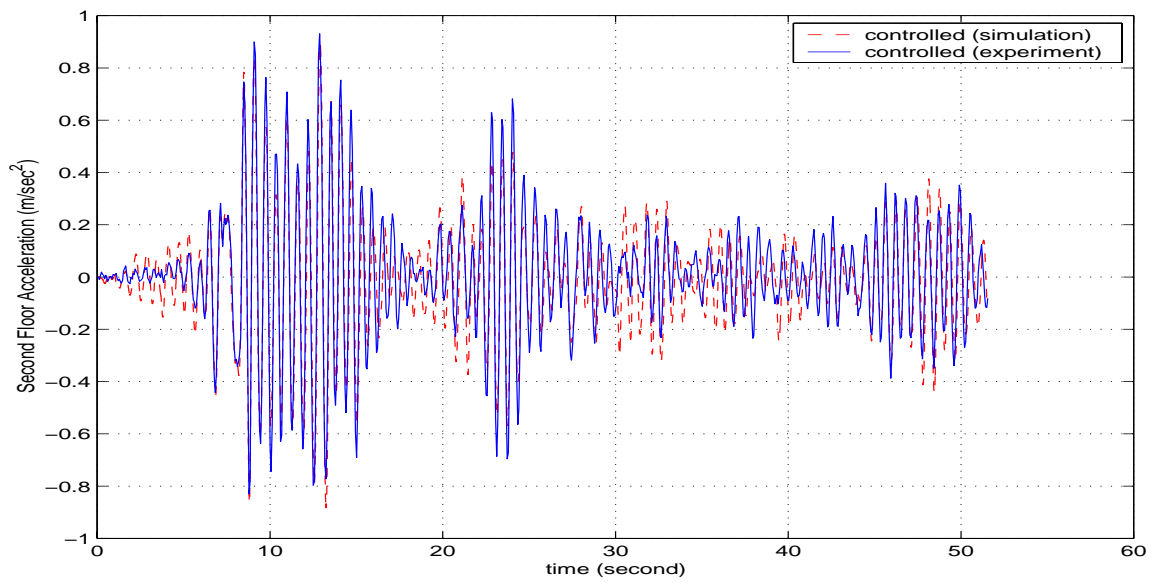


Figure 8.20 Controlled second floor acceleration with acceleration FB ($R=2e5$)

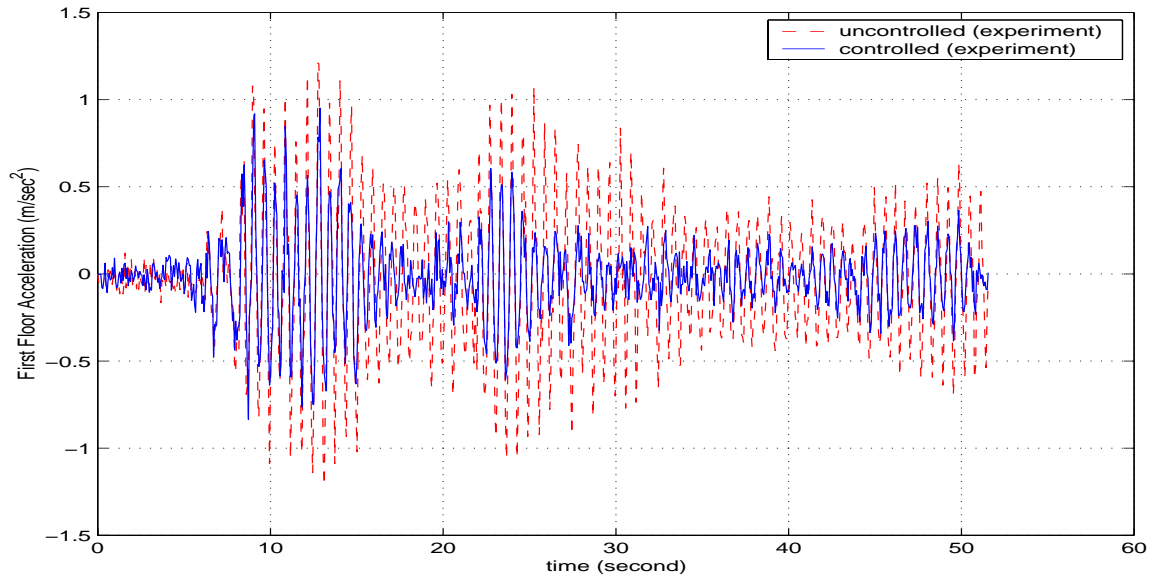


Figure 8.21 Comparison of uncontrolled and controlled first floor acceleration with acceleration FB ($R=2e5$)

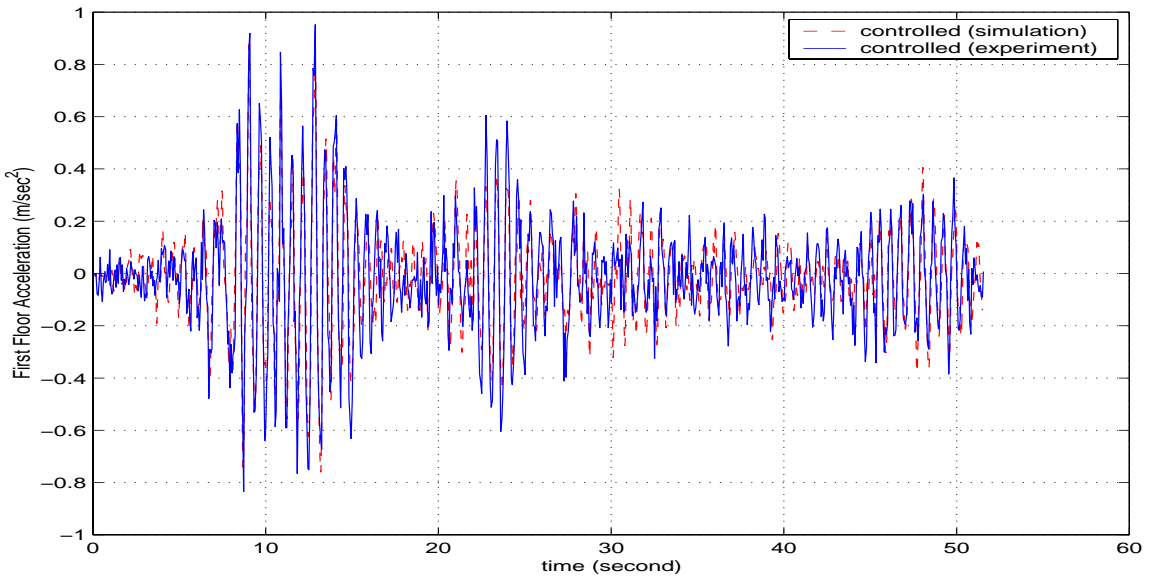


Figure 8.22 Controlled first floor acceleration with acceleration FB ($R=2e5$)

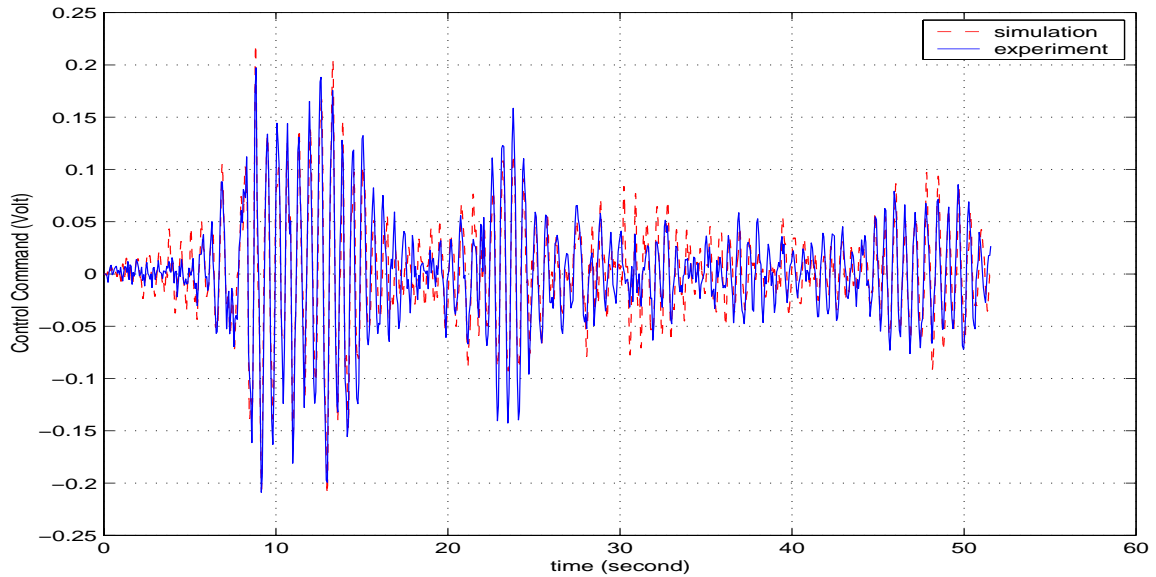


Figure 8.23 Control command of AMD. ($R=2e5$)

Table 8.1 summarizes the results presented in the preceding figures. The tabulated results include RMS and peak response of the uncontrolled system and controlled system based on experiments and simulation. As noted in Fig. 8.19, the experimentally measured second floor acceleration is significantly reduced. This is further supported by the data in Table 8.1. For the experimental data, when R is equal to 200000, the RMS value of the controlled response of the second floor acceleration is 0.241 m/s^2 , which is 43.9% lower than the uncontrolled case. Similarly, for the peak value, the reduction over uncontrolled case is 33.3%. Furthermore, the difference between the experimental control and the simulated control results can be observed from Figs. 8.20, 8.22 and 8.23 and verified in Table 8.1. The difference between these two is 8% for the RMS value and 3% for the peak value of the second floor acceleration response. As regards to the control command, the difference between the experiment and simulation is 10% for the RMS value and 5% for the peak value.

If the weighting of the control force is adjusted, a better control result can be obtained. In this case, the Q matrix remains the same, but R is changed from 200000 to 5000. Figures 8.24 displays the uncontrolled and controlled second floor acceleration responses. Figures 8.25 and 8.26 show the experimental and simulation results of the second floor acceleration and the control command, respectively. The RMS and peak values of accelerations and control command are listed in Table 8.1. For the second floor acceleration, the RMS response is reduced by over 66% and the peak response is reduced by over 48% in the experiment. The difference between the experimental and simulation results of the second floor acceleration is 14% for the RMS value and 5% for the peak value. The difference for the control command is 9.5% for the RMS value and 10.1% for the peak value.

The differences between the simulation and experimental results basically come from two sources. Firstly, there are some mismatches between the actual structure and the structural model used for control design. The cut-off frequency for the structural model is 10 Hz. As a result, the high-frequency structural properties are neglected. Furthermore, for frequencies lower than 0.5 Hz, the structural model is contaminated by noise because accelerometers used in this study cannot provide accurate measurement at very low frequencies. Secondly, it is assumed that, for the simulation model, there is no noise from control operation and acceleration feedback. However, during experiments all kinds of unpredictable disturbance such as loose connections, friction and cable vibrations can occur, which can negatively impact the experimental results.

Table 8.1 Structure Acceleration Response

		$\sigma_{\ddot{x}_{a2}}$ (m/s ²)	$\sigma_{\ddot{x}_{a1}}$ (m/s ²)	σ_u (Volt)	$\max(\ddot{x}_{a2})$ (m/s ²)	$\max(\ddot{x}_{a1})$ (m/s ²)	$\max(u)$ (Volt)
	Uncontrolled	0.429	0.378		1.397	1.211	
R=2e5	experiment	0.241	0.219	0.052	0.931	0.952	0.220
	simulation	0.222	0.186	0.047	0.906	0.880	0.209
R=5e3	experiment	0.144	0.153	0.158	0.713	0.663	0.792
	simulation	0.124	0.111	0.143	0.679	0.674	0.791

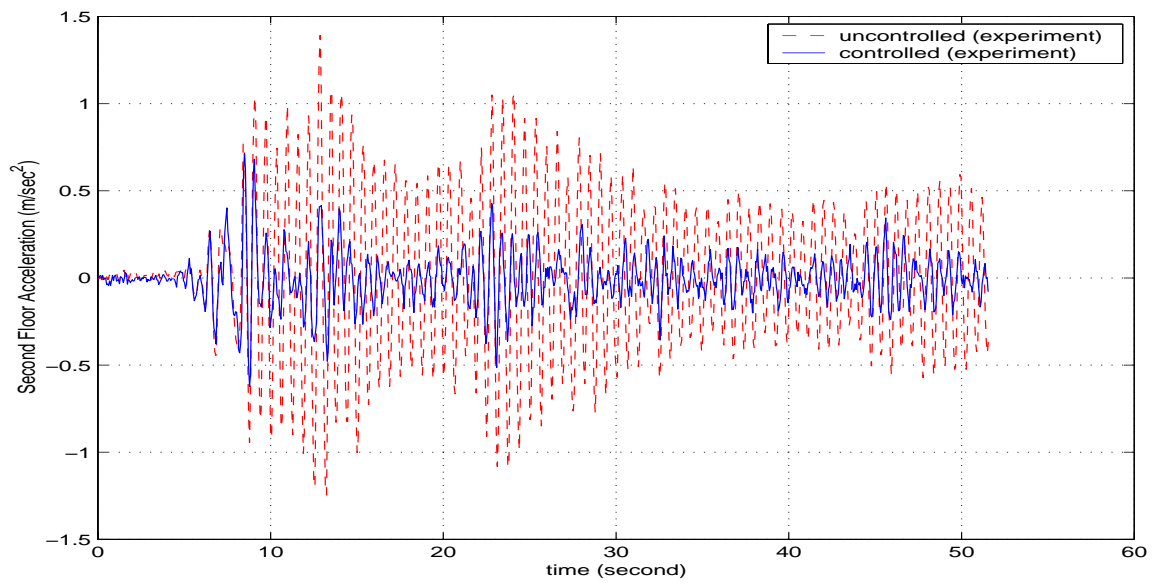


Figure 8.24 Comparison of uncontrolled and controlled second floor acceleration with acceleration FB (R=5000)

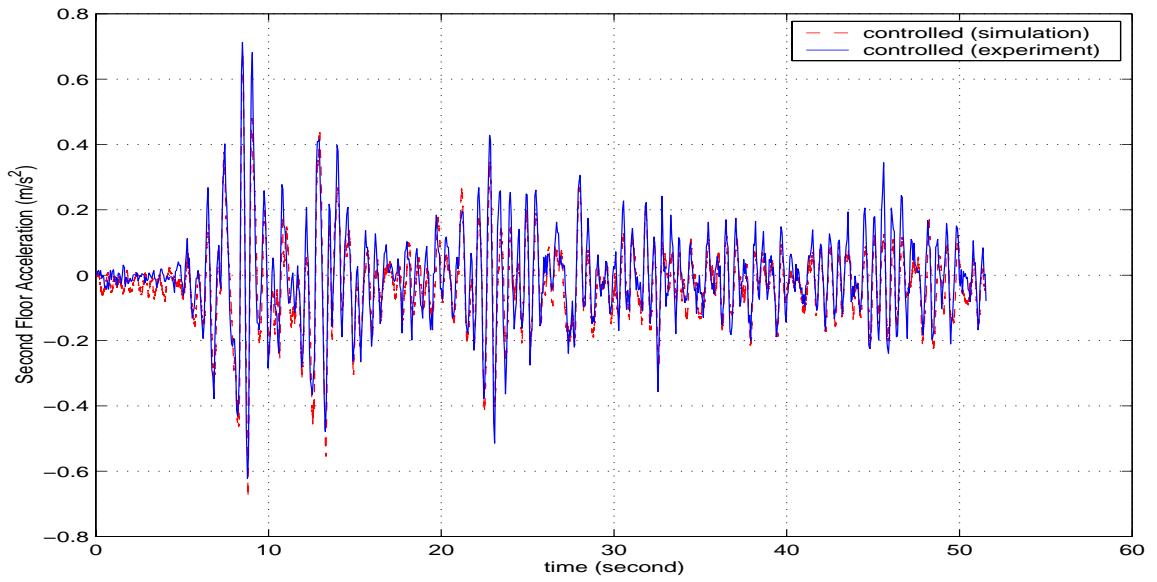


Figure 8.25 Controlled second floor acceleration with acceleration FB ($R=5000$)

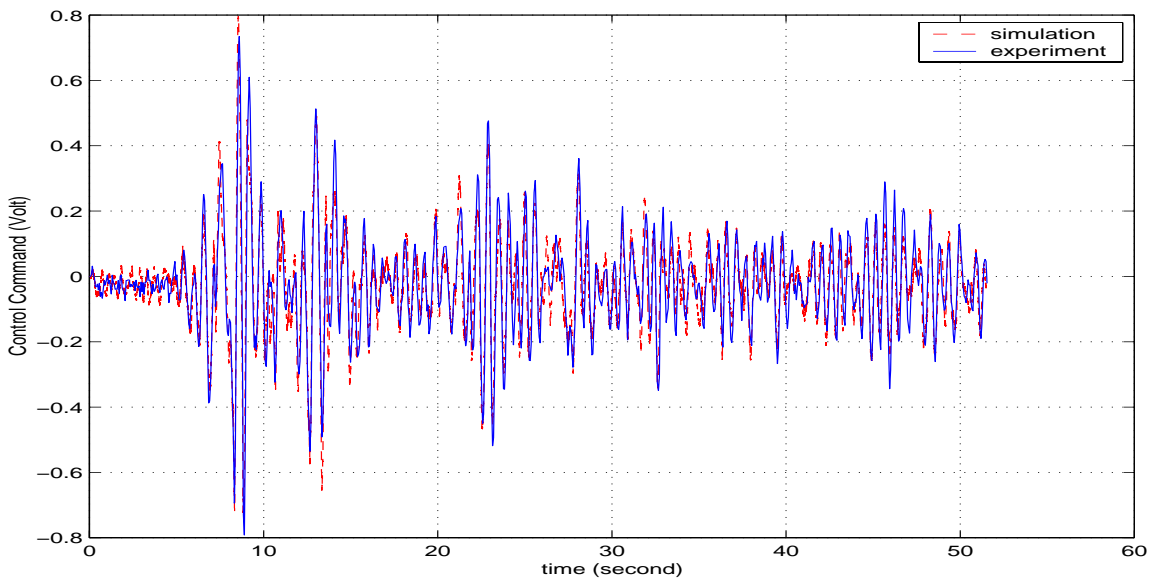


Figure 8.26 Control command of AMD. ($R=5000$)

8.5 Placement of Accelerometers

In the experiment, the number and locations of accelerometers are also varied to examine their effects on the control results. As mentioned before, each floor of the two-story building has one accelerometer attached. Three cases are considered. In case I, both accelerometer feedbacks are used. In case II, only the accelerometer on the first floor is used. In case III, only the second floor accelerometer is used in the observer design. The purpose of the experiment is to see which case can provide the best solution as well as to provide a simple simulation of the scenario where limited number of sensors are available.

Table 8.2 lists the acceleration responses and control command under these cases. As can be seen, Case I gives the smallest control response using the least control force. Case II, in which the accelerometer is attached to the first floor, delivers better performance than case III, in which the accelerometer is attached to the second floor. Table 8.2 also compares the experimental and simulation results. The differences between the simulated and experiment results are less than 15%. These results further reinforce the discussion in Section 5.4.1.2 and Section 5.4.2.2 of Chapter 5, i.e., feedback from the all-floor acceleration provides the best control effect, but if the number of accelerometers is limited, placing the accelerometer on the first floor is more effective than placing them at other locations.

Table 8.2 Structural Acceleration Response with Different Accelerometer Locations

	No control	Case I		Case II		Case III	
		exp.	sim.	exp.	sim.	exp.	sim.
$\sigma_{\ddot{x}_{a2}}$ (m/s ²)	0.429	0.214	0.181	0.214	0.189	0.215	0.207
σ_u (Volt)		0.075	0.064	0.075	0.066	0.075	0.072
$max(\ddot{x}_{a2})$ (cm/s ²)	1.397	0.840	0.754	0.869	0.845	0.924	1.010
$max(u)$ (Volt)		0.340	0.369	0.354	0.353	0.379	0.414

8.6 Feedforward-Feedback Control

In this section, the control performance of the MPC-AR scheme is investigated experimentally. As discussed in Chapter 6, MPC-AR scheme uses a real-time measurement of earthquake for the design of improved controllers. Such a scheme, as demonstrated in Chapter 6, is very robust for a host of different earthquakes with their own salient features. However, due to the limitations on both hardware and software, it is not easy to implement the scheme in real-time at this time. Therefore, to test the control effects of MPC-AR scheme, a simple method referred to here as the pseudo real-time MPC-AR scheme is proposed. Based on this method, the ground motion generated by the shaking table is measured first. Then the MPC-AR control scheme is designed and the simulation results are obtained on the computer. Consequently, the simulated control force is recorded and used directly in the AMD control command under the same ground motion excitation experimentally.

The experimental results under the pseudo-real-time MPC-AR method are shown in Figs. 8.27-8.29, where MPC and MPC-AR are compared. Table 8.3 provides a summary of the comparison. It is noted that the peak and RMS values of the control force under MPC-AR are 3% and 17.0% smaller than those under MPC scheme, respectively. In addition, the peak values of the second and first floor acceleration using the MPC-AR scheme are 15% and 16%, respectively, smaller than those under the MPC scheme. As far as the agreement between the experiment and simulation results is concerned, the peak values shows a better agreement than the RMS values. For example, for the second floor acceleration, the difference between the experiment and simulation is 13% for the RMS value and 8% for the peak value. For the MPC-AR scheme, the same control force is used in the experiment and simulation. These results demonstrate that, as a FF-FB control scheme, MPC-AR scheme can provide better control results than the MPC as noted in Chapter 6.

Table 8.3 Structure Acceleration Response under Scaled El Centro Earthquake (Pseudo Real-Time MPC-AR)

	$\sigma_{\ddot{x}_{a2}}$ (m/s ²)	$\sigma_{\ddot{x}_{a1}}$ (m/s ²)	σ_u (Volt)	$\max(\ddot{x}_{a2})$ (m/s ²)	$\max(\ddot{x}_{a1})$ (m/s ²)	$\max(u)$ (Volt)
Uncontrolled	0.429	0.378		1.397	1.211	
MPC (experiment)	0.181	0.191	0.098	0.850	0.860	0.493
MPC (simulation)	0.155	0.132	0.084	0.840	0.753	0.486
MPC-AR (experiment)	0.172	0.170	0.081	0.720	0.724	0.480
MPC-AR (simulation)	0.149	0.127	0.081	0.776	0.721	0.480

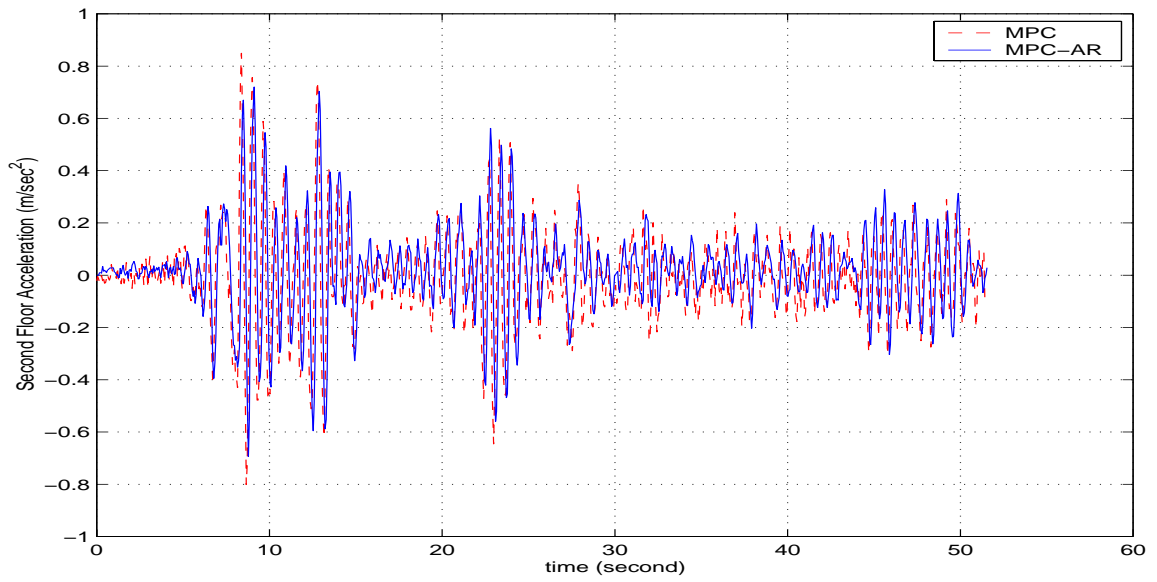


Figure 8.27 The second floor acceleration responses using MPC and MPC-AR schemes under scaled El Centro earthquake

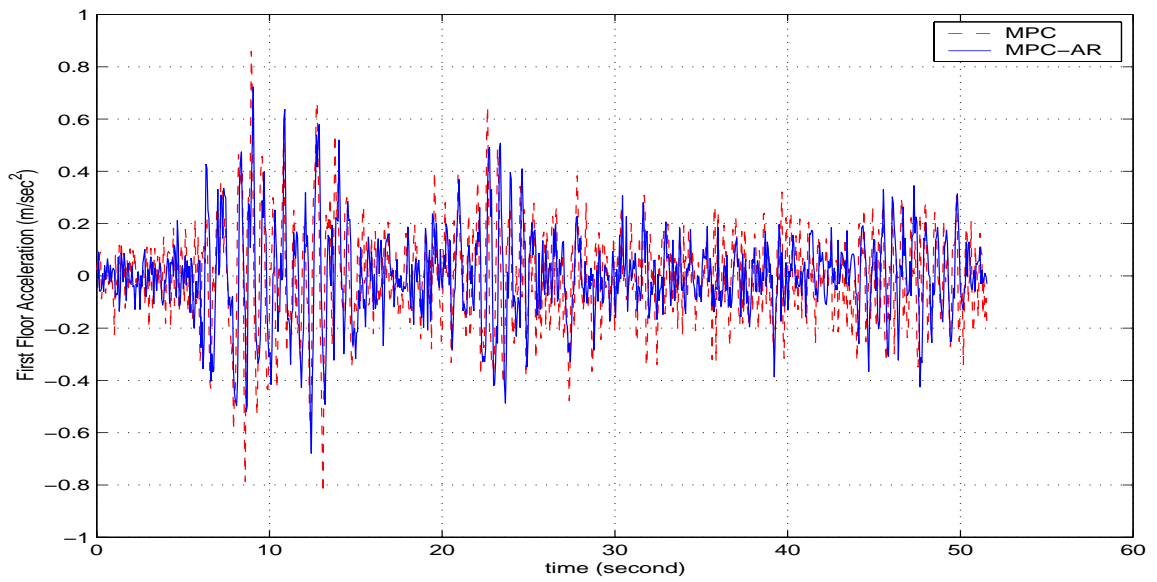


Figure 8.28 The first floor acceleration responses using MPC and MPC-AR schemes under scaled El Centro earthquake

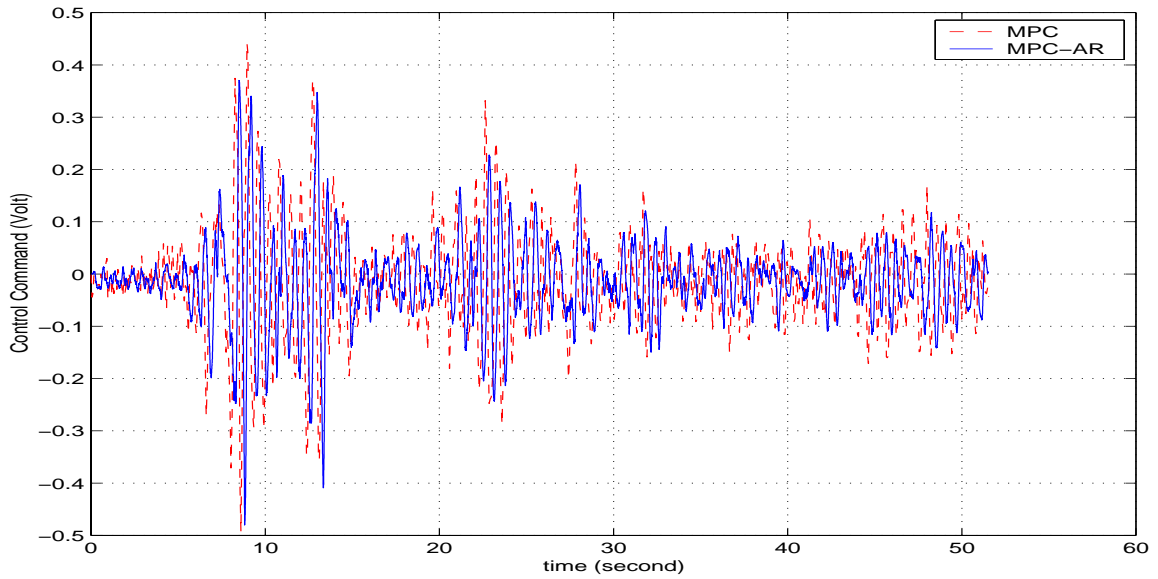


Figure 8.29 The control command using MPC and MPC-AR schemes under scaled El Centro earthquake

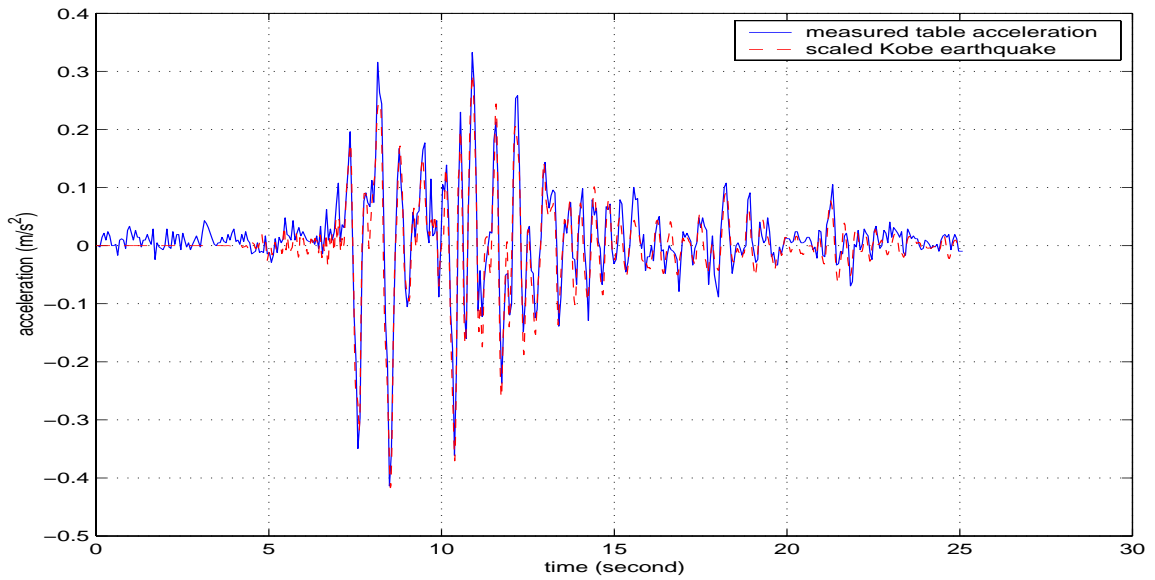


Figure 8.30 5% scaled Kobe earthquake signal and measured table acceleration

Another discussion in Chapter 6 is that MPC-AR can be used under different earthquakes. As signified in the above experiments, scaled El Centro earthquake is used. In the following experiment, the Kobe earthquake signal is applied to the shaking table as ground

motion. Figure 8.30 shows the 5% scaled record data and the measured acceleration from the shaking table. The peak measurement of the table acceleration is 0.4140 m/s^2 and RMS value is 0.0780 m/s^2 . The peak scaled Kobe earthquake is 0.4168 m/s^2 and RMS value is 0.0736 m/s^2 . The difference between the two is 1% for the peak value and 6% for the RMS value.

Table 8.4 shows a comparison of experimental and the simulation results under scaled Kobe earthquake. For the experiment, the maximum control force of the MPC-AR scheme is 8.5% smaller than that of the MPC scheme. The peak acceleration response of the second floor under the MPC-AR scheme is 8.7% smaller than that under MPC scheme. For the MPC-AR scheme, the difference between the experiment and simulation result of the second floor acceleration is 12% for the RMS value and 8% for the peak value. These show a relatively good agreement between the experiment and the computer simulation. More importantly, the results prove the MPC-AR scheme has the adaptive features that cater for the seismic events with unusual and unexpected characteristics.

Table 8.4 Structure Acceleration Response under Scaled Kobe Earthquake (Pseudo Real-Time MPC-AR)

	$\sigma_{\ddot{x}_{a2}}$ (m/s^2)	$\sigma_{\ddot{x}_{a1}}$ (m/s^2)	σ_u (Volt)	$\max(\ddot{x}_{a2})$ (m/s^2)	$\max(\ddot{x}_{a1})$ (m/s^2)	$\max(u)$ (Volt)
Uncontrolled	0.3735	0.3473		1.3783	1.510	
MPC (experiment)	0.223	0.204	0.222	0.960	0.902	0.954
MPC (simulation)	0.201	0.176	0.218	0.899	0.756	0.956
MPC-AR (experiment)	0.214	0.198	0.215	0.876	0.866	0.873
MPC-AR (simulation)	0.188	0.161	0.209	0.807	0.745	0.907

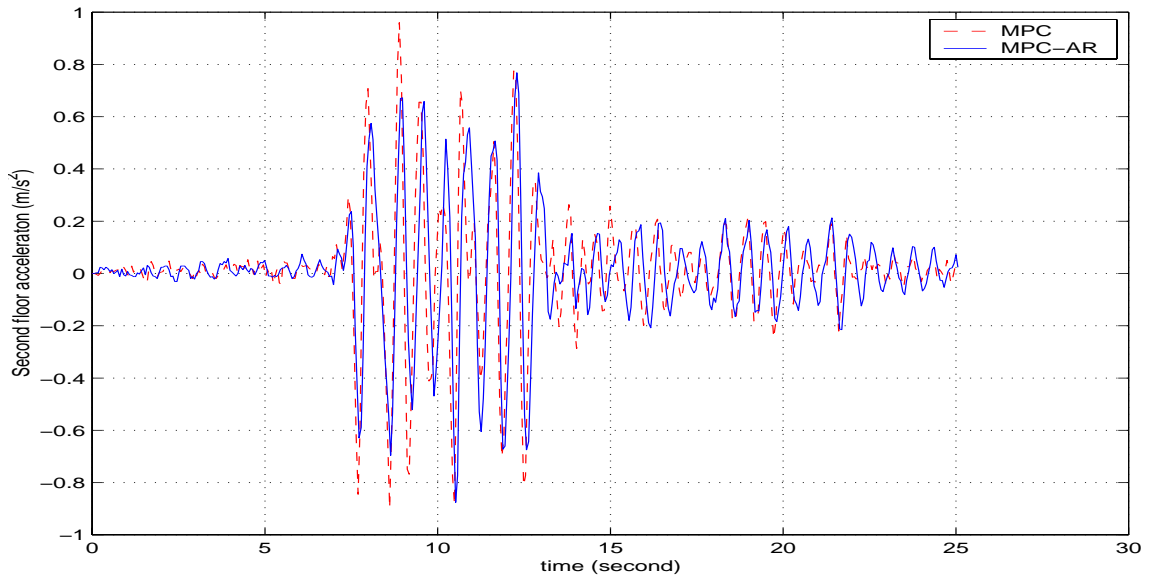


Figure 8.31 The second floor acceleration responses using MPC and MPC-AR schemes under scaled Kobe earthquake

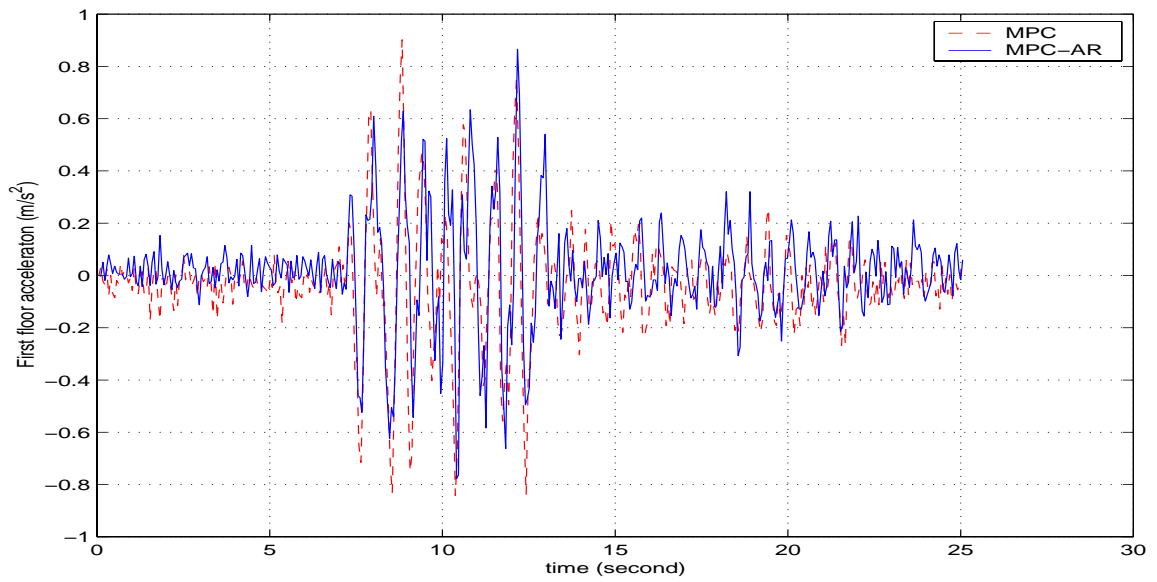


Figure 8.32 The first floor acceleration responses using MPC and MPC-AR schemes under scaled Kobe earthquake

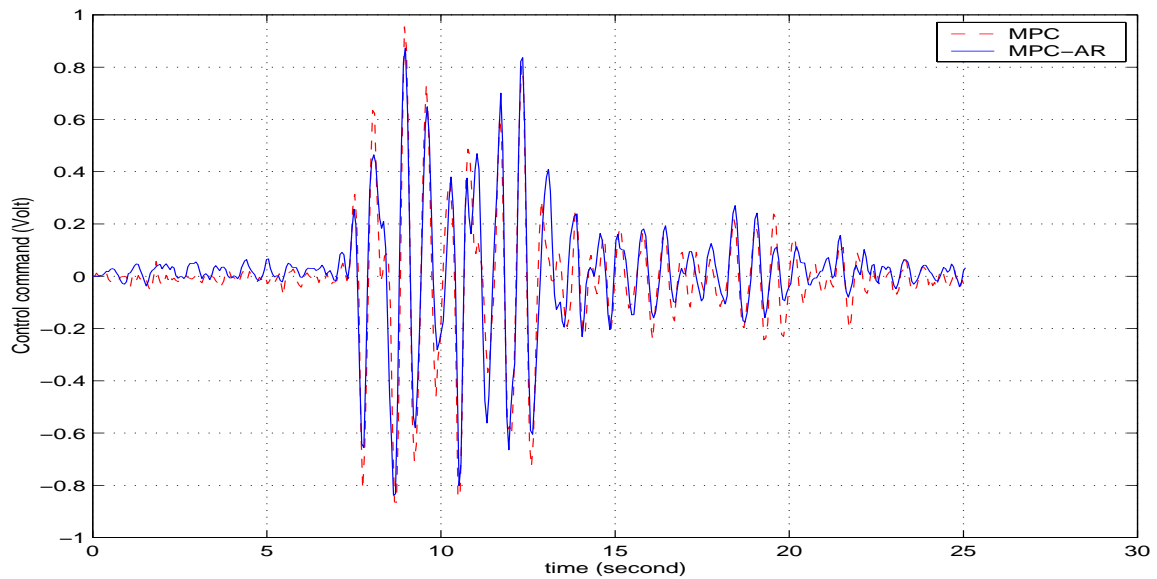


Figure 8.33 The control command using MPC and MPC-AR schemes under scaled Kobe earthquake

8.7 Constrained MPC Scheme

Having tested the MPC using acceleration feedback and MPC-AR scheme, this section is to verify the constrained MPC as discussed in Chapter 3. The pseudo control method is used to in the experiment. First, the constrained MPC is simulated on the computer using the approach presented in Chapter 3. Then the control force is recorded and used in the experiment to drive the AMD.

Two experiments are conducted to test the robustness of constrained MPC scheme under different seismic events. The first one uses the scaled El Centro earthquake as excitation and the maximum voltage of the control command is set to be 0.4 Volt. First the scaled El Centro earthquake is used as excitation. Figures. 8.34-8.36 show the acceleration response and the control command. In the second one, the scaled Kobe earthquake is used

as excitation and the maximum control command is limited to 0.6 Volts. Figures 8.37-8.39 compare the acceleration responses and control command under no control and under the constrained MPC scheme.

Table 8.5 compares the results of these two experiment with the simulation results. It appears that the experimental and simulation results are quite consistent with each other for both cases. The maximum control command remains within the required limits. Both experiments arrive at the same conclusion, i.e., the constrained MPC is quite effective in the reduction of the acceleration responses with its constrained control command.

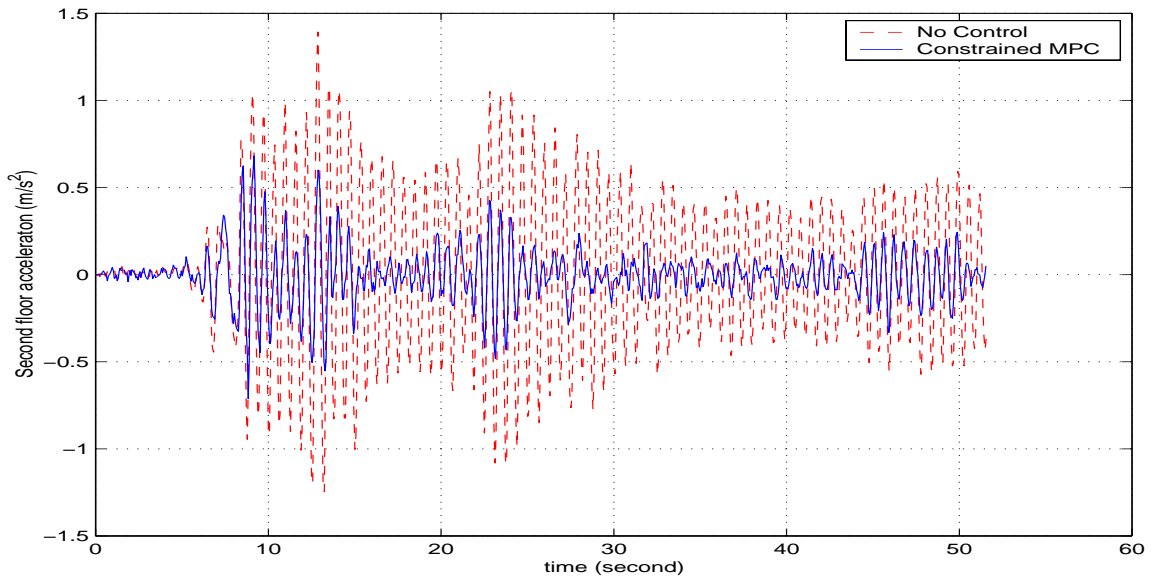


Figure 8.34 The second floor acceleration responses using constrained MPC scheme under scaled El Centro earthquake ($u \leq 0.4$)

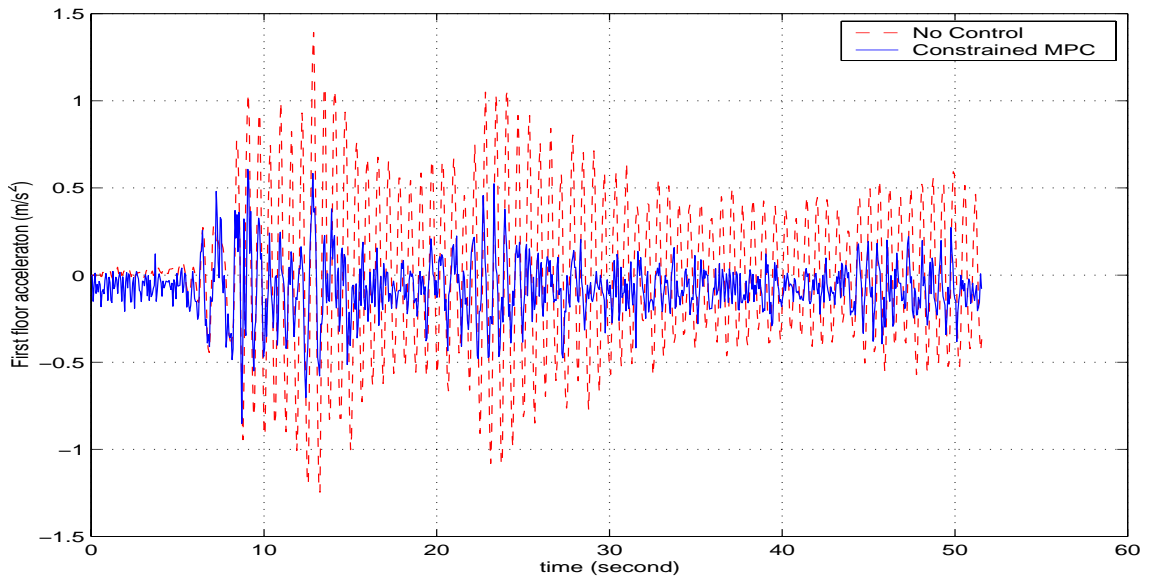


Figure 8.35 The first floor acceleration responses using constrained MPC scheme under scaled El Centro earthquake ($u \leq 0.4$)

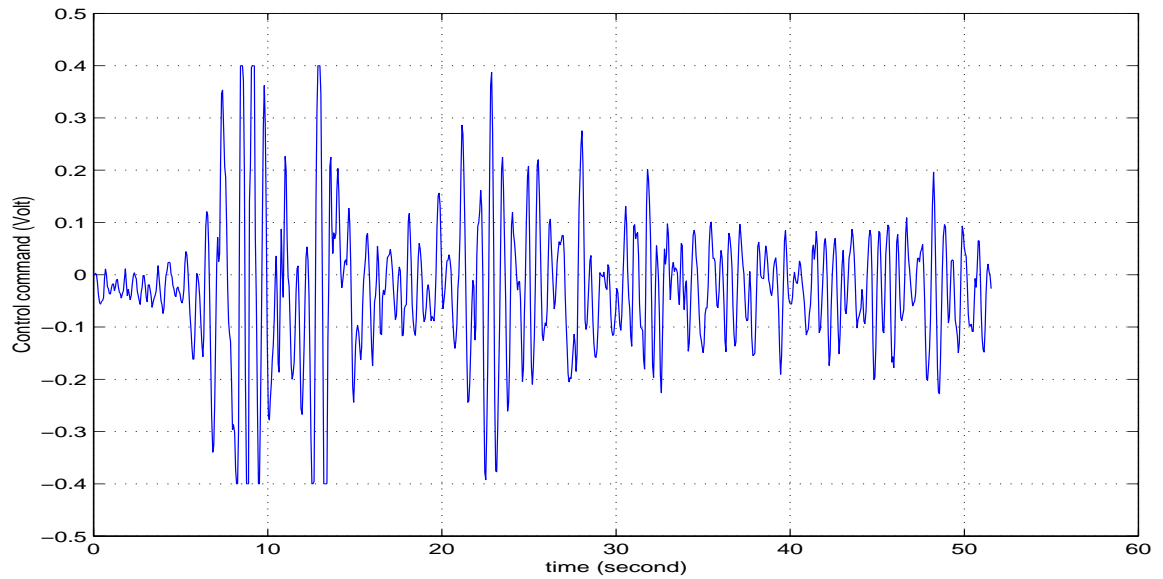


Figure 8.36 The control command using constrained MPC scheme under scaled El Centro earthquake ($u \leq 0.4$)

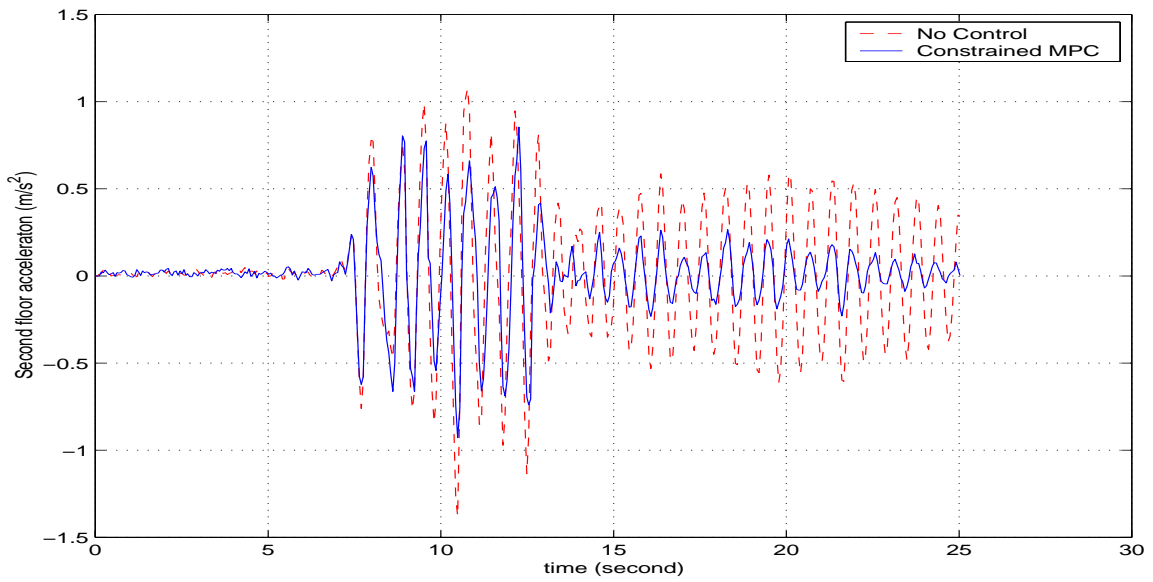


Figure 8.37 The second floor acceleration using constrained MPC scheme under scaled Kobe earthquake ($u \leq 0.6$)

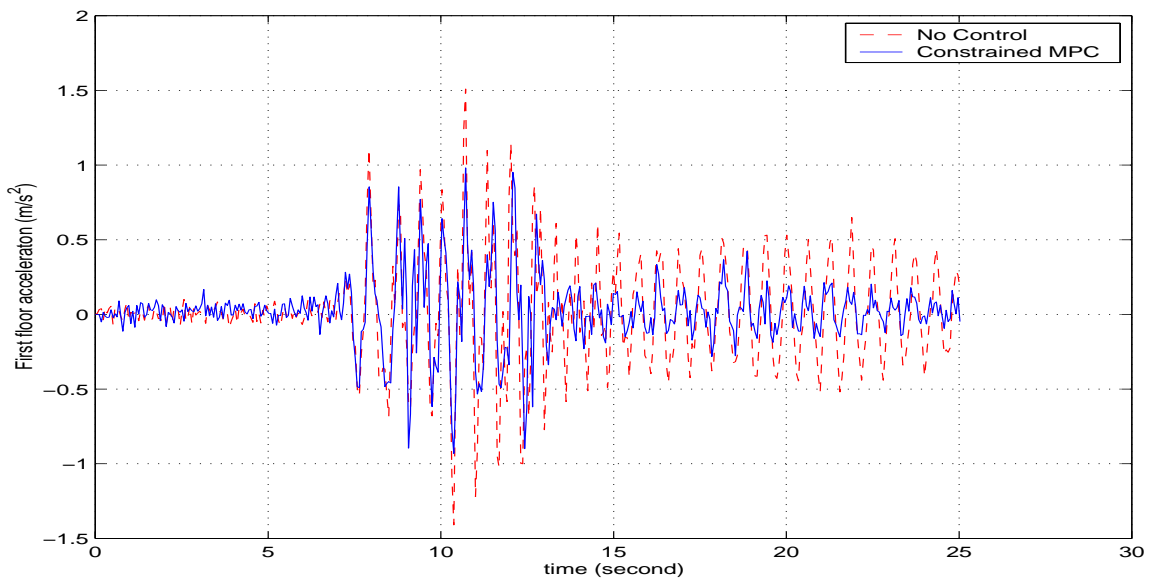


Figure 8.38 The first floor acceleration using constrained MPC scheme under scaled Kobe earthquake ($u \leq 0.6$)

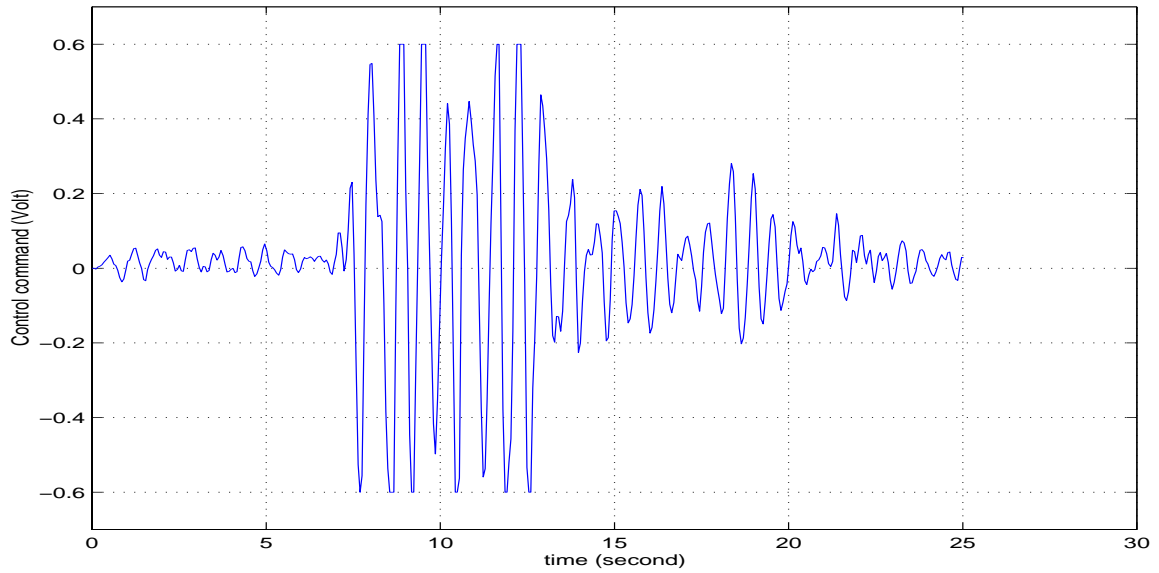


Figure 8.39 The control command using constrained MPC scheme under scaled Kobe earthquake ($u \leq 0.6$)

Table 8.5 Structure Acceleration Response using Constrained MPC

		$\sigma_{\ddot{x}_{a2}}$	$\sigma_{\ddot{x}_{a1}}$	σ_u	$\max(\ddot{x}_{a2})$	$\max(\ddot{x}_{a1})$	$\max(u)$
Scaled El Centro EQ.	Uncontrolled	0.429	0.379		1.397	1.211	
	Constrained MPC (experiment)	0.153	0.162	0.126	0.713	0.852	0.400
	Constrained MPC (simulation)	0.124	0.113	0.124	0.711	0.869	0.400
Scaled Kobe EQ.	Uncontrolled	0.374	0.347		1.378	1.510	
	Constrained MPC (experiment)	0.233	0.231	0.208	0.928	0.981	0.600
	Constrained MPC (simulation)	0.211	0.182	0.208	0.932	0.888	0.600

8.8 Summary

In this chapter, experimental studies of several MPC based schemes using acceleration feedback were presented for controlling structural response under earthquake loads. The experimental system consisted of a two-story building which was controlled by AMD devices, accelerometers and computer control system. MPC controller was designed and implemented experimentally for the whole system made up of the AMD, building and AMD-building interaction. First, the MPC scheme using acceleration feedback was verified under two different weighting parameters. Then the influence of the number and the locations of accelerometers on control design was studied. Using the pseudo-real-time control method, the effectiveness of MPC-AR was then tested with two different earthquake excitations. Finally, the constrained MPC scheme was applied to the experimental building under different earthquakes.

In these experiments, two models were developed. First involved the design of shaking table operation which was used and controlled to simulated the desired ground motion. The other was concerning the model of the AMD, building and AMD-building interaction structural system. The system identification method used for this structural system was shown to be effective and a minimal realization of the system was obtained. MPC scheme using acceleration feedback was employed to study structural control and it was found to be effective. For the response control implementation, the acceleration feedback was indeed convenient in practice and could be used in the structural control design. With an accelerometer attached to each floor, better control results can be achieved. In addition, the MPC-AR scheme used both the feedforward and feedback information from sensors and showed better control performance than the MPC scheme. Furthermore, the robustness of

MPC-AR scheme under different earthquakes was demonstrated. The constrained MPC did limit the control force within the design value. This helped prevent the controller from exceeding its capacity. Overall, the experimental results demonstrated the ability of the MPC based schemes in controlling motion of small-scale structures. This feature will help to promote their future consideration and implementation in full-scale structures.

CHAPTER 9

BENCHMARK PROBLEM FOR WIND EXCITED TALL BUILDINGS

A wide range of control devices and schemes have been proposed and implemented in structures as described in Chapter 1. However, it is very difficult to evaluate their relative effectiveness because each represents a different structure with different control devices and different design criteria. In 1995, the ASCE Committee on Structural Control initiated a benchmark study in structural control. The benchmark study proposed evaluation of the performance of different control strategies and devices with the prescribed design objectives. The first generation benchmark problem considered two benchmark structures. Both were scaled models of a three-story building, employing an active mass driver (AMD) controller and an active tendon controller, respectively. In 1998, the “second generation” benchmark studies were developed at the Second World Conference of Structural Control (SWCSC). One of these related to an earthquake excited building by Spencer et al. (1998), the other concerned a wind-excited building (Yang et al., 1998). After the SWCSC (1998), additional research work modification related to the benchmark problem were undertaken and subsequently the third generation benchmark problems were proposed. One of these is an earthquake-excited nonlinear building (Ohtori et al., 2000) and the other is a wind-excited tall building (Yang et al., 2000).

This chapter investigates the third generation benchmark problem of a wind-excited tall building. In this version of the benchmark problem, the wind loading time history was obtained from a wind tunnel study in Sydney University to facilitate the time domain analysis. A reduced order model for the 76-story concrete building is controlled by MPC using an active tuned mass damper (ATMD). The MPC provides an alternative simple control method with the convenience of handling problems with prescribed constraints (Mei et al., 2000). Two cases are considered here. First is MPC only, which does not include prescribed physical constraints in the objective function. The constraints are satisfied by choosing weighting matrices. The second involves MPC with physical constraints in which an optimal solution is sought in the constrained space. The inequality constraints on the maximum control force and mass damper displacement are included in the optimization objective. At each time step, MPC reduces to an optimization problem subjected to inequality constraints. A quadratic programming algorithm is used to obtain the optimal control force. An optimal solution is found in this constrained space. Accordingly, the control forces and mass damper displacement remain within the prescribed constrained space.

9.1 Problem Description

The benchmark problem in Yang et al. (2000) involves a 76-story and 306-meter concrete office tower subjected to alongwind or acrosswind excitation. An active tuned mass damper (ATMD) was installed on the top floor. The actuator dynamics and controller-structure interaction were neglected. An evaluation model with 48 states was obtained

through a model reduction scheme. These procedures simplified the computational effort.

The equations of motion were expressed in a state space form:

$$\dot{x} = Ax + Bu + EW \quad (9-1)$$

$$z = C_z x + D_z u + F_z W \quad (9-2)$$

$$y = C_y x + D_y u + F_y W + v \quad (9-3)$$

where $x = [\bar{x}, \dot{\bar{x}}]^T$ is the 48-dimensional state vector, $\bar{x} = [x_3, \dots, x_i]$, $i = 6, 10, 13, 16, 20, 23, 26, 30, 33, 36, 40, 43, 46, 50, 53, 56, 60, 63, 66, 70, 73, 76, m$; u is the scalar control force; and W is the wind excitation vector of dimension 24; $z = [\bar{z}, \dot{\bar{z}}, \ddot{\bar{z}}]^T$ and $y = [\dot{\bar{z}}, \ddot{\bar{z}}]^T$ are control output vector and measured output vector of the evaluation model, in which $\bar{z} = [x_1, \dots, x_i]$, $i = 1, 30, 50, 55, 60, 65, 70, 75, 76, m$; v is a vector of measured noise; x_m is the relative displacement of the mass damper with respect to the top floor. Matrices A , B , E , C_z , D_z , F_z , C_y , D_y and F_y were provided in Yang et al. (2000) and have appropriate dimensions.

The wind force data acting on the benchmark building were determined from wind tunnel tests. The prototype scale for the building was 1:400 and the velocity scale was 1:3, which result in a time scale of 1:133. Twenty-seven seconds of wind data were recorded and corresponded to an hour of prototype data. For the performance evaluation of control systems, only the first 900 seconds of acrosswind data were used for the computation of building response.

The time domain analysis was conducted on this evaluation model subjected to the 900 seconds of wind loading. There are 12 evaluation criteria defined for the time domain

response analysis. Both the RMS values and the peak response values of the 76-story building are defined quantities to be calculated and to derive the evaluation criteria. These criteria are:

$$J_1 = \max\{\sigma_{\ddot{x}1}, \sigma_{\ddot{x}30}, \sigma_{\ddot{x}50}, \sigma_{\ddot{x}55}, \sigma_{\ddot{x}60}, \sigma_{\ddot{x}65}, \sigma_{\ddot{x}70}, \sigma_{\ddot{x}75}\} / \sigma_{\ddot{x}75o} \quad (9-4)$$

$$J_2 = \frac{1}{6} \sum_i (\sigma_{\ddot{x}i} / \sigma_{\ddot{x}io}), i = 50, 55, 60, 65, 70, 75 \quad (9-5)$$

$$J_3 = \sigma_{x76} / \sigma_{x76o} \quad (9-6)$$

$$J_4 = \frac{1}{7} \sum_i (\sigma_{x_i} / \sigma_{xio}), i = 50, 55, 60, 65, 70, 75, 76 \quad (9-7)$$

where σ_{x_i} and σ_{xio} are RMS displacement of i -th floor with and without control, respectively, $\sigma_{\ddot{x}i}$ and $\sigma_{\ddot{x}io}$ are RMS acceleration of i -th floor with and without control, respectively.

$$J_5 = \sigma_{x_m} / \sigma_{x76o} \quad (9-8)$$

$$J_6 = \sigma_p = \frac{1}{T} \int_0^T [\dot{x}_m(t)u(t)] dt \quad (9-9)$$

where σ_{x_m} is the RMS displacement value of actuator's stroke, $\sigma_{\dot{x}_m}$ is the RMS relative velocity of the actuator to the top floor, and σ_p denotes the RMS control power. The limitation on the RMS values of control force and actuator stroke are $\sigma_u \leq 100$ kN and $\sigma_{x_m} \leq 30$ cm for acrosswind.

$$J_7 = \max\{\ddot{x}_{p1}, \ddot{x}_{p30}, \ddot{x}_{p50}, \ddot{x}_{p55}, \ddot{x}_{p60}, \ddot{x}_{p65}, \ddot{x}_{p70}, \ddot{x}_{p75}\} / \ddot{x}_{p75o} \quad (9-10)$$

$$J_8 = \frac{1}{6} \sum_i (\ddot{x}_{pi} / \ddot{x}_{pio}), i = 50, 55, 60, 65, 70, 75 \quad (9-11)$$

$$J_9 = x_{p76} / x_{p76o} \quad (9-12)$$

$$J_{10} = \frac{1}{7} \sum_i (x_{pi} / x_{pio}), i = 50, 55, 60, 65, 70, 75, 76 \quad (9-13)$$

where x_{pi} is the peak displacement of i -th floor with control, \ddot{x}_{pi} is peak acceleration of i -th floor with control, and x_{pio} is the peak displacement of i -th floor without control.

$$J_{11} = x_{pm} / x_{p76o} \quad (9-14)$$

$$J_{12} = P_{max} = \max |\dot{x}_{pm}(t)u(t)| \quad (9-15)$$

where x_{pm} is the peak stroke of the actuator, and \dot{x}_{pm} is the peak velocity of the actuator and P_{max} is the peak control power. The actuator capacity constraints include the following: the maximum control force $\max |u(t)| \leq 300$ kN and the maximum stroke $\max |x_m(t)| \leq 95$ cm.

Ten design requirements for ATMD are imposed on the proposed control design. Some standards include the following: maximum 6 sensors can be set up on the building; the sampling time is 0.001 second; one step time delay; and measurement noise has a two sided spectral density of 10^{-9} m²/sec³/Hz; the actuator capacities are as described above.

9.2 Results and Discussion

In this study, three accelerometers are placed on the top two floors and on the ATMD. The Kalman-Bucy filter is used to obtain the feedback gain of the observer. It is obtained from

$$\Gamma_e = PC_y^T(C_yPC_y^T + V)^{-1} \quad (9-16)$$

where P is the unique, symmetric, and positive definite solution of the Riccati equation:

$$P = \Phi[P - PC_y^T[C_yPC_y^T + R_v]^{-1}C_yP]\Phi^T + \Gamma_yQ_w\Gamma_y^T \quad (9-17)$$

and $E[WW^T] = Q_w$, $E[vv^T] = V$, $Q_w = Q_w^T$, $Q_w > 0$, $R_v = R_v^T$, and $R_v > 0$. W and v are assumed to be independent.

In the following examples, the MPC schemes used in Chapters 2 and 3 are employed. The MPC based controllers are designed for the 76-story building with designed stiffness, which is referred to as the nominal building. Furthermore, to show the robustness of the controller, the uncertainty of building stiffness is considered. The controller obtained for the nominal building is applied to buildings with $\pm 15\%$ variations in the stiffness matrix. The peak and RMS response quantities and evaluation criteria for these three buildings are presented and compared to the LQG control design.

9.2.1 Nominal Building

First the nominal building with designed stiffness is studied using MPC scheme without consideration of the hard constraints. The limits on the control force and ATMD's displacement are satisfied by adjusting weighting matrices Q and R . Here the weight R on

control force is chosen as 55. Then MPC considering constraints on the control force and ATMD displacement is applied to this nominal building. Table 9.1 gives performance criteria under different control schemes including passive control (TMD), LQG, MPC¹ (with no constraints) and MPC² (with constraints). Table 9.2 shows the peak values of the displacement and acceleration at different floors under different control schemes. Table 9.3 lists the RMS values of the displacement and acceleration response at different floors under different control strategies.

It has been noted by Rodellar(1987), Mei and Kareem (1998) that the MPC¹ (with no constraints) scheme has equivalent control effectiveness as the LQG control design. As shown in the performance criteria in Table 9.1, MPC scheme is better than TMD and is similar to LQG. Under MPC¹ scheme the peak control force is 118.1 kN while it is 118.2 kN under LQG. The RMS value of the control force is 32.23 kN under MPC¹ and 34.07 kN under LQG. Most of the criteria are a little smaller under MPC¹ except that J_8 (related to average peak displacement reduction) and J_{12} (peak value of control power) are smaller under LQG. The controlled top floor acceleration 9.26 cm/s² is smaller than that of LQG, which is 15.89 cm/s² as listed in Table 9.2. Similar results are obtained for the RMS values in Table 9.3. For example, the RMS values of the 76-th floor acceleration under MPC¹ is 43% smaller than that of the LQG control.

Following the unconstrained case, the controlled response is evaluated using constrained MPC. The weight R on control force is chosen as 50 so that the maximum control force is 128 kN if not constrained. The range of the control force is chosen as $[-118kN \ 118kN]$ in this example. The constraint on the output is the limit on the ATMD displacement, which requires the maximum displacement to be 95 cm. The maximum

control force reaches the constraint (118 kN) and an optimal solution within the boundary is obtained from the constrained MPC scheme. The results for MPC² (with constraints) are shown in Tables 9.1, 9.2 and 9.3. Under MPC² scheme the criteria J_1 to J_4 , and J_7 to J_{10} are smaller, which means better response reduction, while J_5 , J_6 , J_{11} and J_{12} are larger, which implies larger AMD stroke and more control power. This leads to more response reduction than the MPC¹ and LQG schemes while the peak control force remains 118 kN as prescribed.

9.2.2 Buildings with $\pm 15\%$ of Original Stiffness

To show the robustness of the controller, the uncertainty of building stiffness is taken into consideration. In addition to the “nominal building”, two additional buildings are taken into account. One case is with a +15% higher stiffness of the building and the other with a -15% lower stiffness, which are referred to as the +15% building and the -15% building, respectively, in the benchmark problem. The stiffness matrices for the two buildings are obtained by multiplying each element of the stiffness matrix of the nominal building by 1.15 and 0.85, respectively. The controller designed previously for the nominal building is applied to the $\pm 15\%$ buildings. The performance criteria of the $\pm 15\%$ buildings are presented in Table 9.4. The peak and the RMS values of displacement and acceleration of the two buildings are listed in Tables 9.5 and 9.6.

As noted from these tables, MPC¹ and MPC² designed for the nominal building result in reducing the response of the $\pm 15\%$ buildings. As observed from the results of Tables 9.5 and 9.6, like the LQG case, the acceleration response quantities are robust for the MPC schemes. In comparison with the nominal structure, the displacement of the 75-th floor, stroke, active control force, and control power for the -15% building under MPC¹ increase

by about 24.2%, 12.8%, 16.4% and 19.9%, respectively. Under MPC², they increase by 24.7%, 14.0%, 16.8% and 18.8%, respectively. For the +15% building, The displacement, stroke, active control force, and control power in comparison with the nominal building are reduced by 16.6%, 16.7%, 6.2% and 18.6% by MPC¹, respectively. Using MPC², the reductions are 16.1%, 17.4%, 8.4% and 21.2%, respectively. For MPC² scheme, the maximum absolute control force is always limited to be less than 118 kN for both the +15% and the -15% buildings. With a larger control power, the response reduction is better than those of MPC¹ and LQG. The RMS value of the ATMD displacement and the peak value of ATMD displacement both remain within the prescribed limits.

Figures 9.1 and 9.2 compare the changes in the displacement of the 75-th floor, actuator stroke, control force, and control power under LQG, MPC¹ and MPC² schemes when the structural stiffness has variations of $\pm 15\%$. Compared to the LQG scheme (Yang et al. 2000), for the $\pm 15\%$ buildings, the displacement of 75-th floor under MPC schemes is a little more sensitive to the stiffness uncertainty than that under the LQG scheme. However, the required actuator capacity (stroke, control force, and control power) under MPC schemes is much less sensitive to the stiffness uncertainty than those under the LQG scheme (Yang et al., 2000). These trends demonstrate that the MPC schemes are more robust to the uncertainty in the structural stiffness.

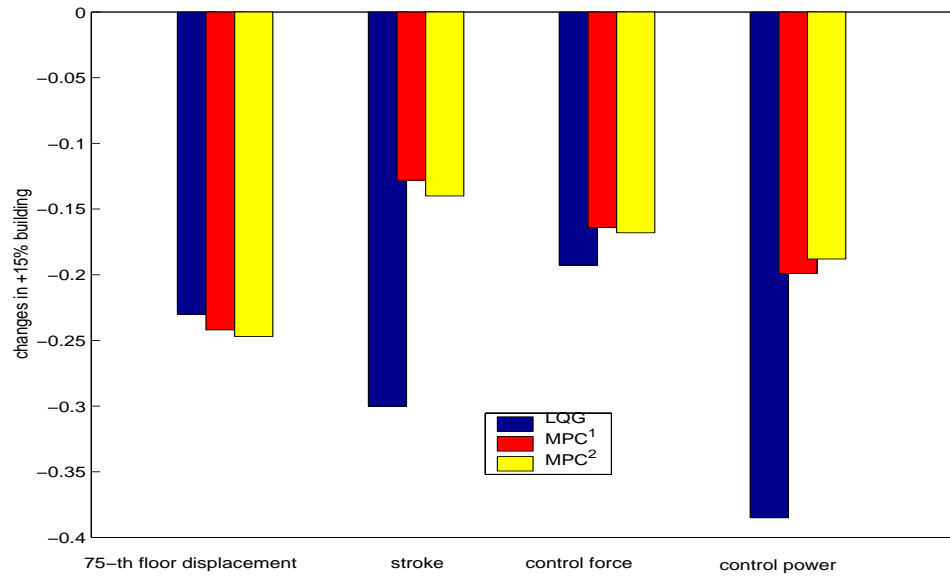


Figure 9.1 Comparison of sensitivities of different control schemes to the +15% change in stiffness

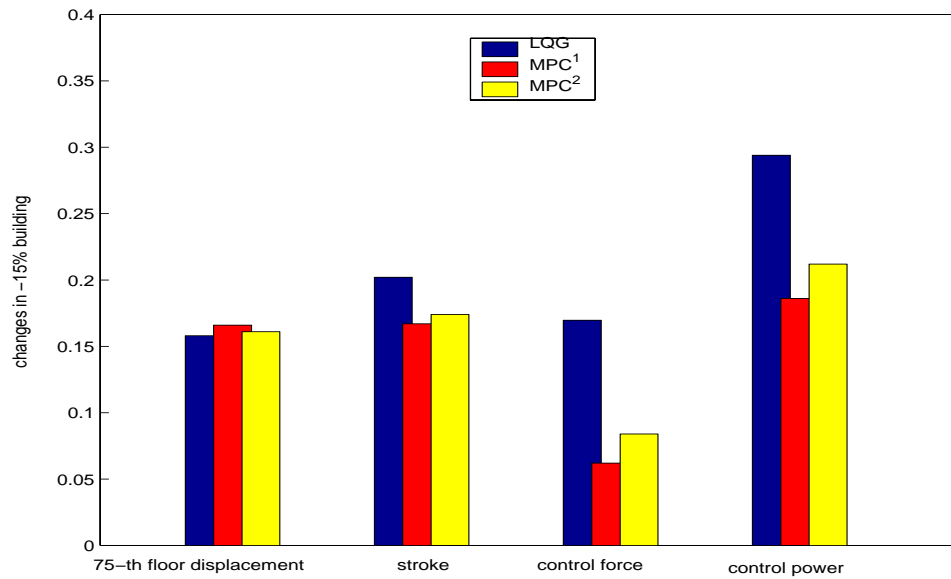


Figure 9.2 Comparison of sensitivities of different control schemes to the -15% change in stiffness

To sum up, from the numerical examples, MPC exhibits effectiveness similar to the LQG method. The $\pm 15\%$ changes in the stiffness of the building does notably affect the

controller performance. MPC based schemes show more robustness in the event of uncertainty in the structural model. The MPC scheme can also address control under constraints more effectively. Simulations show that for the ATMD, MPC with constraints can restrict the control force within the prescribed limits and generate optimal control force at each time step. The damper displacement is also limited within the required range. Above all, the MPC scheme can accommodate practical civil engineering problems and provides a more effective way to handle physical constraints.

9.3 Summary

In this chapter, the MPC scheme was employed to reduce the response of the benchmark problem under wind excitation with input/output inequality constraints imposed on the structure and the control device. At each time step, MPC reduced to an optimal problem subjected to certain constraints on the input and output. This led to a quadratic programming problem with inequality constraints. The numerical results for a building demonstrated the effectiveness of the MPC scheme with or without consideration of the constraints. Two building with $\pm 15\%$ stiffness uncertainty revealed the robustness of the MPC based schemes. The constraints for the control actuator were satisfied in both buildings with uncertainty. The results demonstrated the effectiveness and robustness of the MPC based schemes for full-scale structural applications.

Table 9.1 Evaluation criteria for across-wind excitations

RMS response ($\Delta K=0\%$)				Peak Response ($\Delta K=0\%$)			
Eval. Criteria	LQG	MPC ¹	MPC ²	Eval. Criteria	LQG	MPC ¹	MPC ²
J_1	0.369	0.363	0.346	J_7	0.381	0.381	0.349
J_2	0.417	0.410	0.391	J_8	0.432	0.438	0.428
J_3	0.578	0.572	0.563	J_9	0.717	0.716	0.712
J_4	0.580	0.574	0.565	J_{10}	0.725	0.725	0.720
J_5	2.271	2.260	2.410	J_{11}	2.300	2.282	2.400
J_6	11.99	11.96	14.52	J_{12}	71.87	79.59	88.37
σ_u (kN)	34.07	32.23	36.95	$\max u(t) $	118.24	118.1	118.0
σ_{x_m} (cm)	23.03	22.90	24.44	$\max x_m $	74.29	73.37	77.52

Table 9.2 Peak Response using Passive (TMD), LQG and MPC schemes

Floor No.	No Control		Passive (TMD)		LQG Control $u_{max} = 118.2$ kN		MPC ¹ $u_{max} = 118.1$ kN		MPC ² $u_{max} = 118.0$ kN	
	x_{pio} cm	\ddot{x}_{pio} cm/s ²	x_{pio} cm	\ddot{x}_{pio} cm/s ²	x_{pio} cm	\ddot{x}_{pio} cm/s ²	x_{pio} cm	\ddot{x}_{pio} cm/s ²	x_{pio} cm	\ddot{x}_{pio} cm/s ²
1	0.053	0.22	0.044	0.21	0.041	0.23	0.041	0.24	0.040	0.25
30	6.84	7.14	5.60	4.68	5.14	3.38	5.14	3.92	5.11	3.77
50	16.59	14.96	13.34	9.28	12.22	6.73	12.21	7.09	12.14	6.77
55	19.41	17.48	15.54	10.74	14.22	8.05	14.21	8.15	14.12	8.09
60	22.34	19.95	17.80	12.69	16.27	8.93	16.26	8.86	16.16	8.92
65	25.35	22.58	20.10	14.72	18.36	10.06	18.35	10.13	18.24	10.14
70	28.41	26.04	22.43	16.77	20.48	10.67	20.46	10.79	20.33	10.55
75	31.59	30.33	24.84	19.79	22.67	11.56	22.64	11.55	22.50	10.59
76	32.30	31.17	25.38	20.52	23.15	15.89	23.13	9.26	22.99	16.36
md			42.60	46.18	74.27	72.64	73.70	78.81	77.52	80.31

Table 9.3 RMS Response using Passive (TMD), LQG and MPC schemes

Flo or No.	No Control		Passive (TMD)		LQG Control $\sigma_u = 37.99KN$		MPC ¹ $\sigma_u = 32.23KN$		MPC ² $\sigma_u = 36.95KN$	
	σ_{xi} cm	$\sigma_{\ddot{x}i}$ cm/s ²	σ_{xi} cm	$\sigma_{\ddot{x}i}$ cm/s ²	σ_{xi} cm	$\sigma_{\ddot{x}i}$ cm/s ²	σ_{xi} cm	$\sigma_{\ddot{x}i}$ cm/s ²	σ_{xi} cm	$\sigma_{\ddot{x}i}$ cm/s ²
1	0.017	0.06	0.012	0.06	0.010	0.06	0.010	0.06	0.010	0.06
30	2.15	2.02	1.48	1.23	1.26	0.89	1.24	0.92	1.23	0.89
50	5.22	4.78	3.57	2.80	3.04	2.03	3.01	2.00	2.96	1.92
55	6.11	5.59	4.17	3.26	3.55	2.41	3.51	2.36	3.46	2.28
60	7.02	6.42	4.79	3.72	4.08	2.81	4.03	2.75	3.97	2.66
65	7.97	7.31	5.43	4.25	4.62	3.16	4.57	3.10	4.50	2.99
70	8.92	8.18	6.08	4.76	5.17	3.38	5.11	3.30	5.03	3.16
75	9.92	9.14	6.75	5.38	5.74	3.34	5.67	3.31	5.58	2.97
76	10.14	9.35	6.90	5.48	5.86	4.70	5.80	2.68	5.71	4.70
md			12.757	13.86	23.03	22.40	22.90	24.60	24.43	24.48

Table 9.4 Evaluation criteria for across-wind excitations

RMS response					Peak Response				
Eval. Criteria	$\Delta K=15\%$		$\Delta K=-15\%$		Eval. Criteria	$\Delta K=15\%$		$\Delta K=-15\%$	
	MPC ¹	MPC ²	MPC ¹	MPC ²		MPC ¹	MPC ²	MPC ¹	MPC ²
J_1	0.345	0.335	0.390	0.376	J_7	0.386	0.381	0.461	0.451
J_2	0.389	0.379	0.439	0.425	J_8	0.432	0.430	0.537	0.529
J_3	0.477	0.472	0.710	0.702	J_9	0.607	0.611	0.780	0.751
J_4	0.479	0.474	0.711	0.704	J_{10}	0.614	0.618	0.788	0.760
J_5	1.883	1.992	2.548	2.748	J_{11}	1.840	1.931	2.702	2.750
J_6	9.732	11.440	14.34	17.25	J_{12}	61.69	70.43	99.04	96.54
σ_u (kN)	30.23	33.86	37.50	43.16	$\max u(t) $	112.5	118.0	135.5	118.0
σ_{x_m} cm	19.08	20.19	25.83	27.86	$\max x_m $	59.44	62.35	87.26	88.83

Table 9.5 Results of MPC for +15% building

	MPC ¹ $u_{max} = 112.5$ kN		MPC ² $u_{max} = 118.0$ kN		MPC ¹ $\sigma_u = 30.23$ kN		MPC ² $\sigma_u = 33.86$ kN	
Floor No.	x_{pio} cm	\ddot{x}_{pio} cm/s ²	x_{pio} cm	\ddot{x}_{pio} cm/s ²	σ_{xi} cm	$\sigma_{\ddot{x}i}$ cm/s ²	σ_{xi} cm	$\sigma_{\ddot{x}i}$ cm/s ²
1	0.034	0.24	0.034	0.24	0.01	0.06	0.01	0.06
30	4.34	3.77	4.37	3.71	1.04	0.92	1.03	0.91
50	10.33	6.54	10.40	6.62	2.51	1.91	2.49	1.86
55	12.03	7.83	12.11	7.79	2.93	2.25	2.91	2.20
60	13.77	8.96	13.87	8.90	3.37	2.61	3.34	2.56
65	15.54	10.01	15.66	10.20	3.81	2.95	3.78	2.89
70	17.33	11.13	17.46	10.75	4.26	3.15	4.22	3.07
75	19.19	11.71	19.32	11.55	4.73	3.08	4.68	2.93
76	19.60	17.49	19.74	17.17	4.83	4.54	4.79	4.54
md	59.44	68.58	62.35	72.48	19.08	20.87	20.19	22.10

Table 9.6 Results of MPC for -15% building

	MPC ¹ $u_{max} = 135.5$ kN		MPC ² $u_{max} = 118.0$ kN		MPC ¹ $\sigma_u = 37.50$ kN		MPC ² $\sigma_u = 43.16$ kN	
Floor No.	x_{pio} cm	\ddot{x}_{pio} cm/s ²	x_{pio} cm	\ddot{x}_{pio} cm/s ²	σ_{xi} cm	$\sigma_{\ddot{x}i}$ cm/s ²	σ_{xi} cm	$\sigma_{\ddot{x}i}$ cm/s ²
1	0.044	0.228	0.043	0.23	0.012	0.058	0.012	0.059
30	5.59	3.77	5.39	3.75	1.54	0.99	1.53	0.96
50	13.26	7.98	12.79	7.89	3.72	2.15	3.68	2.08
55	15.44	9.98	14.88	9.89	4.35	2.54	4.30	2.48
60	17.67	11.20	17.03	11.11	5.00	2.97	4.95	2.90
65	19.96	12.72	19.23	12.46	5.67	3.34	5.60	3.26
70	22.27	13.98	21.45	13.68	6.34	3.56	6.27	3.44
75	24.66	13.88	23.75	13.52	7.04	3.42	6.96	3.21
76	25.20	20.10	24.27	19.84	7.20	5.15	7.12	5.16
md	87.25	82.63	88.83	82.96	25.83	23.83	27.86	25.41

CHAPTER 10

CONCLUSIONS

In this study, MPC based control schemes to mitigate the earthquake or wind induced load effects were developed. Active and semi-active controls based on MPC schemes offer attractive opportunities to reduce damage and loss of serviceability caused by earthquakes and hurricanes. The advantages offered by MPC lie in its ability to handle multivariable processes, constraints and disturbances. MPC can optimize the control effort and yet provide a high level of performance with a minimum set of measurements.

The basic concept and general formulation of MPC were outlined. The MPC scheme is based on an explicit use of a prediction model of the system response to obtain the control action by minimizing an objective function. Optimization objectives include minimization of the difference between the predicted and reference response and minimization of the control efforts subjected to prescribed constraints. The effectiveness and the convenience in the use of the MPC scheme were also compared to the H_2 control scheme.

The hard constraints were conveniently taken into account by the MPC based scheme and were written as inequality constraints. The optimization problem was recast as a quadratic programming problem subjected to inequality constraints. This simplifies the constraint issue and calculates the optimal control force in the presence of constraints. At each time step, the MPC based scheme presented an optimal solution which resulted in a new

controller design. Buildings equipped with active tendon and active mass damper were studied to demonstrate the effectiveness of MPC. The constraints on the controller, such as the maximum control force, maximum force variation at each time step and maximum displacement of the damper, were incorporated in the controller design. Using this approach, very effective, economical and practice-oriented controller designs can be achieved.

Structural control using semi-active devices was also investigated. In this study, a semi-active viscous fluid damper and a semi-active Tuned Liquid Column Damper were implemented in the example structures. The MPC scheme was employed to control the position of the damper valve to adjust the volume of fluid passing through it. This adjustment helps to control the damping force based on the variations in the external excitation. This study simplifies the modeling of the damping force variation in semi-active systems and represents it in terms of time-varying constraints. This format facilitates achieving an optimal control design by introducing the constrained MPC scheme. It is shown that the constrained MPC offers a better design for semi-active devices than the customary clipped-LQG control.

This study also investigated the use of acceleration feedback to advance the implementation of this scheme for structural application. An observer based on the Kalman-Bucy filter was designed to estimate the states of the system and to obtain the estimator gain. Potential sensor locations were examined to obtain the most effective and optimal placement. To demonstrate this scheme, an active mass damper and an active tendon system were introduced as active control devices. Numerical results showed that the acceleration feedback control based MPC scheme offered performance that was comparable to the state

feedback framework. This scheme is a more practical and convenient form of feedback which is natural for practical applications.

MPC based feedforward-feedback control was employed adaptively to control the response of structures under earthquakes. The real-time modeling of ground motion was accomplished by using an AR model which was fitted based on the previously measured ground motion records and the difference between the measured and modeled output. The AR model matrices were updated at each time interval and subsequently expressed in terms of the state space representation and augmented to the equations of motion of the structure. It was shown that this approach of real-time modeling of ground motion offered adaptability and robustness in describing ground motions featuring a wide range of characteristics. The MPC-AR control performance index and the control force were updated at each time interval. This resulted in providing a real-time feedforward link to the control design which enriched this scheme with predictive and adaptive features to essentially mitigate the effects of seismic events with unusual and unexpected characteristics.

Besides earthquakes, wind also influences both the serviceability and safety of high-rise buildings and towers. The MPC scheme was also investigated for application to control wind effects on structures. In order to cast wind loading model in terms of the state-space format, a simulation approach based on stochastic decomposition was proposed. This approach helped in capturing the target spectral characteristics of wind load fluctuations, which have not been successfully achieved previously for a general description of space-time correlation structure of wind loads. A state space representation of the wind field was then obtained and a reduced order model was used. This model was added to the equations of motion of the structure to implement the feedforward link in the MPC based feedback

control. The Nanjing Tower in China was used as an example. An active mass damper at the VIP lounge floor was used to control wind induced motion. The feedforward-feedback controller design based on the MPC scheme showed better control performance than the control based only on feedback.

Experiments were conducted to verify the effectiveness of the MPC based schemes. An electro-mechanical shaking table was programmed to simulate a host of ground motion records. A small-scale two-story building with an active mass damper was assembled and excited by simulated ground motions. System identification was carried out by curve-fitting and an eigen-system realization algorithm. The actuator's inherent dynamic features and the controller-structure interactions were included in the design of the control schemes. Acceleration feedback was employed in this study. The experimental results showed significant response reductions using MPC based schemes and its effectiveness in controlling structural motions under earthquakes. Pseudo real-time MPC scheme provide some validation of the real-time based MPC.

Finally, the MPC scheme was employed in a full-scale building to reduce structural response under wind excitation when the structure and control device were subjected to inequality constraints. An optimal solution was found within the prescribed limits for the controller design. Numerical results involving ATMD demonstrated the effectiveness of the MPC scheme in the presence of constraints. This was also verified experimentally using a pseudo constraint scheme. The MPC constrained scheme provides a reliable and computationally convenient way to study and design devices for full-scale structural control under constraints.

In closing, it has been demonstrated that MPC for civil engineering applications offers inherent computational expediency, natural extension to real-time applications, intrinsic convenience in the treatment of constraints, and great potential for future extensions and implementation in full-scale applications.

A list of recommendations for future extension of the study is given below.

Firstly, in this study, the systems are assumed to be in the linear elastic range. In practice, the buildings may show non-linear inelastic behavior during strong earthquakes. The controller may also have non-linear dynamics. Therefore, future studies should consider the non-linear dynamic properties of the structures and/or controller.

Secondly, most structural control designs use only one actuator which is either a passive, active, or semi-active control device. If it fails during earthquake, then the structural control design will not function. A new proposal would include more control devices in the same structure to ensure some redundancy. A combination of passive, active and semi-active devices would not only reduce the size of each, but also increase the reliability of the structural control system thus gaining acceptance from the design professionals. However, in this multiple controllers design, it is important not to ignore the dynamics of the control devices.

Furthermore, with the advanced software and hardware available in the near future, the real-time MPC-AR scheme could be validated experimentally on-line by using updated information at each time step. Utilizing advanced chips which can integrate the data I/O, A/D and D/A convertor and algorithms on one chip, the computation speed can be greatly increased. Also more efficient AR identification schemes need to be considered to further reduce the computational efforts for the digital implementation.

REFERENCES

- Abdel-Rohman, M. and Leipholz, H. H. (1978), "Active Control of Flexible Structures", *J. of the Struct. Div., ASCE*, Vol. 104, No. 8 1251-1266
- Abdel-Rohman, M. and Leipholz, H. H. (1983), "Active Control of Tall Buildings", *J. of the Struct. Div., ASCE*, Vol. 109, No. 3 628-645
- Antsaklis, P. J. and Michel, A. N. (1997), *Linear System*, McGraw-Hill
- Arima, F., Miyazaki, M., Tanaka, H. and Yamazaki, Y. (1988), "A Study on Building With Large Damping Using Viscous Damping Walls", *Proc. Ninth WCEE*, Vol. 5, 821-826.
- Battaini, M., Yang, G., and Spencer, B. F. Jr., "Bench-Scale Experiment for Structural Control," *J. of Engineering Mechanics, ASCE*, Vol.126, No. 2, pp. 140-148, 2000.
- Camacho, E. F. and Bordons C. (1999), *Model Predictive Control*, Springer-Verlag London Limited.
- Carlson, J. D. (1994), "The Promise of Controllable Fluids", *Proc. of Actuator 94*, H. Borgmann, and K. Lenz, eds., AXON Technologie Consult GmbH, 266-270
- Carlson, J. D., and Weiss, K. D. (1994), "A Growing Attraction to Magnetic Fluids", *Machine Des.(Aug.)*, 61-64
- Casciati, F. De Petra, E., Faravelli, L. (1993), "Neural Networks in Structure Control", *Proc. ASCE Structures '93*, Irvine, 790-795
- Casciati, F. and Yao, T. (1994), "Comparison of Strategies for the Active Control of Civil Structures", *Proc. First World Conference on Structure Control*, WA1:3-12
- Chang, J. and Soong, T. T. (1980), "Structural Control Using Active Tuned Mass Dampers", *J. of the Engineering Mechanics, ASCE*, Vol. 106, No. 6, 1091-1098
- Chung, L. L., Reinhorn, A. M. and Soong, T. T. (1988), "Experiments on Active Control of Seismic Structures", *J. of Engineering Mechanics, ASCE*, Vol. 114, 241-256

- Chung, L. L., Lin, R. C., Soong, T. T. and Reinhorn, A. M. (1989), "Experiments on Active Control for MDOF Seismic Structures", *J. of Engineering Mechanics, ASCE*, Vol. 115, No. 8, 1609-1627
- Clough R. W. and Penzien J. (1993), *Dynamics of Structures*, Second Edition, McGraw-Hill, Inc.
- Culter, C. R. and Ramaker, B. L. (1980), "Dynamica Matrix Control-- A Computer Control Algorithm", Proc. Automatic Control Conf., Paper WP5-B, San Francisco, CA
- D'Amato, F. J., and Rotea, M. A. (1998), "Limits of Achievable Performance and Controller Design for the Structural Control Benchmark Problem", *Earthquake Engineering and Structural Dynamics*, Vol, 27, No. 11, 1203-1224.
- Den Hartog, J. P. (1947), *Mechanical Vibrations*, Mcgraw-Hill, Inc., New York, N. Y.
- Deodatis, G. and Shinozuka, M. (1988), "Auto-Regressive Model For Nonstationary Stochastic Processes", *ASCE, J. Engrg. Mech.*, Vol. 114, No. 11, 1995-2012.
- Doyle, J. C., Glover, K., Khargonekar, P. and Francis, B. (1989), "State-Space Solutions to Standard H_2 and H_∞ Control Problems." *IEEE Trans. on Automatic Control*, Vol. 34, pp. 831-847.
- Dyke, J. S., Spencer, Jr., B. F., Quast, P. and Sain M. K. (1995), "The Role of Control-Structure Interaction in Protective System Design", *J. of Engineering Mechanics, ASCE*, Vol. 121, No. 2, 322-338
- Dyke, S. J., Spencer, B. F., Quast, P., Sain, M. K., Kaspari, D. C., and Soong, T. T. (1996), "Acceleration Feedback Control of MDOF Structures," *ASCE, J. Engrg. Mech.*, Vol. 122, No. 9, 907-917.
- Dyke, J. S. (1996), *Acceleration Feedback Control Strategies for Active and Semi-Active Control Systems: Modeling, Algorithm Development and Experimental Verification*, PhD Dissertation, University of Notre Dame
- Dyke, S. J., Spencer, B. F., Jr., Sain, M. K. and Carlson, J. D. (1996), "Modeling and Control of Magnetorheological Dampers for Seismic Response Reduction", *Smart Mat. and Struct.*, Vol. 5, 565-575
- Ehrgott, R. C. and Masri, S. F. (1992), "Modeling the Oscillatory Dynamic Behaviour of Electro-Rheological Materials in Shear", *Smart Mat. and Struct.*, Vol. 1, No. 4, 275-285
- Ehrgott, R. C. and Masri, S. F. (1994), "Experimental Characterization of An Electro-Rheological Material Subjected to Oscillatory Shear Strains", *J. of Vibration and Acoustics*, Vol. 116, 53-60

- Feng, Q., Shinozuka, M. and Fujii, S. (1993), "Friction-Controllable Sliding Isolated Systems", *J. Engrn. Mech.*, ASCE, Vol. 119, No. 9, 1945-1864
- Garcia, C. E. and Morari, M. (1982), "Internal Model Control: 1. A Unifying Review and Some New Results", *Ind. & Eng. Chem. Process Des. and Dev.*, Vol. 21, 308-323
- Garcia, C. E. and Morari, M. (1985a), "Internal Model Control: 2. Design Procedure for Multivariable systems", *Ind. & Eng. Chem. Process Des. and Dev.*, Vol. 24, 472-484
- Garcia, C. E. and Morari, M. (1985b), "Internal Model Control: 3. Multivariable Control Law Computation and Tuning guidelines", *Ind. & Eng. Chem. Process Des. and Dev.*, Vol. 24, 484-494
- Gavin, H. P., Hose, Y. D. and Hanson, R. D. (1994), "Design and Control of Electrorheological dampers", *Proc. of First World Conference on Structure Control*, WP3:83-92
- Gavin, H. P., Hose, Y. D. and Hanson, R. D. (1994), "Testing and Modeling of A Prototype ER Damper for Seismic Structural response Control", *Proc. Int. Workshop on Struct. Control*, USC Publ. No. CE9311, 166-180
- Haroun, M. A., Pires, J. A. (1994), "Active Orifice Control in Hybrid Liquid Column Dampers", *Proceedings of the First World Conference on Structural Control*, Vol. I, Los Angeles.
- Housner, G. W. and Masri, S. F. (Eds.), (1990), *Proceedings of the U.S. National Workshop on Structural Control Research*, USC Publications No. M9013, University of Southern California, Los Angeles, California, Oct. 25-26
- Housner, G. W. and Masri, S. F. (Eds.), (1993), *Proceedings of the International Workshop on Structural Control*, USC Publications No. CE9311, University of Southern California, Los Angeles, California, Oct. 25-26
- Housner, G. W., Soong, T. T., Masri, S. F. (1994), "Second Generation of Active Structure Control of Civil Engineering", *Proceedings of the First World Conference on Structural Control*, Pasadena, CA, August 3-5
- Housner, G. W., Bergman, L. A., Cuaghey, T. K., Chassiakos, A. G., Claus, R. O., Masri, S. F., Skelton, R. E., Soong, T. T., Spencer, B. F., Yao, J. T. P. (1997), "Structural Control: Past, Present and Future", *J. of Engineering Mechanics, ASCE*, Vol. 123, No. 9, 897-971.
- Hrovat, D., Barak, P. and Rabins, M. (1983), "Semi-Active Versus Passive or Active Tuned Mass Damper for Structural Control", *J. Engrg. Mech.*, Vol. 109, No. 3, 691-705

- Johnson, E. A., Voulgaris, P. G. and Bergman, L. A. (1998), "Multi-objective Optimal Structural Control of the Notre Dame Building Model Benchmark", *Earthquake Engineering and Structural Dynamics*, Vol, 27, No. 11, 1165-1188.
- Juang, J. (1994), *Applied System Identification*, Prentice Hall PTR
- Kailath, T. (1980), *Linear Systems*, Prentice Hall, Englewood Cliffs, N. J.
- Kareem, A. (1981), "Wind-Excited response of Buildings in Higher Modes", *J. of Struct. Engrg.*, ASCE, 107(4), 701-706
- Kareem, A. (1983), "Mitigation of Wind Induced Motion of Tall Buildings", *J. of Wind Engineering and Industrial Aerodynamics*, Vol. 11, 273-284.
- Kareem, A. and Li, Y. (1988), "Stochastic Response of Tension Leg Platforms to Wind and Wave Fields", Dept. of Civil Engineering, Technical Report No. UHCE88-18
- Kareem, A. and Li, Y. (1992), "Digital Simulation of Wind Load Effects", *Proc. ASCE Specialty Conference on Probabilistic Mechanics and structural and Geotechnical Reliability*, ASCE, New York, N. Y.
- Kareem, A. (1994), "The Next Generation of Tuned Liquid Dampers", *Proc. First World Conference on Structural Control*, FP5, 19-28
- Kareem, A., Kabat, S., Haan, F. L. J., Mei, G. and Yalla, S. K. (1998), "Modeling and Control of Wind-induced Response of a TV Tower", *Proc. 2nd World Conference on Structural Control, Kyoto, Japan*.
- Kareem, A., Kijewski, T., and Tamura, Y. (1999), "Mitigation of Motions of Tall Buildings with Specific Examples of Recent Applications," *Wind & Structures* Vol. 2, No. 3, 201-251.
- Kareem, A. and Mei, G (1999), "Stochastic Decomposition For Simulation And Domain Space Reduction In Wind Induced Dynamics Of Structures", ICASP8*1999, Australia
- Kay, Steven (1993), *Fundamentals of Statistical Signal Processing Estimation Theory*, Prentice Hall, PTR
- Kelly, J. M. (1982), "Aseismic Base Isolation", *Shock Vib. Dig.* Vol. 14, 17-25
- Kelly, J. M. (1986), "Aseismic Base Isolation: Review and Bibliography", *Soil Dynamics and Earthquake Engineering*, Vol. 5 No. 3, 202-213
- Kelly, J. M., Leitmann, G. and Soldatos, A. G. (1987), "Robust Control of Base-Isolated Structures Under Earthquake excitation", *J. Optim. Th. Appl.*, Vol. 53, 159-180

- Kijewski, T., Kareem, A. and Tamura, Y. (1998), "Overview of Methods to Mitigate the Response of Wind-Sensitive Structures." *Proceedings of Structural Engineering World Congress, July 19-23, San Francisco.*
- Kobori, T. and Minai, R. (1960 a), "Analytical Study on Active Seismic Response Control (Seismic-Response-Controlled structure I)", *ibid*, No. 66, 257-260
- Kobori, T. and Minai, R. (1960 b), "Analytical Study on Active Seismic Response Control (Seismic-Response-Controlled structure II)", *ibid*, No. 66, 253-256
- Kobori, T. (1994), "Future Direction on Research and Development of Seismic-Response-Controlled Structure", *Proceedings of First World Conference on Structure Control*, Panel:19-31
- Koike, Y., Murata, T., Tanida, K., Kobori, T., Ishii, K. and Takenaka, Y. (1994), "Development of V-shaped Hybrid Mass Damper and Its Application to High-Rise buildings", *Proceedings of First World Conference on Structure Control*, FA2:3-12
- Lee, J. H., Morari, M. and Garcia, C. E. (1994), "State-Space Interpretation of Model Predictive Control", *Automatica*, Vol. 30, No. 4, 707-717
- Li, S., Lim, K. Y. and Fisher, D. G. (1989), "A state Space Formulation for Model Predictive Control", *AIChE Journal*, Vol. 35, 241-249
- Li, Y. and Kareem, A. (1989), "Simulation of Multivariate Nonstationary Random Processes by FFT", *J. of Engrg. Mech., ASCE*, Vol. 117, No. 5, 1037-1058
- Li, Y. and Kareem, A. (1993), "Simulation of Multivariate Random Processes: Hybrid DFT and Digital Filtering Approach", *J. of Engrg. Mech., ASCE*, Vol. 119, No. 5, 1078-1098
- Li, Y. & A. Kareem (1995), "Stochastic decomposition and its applications to probabilistic dynamics." *J. of Engrg. Mech., ASCE*. 121(1): 162-174.
- Lopez-Almansa, F., Andrade, R., Rodellar, J. and Reinhorn A. M. (1994a), "Modal Predictive Control of Structures I: Formulation." *ASCE, J. Engrg. Mech.*, Vol. 120, No. 8, pp. 1743-1760.
- Lopez-Almansa, F., Andrade, R., Rodellar, J. and Reinhorn A. M. (1994b), "Modal Predictive Control of Structures II: Implementation." *ASCE, J. Engrg. Mech.*, Vol. 120, No. 8, pp. 1761-1772.
- Lu, J. and Skelton, R. R. (1998), "Covariance Control Using Closed Loop Modeling for Structures", *Earthquake Engineering and Structural Dynamics*, Vol, 27, No. 11, 1367-1384.

- Lundstrom, P., Lee, J. H. Morari, M. and Skogestao, S. (1995), "Limitations of Dynamic Matrix Control", *Computers Chem. Engrg.*, Vol. 19, No. 4, 409-421
- Makris, N., Constantinou, M. C., and Dargush, G. F. (1993a), "Analytical Model of Viscoelastic Liquid Dampers", *J. Struct. Engrg.*, ASCE, Vol. 119, 3310-3325.
- Makris, N., Dargush, G. F. and Constantinou, M. C. (1993b), "Dynamic Analysis of Generalized Viscoelastic Fluids", *J. Engrg. Mech.*, ASCE, Vol. 119, 1663-1679.
- Makris, N., Hill, D., Burton, S., and Jordan, M. (1995), "Electrorheological Fluid Dampers For Seismic Protection of Structures", *Proc., SPIE Conf. on Smart Struct. and Mat.*, I, Chopra, ed., 184-194
- Masri, S. F., Chassiakos, A. G., Caughey, T. K. (1993), "Identification of Nonlinear Dynamic Systems Using Neural Networks", *J. of Applied Mechanics*, Vol. 60, 123-133
- Masri, S. F., Kumar, R. and Ehrgott, R. C. (1995), "Modeling and Control of An Electrorheological Device for Structural Control Applications", *J. Smart Mat. and Struct.*, Vol. 4, Supplement 1A, A121-A131
- Matlab 5.2 (1998), *the MathWorks, Inc.*
- Mei, G. and Kareem, A. and Kantor, J. C. (1998), "Real-Time Model Predictive Control of structures under earthquakes", *Proceedings of 2nd World Conference on Structural Control*, Kyoto, Japan, June 28 to July 2, 1998
- Mei, G., Kareem, A. and Kantor, J. C. (2001a), "Real-Time Model Predictive Control of structures under earthquakes", *Earthquake Engineering and Structural Dynamics*, 30: 995-1019
- Mei, G., Kareem, A. and Kantor, J. C. (2001b), "Model Predictive Control of Structures Under Earthquakes Using Acceleration Feedback", *J. Engrg. Mech*, ASCE, in press.
- Miyazaki, M. and Mitsusaka, Y. (1992), "Design of Building With 20% or Greater Damping", *Proc. 10WCEE*, Vol. 7, 4143-4148
- Mizuno, T., Kobori, T., Hirai, J. Matsumage, Y. and Niwa, N. (1992), "Development of adjustable Hydraulic Dampers for Seismic Response Control of Large Structure", *Proc. ASME PVP Conf.*, Vol. 229, 163-170.
- Mostaghel, N. and Khodaverdian, M. (1987), "Dynamics of Resilient-Friction Base Isolation(R-FBI)", *Earthquake engng., Struct. Dyn.*, Vol. 15, 379-390
- Morari, M., Garcia, C. E., Lee, D. M. and Prett, D. M. (1994), *Model Predictive Control*, Prentice Hall

- Navratil, J. P., Lim, K. Y. and fisher, D. G. (1988), "Disturbance feedback in Model Predictive Control Systems", *Proc. IFAC Workshop on Model-Based Process Control*, 63-68, Atlanta, GA
- Nitta, Y. and Nishitani, A. (1998), "Variable Feedback Gain Based Active Structural Control Accounting For AMD Constraints", *Proceedings of 2nd World Conference on Structural Control*, Kyoto, Japan, 1577-1584.
- Ohtori, Y., Christenson, R. E., Spencer, B. F. Jr. and Dyke, S. J. (2000), "Benchmark Control Problems for Seismically Excited Nonlinear Buildings", <http://www.nd.edu/~quake>
- Patten, W. N., Kuo, C. C., He, Q, Liu, L. and Sack, R. L. (1994), "Seismic Structural Control Via Hydraulic Semiactive Vibration Dampers (SAVD)", *Proc. First World Conference on Structure Control*, FA2. 83-89
- Paola, M. D. (1998), "Digital Simulation of Wind Field Velocity", *J. Wind Engrg. and Industrial Aerodyn.*, Vol. 74-76, 91-109
- Qin, S.J. and Badgwell, T.J. (1996), "An overview of industrial model predictive control technology", *Chemical Process Control-V.*, Proceedings published as AIChE Symposium Series 316, vol. 93, 232-256, CACHE and AIChE.
- Reinhorn, A. M., Soong, T. T. and Wen, C. Y. (1987), "Base-isolated structures with active control", *Proc. ASME PVP Conf.*, PVP-127,413-420
- Reinhorn, A. M., Soong, T. T., Lin, R. C., Wang, Y. P., Fukao, Y., Abe, H. and nakai, M. (1989), *1:4 Scale Model Studies of Active Tendon Systems and Active Mass Dampers fo Aseismic Protection*, Technical Report NCEER-89-0026
- Reinhorn, A. M., Soong, T. T., riley, M. A., Lin, R. C., Aizawa, S. and Higashino, M. (1993), "Full-Scale Implementstion of Active Control II: Installation and Performance." *J. Struct. Engrg.*, ASCE, 119(6), 1935-1960.
- Reinhorn, A. M. and Riley, M. A. (1994), "Control of Bridge vibrations with Hybrid Devices", *Proc. of First World Conference on Structure Control*, TA2, 50-59
- Reinhorn, A. M., Soong, T. T., and Cao, H. (1995), "Preliminary Evaluation of Wind Induced Response of Nanjing Tower", Department of Civil Engineering, SUNY Buffalo, NY
- Richalet, J., Rault, A., Testud, J. L. and papon, J. (1978), "Model Predictive Heuristic Control: Application to Industrial Processes", *Automatica*, Vol. 14, 413
- Ricker, N. L. (1990), "Model Predictive Conttol with State Estimation", *Ind. & Eng. Chem. Res.*, Vol. 29, 374-382

- Rodellar, J., Barbat, A. H. and Matin-Sanchez J. M. (1987), "Predictive Control of Structures." *ASCE, J. Engrg. Mech.*, Vol. 113, No. 6, pp. 797-812.
- Rodellar, J., Chung L. L. Soong T. T. and Reinhorn A. M. (1987), "Experimental Digital Control of Structures" *ASCE, J. Engrg. Mech.*, Vol. 115, No. 6, pp. 1245-1261.
- Roorda, J. (1975), "Tendon Control in Tall Buildings", *J. of the Struct. Div., ASCE*, Vol. 101, No. 3, 505-521
- Rouhani, R. and Mehra, R. K. (1982), "Model Algorithmic Control (MAC): Basic Theoretical Properties", *Automatica*, Vol. 18, 401
- Sack, R. L., Kuo, C. C., Wu, H. C., Liu, L. and Patten, W. N. (1994), "Seismic Motion Control Via Semiactive Hydraulic Actuators", *Proc. U. S. Fifth Nat. Conf. on Earthquake Engrg.*
- Sakamoto, M., Kobori, T., Yamada, T., Takahashi, M. (1994), "Practical Applications of Active and Hybrid Response Control Systems and Their Verifications By Earthquake and Strong Wind Observations", *Proc. First World Conference on Structure Control*, WP2-90-99.
- Schmitendorf, Jabbari, F. and Yang, J. N. (1994a), "Robust Control Techniques for Buildings Under earthquake Excitation", *Earthquake Engrg. and Struct. Dyn.*, Vol. 23, 539-552
- Schmitendorf, W. E., Kose, I. E., Jabbari, F. and Yang, J. N. (1994b), " H_∞ Control of Seismic-Excited Buildings Using Direct Output Feedback", *Proc. of First World Conference on Structure Control*, TA1, 11-20
- Slotine, J. J. E. (1984), "Sliding Controller Design for Nonlinear Systems", *Int. J. Control*, Vol. 40 No. 2
- Soong, T. T. and Skinner G. K. (1981), "An Experimental Investigation of Active Structural Control," *ASCE J. Eng. Mech. Div.*, 107, 1057-1067
- Soong, T. T. (1990), *Active Structure Control: Theory and Practice*, Longman Scientific and Technical, Essex, England
- Soong, T. T. (1998), "Structural Control: Impact On Structural Research in General", *Proceedings of Second World Conference on Structural Control*, Vol. 1, 5-14.
- Spencer, B. F. Jr., Suhardjo, J. and Sain, M. K., (1991), "Frequency Domain Control Algorithms for Civil Engineering Applications", *Proc. of the Int. Workshop on Tech. for Hong Kong's Infrastructure Dev.*, Hong Kong, 169-178

- Spencer, B. F. Jr., Suhardjo, J. and Sain, M. K., (1994), "Frequency Domain Optimal Control for Aseismic Protection", *J. Engrg. Mech., ASCE*, Vol 120, No.1, 135-159
- Spencer, B. F. Jr., Dyke, S. J. and Sain, M. K. (1996), "Magnetorheological Dampers: A New Approach to Seismic Protection of Structures", *Proc. Conf. on Decision and Control*, 676-681
- Spencer, B. F., Jr. and Sain, M. K. (1997), "Controlling Buildings: A New Frontier in Feedback", *IEEE Control System Magazine: Special Issue on Emerging Technologies*, Vol. 17, No. 6, 19-35.
- Spencer, B. F. Jr., Carlson, J. D., Sain, M. K. and Yang, G. (1997), "On the Current Status of Magnetorheological Dampers: Seismic Protection of Full-Scale Structures", *Proc. Am. Control Conf.*
- Spencer, B. F. Jr., Dyke, S. J., Sain, M. K., and Carlson, J. D. (1997), "Phenomenological Model of A Magnetorheological damper", *J. Engrg. Mech., ASCE*, Vol. 123, No. 3, 230-238.
- Spencer Jr., B.F., and Yang, G. (1998). "Earthquake Simulator Control by Transfer Function Iteration", *Proc., Amer. Control Conf.*
- Spencer, Jr., B. F., Dyke, S. J. and Doeskar, H. S., (1998), "Benchmark Problem in Structural Control Part 1: Active Mass Driver system, and Part 2: Active Tendon System", *Earthquake Engrg and Structural Dynamics*, Vol. 27, No. 11, 1127-1147.
- Structural Control (1994), *Proceedings of First World Conference on Structural Control*, Vol. 1,2 and 3.
- Structural Control (1998), *Proceedings of Second World Conference on Structural Control*, Vol. 1,2 and 3.
- Suhardjo, J., Spencer, B. F. Jr. and Sain, M. K. (1990), "Feedback-Feedforward Control of Structures Under Seismic Excitation", *Structural Safety*, Vol. 8, 69-89
- Suhardjo, J. (1990), *Frequency Domain Techniques for Control of Civil Engineering Structures with Some Robustness Considerations*, PhD Dissertation, University of Notre Dame
- Suhardjo, J., Spencer, B. F. Jr. and Kareem A.. (1992), "Frequency Domain Optimal Control of Wind Excited Buildings", *J. Engrg Mech., ASCE*, Vol. 118, No. 12, 2463-2481
- Suhardjo, J. and Kareem, A. (1997), "Structural Control of Offshore Platforms." *Proceedings of the 7th International Offshore and Polar Engineering Conference ISOPE-97*, Honolulu, May 25-30.

- Tanida, K., Koike, K., Mutaguchi, K. and Uno, N. (1991), "Development of hybrid Active Passive Mass Damper", *Active and Passive Damping, ASME, PVP-Vol. 211*, 21-26
- Utkin, V. I. (1977), "Variable Structure Systems with Sliding Modes", *IEEE Trans. on Automatic Control, AC-22*, 212-222
- Wang, Y. P., and Liu, C. J. (1994), "Active Control of Sliding Structures Under Strong earthquakes", *Proc. of First World Conference on Structure Control, FP1*, 23-32
- Welt, F. and Modi, V. J. (1989a), "Vibration Damping Through Liquid Sloshing: Part I--A Nonlinear Analysis", *Proc. diagnostics, Vehicle Dyn. and Spec. Topics, ASME, Des. Engrg. Div.*, Vol. 18-5, 149-156
- Welt, F. and Modi, V. J. (1989b), "Vibration Damping Through Liquid Sloshing: Part II-- Experimental Results", *Proc. diagnostics, Vehicle Dyn. and Spec. Topics, ASME, Des. Engrg. Div.*, Vol. 18-5, 157-165
- Wen, Y. K., Ghaboussi, J., Venini, P. and Nikzad, K. (1992), "Control of Structures Using Neural Networks", *Proc. of the 2nd USA-Italy-Japan Workshop on Structural Control and Intelligent Systems*, USC Publication CE-9210, 232-251
- Wu, J. C., Yang, J. N. and Schmitendorf, W. (1998), "Reduced Order H_∞ and LQR Control for Wind Excited Tall Buildings", *Engrg. Structures*, Vol. 20, No. 3, 222-236.
- Yamada, K. and Kobori T. (1996), "Linear Quadratic Regulator for Structure Under On-line Predicted Future Seismic Excitation." *Earthquake Engineering and Structural Dynamics*, Vol. 25, pp. 631-644
- Yang, G, Ramallo, J.C., Spencer Jr., B.F., Carlson, J.D., and Sain, M.K. (2000) ."Dynamic Performance of Large-Scale MR Fluid Damper", 14th ASCE Engineering Mechanics Conference, Austin, TX, May 21 - 24
- Yang, G. Spencer, B. F. Jr., Carlson, J. D., and Sain, M. K. (2001), "Dynamic Modeling and Performance Considerations on Large-Scale MR Fluid Damper", ICOSAR, Newport Beach, CA, June 17-22
- Yang, J. N. and Yao, J. T. P. (1974), "Formulation of Structural Control", Technical Report CE-STR-74-2, School of Civil Engineering, Purdue University
- Yang, J. N. and Giannopoulos, F. (1978), "Active tendon Control of Structures", *J. of Engrg. Mech., ASCE*, Vol. 104 (EM3), 551-568
- Yang, J. N., Wu, J. C. and Hsu, S. Y. (1994a), "Parametric Control of Seismic-Excited Structures", *Proc. First World Conference on Structure Control*, WP1. 88-97

- Yang, J. N., Wu, J. C., Reinhorn, A. M., Riley, M., Schmitendorf, W. E. and Jabbari, F. (1994b), "Experimental Verifications of H_∞ and Sliding Mode Control for Seismic-Excited Buildings", *Proc. First World Conference on Structure Control*, TP4, 63-72
- Yang, J. N., Wu, J. C., Agrawal A. K. (1998), "A Benchmark Problem For Response Control of Wind-Excited Tall Buildings", *Proc. Second World Conference on Structure Control*.
- Yang J. N., Agrawal A. K., Samali B. and Wu J. C. (2000), "A Benchmark Problem For Response Control of Wind-Excited Tall Buildings", *14-th Engineering Mechanics Conference, Austin, Texas*.
- Yao, J. T. P. (1972), "Concept of Structural Control", *Journal of Structural Division, ASCE*, No. 98(ST7), 1567-1574.
- Yoshida, K. and Wannabe, T. (1994), "Robust Control of Structural Vibrations using Active Dynamics Vibration Absorber Systems", *Proc. of First World Conference on Structure Control*, TP4, 53-62
- Yoshida, K., Yoshida, S. and Takeda, Y. (1998), "Semi-Active Control of Base Isolation Using Feedforward Information of Disturbance", *Proc. Second World Conference on Structure Control*, Vol. 1, 377-386.
- Zhu, G. G. and Skelton, R. E. (1998), "Output Covariance Constraint Problem with Disturbance Feedback", *Proc. First World Conference on Structure Control*, FP4, 4-32-41